Multi Particle Dark Matter: Dynamics and Phenomenological Implications

Purusottam Ghosh

A thesis
submitted for the degree of

Doctor of Philosophy

Supervisor

Dr. Subhaditya Bhattacharya

Department of Physics
Indian Institute of Technology Guwahati
Guwahati - 781039, Assam, India

Multi Particle Dark Matter: Dynamics and Phenomenological Implications

A thesis submitted by

Purusottam Ghosh

to

Indian Institute of Technology Guwahati
in partial fulfillment of the requirements
for the award of the degree of
Doctor of Philosophy in Physics

Supervisor

Dr. Subhaditya Bhattacharya

Department of Physics
Indian Institute of Technology Guwahati
Guwahati - 781039, Assam, India

Dedicated

To

My Family

Declaration

Purusottam Ghosh
Roll No. 146121003
Department of Physics
IIT Guwahati
Guwahati, India

I hereby declare that works presented in the thesis entitled "**Multi Particle Dark Matter: Dynamics and Phenomenological Implications**" has been carried out by me under the supervision of Dr. Subhaditya Bhattacharya at the Department of Physics, Indian Institute of Technology Guwahati, India. The thesis has not been submitted anywhere else for any degree. Works presented in the thesis are all my own unless referenced to the contrary in the thesis.

Purusottam Ghosh

Date

Certificate

Dr. Subhaditya Bhattacharya
Assistant Professor
Department of Physics
Indian Institute of Technology Guwahati
Guwahati, India
email:subha@iitg.ac.in

It is certified that the work contained in the thesis entitled "**Multi Particle Dark Matter: Dynamics and Phenomenological Implications**" by Mr. Purusottam Ghosh (Roll No - 146121003), a Ph.D. student in the Department of Physics, Indian Institute of Technology Guwahati is carried out under my supervision and has not been submitted elsewhere for the award of any other degree.

Dr. Subhaditya Bhattacharya

Date

Acknowledgements

First and foremost, I would like to thank my supervisor Dr. Subhaditya Bhattacharya for all his support and encouragement throughout my PhD work. His friendly behaviour made me comfortable to work with him. I must say it has been a great learning period of my life, not only in academic way, but also to grow up as a responsible person.

I also acknowledge to my Doctoral committee members: Prof. Bipul Bhuyan, Dr. Sayan Chakrabarti and Prof. Partha Sarathi Mandal for their valuable time and insightful comments and suggestions at every point of time. I am thankful to present and former departmental heads Prof. Subhradip Ghosh and Prof. Poulose Poulose for all their help and support during my PhD periods. I should not forget to thank all the faculty members who taught me during my MSc and PhD periods and all non-teaching staffs specially Basab Da and Hemanta Da for timely help in different computational issues. I would also like to thank all the members of HEP Journal Club as well to keep me updated of the latest developments in the field and arguing on possibilities to look forward.

I thank all my collaborators and co-authors: Dr. Arunansu Sil, Dr. Tritha Sankar Ray, Dr. Narendra Sahu, Prof. Poulose Poulose, Dr. Debasish Borah, Dr. Abhijit Saha, Basbendu Barman, Tarak Nath Maity, Dr. Nirakar Sahoo, Shivam Verma and Sourabh Kadam. It was great experience to work with them and I have learned a lot. My special thanks goes to Dr. Arunansu Sil with whom I did my M.Sc. project for introducing me into the fascinating field of High Energy Physics. I am also thankful to my friend cum collaborators Basbendu Baraman, Abhijit Saha and Tarak Nath Maity for having many academic discussions. I would like to thank Dr. Debaprasad Maity for having many discussions beyond my territory.

I extend my gratitude to my seniors Dr. Biswajit Karmakar, Dr. Rashidul Islam and Dr. Sunanda Patra for their academic support in several ways during this period. I also like to thank Dr. Pankaj Saha and Sujay Shil for being in my side whenever I needed them.

I would like to thank all my Phd batchmates: Indu, Goutam, Jayjit, SS Goutam Budha, Gobinda, Ghanashyam, Joy, Jagan, Shrinivas for their support and encouragements. I also take this opportunity to thank my childhood friends Sumit, Anu who always helped me in difficult situations.

Beyond friends and collaborators, I must thank the congenial academic environment at IIT Guwahati and its support to the research scholars to excel in their study, be it the travel grant, computation facilities or readily available administration.

It would be incomplete without thanking the biggest source my strength, my family members: baba: Mr. Satya Narayan Ghosh, ma: Mrs. Manju Ghosh, dada: Mr. Swapan Ghosh, boudi: Mrs. Jothna Ghosh, the sweetest kids of my family: Rubu, Babu (Soumajit) and Shome (Ankit), Late grandmother Sovamani and Late beloved elder sister Sumitra. Without them, I wouldn't be the person I am. I would like to express my heartiest gratitude to my darling and wife Mrs. Sarmila Bhakat for her support, love and care. Thank you.

Acronyms

SM	:	Standard Model
EW	:	Electroweak
EWSB	:	Electroweak Symmetry Breaking
SSB	:	Spontaneous Symmetry Breaking
VEV	:	Vacuum Expectation Value
BSM	:	Beyond Standard Model
DM	:	Dark Matter
CDM	:	Cold Dark Matter
SSDM	:	Scalar Singlet Dark Matter
IDM	:	Inert Doublet Dark Matter
VLF	:	Vector Like Fermion
WIMP	:	Weakly Interacting Massive Particles
FIMP	:	Feebly Interacting Massive Particles
SIMP	:	Strongly Interacting Massive Particles
LHC	:	Large Hadron Collider
ILC	:	International Linear Collider
RGE	:	Renormalization Group Evolution
BR	:	Branching Ratio
BP	:	Benchmark Points
VBF	:	Vector Boson Fusion
h.c.	:	Hermitian Conjugate
UFO	:	Universal FeynRule Output
LFV	:	Lepton Flavour Violation
MeV	:	Mega electron Volt
GeV	:	Giga electron Volt

TeV	:	Tera electron Volt
BEQ	:	Boltzmann Equation
CBEQ	:	Coupled Boltzmann Equation
d.o.f	:	degrees of freedom

Abstract

Discovery of 'Higgs' boson at LHC in 2012 validates the Standard Model (SM) of particle physics as fundamental governing theory of Strong, Weak and Electromagnetic interactions. However many unresolved issues persist. Existence of Dark Matter (DM) is one of them. In spite of many astrophysical hints for DM, we do not have much knowledge about it, barring from its electromagnetic charge neutrality, gravitational effect at large scale and stability. As a result, nature of DM, as a fundamental particle, whether scalar, fermion, vector boson (or with even more exotic spin) or admixture of them in multipartite form remain an open question. The only measured quantity related to DM is its relic density which can be achieved mainly via two mechanisms: (a) thermal freeze-out and (b) non-thermal freeze-in. Weakly interacting massive particles (WIMP) are most popular DM candidates due to their discovery potential at direct and collider searches. The main idea of the thesis is to explore multi-particle DM scenarios in WIMP paradigm with non-negligible DM-DM interaction and study effects in relic density, direct search and collider signal. Apart from DM, explaining correct neutrino mass within SM is a difficult task. We therefore also aim to connect multipartite dark sector to neutrinos and see its phenomenological interpretation. Amongst other constraints, Higgs vacuum stability is studied in elaboration. We choose the simplest single component WIMP like DM framework, a real scalar singlet as a base model. In the first work, we extend it by another scalar singlet to serve as second DM component stabilised by additional $\mathcal{Z}_2 \times \mathcal{Z}_2^{'}$ symmetry, having Higgs portal interactions. We show DM-DM interactions help to achieve a larger allowed parameter space through relic density and direct search constraints. In the second work, a two component DM model is addressed where in addition to scalar singlet DM, a fermion DM is assumed which arises due to singlet-doublet admixture of additional vector like fermions. Presence of a mediator between the dark sectors opens up a large parameter space through DM-DM conversion. Hadronically quiet dilepton signature, arising from the fermion dark sector is aided at LHC by the presence of a lighter scalar DM component. In the last work, inert $SU(2)_L$ scalar doublet acts as the second DM component and aids vacuum stability. Neutrino mass generation is addressed by the presence of heavy right handed neutrinos, which destabilise the Higgs vacuum. While DM-DM interaction helps achieving a large allowed parameter space, high scale validity puts further constraints, for example, on the mass splitting between the charged and neutral component of inert doublet, which has important implication to its leptonic signature(s) at LHC.

List of Publications

1⋆. Subhaditya Bhattacharya, **Purusottam Ghosh**, Poulose Poulose; *"Multipartite Interacting Scalar Dark Matter in the light of updated LUX data"*, Published in **JCAP 1704 (2017) no.04, 043** [1607.08461].

2. Subhaditya Bhattacharya, **Purusottam Ghosh**, Tarak Nath Maity, Tirtha Sankar Ray; *"Mitigating Direct Detection Bounds in Non-minimal Higgs Portal Scalar Dark Matter Models"*, Published in **JHEP 1710 (2017) 088** [1706.04699].

3. **Purusottam Ghosh**, Abhijit Kumar Saha and Arunansu Sil; *"Electroweak Vacuum Stability in an Extended Framework of Dark Matter and Neutrinos"*, Published in **Phys. Rev. D97 (2018) no.7, 075034** [1706.04931].

4⋆. Subhaditya Bhattacharya, **Purusottam Ghosh**, Narendra Sahu; *"Multipartite Dark Matter with Scalars, Fermions and signatures at LHC"*, Published in **JHEP 1902 (2019) 059** [1809.07474].

5. Subhaditya Bhattacharya, **Purusottam Ghosh**, Nirakar Sahoo, Narendra Sahu; *"A Mini-review on Vector-like Leptonic Dark Matter, Neutrino Mass and Collider Signatures"*, Published in **Front.in Phys. 7 (2019) 80** [1812.06505].

6. Basabendu Barman, Subhaditya Bhattacharya, **Purusottam Ghosh**, Saurabh Kadam, Narendra Sahu; *"Fermion Dark Matter with Scalar Triplet at Direct and Collider Searches"*, Published in **Phys.Rev. D100 (2019) no.1, 015027** [1904.07562].

7. Subhaditya Bhattacharya, **Purusottam Ghosh**, Shivam Verma ; *"SIMPler realisation of Scalar Dark Matter"*, Published in **JCAP 2001 (2020) no.01,040** [1902.01217].

8⋆. Subhaditya Bhattacharya, **Purusottam Ghosh**, Abhijit Kumar Saha, Arunansu Sil; *"Two component dark matter with inert Higgs doublet: neutrino mass, high scale validity and collider searches"*, Accepted in **JHEP** [1905.12583].

9. Basabendu Barman, Debasish Borah, **Purusottam Ghosh**, Abhijit Kumar Saha ; *"Flavoured gauge extension of singlet-doublet fermionic dark matter: neutrino mass, high scale validity and collider signatures "*, Published in **JHEP 1910 (2019) 257** [arXiv:1907.10071].

Note: ⋆ marked publications are included in the thesis.

Contents

Chapter 1

Introduction

Contents

1.1 An overview of the Standard Model

The Standard Model (SM) of particle physics is the basic building block of studying fundamental particles and interactions based on quantum field theory and symmetry principle [1–5]. The model describes three fundamental forces of nature namely strong, electromagnetic and weak forces. The underlying local gauge symmetry is $\mathcal{G}_{\rm SM} \equiv SU(3)_C \otimes SU(2)_L \otimes U(1)_Y$ [1–4]. This model contains three generations of quarks, three generation of leptons and their antiparticles; one scalar and four gauge bosons which are the mediator of three fundamental interactions. The particles contained in SM along with their representation under gauge group $\mathcal{G}_{\rm SM}$ are tabulated in Table:1.1.

SM fermion fields ψ (quarks and leptons) can be represented into two chiral states: left handed (LH), ψ_L and right handed (RH), ψ_R. The LH and RH Dirac chiral states are defined as:

$$\psi_L = \frac{1}{2}\Big(1-\gamma_5\Big)\psi \quad \text{and} \quad \psi_R = \frac{1}{2}\Big(1+\gamma_5\Big)\psi. \tag{1.1}$$

The quark sector consists of three up type quarks

$$q^u = u(\text{up}), \qquad c(\text{charm}), \qquad t(\text{top})$$

and their antiparticles. The quarks are triplet under $SU(3)_C$ and take part in strong interaction. Left handed (LH) up and down type quarks together form $SU(2)_L$ quark doublet (with three generations):

$$Q_L = \begin{pmatrix} q^u_L \\ q^d_L \end{pmatrix} : \qquad \begin{pmatrix} u^i_L \\ d^i_L \end{pmatrix}, \qquad \begin{pmatrix} c^i_L \\ s^i_L \end{pmatrix}, \qquad \begin{pmatrix} t^i_L \\ b^i_L \end{pmatrix}$$

Right handed (RH) up and down type quarks are singlet under $SU(2)_L$:

$$q^u_R = u^i_R,\ c^i_R,\ t^i_R \qquad \text{and} \qquad q^d_R = d^i_R,\ s^i_R,\ b^i_R$$

Fields			$SU(3)_C \otimes SU(2)_L \otimes U(1)_Y$
Quarks	LH: $Q_L = \begin{pmatrix} q_L^u \\ q_L^d \end{pmatrix}$	$\begin{pmatrix} u_L^i \\ d_L^i \end{pmatrix}, \begin{pmatrix} c_L^i \\ s_L^i \end{pmatrix}, \begin{pmatrix} t_L^i \\ b_L^i \end{pmatrix}$	$3,\ 2,\ 1/3$
	RH: q_R^u	$u_R^i,\ c_R^i,\ t_R^i$	$3,\ 1,\ 4/3$
	RH: q_R^d	$d_R^i,\ s_R^i,\ b_R^i$	$3,\ 1,-2/3$
Leptons	LH: $L_L = \begin{pmatrix} \nu_{\ell L} \\ \ell_L \end{pmatrix}$	$\begin{pmatrix} \nu_{eL} \\ e_L \end{pmatrix}, \begin{pmatrix} \nu_{\mu L} \\ \mu_L \end{pmatrix}, \begin{pmatrix} \nu_{\tau L} \\ \tau_L \end{pmatrix}$	$1,\ 2,-1$
	RH: ℓ_R	$e_R,\ \mu_R,\ \tau_R$	$1,\ 1,\ -2$
Gauge bosons	$SU(3)_C$ mediator:	G_μ^a	$8,\ 1,\ 0$
	$SU(2)_L$ mediator:	$W_\mu^{1,2,3}$	$1,\ 3,\ 0$
	$U(1)_Y$ mediator:	B_μ	$1,\ 1,\ 0$
Scalar	Higgs: H	$\begin{pmatrix} w^+ \\ \phi_0 \end{pmatrix}$	$1,\ 2,\ 1$

Table 1.1: Charge assignment of SM fields under the gauge group $\mathcal{G}_{\rm SM} \equiv SU(3)_C \otimes SU(2)_L \otimes U(1)_Y$. Electromagnetic charge is obtained by: $Q = I_3 + \frac{Y}{2}$, where I_3 is the third component of isospin and Y is the $U(1)_Y$ hypercharge quantum number. Here $i = r, g, b$ and $a = 1, 2, .., 8$ represent colour charges of quarks and gluon respectively.

Again each quark must have three colour states which is denoted as: $i = r$(red), g(green), b(blue).

The leptons sector consists of three charged lepton as :

$$\ell = e(\text{electron}), \qquad \mu(\text{muon}), \qquad \tau(\text{tau})$$

and three neutral lepton, called neutrinos as:

$$\nu_\ell = \nu_e(\text{electron neutrino}) \quad , \ \nu_\mu(\text{muon neutrino}), \qquad \nu_\tau(\text{tau neutrino})$$

and their antiparticles. LH charged and neutral leptons form $SU(2)_L$ doublet (with three generations) :

$$L_L = \begin{pmatrix} \nu_{\ell L} \\ \ell_L \end{pmatrix} : \qquad \begin{pmatrix} \nu_{eL} \\ e_L \end{pmatrix}, \qquad \begin{pmatrix} \nu_{\mu L} \\ \mu_L \end{pmatrix}, \qquad \begin{pmatrix} \nu_{\tau L} \\ \tau_L \end{pmatrix};$$

RH charged leptons are again singlet under the same $SU(2)_L$:

$$\ell_R = e_R, \qquad \mu_R, \qquad \tau_R.$$

RH neutrinos are absent in SM owing to small/negligible neutrino masses. The leptons are singlet under $SU(3)_C$ and therefore do not interact via strong interaction.

Strong interaction is mediated by gluons ($G_\mu^{a=1,..8}$) as $SU(3)_C$ gauge boson. Weak interaction is mediated by $W^\pm, Z$ (linear combination of $W_\mu^{a=1,2,3}$ and B_μ) whereas the electromagnetic interaction is mediated by photon γ (A_μ) (linear combination of W_μ^3 and B_μ). In this small review, we will mainly focus on electroweak part of SM Lagrangian, which is required for the extension to physics beyond the SM that we consider in this thesis. The symmetry associated with the weak and electromagnetic interaction is $SU(2)_L \otimes U(1)_Y$ and known as the SM electroweak (EW) theory proposed by Glashow, Weinberg and Salam [1–4]. In the scalar sector the minimal possibility

is to introduce one scalar $SU(2)_L$ doublet which is known as Higgs doublet, H (with $Y = 1$) expressed as:

$$H = \begin{pmatrix} w^+ \\ \phi_0 \end{pmatrix}. \tag{1.2}$$

Now we can write SM electroweak (EW) Lagrangian invariant under the weak gauge symmetry $SU(2)_L \otimes U(1)_Y$ as

$$\mathcal{L}_{\rm SM}^{\rm EW} = \mathcal{L}_{\rm Gauge} + \mathcal{L}_{\rm Fermion} + \mathcal{L}_{\rm Yukawa} + \mathcal{L}_{\rm Scalar}. \tag{1.3}$$

Note that the Lagrangian involving $SU(3)_C$ is absent in $\mathcal{L}_{\rm SM}^{\rm EW}$. The $\mathcal{L}_{\rm Gauge}$ in Eqn.1.3 involving $SU(2)_L$ and $U(1)_Y$ gauge fields can be written as

$$\mathcal{L}_{\rm Gauge} = -\frac{1}{4} W^a_{\mu\nu}\, W^{\mu\nu,\,a} - \frac{1}{4} B_{\mu\nu} B^{\mu\nu}, \tag{1.4}$$

where

$$W^a_{\mu\nu} = \partial_\mu W^a_\nu - \partial_\nu W^a_\mu + g_2\, \epsilon^{abc}\, W^b_\mu\, W^c_\nu \qquad \text{and} \qquad B_{\mu\nu} = \partial_\mu B_\nu - \partial_\nu B_\mu.$$

g_2 and g_1 are the gauge coupling constants of $SU(2)_L$ and $U(1)_Y$ gauge group respectively and ϵ^{abc} is the structure constant of $SU(2)_L$.

The kinetic terms for fermions (leptons and quark) are given by

$$\begin{aligned}
\mathcal{L}_{\rm Fermion} &= \overline{Q_L}\, i\gamma^\mu \Big(\partial_\mu - i\, g_2 \frac{\sigma^a}{2}\, W^a_\mu - i\, g_1 \frac{Y_{Q_L}}{2}\, B_\mu\Big) Q_L \\
&+ \overline{q^u_R}\, i\gamma^\mu \Big(\partial_\mu - i\, g_1 \frac{Y_{q^u_R}}{2}\, B_\mu\Big) q^u_R + \overline{q^d_R}\, i\gamma^\mu \Big(\partial_\mu - i\, g_1 \frac{Y_{q^d_R}}{2}\, B_\mu\Big) q^d_R \\
&+ \overline{L_L}\, i\gamma^\mu \Big(\partial_\mu - i\, g_2 \frac{\sigma^a}{2}\, W^a_\mu - i\, g_1 \frac{Y_{L_L}}{2}\, B_\mu\Big) L_L \\
&+ \overline{\ell_R}\, i\gamma^\mu \Big(\partial_\mu - i\, g_1 \frac{Y_{l_R}}{2}\, B_\mu\Big) \ell_R,
\end{aligned} \tag{1.5}$$

where Y_{Q_L}, $Y_{q^u_R}$, $Y_{q^d_R}$, Y_{L_L} and Y_{ℓ_R} denote weak hypercharge (generator of $U(1)_Y$) of Q_L, q^u_R, q^d_R, L_L and ℓ_R fields respectively, mentioned in Table:1.1. $\frac{\sigma^a}{2}$ (with $a = 1, 2, 3$) are the generators of $SU(2)_L$ group where σ^a are the Pauli spin matrices:

$$\sigma^1 = \begin{pmatrix} 0 & 1 \\ 1 & 0 \end{pmatrix}, \quad \sigma^2 = \begin{pmatrix} 0 & -i \\ i & 0 \end{pmatrix}, \quad \sigma^3 = \begin{pmatrix} 1 & 0 \\ 0 & -1 \end{pmatrix}. \tag{1.6}$$

The Yukawa Lagrangian in SM involves the interaction with Higgs boson as,

$$\mathcal{L}_{\rm Yukawa} = -\sum_{i,j=1,2,3} \Big(y^{ij}_u\, \overline{Q_{iL}}\, \widetilde{H}\, q^u_{jR} + y^{ij}_d\, \overline{Q_{iL}}\, H\, q^d_{jR} + y^{ij}_\ell\, \overline{L_{iL}}\, H\, \ell_{jR} + h.c \Big), \tag{1.7}$$

where i, j stands for three generation of quarks and leptons and $\widetilde{H} = i\sigma^2 H^*$.

The scalar part of the Lagrangian is given by

$$\mathcal{L}_{\rm Scalar} = \Big| \Big(\partial_\mu - i\, g_2 \frac{\sigma^a}{2}\, W^a_\mu - i\, g_1 \frac{Y_H}{2}\, B_\mu\Big) H \Big|^2 - V(H), \tag{1.8}$$

where

$$V(H) = -\mu_H^2 \left(H^\dagger H\right) + \lambda_H \left(H^\dagger H\right)^2. \tag{1.9}$$

The SM Higgs scalar doublet, H is defined as

$$H \equiv \begin{pmatrix} w^+ \\ \phi_0 \end{pmatrix} = \begin{pmatrix} \frac{w_1+iw_2}{\sqrt{2}} \\ \frac{h_0+iz}{\sqrt{2}} \end{pmatrix}, \tag{1.10}$$

where w_1, w_2, h_0 and z are the four real scalar degrees of freedom.

The electroweak part of the Lagrangian $\mathcal{L}_{\rm SM}^{\rm EW}$ is invariant under $SU(2)_L \otimes U(1)_Y$ symmetry. SM gauge symmetry do not allow us to write the mass terms of fermions and gauge bosons. So fermions and gauge bosons are massless under the unbroken $SU(2)_L \otimes U(1)_Y$ symmetry which contradict our observation. The mass of the SM particles can be generated through spontaneous symmetry breaking or Higgs mechanism discussed next.

Higgs Mechanism

The scalar Higgs doublet forms a gauge invariant potential $V(H)$ as mentioned above. Mass of the SM particles can be generated with non zero vacuum expectation value of the so called Higgs boson as almost simultaneously identified by Robert Brout, Francois Englert, Peter Higgs, Gerald Guralnik, C. R. Hagen and Tom Kibble through electroweak symmetry breaking (EWSB) mechanism [3–5]. The quartic coupling, λ_H in the Higgs potential $V(H)$ should be positive i.e. $\lambda_H > 0$ to ensure boundedness of the potential. For the situation $\mu_H^2 < 0$ and $\lambda_H > 0$ in Eqn.1.9, the minima of the scalar potential arises at $\langle H \rangle = 0$ and the symmetry of the Lagrangian is preserved. Then, the theory only describes massless fermions and gauge bosons with massive scalar contrary to our observation. But for $\mu_H^2 > 0$ and $\lambda_H > 0$, non zero vacuum arises at $\langle H \rangle = v/\sqrt{2}$ with $v = \sqrt{\frac{\mu_H^2}{\lambda_H}}$. If we choose a specific non-zero vev, the EW gauge group, $SU(2)_L \otimes U(1)_Y$ is broken to a remnant $U(1)_Q$ i.e.

$$\mathcal{G}_{\rm SM}^{\rm EW} \equiv SU(2)_L \otimes U(1)_Y \xrightarrow{\langle H \rangle = v/\sqrt{2}} U(1)_Q \ ,$$

where the electric charge is obtained as the combination of isospin and hypercharge as mentioned before:

$$Q = I_3 + \frac{Y}{2}.$$

We choose the minima along h_0 direction as $h+v$. The Higgs field around the minima is expressed as

$$H = \begin{pmatrix} \frac{w_1+iw_2}{\sqrt{2}} \\ \frac{h+v+iz}{\sqrt{2}} \end{pmatrix} \equiv \begin{pmatrix} w^+ \\ \frac{h+v+iz}{\sqrt{2}} \end{pmatrix}, \tag{1.11}$$

where $w^\pm$ and z are massless Goldstone bosons and h is a physical Higgs boson. Physical $W^\pm$ and Z bosons eat up the Goldstone bosons and become massive [3–5]. The Higgs doublet can then be written in unitary gauge as:

$$H = \begin{pmatrix} 0 \\ \frac{h+v}{\sqrt{2}} \end{pmatrix}, \tag{1.12}$$

and predict the existence of a physical scalar h. After SSB, the mass terms of physical gauge bosons arise from the kinetic term given in Eqn.1.8 as :

$$m_{W^\pm}^2 = \left(\frac{1}{2}g_2 v\right)^2, \quad m_Z^2 = \left(\frac{1}{2}\sqrt{g_2^2+g_1^2}\,v\right)^2, \quad \text{and} \quad m_A^2 = 0\ . \tag{1.13}$$

The physical gauge bosons are expressed as linear combination of $SU(2)_L$ and $U(1)_Y$ gauge fields as follows:

$$W_\mu^\pm = \frac{1}{\sqrt{2}}\Big(W_\mu^1 \mp W_\mu^2\Big), \tag{1.14}$$

$$Z_\mu = \cos\theta_W\ W_\mu^3 - \sin\theta_W\ B_\mu, \tag{1.15}$$

$$A_\mu = \sin\theta_W\ W_\mu^3 + \cos\theta_W\ B_\mu. \tag{1.16}$$

In above expression, Weinberg angle is defined as $\theta_W = \tan^{-1}\left(\frac{g_1}{g_2}\right)$. Now, the fermions (leptons and quarks) obtain masses through the Yukawa interactions as in Eqn.1.8 through non zero Higgs vev,

$$\mathcal{L}_{\text{Yukawa}}^{\text{mass}} = -\sum_{i,j=1,2,3}\Big(\frac{y_u^{ij}v}{\sqrt{2}}\ \overline{q_{iL}^u}\ q_{jR}^u + \frac{y_d^{ij}v}{\sqrt{2}}\ \overline{q_{iL}^d}\ \ q_{jR}^d + \frac{y_\ell^{ij}v}{\sqrt{2}}\ \overline{\ell_{iL}}\ \ell_{jR} + h.c\Big). \tag{1.17}$$

Additionally, Yukawa interactions between fermions (leptons and quarks) with SM Higgs are obtained as,

$$\mathcal{L}_{\text{Yukawa}}^{\text{int.}} = -h\sum_{i,j=1,2,3}\Big(\frac{y_u^{ij}}{\sqrt{2}}\ \overline{q_{iL}^u}\ q_{jR}^u + \frac{y_d^{ij}}{\sqrt{2}}\ \overline{q_{iL}^d}\ \ q_{jR}^d + \frac{y_\ell^{ij}}{\sqrt{2}}\ \overline{\ell_{iL}}\ \ell_{jR} + h.c\Big). \tag{1.18}$$

Most importantly, all of the above predictions have been verified by different experiments to validate SM as the fundamental governing theory of nature. Starting from parity violation in weak interaction (famous beta decay), that dictates chiral interactions of fermions with weak gauge bosons, or asymptotic freedom of strong interaction to confer $SU(3)$ nature of underlying gauge theory to latest discovery of Higgs boson at LHC and consistency with SM gauge boson masses pinpoint to the success of SM as a profound theory. However, there are many limitations still, some of which we discuss next and will lay the stepping stone for the thesis under study.

1.2 Limitations of SM

Apart from its overwhelming success, the SM suffers from some theoretical and phenomenological problems. We mention some of them briefly.

• **Existence of DM:** Existence of DM is supported by many observations to constitute a significant part of energy density of Universe today, around 24%. However there is no such particle within the SM.

• **Non zero neutrino mass:** To understand the observed solar and atmospheric oscillation phenomena, neutrinos are required to possess non-zero but very tiny mass ($\sim$ eV) which can not be explained within SM absent right handed neutrinos.

• **Higgs Vacuum stability:** Current measured value of Higgs mass after Higgs boson discovery at LHC in 2012, $m_h = 125.09$ GeV and top quark mass, $m_t = 173.1$ GeV, the electroweak (EW) vacuum can be unstable, questioning the existence of our universe.

• **Hierarchy problem:** The observed Higgs boson mass is around $m_h \sim 125$ GeV. There is no symmetry that protects SM Higgs mass and therefore, the quantum correction to Higgs mass at high scale ($\sim M_{\rm Pl}$) is much larger than m_h : $\delta m_h^2 \gg m_h^2$. This is known as hierarchy problem.

• **Fermion mass hierarchy:** In SM, it is not clear why the masses of SM fermions span over EV to GeV and why they exhibit various Yukawa coupling strength.

• **A quantum theory of Gravity:** SM is a successful theory of strong, weak and electromagnetic interactions. However, including a quantum theory of gravity in similar framework seems impossible.

Apart, there are strong CP problem, matter-antimatter asymmetry, gauge coupling unifications, none of which can be understood within SM. This overwhelmingly indicates that there must be physics beyond the SM. We address some of the limitations like DM, non-zero neutrino mass and Higgs vacuum stability in our thesis and elaborate in the next chapter.

Chapter 2

Dark Matter, Neutrino, Higgs vacuum stability

Contents

In this chapter we discuss the main issues addressed in this thesis: dark matter, neutrino mass generation and Higgs vacuum stability. We provide a brief account of all these issues and will elaborate them in context of the specific model set up later. As the thesis mainly discuss dark matter problem of the universe, the topic is dealt with a little more rigour than the other topics.

2.1 Dark Matter

The study of redshift in various galaxies present in Coma cluster, Fritz Zwicky in 1933, first proposed the existence of non luminous, non baryonic matter present in the cluster to account for the missing mass and named it as Dark Matter (*"dunkel materie"* in German) [6]. Several hints for Dark Matter (DM) have come from different astrophysical and cosmological observations[7]. Here we illustrate some of them briefly.

2.1.1 Evidences of Dark Matter

Anisotropies in CMBR: DM is postulated to constitute 80% matter density of the Universe, revealed from studies in Big Bang Neuclosynthesis (BBN) and anisotropies in Cosmic Microwave Background Radiation (CMBR) by Willkinson Microwave Anisotropy Probe (WMAP)[8–10] and PLANCK [11] experiment collectively. Data from WMAP and PLANCK suggest that the universe consists of: (i) around 4% baryonic matter like baryons, leptons, gas, stars, galaxies etc. ; (ii) around 23% non baryonic matter known as Dark matter and (iii) rest 73% is known as dark energy [8, 9, 11]. A pie chart of the total energy distribution of present day universe is shown in Fig. 2.1.

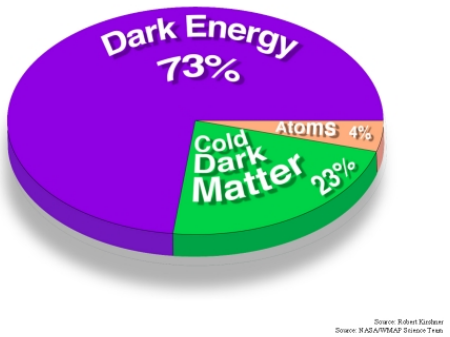

Figure 2.1: The energy distribution of the universe indicated by WMAP and PLANCK data. Source: *Google Images*.

Rotation curve of Galaxy: One of the strongest evidences for the existence of DM came in 1978, when Vera Rubin and Kent Ford observed the flatness behaviour of velocities of Andromeda galaxy via redshift which is unexpected from Newtonian gravity [12]. According to simple Newtonian gravity a star of mass m within a galaxy experience centripetal force due to circular motion of the star which is mathematically expressed as

$$\begin{aligned} \frac{G\ m\ M(R)}{R^2} &= \frac{mv^2(R)}{R} \\ v(R) &= \sqrt{\frac{GM(R)}{R}}, \qquad \text{where} \quad M(R) = 4\pi \int \rho(R) R^2 dR \ . \end{aligned}$$

Here $M(R)$ is the mass contained inside a sphere of radius R from galactic centre and $\rho(R)$ is the mass density profile. Within the galaxy, the velocity of the star follows linear dependence with R i.e. $v(R) \propto R$. If we go beyond the optical disk, the rotation velocity of the star should fall off as $v(R) \propto \frac{1}{\sqrt{R}}$. But the observation shows almost constant behaviour of rotational velocity, shown in Fig. 2.2. The behaviour can be explained if the mass distribution outside the optical disc follows $M(R) \propto R$. This strongly suggests the presence of invisible matter surrounding the optical galaxy.

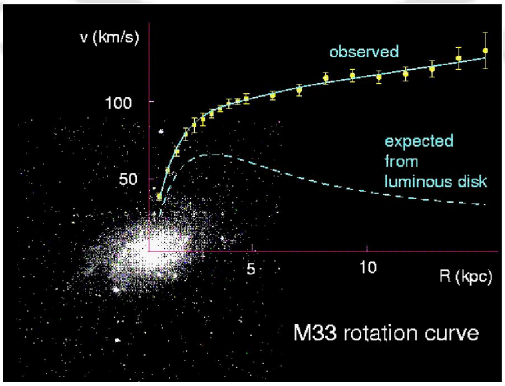

Figure 2.2: Discrepancy in rotation curve of spiral galaxy. Source: *Google Images*.

Bullet Cluster: Observation of bullet cluster, of two colliding cluster of galaxies provides another important evidence for DM [13]. Due to the collision, various

components of two galaxies interact differently which is depicted in Fig.2.3 with different colours. The ordinary matter exhibits electromagnetic interaction and populate the middle of Fig. 2.3 shown in red. Due to non-luminous nature of DM, they pass through which could only be traced through weak gravitational lensing, as shown by the two blue blobs around the central red visible region in Fig. 2.3. This strongly hints towards collision less weakly interacting DM prevailing in the universe [1].

Figure 2.3: Image of Bullet cluster seen by NASA's Hubble Space Telescope. Source: *Google Images*.

2.1.2 Possible DM Candidates

Apart from astrophysical objects like Massive Compact Halo Objects (MACHOs) that can address the macroscopic behaviour of DM [14], an overwhelming belief is that DM is particle like. Evidences suggest that the DM candidates should be [15]:

i) mostly stable otherwise they would have decayed to observable particles,

ii) electromagnetic charge neutral so that they do not interact with photon and hence remain non-luminous or dark,

iii) non baryonic (strong interactions is not possible, although there might be exceptions),

iv) massive particles (so that they contribute significantly to the energy density of the universe),

v) and possess negligible or very week interaction with other visible particles.

Three major classifications of non baryonic DM are:

- **Cold Dark Matter (CDM)**: CDM candidates are non relativistic. Axions, Weekly Interacting Massive Particles (WIMPs), Feebly Interacting Massive Particle (FIMP) and Strongly Interacting Massive Particle (SIMP) are the most popular CDM candidates. DM masses here can have a large mass reange: $\sim MeV - TeV$.

[1] Observations in Bullet cluster is difficult to explain with modified gravity, which otherwise could account for the discrepancy in rotational curve as discussed before.

- **Hot Dark Matter (HDM)**: Such DMs are relativistic. Hot DM candidates can be neutrinos. However, structure formation of the universe goes against the existence of only hot DM candidates.
- **Warm Dark Matter (WDM)**: Such DM candidates have properties in between cold and hot regime. Sterile neutrinos and gravitinos are popular WDM candidates. The masses are usually in the KeV range.

In this thesis we basically focus on CDM candidates. Due to non-relativistic nature, CDM can explain structure formation of the universe. CDM candidates can produce correct relic density of the universe broadly through two different mechanisms: (i) thermal freeze-out and ii) non-thermal freeze-in. A cartoon in Fig.2.4 shows different possibilities of CDM candidates.

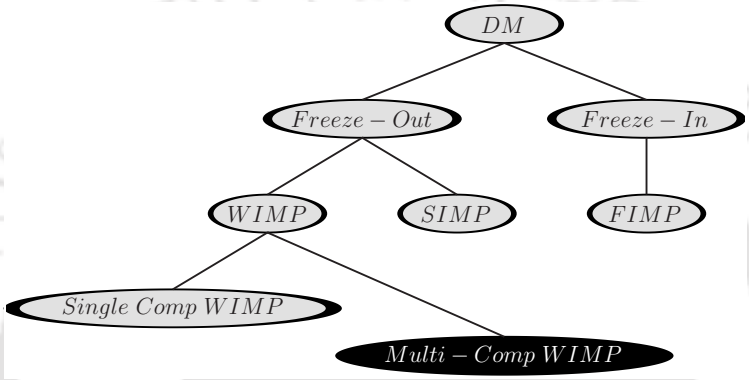

Figure 2.4: Different possible CDM candidates.

Thermal freeze-out:

In such a case, DM particle is assumed to be in thermal and chemical equilibrium with SM particles at early Universe. As temperature cools down and universe expands, at a particular epoch when the interaction rates (Γ) becomes smaller than the universe expansion rate (Hubble constant $\mathcal{H}$), the DM particles freeze-out from thermal bath and becomes relic.
Thermal freeze-out mainly yields two possible DM candidates: WIMP and SIMP.

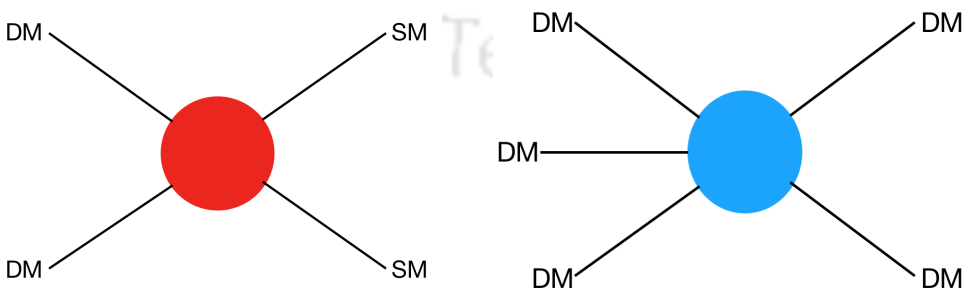

Figure 2.5: [Left] A cartoon of $2_{\rm DM} \to 2_{\rm SM}$ number changing process for WIMP type DM . [Right] A cartoon of $3_{\rm DM} \to 2_{\rm DM}$ number changing process for SIMP type DM. Image Source [16]

WIMP: In this case, depletion in DM number density occurs through $2_{\rm DM} \to 2_{\rm SM}$ annihilation process [17, 18]. A cartoon of $2_{\rm DM} \to 2_{\rm SM}$ annihilation process is shown

in left panel of Fig. 2.5. The annihilation cross-section to produce correct relic density comes out to be of the order of weak interaction cross section and so is the name for the DM. The DM masses in such cases are ideally $\sim \mathcal{O}$ 100 GeV, accessible to the present and future detectors. We will discuss the thermal history of single and multi-component WIMP type DM in next subsection.

SIMP: Freeze-out of DM may also occur through number changing process in the dark sector itself via interactions like $3_{\rm DM} \to 2_{\rm DM}$ (or $4_{\rm DM} \to 2_{\rm DM}$) annihilations (shown in right panel of Fig.2.5). However, the oder of DM mass has to account for the suppression in phase space and comes below MeV to provide correct relic. The coupling for such number changing process also require to be quite large, hence the DM is called Strongly Interacting Massive Particle (SIMP) [16, 19, 20].

Non-thermal freeze-in

FIMP: One may also assume that DM was not present in the early universe thanks to a very feeble interaction with the visible sector. However, the DM can be produced through the decay of some other heavy particle and the production halts after the universe cools down beyond the mass of DM. This mechanism is therefore referred as freeze in. Interestingly, in order to attain the desired relic density, the coupling requires to be very very tiny and the DM is termed as Feebly Interacting Massive Particle (FIMP)[21]. FIMP models are therefore excluded from experimental searches to a great extent.

2.1.3 Thermal History of single component WIMP DM and Boltzmann Equation

In this section, we discuss how WIMP type DM decouples from the hot soup of SM particles and yields the relic density observed in CMB experiments like WMAP and PLANCK. Number density of WIMP type DM is governed by the the number changing process: $2_{\rm DM} \leftrightarrow 2_{\rm SM}$ i.e

$$\text{DM} \quad \text{DM} \quad \leftrightarrow \quad \text{SM} \quad \text{SM} \, . \tag{2.1}$$

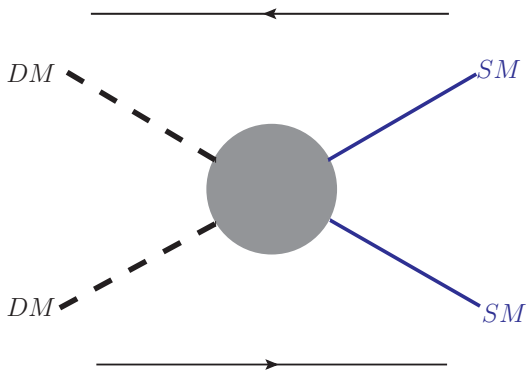

Figure 2.6: Number changing process of WIMP type DM.

Thermal evolution of DM particle can be written as in terms of the phase space distribution of the DM particle, $f_{\rm DM}(\mathbf{r},\mathbf{p},t)$ as [14, 15]

$$\widehat{L}[f_{\rm DM}] \;=\; \widehat{C}[f_{\rm DM}] \;\;, \tag{2.2}$$

where $\widehat{L}$ is the Liouville operator and $\widehat{C}$ be the collision operator. For the isotropic and homogeneous FRW universe: $f_{\rm DM}(\mathbf{r},\mathbf{p},t) \;\rightarrow\; f_{\rm DM}(E,t)$. Above equation can be realised in terms of DM number density, $n_{\rm DM}$ as[14, 15],

$$\frac{n_{\rm DM}}{dt} + 3Hn_{\rm DM} = \frac{g_{\rm DM}}{(2\pi)^3}\int \frac{\widehat{C}[f_{\rm DM}]}{E_{\rm DM}} d^3\mathbf{p}, \tag{2.3}$$

where

$$n_{\rm DM} = \frac{g_{\rm DM}}{(2\pi)^3}\int d^3\mathbf{p}\; f(E,t) \tag{2.4}$$

and $g_{\rm DM}$ is the degrees of freedom (dof) of DM particle and H be the Hubble expansion rate defined in terms of scale factor a, as $H = \frac{\dot{a}}{a}$. The collision term $\widehat{C}[f_{\rm DM}]$ is obtained considering both forward backward reaction between DM and SM following in the Fig.2.6. The Eqn. 2.3 can be expressed as [14, 15]

$$\begin{aligned}\frac{n_{\rm DM}}{dt} + 3Hn_{\rm DM} \;=\; &-\int \frac{g_{\rm DM}\; d^3\mathbf{p_1}}{(2\pi)^3\; 2E_{\rm DM}}\frac{g_{\rm DM}\; d^3\mathbf{p_2}}{(2\pi)^3\; 2E_{\rm DM}}\frac{g_{\rm SM}\; d^3\mathbf{p_3}}{(2\pi)^3\; 2E_{\rm SM}}\frac{g_{\rm SM}\; d^3\mathbf{p_4}}{(2\pi)^3\; 2E_{\rm SM}}\\ &\times(2\pi)^4\delta^4(p_1+p_2-p_3-p_4)\\ &\times\Big[|\mathcal{M}_{\rm DM\to SM}|^2\; f_{\rm DM}\; f_{\rm DM}(1\pm f_{\rm SM})(1\pm f_{\rm SM})\\ &-|\mathcal{M}_{\rm SM\to DM}|^2\; f_{\rm SM}\; f_{\rm SM}(1\pm f_{\rm DM})(1\pm f_{\rm DM})\Big],\end{aligned} \tag{2.5}$$

where $(+)$ sign for bosons and $(-)$ sign for fermions occupancy. $g_{\rm SM}$ be the internal dof of SM particles. The above equation can be simplified as assuming equal amplitude for both forward and backward reaction i.e $|\mathcal{M}_{\rm DM\to SM}|^2 = |\mathcal{M}_{\rm SM\to DM}|^2$ and the phase space occupancy as $1\pm f_{\rm DM}\to 1$ to yield [15]:

$$\begin{aligned}\frac{n_{\rm DM}}{dt} + 3Hn_{\rm DM} \;&=\; -\int \frac{g_{\rm DM}\; d^3\mathbf{p_1}}{(2\pi)^3\; 2E_{\rm DM}}\frac{g_{\rm DM}\; d^3\mathbf{p_2}}{(2\pi)^3\; 2E_{\rm DM}}\frac{g_{\rm SM}\; d^3\mathbf{p_3}}{(2\pi)^3\; 2E_{\rm SM}}\frac{g_{\rm SM}\; d^3\mathbf{p_4}}{(2\pi)^3\; 2E_{\rm SM}}\\ &\quad\times(2\pi)^4\delta^4(p_1+p_2-p_3-p_4)\times|\mathcal{M}_{\rm DM\to SM}|^2\;\Big[\; f_{\rm DM}\; f_{\rm DM} - \; f^{\rm EQ}_{\rm DM}\; f^{\rm EQ}_{\rm DM}\Big]\\ &=\; -\langle\sigma v\rangle_{2_{\rm DM}\to 2_{\rm SM}}\Big[n^2_{DM} - \Big(n^{\rm EQ}_{\rm DM}\Big)^2\Big]\;,\end{aligned} \tag{2.6}$$

where $n_{\rm DM}$ is the number density of DM , $n^{\rm EQ}_{\rm DM}$ is the equilibrium number density and the thermal average annihilation cross-section $\langle\sigma v\rangle_{2_{DM}\to 2_{SM}}$ is defined as [15, 22, 23],

$$\begin{aligned}\langle\sigma v\rangle_{2_{\rm DM}\to 2_{\rm SM}} \;&=\; \frac{1}{n^{\rm EQ}_{\rm DM}\; n^{\rm EQ}_{\rm DM}}\int \frac{g_{\rm DM}\; d^3\mathbf{p_1}}{(2\pi)^3\; 2E_{\rm DM}}\frac{g_{\rm DM}\; d^3\mathbf{p_2}}{(2\pi)^3\; 2E_{\rm DM}}\frac{g_{\rm SM}\; d^3\mathbf{p_3}}{(2\pi)^3\; 2E_{\rm SM}}\frac{g_{\rm SM}\; d^3\mathbf{p_4}}{(2\pi)^3\; 2E_{\rm SM}}\\ &\quad\times(2\pi)^4\delta^4(p_1+p_2-p_3-p_4)\times|\mathcal{M}_{\rm DM\to SM}|^2\;\; f^{\rm EQ}_{\rm DM}\; f^{\rm EQ}_{\rm DM}\\ &=\; \int_{4m^2_{DM}}^{\infty} ds\frac{s\sqrt{(s-4m^2_{DM})}\; K_1(\sqrt{s}/T)\;(\sigma v)_{2_{DM}\to 2_{SM}}}{16\; T\; m^4_{DM}\;[K_2(m_{DM}/T)]^2}.\end{aligned} \tag{2.7}$$

The detailed calculation of Eqn.2.6 and Eqn.2.7 is given in Appendix A.

The entropy density and energy density of the universe are given below [15, 24]:

$$s = \frac{2\pi^2}{45} g_{*s} T^3, \qquad \rho = \frac{\pi^2}{30} g_* T^4, \tag{2.8}$$

where g_{*s} and g_* are the d.o.f for entropy and energy density respectively as

$$\begin{aligned} g_{*s} &= \sum_{i=bosons} g_i \left(\frac{T_i}{T}\right)^3 + \frac{7}{8} \sum_{i=fermions} g_i \left(\frac{T_i}{T}\right)^3 \\ g_* &= \sum_{i=bosons} g_i \left(\frac{T_i}{T}\right)^4 + \frac{7}{8} \sum_{i=fermions} g_i \left(\frac{T_i}{T}\right)^4 \end{aligned} \tag{2.9}$$

The BEQ in Eqn. 2.6 can also be written as:

$$\frac{dY}{dx} = -0.264 \, \frac{g_{*s}}{\sqrt{g_*}} \, M_{pl} \, \frac{m_{DM}}{x^2} \, \langle \sigma v \rangle_{2_{DM} \to 2_{SM}} \left(Y^2 - \left(Y^{\rm EQ} \right)^2 \right) . \tag{2.10}$$

Here $Y = \frac{n_{\rm DM}}{s}$ (co-moving number density) and $x = \frac{m_{\rm DM}}{T}$ where s is the total entropy density of the universe, $m_{\rm DM}$ is the mass of DM, T is the photon temperature and the reduced Plank mass $M_{pl} = \frac{1}{\sqrt{G}} \equiv 1.22 \times 10^{19}$ GeV (G: Newton constant). The co moving equilibrium number density turns out [15]:

$$Y^{\rm EQ}(x) \equiv \frac{n^{\rm EQ}_{\rm DM}}{s} = 0.145 \, \frac{g_{DM}}{g_{*s}} x^{3/2} e^{-x} , \tag{2.11}$$

Due to the thermal history of the universe, all particles shared a common temperature, and it can be approximated as $g_{*s} \simeq g_*$ [15, 24]. Thus, we can write Eq. 2.10 as:

$$\frac{dY}{dx} = -0.264 \, \sqrt{g_*} \, M_{pl} \, \frac{m_{DM}}{x^2} \, \langle \sigma v \rangle_{2_{DM} \to 2_{SM}} \left(Y^2 - \left(Y^{\rm EQ} \right)^2 \right) . \tag{2.12}$$

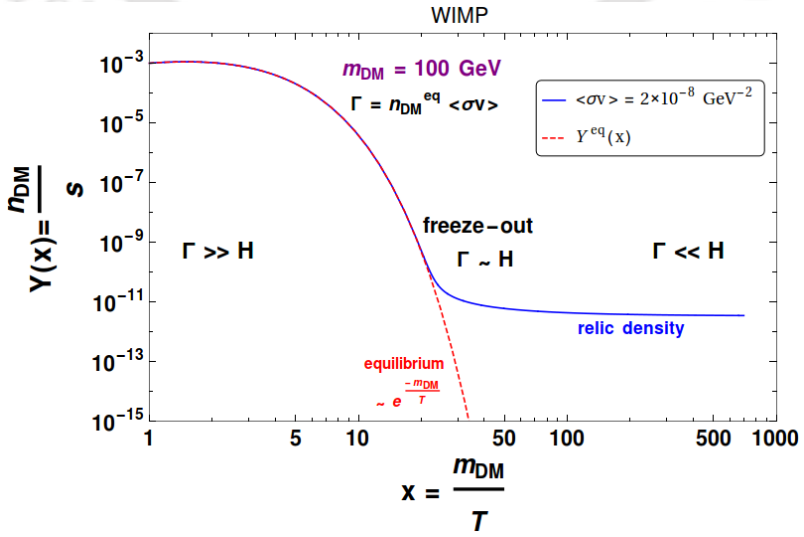

Figure 2.7: Distribution of co-moving number density with x.

Solving the above Eqn.2.12, one can numerically obtain the co-moving number density $Y(x)$. To see the thermal evolution of DM number density with T, we show the solution of BEQ (Eqn. 2.12) in Fig.2.7 for DM mass, $m = 100$ GeV and thermal average cross section, $\langle\sigma v\rangle_{2_{DM}\to 2_{SM}} = 2\times 10^8 \text{GeV}^{-2}$. For DM mass of the order of 100 GeV, $g_{*s} \simeq g_* \approx 106.7$ [15, 24].

We discuss now how DM decouple from thermal bath of SM particles and yields freeze-out number density. At early time, when the universe was hot and dense i.e energies much larger than than mass of each species ($m_{\rm DM} \ll T$ i.e. $x \ll 1$), both DM and SM particles interact with each other equally through forward and backward reaction and maintain the chemical equilibrium. This period of time the interaction rate, Γ $(= n_{DM}\langle\sigma v\rangle_{2_{DM}\leftrightarrow 2_{SM}})$ dominates over Hubble expansion rate H as a result both DM and SM particles are in equilibrium.

$$m_{\rm DM},\ m_{\rm SM} \ll T \quad \text{i.e}\ \ x \ll 1 \quad ;\ \ \Gamma \gg H \quad :\quad \text{DM}\quad \text{DM}\quad \leftrightarrow\quad \text{SM}\quad \text{SM}\ .$$

The Universe cools down with time; when the temperature of the universe lies between $m_{\rm SM} < T < m_{\rm DM}$, the number density $n_{\rm DM}$ follows the non relativistic Boltzmann distribution and it is suppressed by the factor $e^{\frac{-m_{\rm DM}}{T}}$. Hence the backward reaction kinematically stop because $m_{\rm DM} > m_{\rm SM}$. At the temperature, T_f (i.e $x_f = m_{\rm DM}/T_f$), $\Gamma \sim H$, the DM particles decouples from thermal bath. The temperature T_f called freeze-out temperature.

$$m_{\rm SM} < T < m_{\rm DM} \quad \text{i.e}\ \ x \sim x_f \quad ;\ \ \Gamma \sim H \quad :\quad \text{DM}\quad \text{DM}\quad \to\quad \text{SM}\quad \text{SM}\ .$$

However, the universe is not only cooling down, it's also expanding; when the expansion rate of the Universe dominate over interaction rate, DM can not annihilate to SM. At this point, DM totally decouples from thermal bath and the DM number density asymptotically approach a constant, its relic. This behaviour is exactly depicted in Fig.2.7.

$$m_{\rm DM} \gg T \quad \text{i.e}\ \ x \gg x_f \quad ;\ \ \Gamma \ll H \quad :\ \text{DM becomes relic.}$$

One can now numerically obtain DM yields after freeze-out, which is $Y(x\to\infty)$. The relic density of DM in terms of thermal yields is given by [15, 24]:

$$\begin{aligned}\Omega h^2 &= \frac{m_{DM} Y(x\to\infty)}{s_0\ \rho_c} h^2 \\ &= 2.752\times 10^8 \left(\frac{m_{DM}}{\text{GeV}}\right) Y(x\to\infty)\ ,\end{aligned} \tag{2.13}$$

where $\rho_c = 1.05\times 10^{-5} h^2$ GeV cm^{-3} and entropy density $s_0 = 2889.2 cm^{-3}$ [7] refers to that of today.

For the sake of computational purpose, one can further parametrise the above BEQ. in Eqn.2.12 as:

$$\frac{dy}{dx} = \frac{1}{x^2}\ \langle\sigma v\rangle_{2_{DM}\to 2_{SM}}\ \left(y^2 - \left(y^{\rm EQ}\right)^2\right)\ , \tag{2.14}$$

where

$$y = 0.264\sqrt{g_*} M_{Pl} m_{\rm DM} Y \quad \text{and} \quad y^{\rm EQ} = 0.264\sqrt{g_*} M_{Pl} m_{\rm DM} Y^{\rm EQ}.$$

One can then also compute relic density by using given form,

$$\Omega h^2 \;=\; \frac{854.45\times10^{-13}}{\sqrt{g_*}} y(x\to\infty)\ , \tag{2.15}$$

where $y(x\to\infty)$ comes from solving the BEQ in Eqn.2.16.

Approximate Analytic solution of BEQ :
We can numerically solve BEQ, to find the yield at present temperature, and hence find the relic density. It is however helpful to solve BEQ analytically in an approximate way and hence find out the solution. We now evaluate approximate analytical solution for the BEQ in Eqn.2.12. We first rewrite the BEQ in Eqn.2.12 in terms of $\Delta = Y - Y^{\rm EQ}$, departure from equilibrium as [15]

$$\frac{d\Delta}{dx} + \frac{dY^{\rm EQ}}{dx} = -\frac{A}{x^2}[\Delta^2 + 2\ \Delta Y^{\rm EQ}], \tag{2.16}$$

where

$$A = 0.264\ \sqrt{g_*}\ M_{pl}\ m_{DM}\ \langle\sigma v\rangle_{2_{DM}\to 2_{SM}}\ .$$

At early time ($x \ll x_f$), Y tracks $Y^{\rm EQ}$ very closely. Both Δ and $\frac{d\Delta}{dx}$ are small. Then the Eqn. 2.16 reads as [15]

$$\frac{dY^{\rm EQ}}{dx} = -\frac{A}{x^2}[\Delta^2 + 2\ \Delta Y^{\rm EQ}], \tag{2.17}$$

At $x\sim x_f$, near freeze-out lets assume $\Delta(x_f) = cY^{\rm EQ}(x_f)$, where c is the unknown constant. Now the above Eqn. 2.17 turns out to be:

$$\begin{aligned}
\frac{dY^{\rm EQ}}{dx}|_{x=x_f} &= -\frac{A}{x^2}\Big(Y^{\rm EQ}\Big)^2[c^2+2\ c]|_{x=x_f}\\
(1-\frac{3}{2x_f}) &= -\frac{A}{x_f^2}(c^2+2\ c)Y^{\rm EQ}(x_f)\\
(1-\frac{3}{2x_f}) &= -\frac{A}{x_f^2}c(c+2)\Big(0.145\ \frac{g_{DM}}{g_{*s}}x^{3/2}e^{-x}\Big)\\
x_f &\approx \ln\Big[0.038\ \frac{g_{DM}}{\sqrt{g_*}}\ M_{Pl}\ m_{DM}\ (c+2)c\ \langle\sigma v\rangle_{2_{DM}\to 2_{SM}}\Big]\\
&\quad -\frac{1}{2}\ln\ln\Big[0.038\ \frac{g_{DM}}{\sqrt{g_*}}\ M_{Pl}\ m_{DM}\ (c+2)c\ \langle\sigma v\rangle_{2_{DM}\to 2_{SM}}\Big].
\end{aligned} \tag{2.18}$$

After freeze-out $x\gg x_f$, $Y^{\rm EQ}$ becomes zero, hence $\Delta\sim Y$. The Eqn. 2.18 simplifies to :

$$\frac{d\Delta}{dx} = -\frac{A}{x^2}\Delta^2 \tag{2.19}$$

$$\to \int_{\Delta(x_f)}^{\Delta(\infty)} -\frac{d\Delta}{\Delta^2} = A\int_{x_f}^{\infty}\frac{dx}{x^2}$$

$$\to \Delta(\infty) = \frac{x_f}{A} \tag{2.20}$$

Now, one can write the expression of relic density using Eqn.2.13 and Eqn. 2.18 as follows [15]:

$$\Omega h^2 = \frac{854.45 \times 10^{-13}}{\sqrt{g_*}} x_f \frac{\text{GeV}^{-2}}{\langle \sigma v \rangle_{2_{DM} \to 2_{SM}}}. \tag{2.21}$$

We will see that for multipartite DM scenarios, obtaining an approximate analytical solution for the coupled BEQ is harder. We will illustrate it for one such model.

2.1.4 DM searches

WIMP models are popular due to their possibility of getting unravelled in direct and collider search experiments [25–28]. This is essentially due to the presence of $2_{\text{DM}} \to 2_{\text{SM}}$ number changing process to govern the freeze-out. The same interaction, when turned upside down, as shown in cartoon Fig. 2.8 can yield a direct search signal for DM; or when it is reversed can yield a production at high energy collider, such as LHC.

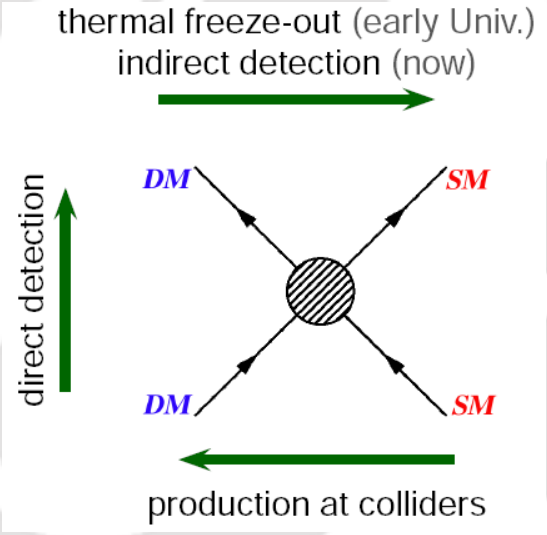

Figure 2.8: Cartoon of DM searches. Source: *Google Images*

We elaborate briefly on the possibility of direct and collider search of WIMP DM.

Direct Detection

Direct search of DM is possible as our galaxy is assumed to be immersed in DM halo. WIMPs in the DM halo have a velocity distribution. Therefore, the DM can interact with detector placed deep underground and can have elastic scattering as $DM + SM \to DM + SM$ and can produce nuclear recoil. Therefore, the presence of such DM can be realised through nuclear recoil if observed. The recoil energy can be measured as [25, 29]

$$E_R = \frac{q^2}{2m_N} = \frac{\mu^2 v^2}{m_N}(1 - \cos\theta), \tag{2.22}$$

where q is the momentum transfer, μ is the reduced mass, m_N is the target nucleus mass, v is the mean WIMP velocity with respect to the target and θ is the scattering

angle in the center-of-mass frame. We may note here that observables for the process are: recoil energy of the nucleus E_R and scattering angle θ. In a standard scenario, the differential scattering rate spectrum of WIMPs in under ground detectors can be parametrised as [25, 29, 30]

$$\frac{dN}{dE_R} \sim \frac{\rho_0}{2m_{DM}\mu}\left[\sigma^{SI}F_{SI}^2 + \sigma^{SD}F_{SD}^2\right]\int_{v_{min}}^{v_{max}} \frac{\hat{\mathbf{f}}_{lab}(\hat{v},t)}{v} d^3v. \tag{2.23}$$

In above expression, m_{DM} denote DM mass, σ^{SI}, σ^{SD} are WIMP-nucleon spin-independent and spin dependent interaction cross sections respectively. These are the quantities that are specific to a WIMP model and can be computed from its interactions with SM following the cartoon diagram in Fig. 2.8. $\rho_0 \sim 0.2 - 0.56$ GeV cm^{-3} denotes local DM density at the Solar radius. $\hat{\mathbf{f}}_{lab}(\hat{v},t)$ is the lab frame WIMP velocity distribution (Maxwell-Boltzmann distribution to a good approximation) and is an astrophysical input. F_{SI}, F_{SD} are the spin independent and spin dependent nuclear form factor, specific to the detector. In the limit of non-relativistic WIMP velocity ($v \sim 10^{-3}c$), scalar interaction provides spin independent cross-section while axial interaction yields spin dependent cross-section. Several experiments like XENON, LUX, PANDA have

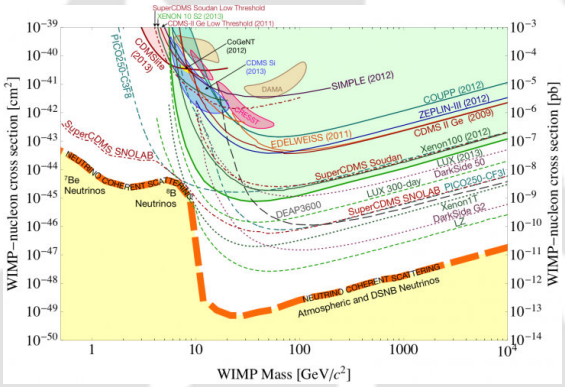

Figure 2.9: Status of direct search experiments for DM so far. Image Source[31].

been looking for direct search interaction of DM. But no evidences have been observed yet. Inevitably, they produce bounds on DM-SM interactions and the limits are provided in terms of WIMP mass as shown in Fig. 2.9. The bound is getting strict with larger detector sensitivity and is causing a threat to WIMP DM. For example, XENON1T has ruled out WIMP-nucleon interaction cross sections larger than $\sim 10^{-46}$cm^2 for DM mass ~ 100 GeV. We will discuss this issue later in details in context of specific DM models, but the root cause of the worry is the interaction that drives the freeze-out of WIMPs to yield correct relic, is also responsible to generate direct search cross-section. Therefore, it is a challenge for the WIMP class of models to satisfy relic density and still be available by direct search. It is also important to note that, the sensitivity of WIMP nucleon interaction will soon hit 'neutrino floor' as shown in Fig. 2.9 by yellow band, merging with the sensitivity of neutrino interaction. In such situations, distinguishing dark matter signal becomes even more harder.

Collider Searches

It has already been indicated that for WIMP models, the same $DM+DM \to SM+SM$ interaction that governs the freeze-out can produce DM at high energy collider through

the reverse process i.e. $SM + SM \to DM + DM$. Models where DM is a singlet under SM (which consists a large class of simple DM frameworks), the collider detection has to bank on mono-X plus missing energy ($\not{E}_T$), where X can be a gluon (jet), photon, Higgs, W or Z coming out of initial state radiation (ISR)[32, 33]. Missing energy has been used as a key variable to segregate DM signal at collider defined as:

$$\text{Typical DM Signal}: \quad \text{Mono} - \text{X} + \not{E}_T; \quad \text{X} = \{\text{jet}, \text{H}, \text{W}, \text{Z}\};$$
$$\not{E}_T = -\sqrt{(\sum_{\ell,j,unc.} p_x)^2 + (\sum_{\ell,j,unc.} p_y)^2} \quad . \tag{2.24}$$

The sum in the above equation runs over all visible objects at collider detector that include the leptons and jets, and the unclustered components. Richer signal can only be obtained in presence of a multipartite dark sector, with heavier charged fields (in presence of higher multiplets for example) decaying to DM and produce a signal like:

$$\text{Richer DM Signal}: \quad \text{n}\ \ell + \text{m jets} + \not{E}_T; \quad \ell = \{\text{e}^{\pm}, \mu^{\pm}\}. \tag{2.25}$$

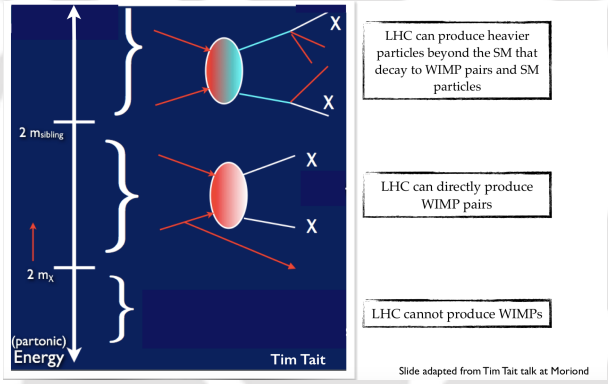

Figure 2.10: Possible DM Signals at Collider. Source: *Google Images*

These possibilities are nicely documented in Fig. 2.10 (figure adapted from a talk by Tim Tait at Moriond), where we clearly see that if the center-of-mass energy is just beyond the threshold of twice the DM mass ($> 2m_{DM}$), one will be able to probe mono-jet channels, whereas for a multipartite framework, if the centre-of-mass energy limit crosses the threshold of twice the heavier particle mass ($> m_{sibling}$), then those can be produced to further decay to DM associated with leptons and jets. Again, we will postpone a specific discussion of collider signals to a specific DM model set up taken up in the thesis. Unfortunately, LHC has been looking for all possible DM signals as elaborated, and have not been able to see any excess. Missing energy distribution for mono-jet and mono-V search at CMS is demonstrated in Fig. 2.11 at $\sqrt{s} = 13$ TeV, where the signal matches very closely to the possible SM background contribution. Therefore, it is also important to abide by the DM-SM limit that we obtain from non-observation of DM at collider. Importantly, the signal production cross-section for DM of mass ~ 100 GeV at LHC is quite small compared to SM background and therefore the limit is also much less restrictive than direct search bound.

Indirect Detection

Indirect Detection is the another possibility through which DM can be probed. This is possible, via production of SM particles either through DM annihilation or via decay.

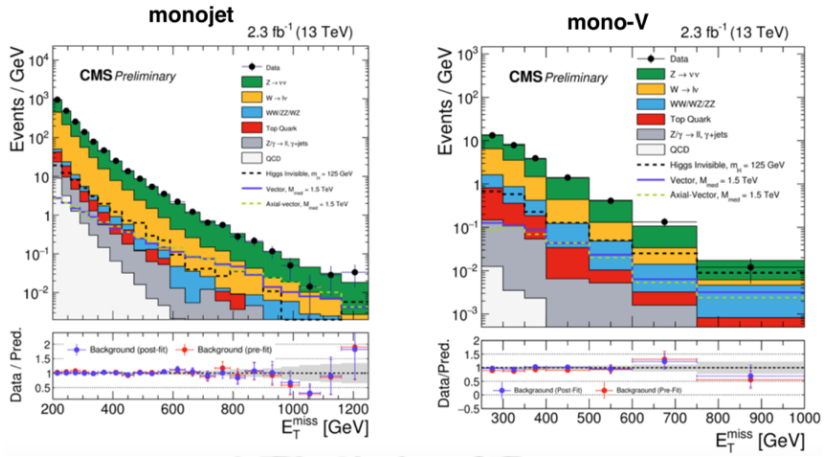

Figure 2.11: Absence of DM signal at CMS mono jet and mono-V search at LHC.

The stable SM particles like photon, neutrinos which are produced via DM annihilation or decay, can travel from their production sites to Earth without getting affected much by intermediate regions. Such gamma rays or photons and neutrinos are the ideal messenger of DM searches for indirect detection. Two current experiments like space based telescopes Fermi-LAT (Fermi Large Area Telescope) and ground based telescopes MAGIC (Major Atmospheric Gamma-ray Imaging Cherenkov) are looking for WIMP signal coming from dwarf spheroidal satellite galaxies (dSphs)[28]. Gamma rays may be produced directly or in shower of secondary particles from WIMP annihilation. Depending on WIMP mass, those gamma rays could be detectable with these experiments. But after so many years of successive run, they are not getting any DM signal. From null results they put limits on annihilation cross section for DM masses ranging between GeV - TeV.

The integrated gamma ray flux, produced by DM annihilation in specific energy range ($E_{min} < E < E_{max}$) and region of interest on the sky is given by [28]:

$$\begin{aligned}\Phi(\Delta\Omega) &= \frac{1}{4\pi}\frac{<\sigma v>_{ann}}{2m_{DM}^2}\int_{E_{min}}^{E_{max}}\frac{dN_\gamma}{dE_\gamma}dE_\gamma \times \int_{\Delta\Omega}d\Omega'\int_{l.o.s}dl\ \ \rho_{DM}^2(l,\Omega') \\ &= \frac{1}{4\pi}\frac{<\sigma v>_{ann}}{2m_{DM}^2}\int_{E_{min}}^{E_{max}}\frac{dN_\gamma}{dE_\gamma}dE_\gamma \times J \ , \end{aligned} \tag{2.26}$$

where $\Delta\Omega$ is the solid angle corresponding to the observation region of the sky, $<\sigma v>_{ann}$ is the thermally averaged DM annihilation cross-section, $\frac{dN_\gamma}{dE_\gamma}$ is the differential gamma rays spectrum per annihilation and $\rho_{DM}(l,\Omega')$ is the DM halo density distribution. Here in Eq.2.26, the first term corresponds to particle properties of DM, while second term (called astrophysical J factor) incorporates the information about the distribution of DM along the line of sight (l.o.s). A commonly used DM distribution is called Navarro-Frenk-White (NFW) profile, modelled in the halos of the dSphs as [28]:

$$\rho(r) = \frac{\rho_0 r_s^3}{r(r_s+r)^2} \ , \tag{2.27}$$

where r_s and ρ_0 are the NFW scale radius and characteristic density.

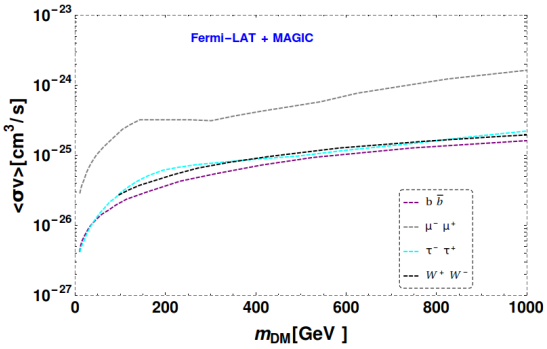

Figure 2.12: 95 % CL upper limits on the thermally-averaged cross-section for DM annihilation into $b\,\bar{b}$ (Purple), $\mu^-\,\mu^+$ (Gray) ,$\tau^-\,\tau^+$ (Green) and W^-W^+ (Black) pairs.

Since DM are electromagnetically neutral, so they do not directly couple to photon but they can be produced from final states particles of DM annihilation like $b\bar{b}$, $\mu^-\mu^+$, $\tau^-\tau^+$, and $\mathrm{W^-W^+}$. Measuring flux from experiments and using standard astrophysical inputs in the above equation Eqn. 2.26, one can constrain DM annihilation into the different final states like $b\bar{b}$, $\mu^-\mu^+$, $\tau^-\tau^+$and $\mathrm{W^-W^+}$. The upper bounds of thermal averaged annihilation cross section ($<\sigma v>$) for different processes are depicted in Fig.2.12. The bound from indirect searches are much weaker than direct and collider searches, and we will not elaborate upon this further in the thesis.

2.1.5 Multi component WIMP DM

Let us now turn to multicomponent DM scenarios. The evolution of DM number density in such cases is governed by coupled BEQs. We will prescribe a general formalism here, which will be discussed in terms of specific models later in the subsequent chapters of the thesis. Let us assume two types of DM particles as:

$$\phi \;\text{ type DM} : \phi : \{\phi_1\ (\text{LSP}),\ \phi_2\ (\text{NLSP}), ...\}\ ,$$

$$\chi \;\text{ type DM} : \chi : \{\chi_1\ (\text{LSP}),\ \chi_2\ (\text{NLSP}), ...\}\ .$$

Lightest particle in each sector becomes a stable DM candidate named as Lightest Stable Particle (LSP). The heavier one (called as Next Lightest Stable Particle (NLSP)) in each sector can decay to LSP. Therefore, the scenario gives us two component stable DM framework with DMs ϕ_1 and χ_1. Due to presence of heavier particles in each sector, there are different type of number changing processes enter into CBEQs shown in Fig 2.13:

Considering all types of number changing processes, the cBEQ will be given by

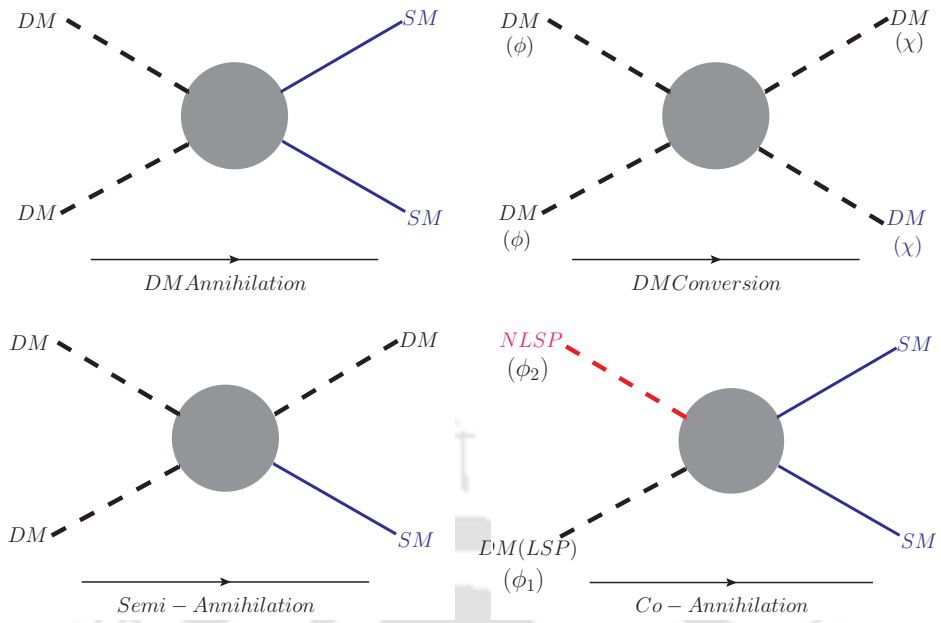

Figure 2.13: Number changing processes for Multicomponent DM scenario considered here.

[15, 23, 34]:

$$
\begin{aligned}
\frac{dn_{\phi_1}}{dt}+3Hn_{\phi_1} &= -\Big[\sum_{\text{anni,co-anni}}\Big(\langle\sigma v\rangle_{\phi_1\phi_1\to \text{SM SM}}+\big(\frac{m_{\phi_j}-m_{\phi_1}}{m_{\phi_1}}\big)^{\frac{3}{2}}e^{-\frac{m_{\phi_j}-m_{\phi_1}}{T}}\\
&\times\langle\sigma v\rangle_{\phi_1\ \phi_j\to \text{SM SM}}\Big)\Big(n_{\phi_1}^2-(n_{\phi_1}^{\text{EQ}})^2\Big)\Theta(m_{\phi_1}-m_{\text{SM}})\\
&+\sum_{\text{semi-anni}}\langle\sigma v\rangle_{\phi_1\ \phi_1\to\phi_1\ \text{SM}}\Big(n_{\phi_1}^2-n_{\phi_1}\ n_{\phi_1}^{\text{EQ}}\Big)\Theta(m_{\phi_1}-m_{\text{SM}})\\
&-\sum_{\text{conv}}\langle\sigma v\rangle_{\phi_1\ \phi_i\to\chi_j\ \chi_k}\Big(n_{\phi_1}\ n_{\phi_j}-\frac{n_{\phi_1}^{\text{EQ}}n_{\phi_i}^{\text{EQ}}}{n_{\chi_j}^{\text{EQ}}n_{\chi_k}^{\text{EQ}}}n_{\chi_j}n_{\chi_k}\Big)\Theta(m_{\phi_1}+m_{\phi_i}-m_{\chi_j}-m_{\chi_k})\\
&+\sum_{\text{conv}}\langle\sigma v\rangle_{\chi_i\ \chi_j\to\phi_1\ \phi_k}\Big(n_{\chi_i}\ n_{\chi_j}-\frac{n_{\chi_i}^{\text{EQ}}n_{\chi_j}^{\text{EQ}}}{n_{\phi_1}^{\text{EQ}}n_{\phi_k}^{\text{EQ}}}n_{\phi_1}n_{\phi_k}\Big)\Theta(m_{\chi_i}+m_{\chi_j}-m_{\phi_1}-m_{\phi_k}),\\
\frac{dn_{\chi_1}}{dt}+3Hn_{\chi_1} &= -\Big[\sum_{\text{anni,co-anni}}\Big(\langle\sigma v\rangle_{\chi_1\chi_1\to \text{SM SM}}+\big(\frac{m_{\chi_j}-m_{\chi_1}}{m_{\chi_1}}\big)^{\frac{3}{2}}e^{-\frac{m_{\chi_j}-m_{\chi_1}}{T}}\\
&\times\langle\sigma v\rangle_{\chi_1\ \chi_j\to \text{SM SM}}\Big)\Big(n_{\chi_1}^2-(n_{\chi_1}^{\text{EQ}})^2\Big)\Theta(m_{\chi_1}-m_{\text{SM}})\\
&+\sum_{\text{semi-anni}}\langle\sigma v\rangle_{\chi_1\ \chi_1\to\chi_1\ \text{SM}}\Big(n_{\chi_1}^2-n_{\chi_1}\ n_{\chi_1}^{\text{EQ}}\Big)\Theta(m_{\chi_1}-m_{\text{SM}})\\
&+\sum_{\text{conv}}\langle\sigma v\rangle_{\phi_i\ \phi_j\to\chi_1\ \chi_k}\Big(n_{\phi_i}\ n_{\phi_j}-\frac{n_{\phi_i}^{\text{EQ}}n_{\phi_i}^{\text{EQ}}}{n_{\chi_1}^{\text{EQ}}n_{\chi_k}^{\text{EQ}}}n_{\chi_1}n_{\chi_k}\Big)\Theta(m_{\phi_i}+m_{\phi_j}-m_{\chi_j}-m_{\chi_k})\\
&-\sum_{\text{conv}}\langle\sigma v\rangle_{\chi_1\ \chi_i\to\phi_j\ \phi_k}\Big(n_{\chi_1}\ n_{\chi}-\frac{n_{\chi_1}^{\text{EQ}}n_{\chi_i}^{\text{EQ}}}{n_{\phi_j}^{\text{EQ}}n_{\phi_k}^{\text{EQ}}}n_{\phi_j}n_{\phi_k}\Big)\Theta(m_{\chi_1}+m_{\chi_i}-m_{\phi_j}-m_{\phi_k}),
\end{aligned}
\tag{2.28}
$$

where $i,j,k = 1,2$. It is important to note here, that in above cBEQ, we have augmented each annihilation, co-annihilation and DM-DM conversion terms with a heavyside Theta function (Θ), to indicate the dominant contribution arising given a mass hierarchy. However, it is not completely true that smaller initial mass states can not produce a heavier final state as the annihilations are all thermal averaged ($\langle\sigma v\rangle$) and integrated over centre-of-mass energy from threshold to very high temperature, i.e. $s : (m_1+m_2)^2 \to \infty$ (see Eq. 2.7). Therefore, ideally, the Θ functions are absent in cBEQ, although it is straightforward to compute that numerical contribution below the kinematic threshold is much smaller. We have adopted the same notation of writing cBEQ with heavyside Theta functions throughout the thesis

for different specific model constructs, but this should be considered with the above caveat. Also, it is worthy to point out, that scans of the allowed parameter space of the specific models have been done further using numerical implementation of the model in the code `MicrOmega`, which automatically takes care of the annihilation/co-annihilation/conversion processes below the kinematic threshold. Evidently, relic density of the two component model described above will have contribution from both DMs to yield:

$$\Omega_T = \Omega_{\phi_1} + \Omega_{\chi_1}. \tag{2.29}$$

Given a specific multipartite framework, the exercise will be to find relic density allowed parameter space of the model governed by above equation.

2.2 Neutrino Mass

Neutrinos are the most illusive particles discovered so far. They are electromagnetic charge neutral and hence interact only via weak interaction. This ideally makes them potential DM candidates, but the problem lies elsewhere. In SM, neutrinos are assumed to be massless and therefore, to prevent them acquiring mass, via the Dirac Yukawa interaction with Higgs, we assume that there exist no right handed neutrino. Neutrinos being massless, was supported by beta decay spectrum after its discovery. However, when people started working on the solar ν_e that we receive at earth, only one third of the flux could be received. This indicated that solar neutrinos must have oscillated into other flavour producing solar neutrino deficit. Following an elementary quantum description, it is easy to appreciate that such a phenomena is only possible if the flavour states are not mass eigenstates, or in other words, neutrinos are rather massive instead of being massless. Now, there several limits coming from different experiments which predict how massive neutrinos are. It turns out that they only have very tiny mass, for example a limit set by cosmology yields [35]:

$$\sum_{i=1}^{3} m_i \leq 0.23 \text{ eV} \tag{2.30}$$

However, like other SM fermions, massive neutrinos can very well be addressed by postulating a right handed neutrino (ν_r) and writing

$$\mathcal{L}^{\nu}_{Yuk} \sim Y_\nu \bar{L}_L H \nu_R + \text{ hc}, \tag{2.31}$$

where L_L is the SM left handed lepton doublet and H is the Higgs doublet, which can easily generate Dirac neutrino mass after SSB: $m_\nu(\bar{\nu_L}\nu_R + \text{ hc})$, with $m_\nu = Y_\nu v$ (v is the Higgs vev). The trouble is in order to generate neutrino mass of eV scale, the Yukawa interaction turns extremely fine tuned with $Y_\nu \sim 10^{-12}$. Therefore, the presence of tiny neutrino masses ($\sim$ eV), which suffers from huge fine tuning once assumed just to have a Dirac mass term like other SM fermions, very strongly indicate the existence of physics beyond the SM.

Interestingly, one can have SM gauge invariant dimension five operator of the form

$$\mathcal{O}_5 \sim \frac{1}{\Lambda}\, \bar{L^c_L} L_L H H, \tag{2.32}$$

also known as Weinberg operator, where L_L represents SM lepton doublet, H represents SM Higgs doublet and Λ is an unknown heavy physics scale [36]. One can generate light neutrino mass from such a term after spontaneous symmetry breaking through $\langle H \rangle = v$ to yield:

$$m_\nu \sim \frac{v^2}{\Lambda}. \tag{2.33}$$

It is rather easy to predict light neutrino mass in the right ballpark, by assuming Λ to be heavy. Now, the question is what is the unknown heavy Λ. Given the fact that right handed neutrinos can possess Majorana masses ($1/2 M \nu_R^T C^{-1} \nu_R$), they can exactly fit into the picture and one just needs to postulate $M_R = \Lambda$. The mechanism goes under the name of seesaw, as one generate light neutrino mass, after having a heavy mass in the denominator. A cartoon shown in Fig. 2.14 illustrates this beautiful idea.

Figure 2.14: Cartoon of generating light neutrino mass through seesaw mechanism. Fig courtesy: Google Images.

Technically, the methodology described above is called Type-I seesaw, which is the simplest possibility, which predict the presence of heavy right handed (RH) neutrinos to yield correct light neutrino mass through additional Yukawa coupling with SM Higgs [37]. Some other possibilities in canonical seesaw model include Type II and Type III, where light neutrino mass is generated through the same Weinberg operator in presence of scalar triplet and fermion triplet respectively as shown in Fig. 2.15. They all necessarily predict BSM physics with important and interesting phenomenological consequences. Apart from the canonical seesaw mechanisms, there exist several other possibilities including inverse seesaw, scotogenic and radiative Dirac model etc. In the thesis, we will mainly focus on Type I seesaw and connect it to dark sector.

To end this section, we remind that it is the lightness of the neutrino, which prohibit it to constitute the DM component of the universe, as being relativistic, they will create trouble for structure formation, one of the important motivations to have DM on board. Secondly, the relic density turns out to be extremely small as well. However, the very fact that neutrinos have similar charge neutrality and weak interaction, as similar to WIMP DM, it is intriguing to study DM and neutrino under same umbrella of physics beyond the SM.

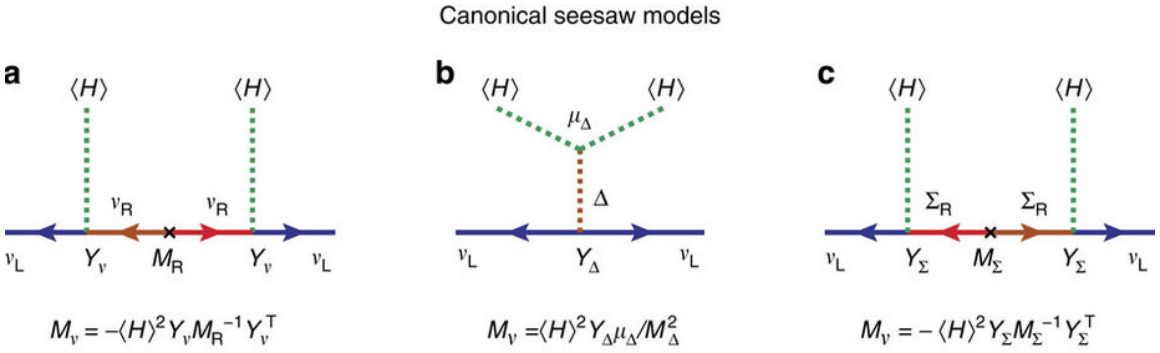

Figure 2.15: Some of major neutrino mass generation models. Fig courtesy: Slide from Zhi zhong-Xing at ICHEP.

2.3 EW Higgs vacuum stability

Another crucial issue lies in the spontaneous symmetry breaking and Higgs sector of the Standard Model. Given that current measured value of Higgs boson is $m_h = 125.09$ GeV and top quark mass $m_t = 173.1$ GeV [38], the electroweak (EW) vacuum can be unstable, questioning the existence of our universe [39]. This suggests that existence of another deeper minimum at high energy scale ($\Lambda_I \sim 10^{9-10}$ GeV) where running of Higgs quartic coupling λ_H can turn negative is a finite possibility. In Fig. 2.16, blue lines depict the running of Higgs quartic coupling towards the negative direction for different top quark masses. The negative contributions arise due to fermionic couplings in renormalization group (RG) running of Higgs quartic coupling λ_H. To study this effect, need to solve RG running of all SM couplings which are provided in AppendixB. In presence of right handed neutrinos, to address seesaw mechanism as described above, the additional Yukawa coupling further affects the running of Higgs quartic coupling negatively. As a result the instability scale could be lower than $\Lambda_I^{\rm SM}$ which is also shown in same Fig.2.16 with red lines for a fixed right handed neutrino mass and Yukawa coupling. The negative affects can be compensated by introducing additional BSM scalars which can also serve as DM components within the instability scale. We will discuss such effects in a specific model in chapter 5.

2.4 Objective of the thesis

The thesis mainly focuses in WIMP type DM scenarios due to its simplicity and predictability with less fine tuning. The WIMP paradigm however, suffers from a serious threat due to non-observation of DM in direct search experiments. Direct search experiments such as LUX [40, 41], XENON [27, 42–44], PANDA [45, 46] have been looking for WIMP-like DM to interact with earthly detectors and so far no such events have been reported. This in turn is predicting feebler DM-visible sector interaction. In fact, in a few years from now the DM-nucleon cross-section at direct search experiments may hit the neutrino floor, where neutrino-nucleon cross-section will be a huge background for DM detection. In a single component WIMP paradigm, relic density and direct search cross-sections of DM are mostly incompatible, as the

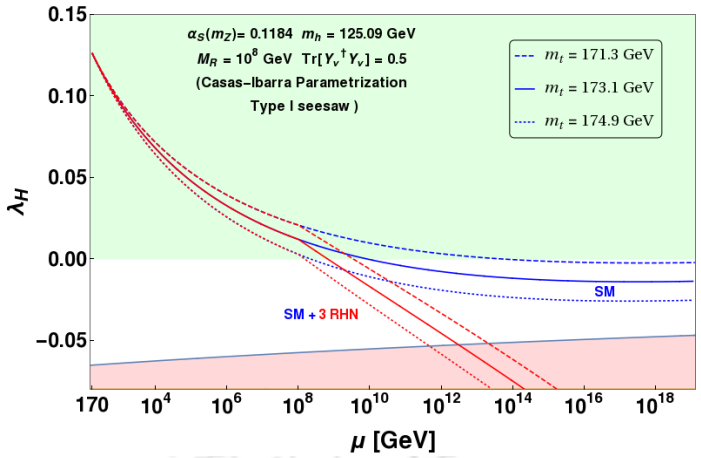

Figure 2.16: RG running of Higgs quartic coupling in presence of right handed neutrino.

interactions which lead to the freeze-out of DM in the early Universe, also yields DM-nucleon cross-section in direct search experiments. a similar argument is applicable to non-observation of DM in collider searches as well. The only distinction to collider search for a WIMP of 100 GeV is that the production of DM at collider is very suppressed (with no electromagnetic or strong interactions with SM), so that non-observation of DM in collider searches provide lesser threat to WIMP DM and yield a weaker constraint.

Multipartite DM frameworks can provide a cushion to the tension of WIMP like particles to satisfy relic density and direct search [34, 47–64]. This is essentially due to the presence of additional processes which can still contribute to the depletion of DM number density for thermal freeze-out, but do not contribute to direct search cross-section. The main two contributions of such kind can arise from (*i*) Co-annihilation of DM with a heavier particle, which can not be produced in direct search for kinematic suppression or (*ii*) DM-DM interactions, where the heavier DM component can annihilate to the lighter one to yield thermal relic, and also do not contribute to direct search. In this thesis we will investigate possible phenomenological aspects of such multipartite WIMP type DM scenarios. It is also intriguing to note while visible sector of the universe consisting only 5% of total energy budget of the universe possesses so many different fundamental particles (quarks, leptons, gauge bosons etc) with different strengths and characteristics of their interactions (strong, weak and electromagnetism), it is perhaps way too simple to assume only one kind of DM with one specific interaction to consist 20% of the universe.

Therefore the main idea of this thesis is to address all the phenomenological issues discussed above including DM, neutrinos and vacuum stability together. We aim to demonstrate these in multipartite DM scenarios. Our idea is to build such multipartite frameworks from the simplest possibility of accommodating a DM in extensions of SM, namely a scalar singlet stabilized by Z_2 symmetry. Future detection of DM is also a crucial point addressed in the thesis. However, singlet DMs have limited colliders search possibilities, due to lack of interaction with visible sector. The search strategy for such DM is therefore limited to mono-X signature with missing energy, where X can be jet, W, Z or Higgs [65] as illustrated before. Such signal arises out of initial state radiation (ISR) and suffers from huge SM background. Higher multiplet in dark sector, being equipped with charge components have better possibilities of getting

unravelled in future collider search experiments, but tighter constraints may arise from dark sector. Therefore, we will not elaborate the collider signal on two component scalar singlet DM scenario. However, we will discuss collider search strategies for two component set up involving singlet-doublet fermion and with inert Higgs.

Chapter 3

Multipartite Singlet Scalar Dark Matter

Contents

3.1 Introduction

A SM gauge singlet real scalar which is odd under a $\mathcal{Z}_2$ symmetry, while the SM is even under $\mathcal{Z}_2$, provides with a simplest dark matter candidate which has portal interactions through the SM Higgs. This model has been studied extensively for its simplicity and predictability [22, 66–71]. This model is also known to reduce the fine-tuning problem SM Higgs is plagued with [72]. One can accommodate as many of them as possible to extend to a multicomponent DM framework. The model can inherently carry a $\mathcal{O}(N)$ symmetry for N components on top of the individual $\mathcal{Z}_2$ symmetry, which however makes all the DMs having equal masses and same coupling strength to SM [69]. This particular feature restricts the model not to have non-zero interaction between different DM species, although such terms are present in the scalar potential. Hence, it results in no change to the thermal freeze out of each DM component compared to the single component scenario. The departure in allowed parameter space from the singlet scalar DM framework to such a multipartite framework is significant subject to the number of DM components, however equally restrictive. On the contrary, if one ignores the $\mathcal{O}(N)$ symmetry the masses of different DM components and their interactions with the SM can be set to be different from each other. Further, the absence of $\mathcal{O}(N)$ symmetry leads to non-zero interactions between the DM components. We study such interacting

multipartite scalar DM scenario, specifically for two component case. Generalisation to three or more components is straight forward, but not discussed in this report. We demonstrate the case when there are two distinct $\mathcal{Z}_2$ symmetry on each of the components and call that a model under $\mathcal{Z}_2 \times \mathcal{Z}_2^{'}$. It is important to note that when we have two DM scalar singlets odd under same $\mathcal{Z}_2$, i.e. a framework with $\mathcal{Z}_2 \times \mathcal{Z}_2$, there is inevitably one DM component, lighter of the two; the heavier one will decay to the lighter one at tree level or through loop generated process, depending on the mass splitting between the components.

Although the models have been discussed earlier [34, 47–51], we perform a systematic comparative analysis of the DM-allowed parameter space of the two-component framework. We explore the viability of $\mathcal{Z}_2 \times \mathcal{Z}_2^{'}$ model for relic abundance constraints from WMAP [9, 73], PLANCK [11] data, and direct detection constraint from XENON [27, 42, 43], LUX [40] as well as from updated LUX bound [41]. We specifically indicate that direct search constraints can be shown to be somewhat relaxed in presence of DM-DM interactions in multicomponent framework, allowing the DM components to be delayed till XENON1T limit.

The chapter is organised as follows: we discuss the singlet scalar single and multicomponent DM frameworks in Sec. 3.2; thermal freeze out and corresponding Boltzmann Equations are discussed in Sec. 3.3; parameter space scan on relic density of $\mathcal{Z}_2 \times \mathcal{Z}_2^{'}$ framework is discussed in Sec. 3.4 and approximate analytical solution of such a case is discussed in Sec. 3.5; direct search constraints are discussed next in Sec. 3.6. Finally we conclude the chapter.

3.2 Models for the Singlet Scalar DM

3.2.1 Single Component framework

Let us first review the DM model with a real singlet scalar ϕ [66]. The interaction with the SM can be written in general of the form $\frac{1}{\Lambda^{n-4}}\mathcal{O}_{DM}\mathcal{O}_{SM}$. Here $\mathcal{O}_{SM}$ is gauge invariant operator composed of the SM fields, whereas $\mathcal{O}_{DM}$ are those involving the DM fields. Λ is the new physics scale in effective theory formalism, whose power is determined by the dimension of the operator product, n. Since we are interested in renormalisable interaction terms, we consider only operators with $n \leq 4$. Stability of the DM is achieved through imposing a Z_2 symmetry, under which ϕ is specified to be odd with other fields are taken to be even. This necessitates ϕ to appear in even powers in the operators. Thus, the scalar potential, including the DM ϕ interacts with the SM through the Higgs portal term reads as [71, 74]

$$V(H,\phi) = -\mu_H^2 H^\dagger H + \lambda_H (H^\dagger H)^2 + \frac{1}{2}\mu_\phi^2\phi^2 + \frac{1}{4!}\lambda_\phi\phi^4 + \frac{1}{2}\lambda_1 H^\dagger H\phi^2\,, \tag{3.1}$$

where λ_1 parametrizes the 'Higgs-portal' interaction discussed above, with H denoting the SM Higgs isodoublet. The Lagrangian density for the scalar sector is then given by:

$$\mathcal{L}_{\text{scal}} = \frac{1}{2}\partial_\mu\phi\partial^\mu\phi + D_\mu H^\dagger D^\mu H - V(H,\phi) \tag{3.2}$$

where D_μ is the covariant derivative related to the SM gauge symmetry. Electroweak symmetry breaking (EWSB) occurs via non-zero vacuum expectation value of the

Higgs doublet $\langle H\rangle = (0, v/\sqrt{2})^T$, with $v = 246$ GeV. On the other hand, unbroken Z_2 symmetry requires $\mu_\phi^2 > 0$, ensuring $\langle\phi\rangle = 0$, which yields DM mass term $m_\phi^2 = \mu_\phi^2 + \frac{\lambda_1 v^2}{2}$.

In order to stabilize the vacuum we require that the scalar potential in eq. (3.1) is bounded from below. At the tree level it implies the following conditions [75, 76]

$$\lambda_\phi > 0\,, \quad \lambda_H > 0\,, \quad \lambda_1 + \sqrt{\frac{2}{3}\,\lambda_\phi\lambda_H} \quad > 0\,. \tag{3.3}$$

Tree-level unitarity constraints imply [77]

$$\begin{aligned} |\lambda_H| < 4\pi, \quad |\lambda_1| < 8\pi \\ |\ 12\lambda_H + \lambda_\phi \pm \sqrt{(\lambda_\phi - 12\lambda_H)^2 + 16\lambda_1^2}\ | < 32\pi \quad . \end{aligned} \tag{3.4}$$

Finally, the condition that the global $\mathcal{Z}_2$ symmetry remains unbroken requires $\mu_\phi^2 > 0$, which leads to $m_\phi^2 > \lambda_1 v^2/2$. DM relic density and direct search constraints are relevant for this model in a two dimensional parameter space denoted by the DM mass and the Higgs-portal coupling as

$$\{m_\phi, \lambda_1\} \tag{3.5}$$

The phenomenology and the allowed parameter space for such a model has been discussed by many authors [22, 68, 78–81]. In this report we shall limit our discussion in citing some of the important outcomes of this model in the comparative analysis with two component interacting DM frameworks that we analyse shortly in details.

3.2.2 Multipartite framework with $\mathcal{O}(N)$ symmetry

Simplest extension of a single component scalar DM framework to a multipartite case is obtained by assuming $N(\geq 2)$ such components of DM having same mass and coupling to the SM, replacing ϕ in above section by

$$\vec{\phi} \equiv \{\phi_1, \phi_2, \phi_3 ... \phi_N\}, \tag{3.6}$$

so that the scalar potential reads [69]:

$$V(H,\varphi) = -\mu_H^2 H^\dagger H + \lambda_H (H^\dagger H)^2 + \frac{1}{2}\mu_{\vec{\phi}}^2 \vec{\phi}^2 + \frac{1}{4!}\lambda_{\vec{\phi}} \left(\vec{\phi}^2\right)^2 + \frac{1}{2}\lambda_1 H^\dagger H \vec{\phi}^2\,. \tag{3.7}$$

Note here that the presence of an unbroken $\mathcal{O}(N)$ symmetry in the Lagrangian implies the same couplings $\mu_{\vec{\phi}}$, $\lambda_{\vec{\phi}}$ and λ_1 for all the DM components. This makes sure that each of the DM acquires same mass after EWSB as $m_{\vec{\phi}}^2 = \mu_{\vec{\phi}}^2 + \frac{\lambda_1 v^2}{2}$ and of course have same coupling to SM sector, λ_1. The term $\left(\vec{\phi}^2\right)^2$ in Eq. 3.7 although indicate the presence of interaction vertices between different DM components, the fact that all the DM components acquire same mass, yields effectively zero DM-DM interaction cross-section and thus drastically reduces the phenomenological possibilities of this model. This multipartite DM framework has been discussed in great details in [69] and we will refer to some of its important features in the following comparative analysis. It should

be noted here that on top of the $\mathcal{O}(N)$, a separate $\mathcal{Z}_2$ symmetry has to be imparted to each of the DM components for their stability so that

$$\phi_i \xrightarrow{\mathcal{Z}_2} -\phi_i \tag{3.8}$$

Vacuum stability of the potential dictates similar constraints as that of the single component case on the dimensionless couplings introduced here. This model has then three parameters as

$$\{m_\phi,\ \lambda_1,\ N\} \tag{3.9}$$

where the cross-sections are essentially governed by the same DM mass and coupling. The third parameter, N is the number of DMs considered in the model, which crucially changes the outcome, as we will see later. However it must be pointed out that, $\mathcal{O}(N)$ symmetry is not a necessary requirement for the components to be DM candidates. In the following, we shall explore some of the possibilities when the $\mathcal{O}(N)$ is not respected.

3.2.3 Two Component framework with $\mathcal{Z}_2 \times \mathcal{Z}_2'$ symmetry

When we break the global $\mathcal{O}(N)$ symmetry as described above and impose a separate $\mathcal{Z}_2$ on each of the components the scenario gets phenomenologically more interesting with interaction between different DM candidates. The simplest multipartite framework is to consider a two component DM set up by imposing two distinguishable $\mathcal{Z}_2 \times \mathcal{Z}_2'$ symmetry under which the two singlet scalars (ϕ_1, ϕ_2) stabilize. That means, under $\mathcal{Z}_2 \times \mathcal{Z}_2'$, different fields transform as: SM $[+,+]$, $\phi_1[-,+]$, $\phi_2[+,-]$. The new Lagrangian involves a few more parameters compared to the previous case respecting $\mathcal{O}(N)$ symmetry. The part of the Lagrangian involving only singlet scalar fields read as

$$\mathcal{L}_{DM} = \frac{1}{2}(\partial_\mu\phi_1)^2 + \frac{1}{2}(\partial_\mu\phi_2)^2 - \frac{1}{2}\mu_1^2\phi_1^2 - \frac{1}{2}\mu_2^2\phi_2^2 - \frac{1}{4}\lambda_3\phi_1^2\phi_2^2 - \frac{1}{4!}\lambda_4\phi_1^4 - \frac{1}{4!}\lambda_5\phi_2^4 \tag{3.10}$$

The part of the Lagrangian describing the interaction of DM fields with the SM Higgs fields is given by

$$-\mathcal{L}_{SM-DM} = \frac{1}{2}\lambda_1\phi_1^2 H^\dagger H + \frac{1}{2}\lambda_2\phi_2^2 H^\dagger H. \tag{3.11}$$

The scalar potential hence read:

$$\begin{aligned} V(\phi_1,\phi_2,H) = {} & \frac{1}{2}\mu_1^2\phi_1^2 + \frac{1}{2}\mu_2^2\phi_2^2 + \frac{1}{4}\lambda_3\phi_1^2\phi_2^2 + \frac{1}{4!}\lambda_4\phi_1^4 + \frac{1}{4!}\lambda_5\phi_2^4 \\ & -\mu_H^2 H^\dagger H + \lambda_H (H^\dagger H)^2 + \frac{1}{2}\lambda_1\phi_1^2 H^\dagger H + \frac{1}{2}\lambda_2\phi_2^2 H^\dagger H \end{aligned} \tag{3.12}$$

Stability of this potential requires [76, 82]

$$\begin{gathered} \lambda_4 > 0 \quad , \lambda_5 > 0 \quad , \lambda_H > 0 \quad , \\ \lambda_1 + \sqrt{\frac{2}{3}\lambda_4\lambda_H} > 0 \quad \lambda_2 + \sqrt{\frac{2}{3}\lambda_5\lambda_H} > 0 \ , \ \lambda_3 < \sqrt{\frac{1}{9}\lambda_4\lambda_5} > 0. \end{gathered} \tag{3.13}$$

We may note that, unlike the case where $\mathcal{O}(N)$ symmetry is realised (Eq. 3.7), here the couplings of ϕ_1 and ϕ_2 could be independent of each other. After the electroweak phase transition, with the vacuum expectaion values of fields given by $\langle H \rangle = (0, v/\sqrt{2})^T$, where $v = 246$ GeV, $\langle \phi_1 \rangle = \langle \phi_2 \rangle = 0$, the part of the Lagrangian involving the DM fields takes the form

$$\begin{aligned}\mathcal{L}_{DM} + \mathcal{L}_{SM-DM} &= \frac{1}{2}(\partial_\mu \phi_1)^2 + \frac{1}{2}(\partial_\mu \phi_2)^2 - \frac{1}{2}m_{\phi_1}^2 \phi_1^2 - \frac{1}{2}m_{\phi_2}^2 \phi_2^2 \\ &- \frac{1}{4}\lambda_3 \phi_1^2 \phi_2^2 - \frac{1}{4!}\lambda_4 \phi_1^4 - \frac{1}{4!}\lambda_5 \phi_2^4 \\ &- \frac{1}{4}\lambda_1 \phi_1^2 h^2 + \frac{1}{4}\lambda_2 \phi_2^2 h^2 \\ &- \frac{1}{2}\lambda_1 v h \phi_1^2 + \frac{1}{2}\lambda_2 v h \phi_2^2. \end{aligned} \tag{3.14}$$

Here the mass of the DM candidates are $m_{\phi_1}^2 = (\mu_1^2 + \frac{\lambda_1 v^2}{2})$ and $m_{\phi_2}^2 = (\mu_2^2 + \frac{\lambda_2 v^2}{2})$. In the absence of $\mathcal{O}(2)$ symmetry, the parameters λ_i and μ_i^2 are not necessarily the same for different fields, leading to a wide range of mass splittings between different DM components. Presence of the mutual interaction coupling, λ_3, along with the mass splitting could have dramatic effects, resulting in clearly distinguishable features. It might be helpful to remind that in presence of $\mathcal{O}(2)$ symmetry, the DM masses are degenerate, so in spite of having $\lambda_3 \phi_1^2 \phi_2^2$ term in the Lagrangian, the DM conversion process ($\phi_1 \phi_1 \rightarrow \phi_2 \phi_2$) is not effective. The main focus of this work is to encapsulate the effect of DM-DM conversion, which we shall do in the following sections in detail.

The relevant DM phenomenology of such a two-component framework is mainly dictated by the five parameters:

$$\{m_{\phi_1}, m_{\phi_2}, \lambda_1, \lambda_2, \lambda_3\}. \tag{3.15}$$

The parameter λ_3 solely determines the direct interaction between the two DM components. As we shall demonstrate, presence of non-zero value of λ_3 marks a significant departure in the allowed DM parameter space in terms of relic density and direct search constraints. It is straightforward to extend such a model to multipartite framework by considering n such DM components $\{\phi_1, \phi_2, ...\phi_n\}$ stabilised by $\mathcal{Z}_2^{(1)} \times \mathcal{Z}_2^{(2)} ... \times \mathcal{Z}_2^{(n)}$ symmetry, which involves $(n + n + {}^nC_2)$ parameters over and above the SM parameters. In line with Eq. 3.15 these parameters could be considered to be the masses and couplings denoted as

$$\{m_{\phi_1}, ..m_{\phi_n}, \lambda_1, ..\lambda_n, \lambda_{12}^{'}, ..\lambda_{(n-1)n}^{'}\} \tag{3.16}$$

where λ_i denote the interactions of ϕ_i to the SM Higgs, whereas $\lambda_{ij}^{'}$ denotes the direct interaction between the DM components ϕ_i and ϕ_j. Such a multi-component system with a large number of independent parameters is hard to analyse in a meaningful way, without further assumptions. However, all the essential features of such a scenario could be captured by a two-component case, and we shall limit ourselves to discuss the case of the two-component DM case in this work.

3.3 Thermal freeze out and Boltzmann Equations

Our goal in this section is to determine the thermal freeze out of the DM components. We start with formulating the Boltzmann equations (BEQ) that govern cosmological evolution of the scalar singlets (ϕ) DM in a single component framework. This has already been discussed to some extent before; nevertheless it is good to remind the basic framework once more to set up multipartite analysis taken up next. The BEQ for the single component framework reads [15]:

$$\begin{aligned}\dot{n}_\phi + 3Hn_\phi &= -\int \frac{\zeta_\phi d^3p}{(2\pi)^3 2E_p}\frac{\zeta_\phi d^3p'}{(2\pi)^3 2E'_p}\frac{\zeta_{SM} d^3q}{(2\pi)^3 2E_q}\frac{\zeta_{SM} d^3q'}{(2\pi)^3 2E'_q}\delta^4(p+p'-q-q')\times \\ &\quad |\mathcal{M}_{\phi\phi\to SMSM}|^2\left(\tilde{f}_\phi\tilde{f}_\phi - \tilde{f}^{EQ}_\phi\tilde{f}^{EQ}_\phi\right) \end{aligned} \tag{3.17}$$

where n_ϕ denote the number density of ϕ, n^{EQ}_ϕ the corresponding equilibrium density, $\dot{n}_\phi$ is the time derivative of the number density, $\mathcal{M}_{i\to f}$ is the amplitude for the process $i \to f$, including the spin average and symmetry factors, H denotes the Hubble parameter and ζ_ϕ indicates the internal degrees of freedom associated to the particular DM species and for singlet scalar, we have $\zeta_\phi = 1$. A phase space density $\tilde{f}_\phi$ and an equilibrium density $\tilde{f}^{EQ}_\phi$ are related to corresponding number densities as follows:

$$n_\phi = \int \frac{\zeta_\phi d^3p}{(2\pi)^3 2E}\tilde{f}_\phi, \quad n^{EQ}_\phi = \int \frac{\zeta_\phi d^3p}{(2\pi)^3 2E}\tilde{f}^{EQ}_\phi, \quad \tilde{f}^{EQ}_\phi = \frac{1}{e^{E/T}-1} \tag{3.18}$$

To simplify BEQs we will use the thermally averaged cross section $\langle\sigma_{ab\to cd}\, v\rangle$, defined as [15, 22, 24]:

$$\begin{aligned}\langle\sigma_{ab\to cd}v\rangle &\equiv \frac{1}{\left(n^{EQ}_a n^{EQ}_b\right)}\int \frac{\zeta_a d^3p}{(2\pi)^3 2E_p}\frac{\zeta_b d^3p'}{(2\pi)^3 2E'_p}\frac{\zeta_c d^3q}{(2\pi)^3 2E_q}\frac{\zeta_d d^3q'}{(2\pi)^3 2E'_q}\times \\ &\quad \delta^4(p+p'-q-q')|\mathcal{M}_{ab\to cd}|^2 e^{-(E_p+E'_p)/T} \\ &= \int_{(m_a+m_b)^2}^{\infty} ds\, \frac{s\sqrt{s-(m_a+m_b)^2}\; K_1(\frac{\sqrt{s}}{T})\; (\sigma v)_{ab\to cd}}{16T\; m_a^2 m_b^2\; K_2(\frac{m_a}{T})K_2(\frac{m_b}{T})} \end{aligned} \tag{3.19}$$

where in the last line we recast the thermal average cross-section in terms of the Mandelstam variable $s = (E_a + E_b)^2$ in the c.o.m frame, $K_{1,2}$ represent first and second Bessel functions in terms of appropriate variables and T is the temperature of the universe. The threshold s required is $s_0 = (m_a + m_b)^2$ for the reactions to occur. Assuming kinetic equilibrium of DM with SM fields and neglecting possible effects of quantum statistics the BEQ for the single-component case simplify [15]:

$$\dot{n}_\phi + 3Hn_\phi = -\langle\sigma_{\phi\phi\to SM}v\rangle\left(n^2_\phi - n^{EQ2}_\phi\right) \tag{3.20}$$

The diagrams contributing to $\phi_i\phi_i$ annihilation to SM particles are shown in Fig. 3.1. Dominant annihilation cross-section is obtained to gauge boson final states while the one to light fermions are small due to small Yukawa couplings. The corresponding cross sections are available in the literature (e.g. [67, 79]). In a single component framework, there is no scope for DM-DM interaction. While we move on to two-component framework, DM-DM interaction plays a crucial role and possible diagrams are shown in the Fig. 3.2.

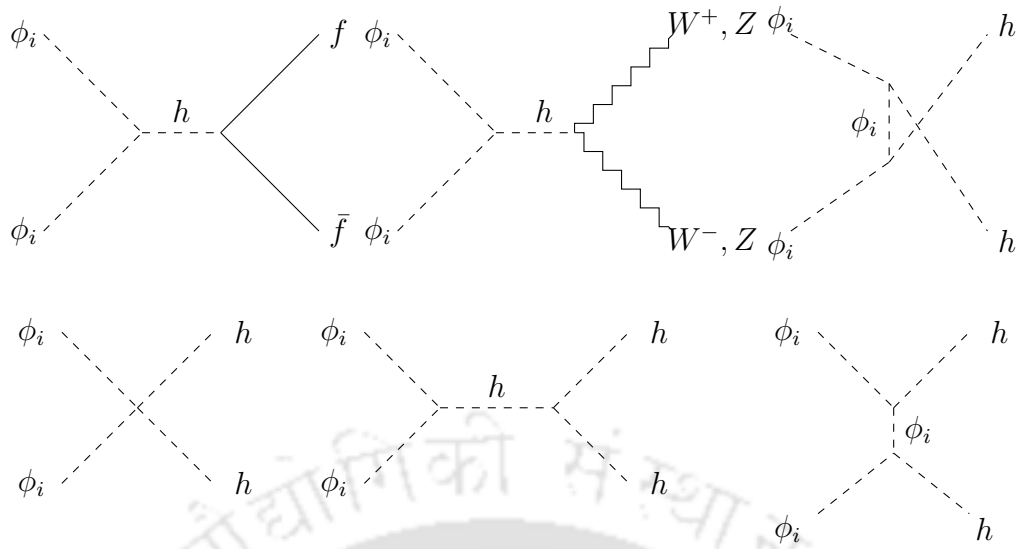

Figure 3.1: Diagrams contributing to $\phi_i\phi_i$ annihilation to SM particles ($i = \{1, 2\}$ in two component set up).

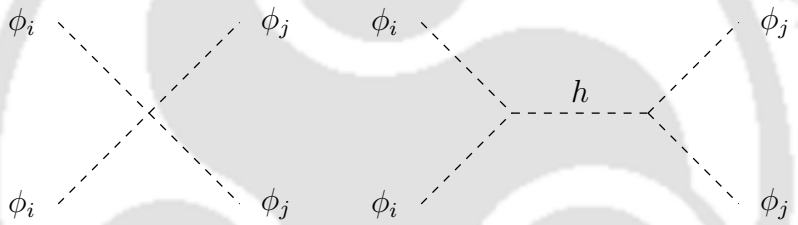

Figure 3.2: Diagrams contributing to DM conversion in $\mathcal{Z}_2 \times \mathcal{Z}_2^{'}$ model ($i, j = 1, 2;\ i \neq j$).

We now argue that in case of scalar DM interactions, instead of using the whole expression of thermal average cross-section $\langle\sigma v\rangle$ in BEQ, as in Eq. 3.19, we can use (σv) at threshold $s = s_0 = (m_a + m_b)^2$ as [83]:

$$(d\sigma\ v)_{ab\to cd} = \frac{|\mathcal{M}|^2_{ab\to cd}\ dQ}{4m_a m_b} \tag{3.21}$$

where dQ is the phase space differential and $|\mathcal{M}|^2$ is the matrix element square averaged and $m_{a,b}$ are the masses of annihilating particles. This essentially corresponds to the so called $s-$ wave contribution to annihilation cross-section and in presence of this term, the v^2 dependent terms (p wave, for example) can be neglected. We will show that $(\sigma v)_{ab\to cd}$ is almost the same as to the thermal averaged $\langle\sigma v\rangle_{ab\to cd}$ even at low $x = \frac{m}{T}$. The advantage of using $(\sigma v)_{ab\to cd}$ is the absence of temperature dependence in it, which helps solving the BEQs relatively easier; particularly in case of coupled BEQ which we need for the DM analysis of the model. Hence, we rewrite the DM annihilation cross-sections to SM in terms of (σv) adopting Eq. 3.21 as follows [67, 79]:

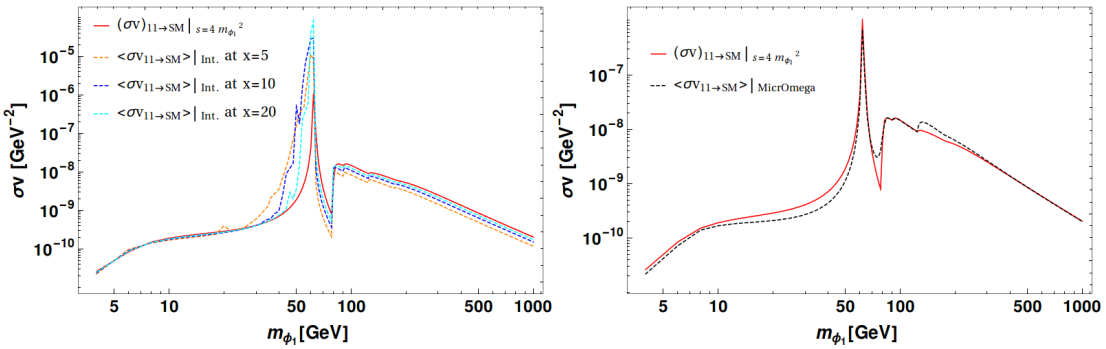

Figure 3.3: Left: Comparison of $(\sigma v)_{\phi_1\phi_1\to SM}$ (red thick line) as in Eq. 3.23 with thermal average cross-section $\langle\sigma v\rangle_{\phi_1\phi_1\to SM}$ as in Eq. 3.19. $\langle\sigma v\rangle$ is evaluated at $x = \frac{m_{\phi_1}}{T} = 5$ (Orange dashed), 10 (Blue dashed), 20 (Cyan dashed). Right: Comparison of $(\sigma v)_{\phi_1\phi_1\to SM}$ (red thick line) to $\langle\sigma v\rangle_{\phi_1\phi_1\to SM}$ extracted from code `MicrOMEGAs` (black dots). The plot is shown as a function of DM mass m_{ϕ_1} [GeV] for single component scalar singlet DM ϕ_1. We choose the DM-SM coupling $\lambda_1 = 0.1$ for illustration.

$$
\begin{aligned}
(\sigma v)_{\phi_1\phi_1\to f\bar{f}} &= \frac{1}{4\pi s\sqrt{s}}\frac{N_c\lambda_1^2 m_f^2}{(s-m_h^2)^2+m_h^2\Gamma_h^2}(s-4m_f^2)^{\frac{3}{2}} \\
(\sigma v)_{\phi_1\phi_1\to W^+W^-} &= \frac{\lambda_1^2}{8\pi}\frac{s}{(s-m_h^2)^2+m_h^2\Gamma_h^2}(1+\frac{12m_W^4}{s^2}-\frac{4m_W^2}{s})(1-\frac{4m_W^2}{s})^{\frac{1}{2}} \\
(\sigma v)_{\phi_1\phi_1\to ZZ} &= \frac{\lambda_1^2}{16\pi}\frac{s}{(s-m_h^2)^2+m_h^2\Gamma_h^2}(1+\frac{12m_Z^4}{s^2}-\frac{4m_Z^2}{s})(1-\frac{4m_Z^2}{s})^{\frac{1}{2}} \\
(\sigma v)_{\phi_1\phi_1\to hh} &= \frac{\lambda_1^2}{16\pi s}\left[1+\frac{3m_h^2}{(s-m_h^2)}-\frac{4\lambda_1 v^2}{(s-2m_h^2)}\right]^2(1-\frac{4m_h^2}{s})^{\frac{1}{2}} \\
(\sigma v)_{\phi_1\phi_1\to SM} &= (\sigma v)_{\phi_1\phi_1\to f\bar{f}}+(\sigma v)_{\phi_1\phi_1\to W^+W^-}+(\sigma v)_{\phi_1\phi_1\to ZZ} \\
&\quad +(\sigma v)_{\phi_1\phi_1\to hh}
\end{aligned}
\tag{3.22}
$$

where $\sqrt{s}$ is the centre-of-mass energy and Γ_h [68] denotes Higgs decay width at resonance. $N_c = 3$ is the colour factor for quarks, for leptons it is unity. Similarly annihilation cross-sections for the second component: $(\sigma v)_{\phi_2\phi_2\to SM}$ can be written replacing λ_1 by λ_2 in Eq. 3.22. In Fig. 3.3, we show that the $(\sigma v)_{\phi_1\phi_1\to SM}$ (as in Eq. 3.22) in red thick line, closely mimics the thermal average annihilation cross-section $\langle\sigma v\rangle_{\phi_1\phi_1\to SM}$ (as in Eq. 3.19). In the left panel of Fig. 3.3, we choose three different values of $x = \frac{m_{\phi_1}}{T} = 5$ (Orange dashed), 10 (Blue dashed), 20 (Cyan dashed) to evaluate $\langle\sigma v\rangle_{\phi_1\phi_1\to SM}$. It clearly shows, that excepting some fluctuations near the resonance region ($m_{\phi_1} = \frac{m_h}{2}$) for small values of x, thermal average cross-section agrees well to $(\sigma v)_{\phi_1\phi_1\to SM}$. In the right panel of Fig. 3.3, we compare the same $(\sigma v)_{\phi_1\phi_1\to SM}$ with the thermal average cross-section that code `MicrOMEGAs` [84] generates (black dots) to further establish the claim. The annihilation cross-section is plotted as a function of DM mass m_{ϕ_1} [GeV] with a specific choice of $\lambda_1 = 0.1$. For other values of λ_1, the behaviour remains the same. In the expressions of $(\sigma v)_{\phi_1\phi_1\to SM}$ as in Eq. 3.22, we have used threshold value of $s = s_0 = 4m_{\phi_1}^2$. We will use it throughout the analysis and even if not explicit, we will mean

$$
(\sigma v)_{ab\to cd} \equiv (\sigma v)_{ab\to cd}|_{s=(m_a+m_b)^2} \tag{3.23}
$$

For $\mathcal{Z}_2 \times \mathcal{Z}_2^{'}$ model, the interaction between DM components ($\phi_1\phi_1 \to \phi_2\phi_2$) are governed by the diagrams in Fig. 3.2. Assuming $m_{\phi_1} > m_{\phi_2}$,

$$(\sigma v)_{\phi_1\phi_1\to\phi_2\phi_2} = \frac{\sqrt{s-4m_{\phi_2}^2}}{8\pi s\sqrt{s}}\left[\frac{v^4\lambda_1^2\lambda_2^2}{(s-m_h^2)^2+m_h^2\Gamma_h^2} + \frac{2(s-m_h^2)v^2\lambda_1\lambda_2\lambda_3}{(s-m_h^2)^2+m_h^2\Gamma_h^2} + \lambda_3^2\right] \quad (3.24)$$

In absence of the contact interaction (first diagram in the top panel of Fig. 3.2), i.e. $\lambda_3 \to 0$, the expression simplifies to:

$$(\sigma v)_{\phi_1\phi_1\to\phi_2\phi_2} = \frac{v^4\lambda_1^2\lambda_2^2}{8\pi s\sqrt{s}}\frac{\sqrt{s-4m_{\phi_2}^2}}{(s-m_h^2)^2+m_h^2\Gamma_h^2} \quad (3.25)$$

We would like to mention here that in $\mathcal{O}(2)$ model, the DM-DM interactions as in Fig. 3.2, are all present, but the contribution is identically zero with masses of the two DM components identical. For $m_{\phi_2} > m_{\phi_1}$, we similarly obtain $(\sigma v)_{\phi_2\phi_2\to\phi_1\phi_1}$. A

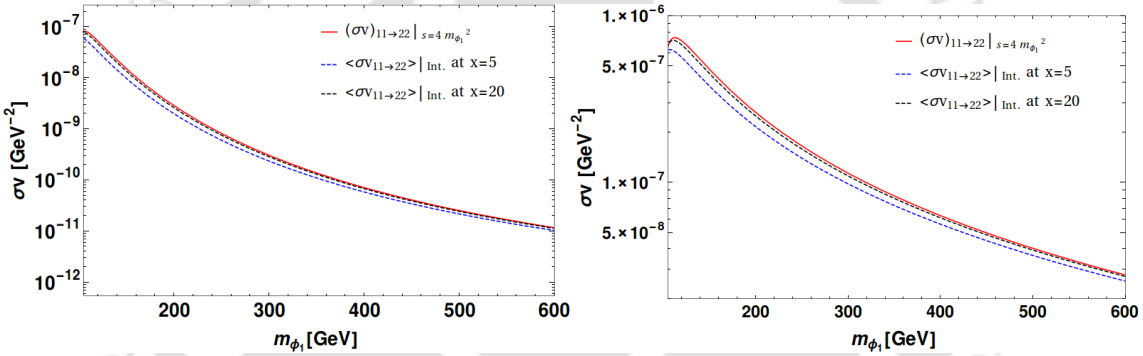

Figure 3.4: Comparison of $(\sigma v)_{\phi_1\phi_1\to\phi_2\phi_2}$ (as in Eq. 3.24) in red thick line with thermal average cross-section $\langle\sigma v\rangle_{\phi_1\phi_1\to\phi_2\phi_2}$ for DM-DM interactions in $\mathcal{Z}_2 \times \mathcal{Z}_2^{'}$ model is shown as a function of DM mass m_{ϕ_1} [GeV]. We choose parameters $\{\lambda_1, \lambda_2, \lambda_3, m_{\phi_2}\} = \{0.5, 0.5, 0.01, 100\}$ (left), $\{0.5, 0.5, 1.0, 100\}$ (right) for illustration. $\langle\sigma v\rangle$ is evaluated at two different values: $x = \frac{m}{T} = 5$ (Blue dashed), 20 (Black dashed).

detailed comparison of DM annihilation to SM with DM-DM interaction will be performed in the next section. In Fig. 3.4, we demonstrate the comparison of $(\sigma v)_{\phi_1\phi_1\to\phi_2\phi_2}$ (red line) to the thermally averaged DM-DM interactions $\langle\sigma v\rangle_{\phi_1\phi_1\to\phi_2\phi_2}$ for two different choices of $x = \frac{m}{T} = 5$ (Blue dashed), 20 (Black dashed). We illustrate two different parameter sets $\{\lambda_1, \lambda_2, \lambda_3, m_{\phi_2}\} = \{0.5, 0.5, 0.01, 100\}$ (left), $\{0.5, 0.5, 1.0, 100\}$ (right); and both of them show a very good agreement of s-wave cross-section to the thermal average DM-DM interaction cross-section.

It is already understood that the thermal average cross-section inherently poses a temperature dependence, which is explicitly demonstrated in Fig. 3.5. Here we show the variation in $\langle\sigma v\rangle_{\phi_1\phi_1\to SM}$ with respect to temperature T for single component case in the left panel and $\langle\sigma v\rangle_{\phi_1\phi_1\to\phi_2\phi_2}$ for the two component case in the right panel. We can see that the temperature dependence is more for small x or large T regions, although the variation is limited within an order of magnitude. For the two component case, we deliberately choose the masses of the DMs close to each other as the temperature dependence is more sensitive for such a scenario. However, we clearly see

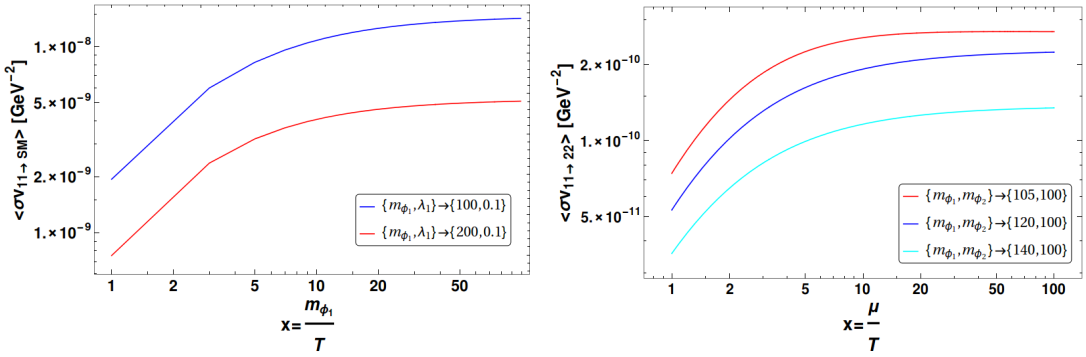

Figure 3.5: Variation of thermal average annihilation cross-section with T. Left: $\langle\sigma v\rangle_{\phi_1\phi_1\to SM}$ as in Eq. 3.19 for single component case is depicted with two different choices of DM mass $m_{\phi_1} = \{100\text{ (Blue)},\ 200\text{ (Red)}\}$ GeV for a fixed $\lambda_1 = 0.1$. Right: Variation of DM-DM interaction $\langle\sigma v\rangle_{\phi_1\phi_1\to\phi_2\phi_2}$ is shown for two component $\mathcal{Z}_2\times\mathcal{Z}_2^{'}$ model for three different DM mass combinations: $\{m_{\phi_1}, m_{\phi_2}\} = \{105, 100\}$ (Red), $\{120, 100\}$ (Blue), $\{140, 100\}$ (Cyan); $\{\lambda_1, \lambda_2, \lambda_3\} = \{0.1, 0.1, 0.01\}$ are chosen for illustration.

that for $x > 5$, the annihilation cross-sections are almost independent of T and we can safely use (σv) for this model.

Let us now turn to the coupled BEQs that govern the two component DM freeze out. We will recast the BEQs in terms of yield $Y = \frac{n_{\phi_i}}{s}$ so as to indicate the number density in comoving volume, where n_{ϕ_i} is the number density of ϕ_i and s is the entropy density of the universe given by [15]

$$s = \frac{2\pi^2}{45} g_s(T) T^3\,; \quad g_s(T) = \sum_k r_k g_k \left(\frac{T_k}{T}\right)^3 \theta(T - m_k)\,; \tag{3.26}$$

here k runs over all particles, T_k is the temperature of particle k and g_k its number of internal degrees of freedom, and $r_k = 1\,(7/8)$ when k is a bosons (fermion).

The BEQs can be written as a function of temperature (T) or in terms of $x = \frac{m}{T}$ where m is the mass of the DM particle. However, using x as a common variable for two-component case is problematic as mass m here represents two different variables (m_{ϕ_1}, m_{ϕ_2}) for two DM species. Hence, one way to obtain a common variable is to introduce a reduced mass μ for the two component DM system and define x with respect to reduced mass as $x = \frac{\mu}{T}$ where $\frac{1}{\mu} = \frac{1}{m_{\phi_1}} + \frac{1}{m_{\phi_2}}$ i.e $\frac{1}{x} = \frac{T}{\mu} = \frac{1}{x_1} + \frac{1}{x_2}$. In terms

of reduced x the BEQs read [34, 85]:

$$\begin{aligned}
\frac{dY_1}{dx} &= -0.264 M_{Pl}\sqrt{g}_*\frac{\mu}{x^2}\Big[\langle\sigma v_{11\to SM}\rangle(Y_1^2 - Y_1^{EQ^2}) \\
&\quad +\langle\sigma v_{11\to 22}\rangle(Y_1^2 - \frac{Y_1^{EQ^2}}{Y_2^{EQ^2}}Y_2^2)\Theta(m_{\phi_1}-m_{\phi_2}) \\
&\quad -\langle\sigma v_{22\to 11}\rangle(Y_2^2 - \frac{Y_2^{EQ)}}{Y_1^{EQ^2}}Y_1^2)\Theta(m_{\phi_2}-m_{\phi_1})\Big] \\
\frac{dY_2}{dx} &= -0.264 M_{Pl}\sqrt{g}_*\frac{\mu}{x^2}\Big[\langle\sigma v_{22\to SM}\rangle(Y_2^2 - Y_2^{EQ^2}) \\
&\quad +\langle\sigma v_{22\to 11}\rangle(Y_2^2 - \frac{Y_2^{EQ^2}}{Y_1^{EQ^2}}Y_1^2)\Theta(m_{\phi_2}-m_{\phi_1}) \\
&\quad -\langle\sigma v_{11\to 22}\rangle(Y_1^2 - \frac{Y_1^{EQ^2}}{Y_2^{EQ^2}}Y_2^2)\Theta(m_{\phi_1}-m_{\phi_2})\Big]
\end{aligned} \tag{3.27}$$

where the equilibrium distributions now recast in terms of μ has the form

$$Y_i^{EQ}(x) = 0.145\frac{g}{g_*}x^{\frac{3}{2}}(\frac{m_{\phi_i}}{\mu})^{\frac{3}{2}}e^{-x(\frac{m_{\phi_i}}{\mu})} \tag{3.28}$$

In above equations, $M_{Pl} = \frac{1}{\sqrt{G}} = 1.22\times 10^{19}$ GeV and $g_* = 106.7$ [15]. One should note additional contributions due to DM-DM conversions in the coupled Eqs.3.27. Depending on the mass hierarchy, one of $11 \to 22$ or $22 \to 11$ will contribute. We have used Θ functions appropriately to illustrate that fact. In the following analysis, we will demonstrate that in certain regions of the multipartite DM parameter space, DM-DM interaction is large enough to claim a change in DM freeze out and hence in relic density.

Even further simplification occurs to the coupled BEQ by pulling out the large numerical factors from Y_i $(i = 1, 2)$ in terms of modified y_i as

$$y_i = 0.264 M_{Pl}\sqrt{g_*}\mu Y_i \;;\quad y_i^{EQ} = 0.264 M_{Pl}\sqrt{g_*}\mu Y_i^{EQ} \tag{3.29}$$

In terms of y_i the BEQs for $\mathcal{Z}_2\times\mathcal{Z}_2^{'}$ model:

$$\begin{aligned}
\frac{dy_1}{dx} &= -\frac{1}{x^2}\Big[\langle\sigma v_{11\to SM}\rangle(y_1^2 - y_1^{EQ^2}) + \langle\sigma v_{11\to 22}\rangle(y_1^2 - \frac{y_1^{EQ^2}}{y_2^{EQ^2}}y_2^2)\Theta(m_{\phi_1}-m_{\phi_2}) \\
&\quad -\langle\sigma v_{22\to 11}\rangle(y_2^2 - \frac{y_2^{EQ^2}}{y_1^{EQ^2}}y_1^2)\Theta(m_{\phi_2}-m_{\phi_1})\Big] \\
\frac{dy_2}{dx} &= -\frac{1}{x^2}\Big[\langle\sigma v_{22\to SM}\rangle(y_2^2 - y_2^{EQ^2}) - \langle\sigma v_{11\to 22}\rangle(y_1^2 - \frac{y_1^{EQ^2}}{y_2^{EQ^2}}y_2^2)\Theta(m_{\phi_1}-m_{\phi_2}) \\
&\quad +\langle\sigma v_{22\to 11}\rangle(y_2^2 - \frac{y_2^{EQ^2}}{y_1^{EQ^2}}y_1^2)\Theta(m_{\phi_2}-m_{\phi_1})\Big]
\end{aligned} \tag{3.30}$$

We solve the coupled equations in Eq. 3.30 numerically (as we will argue that solving the equations analytically is much harder) to find out the freeze out of the DM

components and hence compute relic density of the DM species by [47, 86, 87]

$$\begin{aligned}\Omega_1 h^2 &= \frac{854.45\times10^{-13}}{\sqrt{g_*}}\frac{m_{\phi_1}}{\mu}\, y_1\left[\frac{\mu}{m_{\phi_1}}x_\infty\right],\\ \Omega_2 h^2 &= \frac{854.45\times10^{-13}}{\sqrt{g_*}}\frac{m_{\phi_2}}{\mu}\, y_2\left[\frac{\mu}{m_{\phi_2}}x_\infty\right],\\ \Omega_T h^2 &= \Omega_1 h^2+\Omega_2 h^2 \end{aligned} \tag{3.31}$$

In Eq. 3.31, $y_1\left[\frac{\mu}{m_{\phi_1}}x_\infty\right]$ indicates the value of y_1 evaluated at $\frac{\mu}{m_{\phi_1}}x_\infty$, where x_∞ indicates a very large value of x after decoupling. In numerical analysis, $x\sim100$ is good enough to indicate freeze out of scalar DM in such a model while we choose $x=500$ to be on the safe side. We will demonstrate freeze out of the DM components in the next section in different regions of parameter space to validate above claim. Also note here that the solution of the coupled BEQ yields y_i as a function of $x=\frac{\mu}{T}$, while relic density of individual components should be expressed in terms of $x_i=\frac{m_i}{T}$. Hence, in Eq. 3.31, we substitute $x=\frac{\mu}{T}=\frac{\mu}{m_{\phi_i}}x_i$ $(i=1,2)$.

Multipartite DM framework with $\mathcal{O}(N)$ symmetry predicts degenerate DM scenario and hence do not yield non-zero DM-DM interactions as has already been stated. Hence, the BEQ mimics as single component BEQ as in Eq. 3.20. The annihilation cross-sections also remain exactly the same although relic density in such a case is simply scaled by the number of DM components (N) all of which interact to SM in a similar way [69]:

$$\Omega_T = N\Omega_i \tag{3.32}$$

Ω_i is the relic density of an individual components ϕ_i given approximately by the inverse of annihilation cross-section of ϕ_i to SM as

$$\Omega_i = \frac{854.45\times10^{-13}}{\sqrt{g_*}}y_i[x_\infty]\simeq\frac{0.1\text{ pb}}{\langle\sigma v\rangle_i} \tag{3.33}$$

In literature coupled BEQ for multi-partite scalar singlet DM have been mentioned in many cases [49, 69], however an elaborate scan of the available parameter space has not been performed with DM-DM interactions kept on. In the following, we take up a systematic analysis of the two component DM scenario in $\mathcal{Z}_2\times\mathcal{Z}_2^{'}$ model to find out accessible parameter space by relic density and direct search constraints and indicate possible distinctive features of having DM-DM interactions.

3.4 Relic Density Analysis

Our goal of this part of the analysis is to find the available parameter space of the two component DM framework in $\mathcal{Z}_2\times\mathcal{Z}_2^{'}$ model from relic density constraint as well as indicate the departure in freeze-out due to interactions between two DM components. Multicomponent DM freeze-out is dependent on annihilations to SM and on the conversions between DM components. Annihilation cross-sections to SM for scalar singlet DM with Higgs portal coupling is well studied and understood, as pointed out in Eq. 3.22 and shown in Fig. 3.6. We demonstrate the annihilation $\phi_1\phi_1\to SM$ as a function of m_{ϕ_1} in the top panel of Fig. 3.6 for three different values of $\lambda_1=\{0.01,0.1,1.0\}$ in

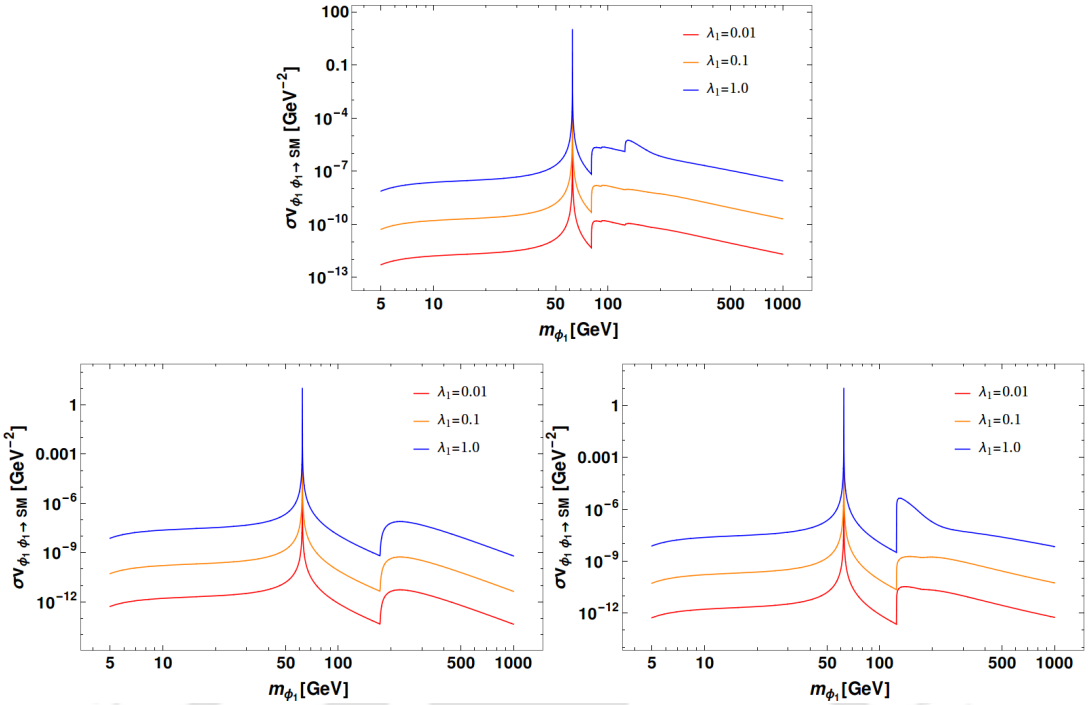

Figure 3.6: Top: $(\sigma v)_{\phi_1\phi_1\to SM}$ is plotted as a function of m_{ϕ_1}; Bottom Left: Annihilations to WW, ZZ, hh are prohibited; Bottom right: Annihilations to WW, ZZ are prohibited. Three different values of $\lambda_1 = \{0.01$ (Red), 0.1 (Orange), 1.0 (Blue)$\}$ are chosen from bottom to up respectively.

red, orange and blue respectively. The Higgs resonance is clearly seen at $m_{\phi_1} = m_h/2$, while there is a significant bump observed at $m_{\phi_1} = 80$ GeV, when WW channel opens up. For large value of $\lambda_1 = 1.0$ (blue curve) in top panel of Fig. 3.6, a small bump is seen at $m_{\phi_1} \sim m_h = 125$ GeV, indicating large annihilation contributions opening to hh channel which has a larger sensitivity to λ_1. To illustrate the contributions to different SM final states, in the bottom left panel we stop WW, ZZ, hh annihilations to show the bump in annihilation cross-section at $m_{\phi_1} \sim m_t = 173$ GeV. In the bottom right panel, we similarly stop WW, ZZ channel to show the contribution to hh final state. Annihilation cross-section for $\phi_2\phi_2 \to SM$ is similar as a function of m_{ϕ_2} and λ_2. Interaction between DM components $\phi_1\phi_1 \to \phi_2\phi_2$ or $\phi_2\phi_2 \to \phi_1\phi_1$ occurs depending on $m_{\phi_1} > m_{\phi_2}$ or $m_{\phi_2} > m_{\phi_1}$. In Fig. 3.7, the DM conversion is shown as a function of m_{ϕ_1} keeping m_{ϕ_2} fixed at 100 GeV (left) and 300 GeV (right). When $m_{\phi_1} < m_{\phi_2}$, $\phi_2\phi_2 \to \phi_1\phi_1$ is present and it dies when $m_{\phi_1} \sim m_{\phi_2}$. When $m_{\phi_1} > m_{\phi_2}$, $\phi_1\phi_1 \to \phi_2\phi_2$ process start contributing; the cross-section decreases with larger DM mass followed from the expressions in Eq. 3.24. A change in DM freeze out is possible when DM-DM interactions are of the same order as to the annihilations to SM. A comparison is illustrated in Fig. 3.8, where both the processes, annihilations to SM and DM-DM interactions are plotted together as a function of m_{ϕ_1} in the limit of zero contact interaction, $\lambda_3 = 0$. The other DM mass is kept fixed, $m_{\phi_2} = 80$ GeV (left) and 300 GeV (right) of Fig. 3.8. We choose $\lambda_2 = 0.1$ and three different choices of $\lambda_1 = \{0.01, 0.1, 1.0\}$ (red, blue and green respectively) for illustration. Fig. 3.8 shows that for small $m_{\phi_2} = 80$ GeV (left), DM-DM interaction is of the same order as with the annihilations to SM with $\lambda_3 = 0$. When m_{ϕ_2} is larger, for example, 300 GeV (right), DM conversion cross-section gets smaller than annihilations to SM as expected (see Fig. 3.7 for example).

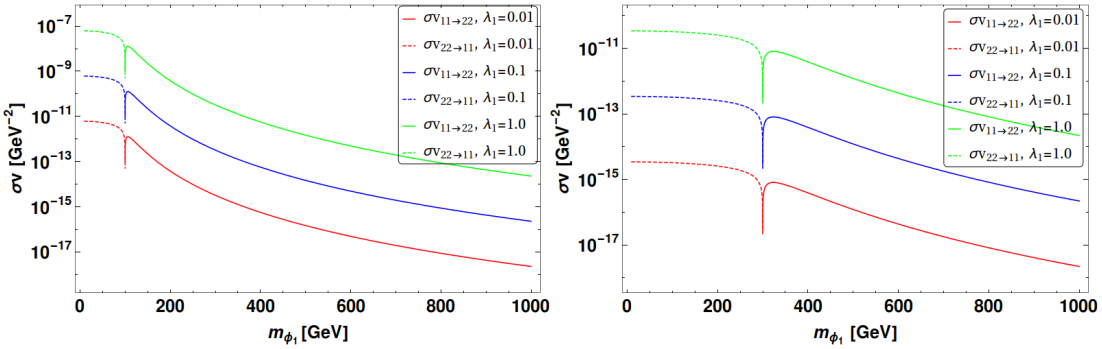

Figure 3.7: (σv) for DM conversions: $\phi_2\phi_2 \to \phi_1\phi_1$ or $\phi_1\phi_1 \to \phi_2\phi_2$ as a function of m_{ϕ_1} for constant $m_{\phi_2} = 100$ GeV (left), 300 GeV (right). $\lambda_2 = 0.1$ and contact interaction $\lambda_3 = 0$ are kept fixed for illustration while three different choices of $\lambda_1 = \{0.01\ (\text{Red}), 0.1\ (\text{Blue}), 1.0\ (\text{Green})\}$ (bottom to up respectively) are plotted.

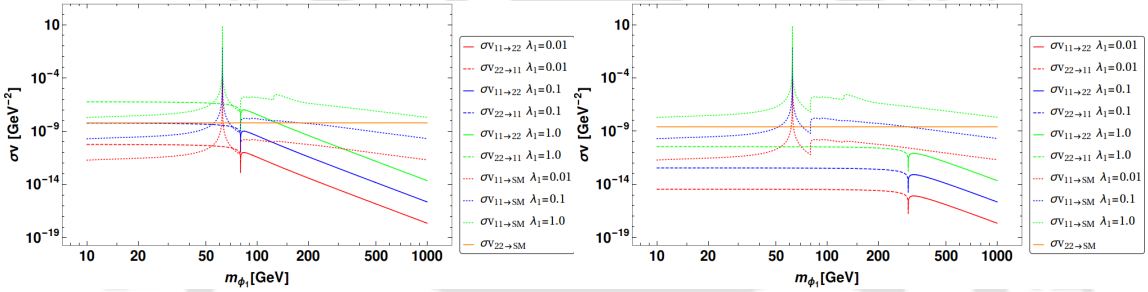

Figure 3.8: DM annihilations to SM is compared to DM-DM interactions as a function of m_{ϕ_1} in absence of λ_3. $m_{\phi_2} = 80$ (left), 300 (right) GeV are fixed. $\lambda_2 = 0.1$ is chosen for illustration while three different choices of $\lambda_1 = \{0.01\ (\text{Red}), 0.1\ (\text{Blue}), 1.0\ (\text{Green})\}$ (bottom to up respectively) are plotted.

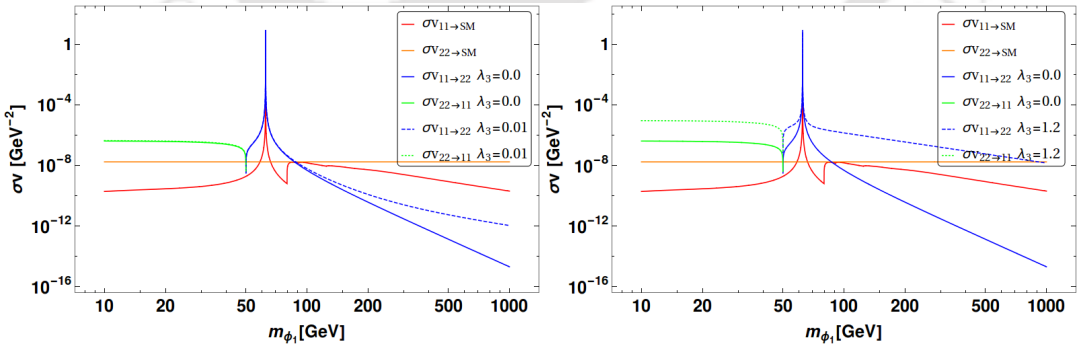

Figure 3.9: DM annihilation to SM is compared to DM interaction as a function of m_{ϕ_1} in presence of non-zero λ_3. We choose $\lambda_3 = 0.01$ (left), 1.2 (right); $\lambda_1 = 0.1, \lambda_2 = 0.3, m_{\phi_2} = 50$ GeV are chosen for illustration.

In Fig. 3.9, we show a comparison for all the relevant cross-sections in presence of non-zero λ_3. In the left panel, we choose small non-zero $\lambda_3 = 0.01$ and show that DM-DM interaction remains the same as $\lambda_3 = 0$ case, as both blue and green solid ($\lambda_3 = 0$)

and dashed ($\lambda_3 = 0.01$) lines almost superpose on top of each other. We choose a small value of $m_{\phi_2} = 50$ GeV for illustrating this case. The cross-sections are varied as a function of m_{ϕ_1}. For $m_{\phi_1} < m_{\phi_2}$, $\phi_2\phi_2 \to \phi_1\phi_1$ occurs. After $m_{\phi_1} > m_{\phi_2}$, $\phi_1\phi_1 \to \phi_2\phi_2$ takes over and the Higgs resonance peak appears for $m_{\phi_1} = \frac{m_h}{2}$ as can be seen in blue line. This of course coincides with the resonance peak for $\phi_1\phi_1 \to SM$ annihilations as shown in red. Only at a larger $m_{\phi_1} > 100$ GeV, small λ_3 starts showing up and the blue dashed curve separates out from the solid one in the left panel of Fig. 3.9. In the right panel of Fig. 3.9, the case for a moderately large DM contact interaction $\lambda_3 = 1.2$ has been depicted. This shows a sizeable difference in DM-DM interaction (see blue and green dashed and solid lines well separated) as expected. It is trivial to note that $\phi_2\phi_2 \to SM$ remains constant with constant m_{ϕ_2}, λ_2 shown by orange line in both Fig. 3.8 and in Fig. 3.9. These together imply that a non-zero but moderate choice of λ_3 will alter the total annihilation cross-section of DM components and hence affect the freeze out and relic density of DM.

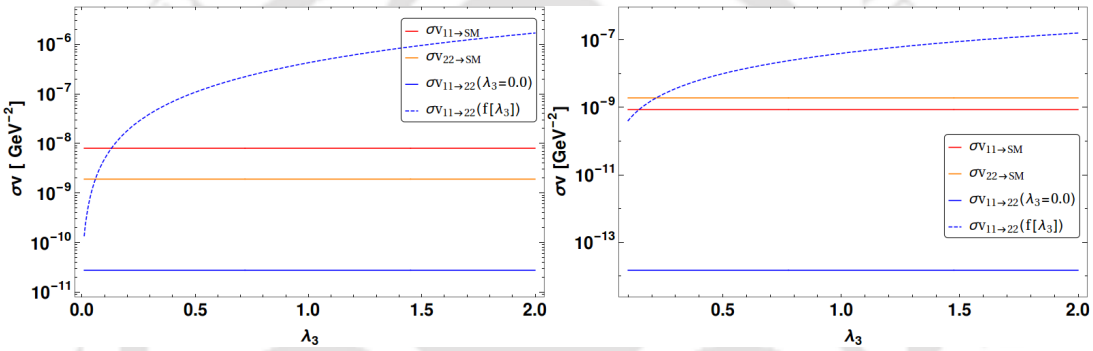

Figure 3.10: Variation of DM conversion as a function of λ_3. Other parameters are chosen as follows: $\{\lambda_1, \lambda_2, m_{\phi_1}, m_{\phi_2}\} = \{0.1, 0.1, 150, 50\}$ (left), $\{0.1, 0.1, 500, 50\}$ (right). All the masses are in GeV.

It is clear from Eq. 3.22 that annihilations $\phi_1\phi_1 \to SM$ is a quadratic function of λ_1. DM conversion $\phi_1\phi_1 \to \phi_2\phi_2$ are although dominantly quadratic function of λ_1, λ_2 and λ_3, there is an interference term proportional to $\lambda_1\lambda_2\lambda_3$ as can be seen from Eq. 3.24. However this interference term plays a crucial role when we choose any of those couplings negative. We do not analyse negative couplings in this report to be on the safe for vacuum stability of the potential (see Eq. 3.13). Cross-sections as a function of λ_3 and λ_1 are presented in Fig. 3.10 and Fig. 3.11 respectively.

In left panel of Fig. 3.11, for both $\lambda_3 = 0$ and $\lambda_3 \neq 0$, $(\sigma v)_{\phi_1\phi_1 \to \phi_2\phi_2}$ changes similarly with λ_1. However, on the right panel, $\lambda_3 = 0.1$ (blue dashed line) do not change much with the change in λ_1. This is specifically due to the fact that with large $m_{\phi_1} = 500$ GeV, chosen for the plot in right hand side, the terms proportional to λ_1^2, or λ_1, have large suppression from $1/(4m_{\phi_1}^2 - m_h^2)^2$, which the term proportional to λ_3^2 do not contain (see Eq. 3.24). Hence a non-zero λ_3 yields a larger contribution making the DM conversion cross-section a slow function of λ_1 in this particular case.

Let us now turn to freeze out of the DM components due to the combined effect of annihilation and DM conversions processes in $\mathcal{Z}_2 \times \mathcal{Z}_2'$ model governed by Eq. 3.30. We show in Fig. 3.12 four different regions of parameter space where the decoupling of ϕ_1 and ϕ_2 has been indicated in red and blue lines from equilibrium distribution (black

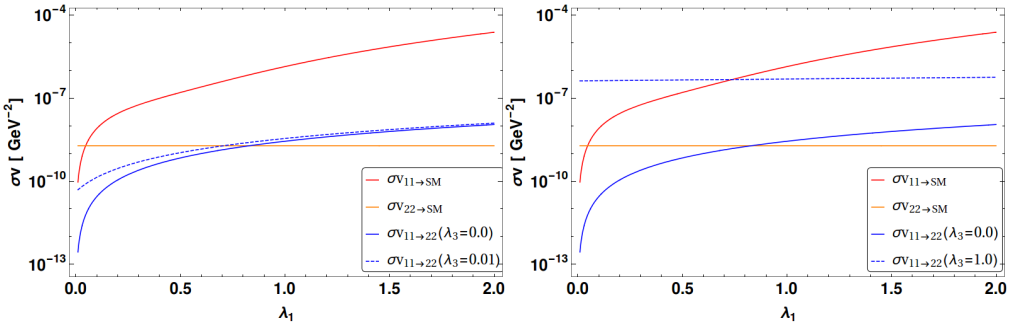

Figure 3.11: Variation of Annihilation cross-section and DM conversion as a function of λ_1. Other parameters are chosen as follows: $\{\lambda_2, \lambda_3, m_{\phi_1}, m_{\phi_2}\} = \{0.1, 0.01, 150, 50\}$ (left), $\{0.1, 1.0, 150, 50\}$ (right). All the masses are in GeV.

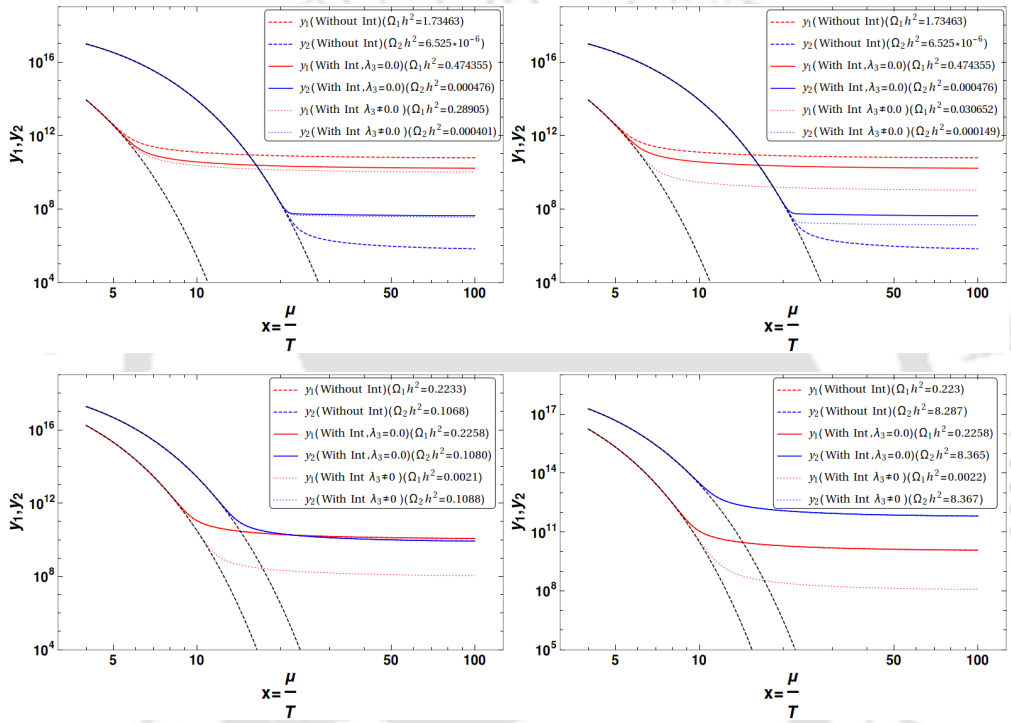

Figure 3.12: Freeze out of ϕ_1, ϕ_2 (Red and Blue respectively) from equilibrium in $y - x$ plane for $\mathcal{Z}_2 \times \mathcal{Z}_2^{'}$ model. Dashed line indicates freeze out without any DM-DM interaction, solid line denotes $\phi_1 - \phi_2$ interacting with $\lambda_3 = 0$ and dotted line depicts interaction with non-zero λ_3. The equilibrium distributions are indicated through black dashed lines. The parameters are chosen as follows: $\{\lambda_1, \lambda_2, \lambda_3, m_{\phi_1}, m_{\phi_2}\} = \{0.01, 3.2, 0.01, 150, 60\}$ (top left), $\{0.01, 3.2, 0.1, 150, 60\}$ (top right), $\{0.1, 0.1, 2.0, 500, 350\}$ (bottom left), $\{0.1, 0.01, 2.0, 500, 350\}$ (bottom right). All the masses are in GeV.

dashed line). We have chosen the case of $m_{\phi_1} > m_{\phi_2}$ for illustration. We classify three possibilities :

- No DM-DM interaction ($\sigma v_{\phi_1\phi_1 \to \phi_2\phi_2} = \sigma v_{\phi_2\phi_2 \to \phi_1\phi_1} = 0$, indicated by *dashed* lines)
- DM-DM interaction with $\lambda_3 = 0$ (Indicated by *solid* lines)
- DM-DM interaction with $\lambda_3 \neq 0$ (Indicated by *dotted* lines)

The plots in Fig. 3.12 are shown in $y - x$ plane (see Eq. 3.30). One of the crucial features that is observed for ϕ_1 decoupling is as follows: *dashed* red lines appear on top and *dotted* red lines appear at the bottom with *solid* lines in the middle. This indicates the yield y for ϕ_1 DM and therefore the relic density is larger for the *dashed* line, smaller for the *solid* line and smallest for the *dotted* ones. One can correlate this feature as the *dotted* ones have largest annihilation contributions through DM-DM interactions with $\lambda_3 \neq 0$, the freeze out is delayed compared to solid and dashed lines. For the heavier component (ϕ_1 here), we can appreciate the fact by simply assuming

$$\Omega_1 h^2 \propto (\langle\sigma v\rangle_{\phi_1\phi_1\to \text{SM}} + \langle\sigma v\rangle_{\phi_1\phi_1\to\phi_2\phi_2})^{-1} \tag{3.34}$$

which we will explicitly demonstrate in the approximate analytic solutions in Sec 3.5. On the other hand, for ϕ_2, indicated in blue, *dashed, solid and dotted* lines have different freeze-out sequence. As $\phi_1\phi_1 \to \phi_2\phi_2$ is the only possibility with $m_{\phi_1} > m_{\phi_2}$, ϕ_2 is produced from ϕ_1. Hence, for ϕ_2, the case without DM-DM interaction, shown in *dashed* line appears at the bottom with lowest yield, while *dotted* and *solid* lines yield larger DM density. The splitting between the *dashed, solid* and *dotted* lines depend on the strength of the couplings and also on the DM masses as can be observed for different parameter space regions in Fig. 3.12. For example, we see that with small $\lambda_3 \sim 0.01$, the thick and the dotted lines are close enough (top left in Fig. 3.12). Also, one can see that with small $\lambda_2 = 0.01$ (bottom right), where the annihilations of $\phi_2\phi_2 \to SM$ is very tiny, all the blue lines (*dashed, solid, dotted*) marge together as DM conversion play little role in decoupling of ϕ_2, which is dominantly controlled by small interactions to SM yielding an early freeze out and large density. Also, with $m_{\phi_1} > m_{\phi_2}$, the annihilation cross-section for ϕ_1 is smaller compared to ϕ_2 due to the inverse mass square dependence, yielding an early freeze-out and hence a larger density for ϕ_1. This is what is observed in two of the cases in upper panel of Fig. 3.12. In bottom left panel, λ_1, λ_2 are kept same with large λ_3. This clearly shows that due to DM-DM conversion the ϕ_1 freeze out is delayed with reduced yield y_1 (compare red dotted line with the red thick one). In same analogy, there is production of ϕ_2 from DM-DM conversion, which should result in a visible upward shift of ϕ_2 relic density. However, this is not visible. The reason for not being able to spot the shift is actually due to the log scaling of the figure along y axis. The change of y in the upper direction is much steeper and hence changes in the yield even upto an order of magnitude due to DM-DM conversion for large and non-zero λ_3 is not clearly distinguishable for ϕ_2. This is true for all the graphs in Fig. 3.12.

In order to highlight the importance of DM-DM interaction in the freeze-out of DM components we draw Fig. 3.13, where on the left hand side, we choose $\lambda_3 = 0$. Here, due to smaller $\lambda_1 = 0.01$, ϕ_1 has an early freeze out and larger density. On the right hand side, we take large contact term $\lambda_3 = 1.0$. With larger DM conversion $\phi_1\phi_1 \to \phi_2\phi_2$, the effective annihilation cross-section for ϕ_1 is larger and yields a smaller DM density. Such examples play a crucial role in multipartite DM with DM-DM interactions.

However, in Fig. 3.12, we have missed one important outcome in the freeze out of the two component DM scenario. Given $m_{\phi_1} > m_{\phi_2}$, if we can have an early freeze out of ϕ_2 (by choosing smaller λ_2), then ϕ_1 can still sufficiently annihilate to ϕ_2 remaining in thermal contact with SM, yielding a modified equilibrium before finally freezing out. This shows a bump in the freeze out of ϕ_1 as has been shown in Fig. 3.14. The modified equilibrium can be identified from BEQ (with $m_{\phi_1} > m_{\phi_2}$) as h_1^{EQ} and plotted

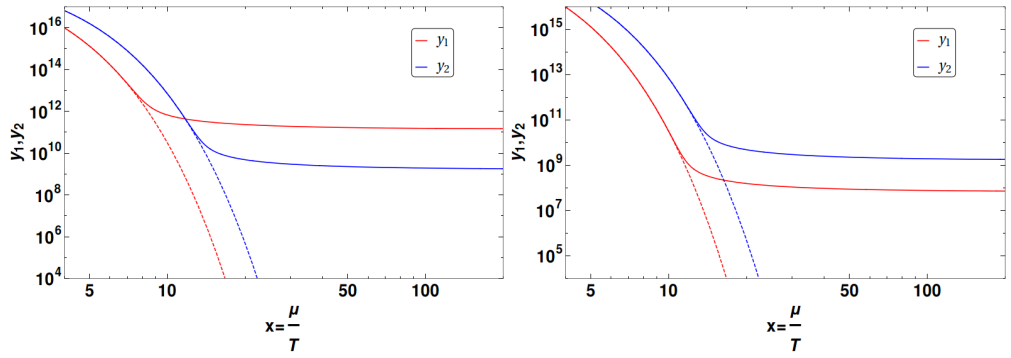

Figure 3.13: Freeze out of ϕ_1, ϕ_2 from equilibrium in $y-x$ plane for $\mathcal{Z}_2 \times \mathcal{Z}_2^{'}$ model. ϕ_1 decoupling is shown in red thick line, ϕ_2 in blue thick line. Equilibrium distributions are shown in dashed lines. Parameters chosen are as follows: $\{\lambda_1, \lambda_2, \lambda_3, m_{\phi_1}, m_{\phi_2}\} = \{0.01, 0.1, 0.0, 200, 150\}$ (left), $\{0.01, 0.1, 1.0, 200, 150\}$ (right). All the masses are in GeVs.

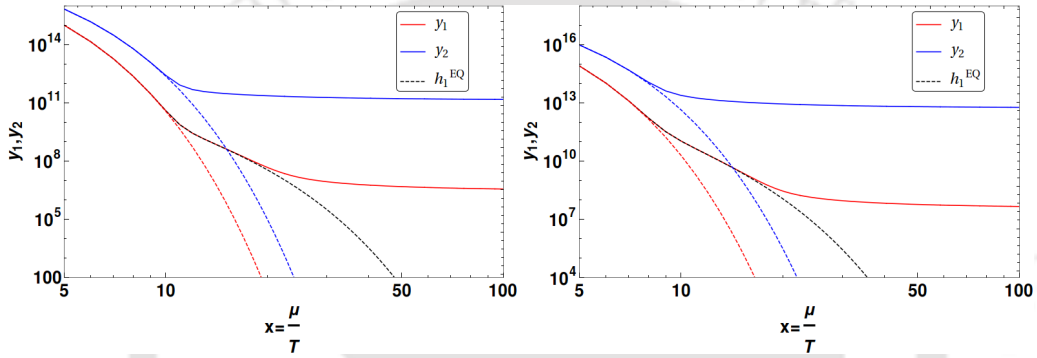

Figure 3.14: Freeze out of ϕ_1, ϕ_2 from equilibrium in $y-x$ plane for $\mathcal{Z}_2 \times \mathcal{Z}_2^{'}$ model. ϕ_1 decoupling is shown in red thick line, ϕ_2 in blue thick line. Equilibrium distributions are shown in dashed lines. Parameters chosen are as follows: $\{\lambda_1, \lambda_2, \lambda_3, m_{\phi_1}, m_{\phi_2}\} = \{1.0, 0.01, 3.0, 100, 80\}$ (left), $\{0.1, 0.001, 1.0, 120, 90\}$ (right). All the masses are in GeVs.

in Fig. 3.14 through black dashed lines to match the bump exactly as follows:

$$\begin{aligned} \frac{dy_1}{dx} &= -\frac{\langle\sigma v_{11\to SM}\rangle + \langle\sigma v_{11\to 22}\rangle}{x^2}[y_1^2 - h_1^{EQ^2}]; \\ h_1^{EQ^2} &= y_1^{EQ^2}[\frac{\langle\sigma v_{11\to SM}\rangle}{\langle\sigma v_{11\to SM}\rangle + \langle\sigma v_{11\to 22}\rangle} + \frac{\langle\sigma v_{11\to 22}\rangle}{\langle\sigma v_{11\to SM}\rangle + \langle\sigma v_{11\to 22}\rangle}(\frac{y_2}{y_2^{EQ}})^2] \end{aligned} \quad (3.35)$$

One can note here that in order for such a situation to arise, we have to have the lighter DM component freeze-out earlier, so that the heavier one can annihilate to the lighter component through DM-DM interaction and reaches a modified equilibrium. But for the lighter component to freeze out early, we need much smaller DM-SM coupling compared to the heavier one as has been shown in Fig. 3.14. This is a generic feature associated to interacting multicomponent DM frameworks as also have been pointed out earlier in scalar-fermion two component DM set up in [48]. It is obvious that all the features of DM freeze out that have been discussed above with $m_{\phi_1} > m_{\phi_2}$, can also be extended for the case of $m_{\phi_2} > m_{\phi_1}$.

We will discuss now the outcome of the parameter space scan of this model that yields correct relic density. We scan essentially five dimensional parameter space of $\mathcal{Z}_2 \times \mathcal{Z}_2^{'}$ model as follows

$$\{10 \text{ GeV} < m_{\phi_1}, m_{\phi_2} < 1000 \text{ GeV},\ 0.005 < \lambda_1, \lambda_2 < 1.5,\ 0.1 < \lambda_3 < 3\} \quad (3.36)$$

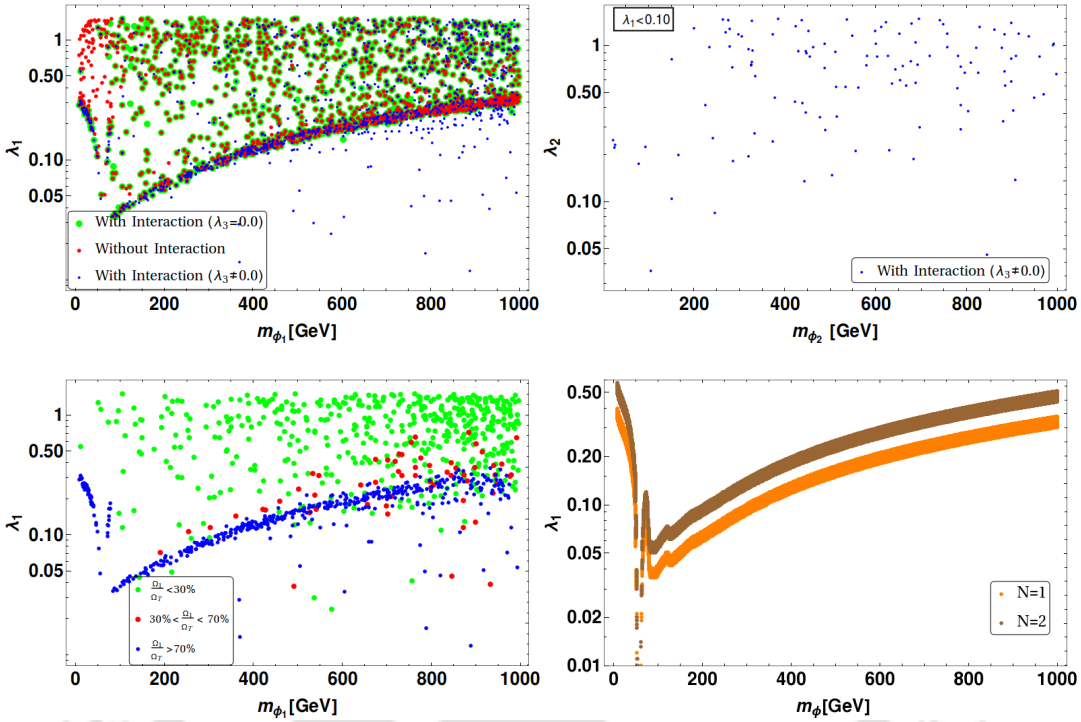

Figure 3.15: Top Left: Relic density allowed parameter space of $\mathcal{Z}_2 \times \mathcal{Z}_2^{'}$ model in $m_{\phi_1} - \lambda_1$ plane for three different cases: without DM-DM interaction (Red points), DM-DM interaction with $\lambda_3 = 0$ (Green points), DM-DM interaction with $\lambda_3 \neq 0$ (Blue points); Top right: The blue points of top left figure with $\lambda_1 \leq 0.1$ in $m_{\phi_2} - \lambda_2$ plane; Bottom left: Allowed points with DM-DM interaction ($\lambda_3 \neq 0$) in $m_{\phi_1} - \lambda_1$ plane showing different DM contributions, $\frac{\Omega_1}{\Omega_T} < 30\%$ (Green), $30\% < \frac{\Omega_1}{\Omega_T} < 70\%$ (Red), $\frac{\Omega_1}{\Omega_T} > 70\%$ (Blue); Bottom right: Relic density constraint on single component framework (Orange) and on two component case with $\mathcal{O}(2)$ symmetry (Brown) are shown.

Note here that the specific values of the masses in the above limit do not convey anything special; excepting for covering a large range of DM masses allowed by relic density including the Higgs resonance region where annihilations of DM are mediated by Higgs portal coupling. We choose both possible mass hierarchies in uncorrelated way. We have confined ourselves to positive couplings only within a broad range to be compatible with vacuum stability. We solve the coupled BEQ for $\mathcal{Z}_2 \times \mathcal{Z}_2^{'}$ model in Mathematica (see Eq. 3.30) and then identify the allowed region of correct relic abundance satisfying WMAP [9] constraint [1]

$$0.09 \leq \Omega_{\rm DM} h^2 \leq 0.12\,. \tag{3.37}$$

The first scan of the allowed parameter space is presented in terms of $m_{\phi_1} - \lambda_1$ plane in top left panel of Fig. 3.15. Three different cases have been indicated in the scan: the case without any DM-DM interaction is indicated by red dots, the case with interaction, but assuming $\lambda_3 = 0$ is indicated by green dots and the case with $\lambda_3 \neq 0$ is indicated through blue dots. The image can be compared with a similar parameter space scan allowed by by relic density in the single component framework and the one with two components but protected by a $\mathcal{O}(2)$ symmetry as shown in the bottom right

[1] The range we use corresponds to the WMAP results; the PLANCK constraints $0.112 \leq \Omega_{\rm DM} h^2 \leq 0.128$ [11], though more stringent, do not lead to significant changes in the allowed regions of parameter space.

panel of Fig. 3.15. We see that a significantly larger parameter space is available to the two-component set up under $\mathcal{Z}_2 \times \mathcal{Z}_2^{'}$ compared to the single component or the two component case with $\mathcal{O}(2)$ symmetry. We also see that the case without interaction (red dots) and the ones with $\lambda_3 = 0$ (green dots) yield identical allowed space in $m_{\phi_1} - \lambda_1$ plane. Such a phenomena is observed because the interaction between DM components in absence of λ_3 occurs via λ_1, λ_2 which also controls their respective annihilations to SM. Hence if one or the other or both of λ_1, λ_2 is increased for large DM interaction, the annihilation to SM also gets significantly enhanced beyond the relic density limit. Hence, in absence of λ_3, the DM interaction is automatically controlled by the annihilation processes and that is why no new region of parameter space opens up within the relic density allowed region of parameter space. However, the situation alters in presence of λ_3, which indeed can expedite DM-DM interaction and alter relic density contribution of one without affecting the annihilations to SM for the other. Hence, we achieve points below $\lambda_1 < 0.1$, allowed by relic density (which otherwise is not available with no DM-DM interaction or with $\lambda_3 = 0$) as shown by the blue points in the top left panel of Fig. 3.15. The smaller values of λ_1 gets allowed for this case albeit small annihilations of ϕ_1 to SM because $\phi_1\phi_1 \to \phi_2\phi_2$ interaction supplements it in presence of non-zero λ_3, yielding ϕ_1 relic density within the desirable range. In order to understand what happens to ϕ_2 in such a situation with $\lambda_1 < 0.1$, we see the corresponding $m_{\phi_2} - \lambda_2$ scan of *these* points and observe that they lie in moderate to large λ_2 region: $\sim \{0.1 - 1\}$ as shown in the top right panel of Fig. 3.15. One can conclude hence, that the points below $\lambda_1 < 0.1$, although is dominated by the first component ϕ_1, may have significant second component present. The DM composition of this two-component framework for correct relic density is shown in the bottom left panel of Fig. 3.15 in $m_{\phi_1} - \lambda_1$ plane. We see that blue points where the first component dominates ($\frac{\Omega_1}{\Omega_T} > 70\%$) populate low λ_1 regions as expected with some minor presence of green ($\frac{\Omega_1}{\Omega_T} < 30\%$) and red points ($30\% < \frac{\Omega_1}{\Omega_T} < 70\%$). The allowed region with larger λ_1 is mostly dominated by ϕ_2 green points, while equal contributions from both the DM components (red points) populate mostly the mid range of λ_1 in the bottom left panel of Fig. 3.15. In the bottom right panel of Fig. 3.15, we show the two component case with $\mathcal{O}(2)$ symmetry (brown points), which requires larger coupling λ_1 for a given m_ϕ compared to the single component case (orange points). This happens because the individual DM density in $\mathcal{O}(2)$ case is reduced to half of total DM density $\Omega_1 = \Omega_2 = \frac{\Omega_T}{2}$ (see Eq. 3.32); consequently the annihilation has to be twice as large than the single component case. We also figure out the resonance drop at $m_{\phi_1} \sim \frac{m_h}{2}$ in all of the scans and resemblance of single component situation through larger population of points in $\lambda_1 - m_{\phi_1}$ scan.

A very similar situation arises when we recast the scan in $m_{\phi_2} - \lambda_2$ plane as shown in Fig. 3.16. We once again point out that a clear distinction of points with non-zero λ_3 appearing below $\lambda_2 < 0.1$ for $m_{\phi_2} \sim \{300,\ 1000\}$ GeV, where the DM content is primarily dominated by the second (ϕ_2) component.

In Fig. 3.17, the $m_{\phi_1} - \lambda_1$ parameter space allowed by relic density constraint is shown in terms of different ranges of λ_2 (left) and m_{ϕ_2} (right) for $\lambda_3 \neq 0$ case. In the left panel different ranges of λ_2 are chosen as follows: $\{0.05 - 0.1\}$ (Green), $\{0.1 - 0.5\}$ (Blue), $\{0.5 - 1\}$ (Grey), $\{1.0 - 2.0\}$ (Red). Here we note that while the small $\lambda_2 (< 0.5)$ (Blue and Green dots) span the most of the $m_{\phi_1} - \lambda_1$ parameter space, larger values of $\lambda_2 (> 0.5)$ tend to populate similar to the single component case. This can be understood as follows: due to very large annihilation cross-section

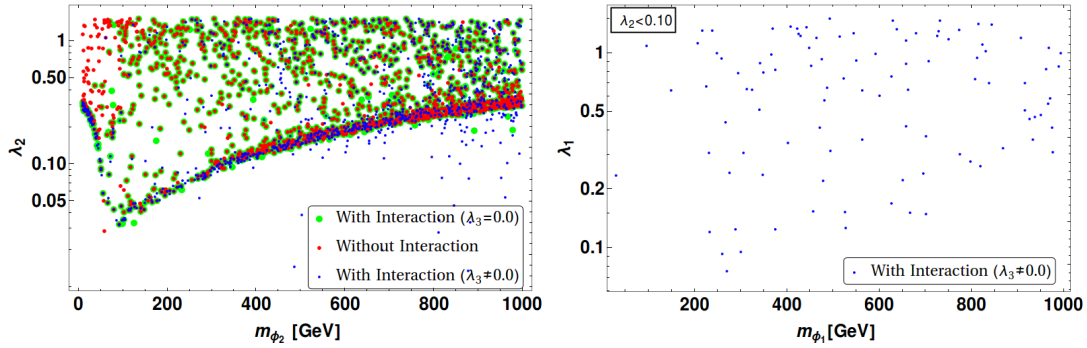

Figure 3.16: Left: Relic density allowed parameter space of $\mathcal{Z}_2 \times \mathcal{Z}_2^{'}$ in $m_{\phi_2} - \lambda_2$ plane for three different cases: without DM-DM interaction (Red points), DM-DM interaction with $\lambda_3 = 0$ (Green points), DM-DM interaction with $\lambda_3 \neq 0$ (Blue points); Right: The blue points of left figure with $\lambda_2 < 0.1$ in $m_{\phi_1} - \lambda_1$ plane.

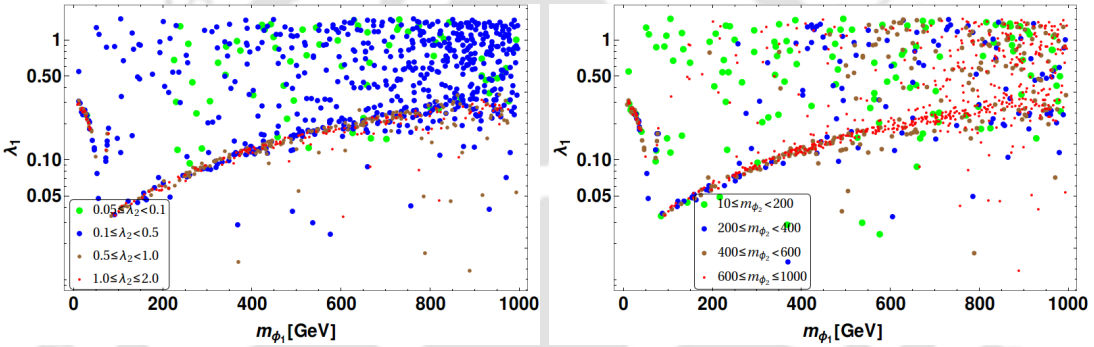

Figure 3.17: Relic density allowed parameter space of $\mathcal{Z}_2 \times \mathcal{Z}_2^{'}$ model in $m_{\phi_1} - \lambda_1$ plane. The case with DM interaction ($\lambda_3 \neq 0$) is depicted. Left: Different ranges of λ_2: $\{0.05 - 0.1\}$ (Green), $\{0.1 - 0.5\}$ (Blue), $\{0.5 - 1\}$ (Grey), $\{1.0 - 2.0\}$ (Red) are shown. Right: Different ranges of m_{ϕ_2}: $\{10 - 200\}$ (Green), $\{200 - 400\}$ (Blue), $\{400 - 600\}$ (Grey), $\{600 - 1000\}$ (Red) are shown. All the masses are in GeV.

with large λ_2, ϕ_2 barely contributes to relic density and it approximates to a single component case with ϕ_1. In the right hand side of the Fig. 3.17 different mass ranges of the second component (m_{ϕ_2}) is indicated as $\{10-200\}$ (Green), $\{200-400\}$ (Blue), $\{400 - 600\}$ (Grey), $\{600 - 1000\}$ (Red), all in GeV. However, this doesn't show a necessary distinction amongst different ϕ_2 mass ranges with all ranges couplings (λ_2) included in the scan indicating m_{ϕ_2} is insensitive to $m_{\phi_1} - \lambda_1$ scan unless we choose a specific range of λ_2.

Another possible representation of relic density allowed parameter space of the two component DM in $\mathcal{Z}_2 \times \mathcal{Z}_2^{'}$ framework is $\lambda_1 - \lambda_2$ plane as has been shown in Fig. 3.18. Essentially this plane yields an L-shaped figure with the allowed region extending to as large possible value of the coupling as one wishes (upto perturbative limit). This is attributed to the presence of second DM component that the individual coupling of one DM with SM can be as large as possible while keeping the other in the correct ball park. In Fig. 3.18, we show three different regions: the ones indicated through red dots are those where ϕ_2 constitutes 90% or more of the DM and understandably lives on the axis with larger λ_1; the ones in green dots show the region where ϕ_1 constitutes 90% or

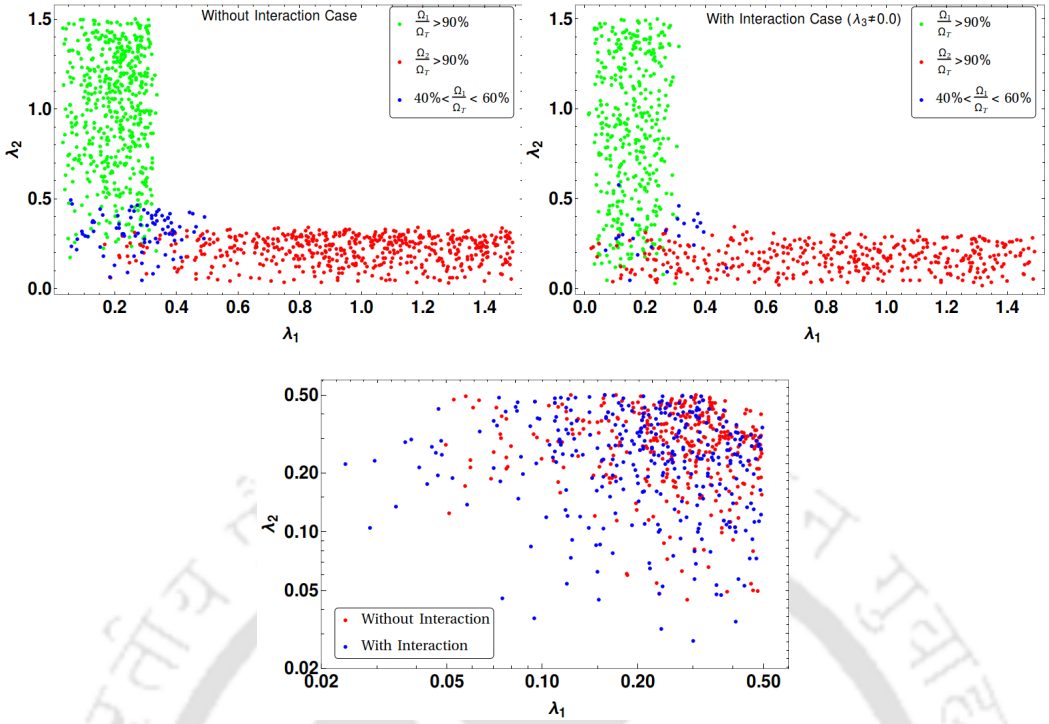

Figure 3.18: Relic density allowed parameter space of $\mathcal{Z}_2 \times \mathcal{Z}_2^{'}$ model in $\lambda_1 - \lambda_2$ plane. Top Left: The case without DM-DM interaction, Top Right: The case with interaction ($\lambda_3 \neq 0$) are shown. Different colors indicate the composition of the relic density; Blue: $40\% < \frac{\Omega_1}{\Omega_T} < 60\%$, Green: $\frac{\Omega_1}{\Omega_T} > 90\%$, Red: $\frac{\Omega_2}{\Omega_T} > 90\%$. Bottom: $\lambda_1 - \lambda_2$ scan for $\lambda_1, \lambda_2 < 0.5$: Red: Without DM-DM interaction, Blue: With interaction ($\lambda_3 \neq 0$).

more of the DM and extends along λ_2; the ones with blue dots show the region where both of the components contribute in a similar way to relic density of the universe. When λ_1 is large, corresponding annihilation of the ϕ_1 component is large enough to have a tiny contribution to relic density and vice versa. On the other had, when $40\% < \frac{\Omega_1}{\Omega_T} < 60\%$, there is a limit to which $\lambda_1 - \lambda_2$ can be large or small as seen in the blue dots accumulating in a small region at the corner of allowed $\lambda_1 - \lambda_2$ plane. The thickness of each leg is essentially determined by the width of the DM relic density (Ωh^2: 0.09-0.12). It is also worthy of mentioning that large values of both λ_1 & λ_2 are strongly disfavoured by direct search bounds as we will discuss later. The two cases of having no DM-DM interaction (top left panel of Fig. 3.18) or with interaction (top right panel of Fig. 3.18) makes no visible difference unless one looks carefully into the smaller coupling regions. This is what has been displayed in the bottom panel of Fig. 3.18, with $\lambda_1, \lambda_2 < 0.5$. The cases of having DM-DM interaction is shown in blue while the red points do not have any interactions between the DM components. It is clear that the blue points tend to acquire smaller values than the red ones, showing that with DM-DM interaction, the two component DM models essentially gets allowed to smaller coupling strength marking a significant difference with the models without DM-DM interactions.

3.5 Approximate Analytic Solution for Coupled BEQ

In this section, we will evaluate approximate analytical solution for the coupled BEQ in $\mathcal{Z}_2 \times \mathcal{Z}_2^{'}$ framework and try to validate with the numerical solution obtained in previous section. Approximate analytical solutions help using them without actually solving the coupled differential equations numerically for such a model in general. In order to obtain analytical solution we will assume $m_{\phi_1} > m_{\phi_2}$. The case for $m_{\phi_2} > m_{\phi_1}$ will be similar of course. BEQs for $m_{\phi_1} > m_{\phi_2}$ reads:

$$\begin{aligned}
\frac{dy_1}{dx} &= -\frac{1}{x^2}\Big[\sigma_1(y_1^2 - y_1^{EQ^2}) + \sigma_{12}(y_1^2 - \frac{y_1^{EQ^2}}{y_2^{EQ^2}}y_2^2)\Big] \\
\frac{dy_2}{dx} &= -\frac{1}{x^2}\Big[\sigma_2(y_2^2 - y_2^{EQ^2}) - \sigma_{12}(y_1^2 - \frac{y_1^{EQ^2}}{y_2^{EQ^2}}y_2^2)\Big]
\end{aligned} \tag{3.38}$$

where we rewrite the cross-sections for notational simplicity as: $\langle\sigma v_{11\to SM}\rangle \equiv \sigma_1$, $\langle\sigma v_{22\to SM}\rangle \equiv \sigma_2$ and $\langle\sigma v_{11\to 22}\rangle \equiv \sigma_{12}$. Let us consider the difference between the actual yield from the equilibrium for ϕ_1 as $\Delta_1 = y_1 - y_1^{EQ}$ and for ϕ_2 as $\Delta_2 = y_2 - y_2^{EQ}$ which helps parametrising the freeze out of the DM components. In terms of $\Delta_{1,2}$, the BEQs become [15]

$$\begin{aligned}
\frac{d\Delta_1}{dx} + \frac{dy_1^{EQ}}{dx} &= -\frac{1}{x^2}\Big[\sigma_1(\Delta_1^2 + 2\Delta_1 y_1^{EQ}) + \sigma_{12}[(\Delta_1^2 + 2\Delta_1 y_1^{EQ}) - (\frac{y_1^{EQ}}{y_2^{EQ}})^2(\Delta_2^2 + 2\Delta_2 y_2^{EQ})]\Big] \\
\frac{d\Delta_2}{dx} + \frac{dy_2^{EQ}}{dx} &= -\frac{1}{x^2}\Big[\sigma_2(\Delta_2^2 + 2\Delta_2 y_2^{EQ}) - \sigma_{12}[(\Delta_1^2 + 2\Delta_1 y_1^{EQ}) - (\frac{y_1^{EQ}}{y_2^{EQ}})^2(\Delta_2^2 + 2\Delta_2 y_2^{EQ})]\Big]
\end{aligned} \tag{3.39}$$

Solving above set of coupled differential equations analytically is difficult. Hence, we would like to recast the equations to the nearest possible approximation, where solving two of these equations separately is viable. The term that can be neglected here is $\sigma_{12}(\frac{y_1^{EQ}}{y_2^{EQ}})^2$. $\frac{y_1^{EQ}}{y_2^{EQ}} \sim (\frac{m_{\phi_1}}{m_{\phi_2}})^{\frac{3}{2}} e^{-\frac{m_{\phi_1}}{m_{\phi_2}}x} < 1$ in the limit of $m_{\phi_1} > m_{\phi_2}$. However, when $\sigma_{12} \gg \sigma_{1,2}$ this approximation will fail. Generically, a moderate $\lambda_3 \sim 0.1$ will justify our approximation. With such approximations, the BEQ turns into

$$\begin{aligned}
\frac{d\Delta_1}{dx} + \frac{dy_1^{EQ}}{dx} &= -\frac{1}{x^2}[\sigma_1(\Delta_1^2 + 2\Delta_1 y_1^{EQ}) + \sigma_{12}(\Delta_1^2 + 2\Delta_1 y_1^{EQ})] \\
\frac{d\Delta_2}{dx} + \frac{dy_2^{EQ}}{dx} &= -\frac{1}{x^2}[\sigma_2(\Delta_2^2 + 2\Delta_2 y_2^{EQ}) - \sigma_{12}(\Delta_1^2 + 2\Delta_1 y_1^{EQ})]
\end{aligned} \tag{3.40}$$

At smaller values of x, i.e. before freeze-out of the DM components $x < x_f^i$ $(i = 1, 2)$, the number density follows the equilibrium distribution very closely : $\frac{d\Delta_i}{dx} \to 0$. BEQs in such a situation

$$\begin{aligned}
\frac{dy_1^{EQ}}{dx} &= -\frac{1}{x^2}[(\sigma_1 + \sigma_{12})(\Delta_1^2 + 2\Delta_1 y_1^{EQ})] \\
\frac{dy_2^{EQ}}{dx} &= -\frac{1}{x^2}[\sigma_2(\Delta_2^2 + 2\Delta_2 y_2^{EQ}) - \sigma_{12}(\Delta_1^2 + 2\Delta_1 y_1^{EQ})]
\end{aligned} \tag{3.41}$$

Now, when we approach freeze-out, at $x \sim x_f^i$, one can parametrise the difference in the yield to scale the equilibrium distribution by some factor c_i as $\Delta_i[x_f^i] = c_i y_i^{EQ}[x_f^i]$ [15]. Using this, one can easily find the freeze-out of the first component as [15]

$$e^{(\frac{m_{\phi_1}}{\mu})x_f^1} = 0.03828 M_{Pl} \frac{g}{\sqrt{g_*}} \frac{m_{\phi_1}(\sigma_1+\sigma_{12})(2+c_1)c_1}{\sqrt{\frac{m_{\phi_1}}{\mu}}\sqrt{x_f^1}} \tag{3.42}$$

Considering $x_f^1 > \frac{3}{2}$, one finds approximately the freeze out of ϕ_1

$$\begin{aligned} x_f^1 \;\approx\; & (\frac{\mu}{m_{\phi_1}})\ \ln\left[0.03828 M_{Pl}\frac{g}{\sqrt{g^*}} m_{\phi_1}\frac{(\sigma_1+\sigma_{12})(c_1+2)c_1}{\sqrt{\frac{m_{\phi_1}}{\mu}}}\right] \\ - \;& \frac{1}{2}(\frac{\mu}{m_{\phi_1}})\ \ln\left[(\frac{\mu}{m_{\phi_1}})\ln[0.03828 M_{Pl}\frac{g}{\sqrt{g^*}} m_{\phi_1}\frac{(\sigma_1+\sigma_{12})(c_1+2)c_1}{\sqrt{\frac{m_{\phi_1}}{\mu}}}]\right] \end{aligned} \tag{3.43}$$

Similarly,

$$\begin{aligned} x_f^2 \;\approx\; & (\frac{\mu}{m_{\phi_2}})\ln\left[0.03828 M_{Pl}\frac{g}{\sqrt{g^*}} m_{\phi_2}\frac{\sigma_2(c_2+2)c_2}{\sqrt{\frac{m_{\phi_2}}{\mu}}}\right] \\ - \;& \frac{1}{2}(\frac{\mu}{m_{\phi_2}})\ln\left[(\frac{\mu}{m_{\phi_2}})\ln[0.03828 M_{Pl}\frac{g}{\sqrt{g^*}} m_{\phi_2}\frac{\sigma_2(c_2+2)c_2}{\sqrt{\frac{m_{\phi_2}}{\mu}}}]\right] \end{aligned} \tag{3.44}$$

We note here that the reduced freeze-out x_f^i evaluated from the coupled BEQ has to be rescaled to the individual ones as follows:

$$x_{if} = \frac{m_{\phi_i}}{T_{if}} = \frac{m_{\phi_i}}{\mu} x_f^i \tag{3.45}$$

where T_{if} is the freeze-out temperature of i^{th} $(i = 1, 2)$ DM component. In the limit of $m_{\phi_1} >> m_{\phi_2}$: $\frac{m_{\phi_2}}{\mu} \to 1$, the freeze-out of the second component reduces to

$$\begin{aligned} x_{2f} \equiv x_f^2 \;\approx\; & \ln\left[0.03828 M_{Pl}\frac{g}{\sqrt{g^*}} m_{\phi_2}\sigma_2(c_2+2)c_2\right] \\ - \;& \frac{1}{2}\ln\ln\left[0.03828 M_{Pl}\frac{g}{\sqrt{g^*}} m_{\phi_2}\sigma_2(c_2+2)c_2\right] \end{aligned} \tag{3.46}$$

which exactly mimics the single component case [15]. Before proceeding further, let us study the dependence of freeze-out temperature of ϕ_1 (T_{1f}) on DM mass m_{ϕ_1} as is shown in Fig. 3.19 as obtained from approximate analytical solutions of BEQ as in Eq. 3.43,3.44 and Eq. 3.45. Two cases have been compared here: single component case, in absence of ϕ_2 (red) and two-component case with DM-DM interaction (blue dotted) for the following choices of parameters $\{\lambda_1, \lambda_2, \lambda_3, m_{\phi_2}\} = \{0.1, 0.1, 0.0, 40\}$ (top left), and $\{0.1, 0.1, 1.0, 40\}$ (top right). It is clear from the figure that presence of $\lambda_3 = 1.0$ in the top right panel, shows a different freeze-out curve for the first component compared to the case when there is no other DM. This is simply because the presence of DM interaction enhances the effective annihilation cross-section and

leads to early decoupling of the ϕ_1 DM. Freeze out for the single component case with different choice of coupling $\lambda_1 = \{0.01, 0.1, 1.0\}$ is shown in red blue and green respectively at the bottom left panel of Fig. 3.19 (T_f in the left and x_f on the right bottom panel). Again, the larger is the coupling, the larger is annihilation cross-section and the earlier the DM freezes-out. Also, it is easy to appreciate that with larger DM mass the freeze out also gets delayed with smaller annihilation cross-sections. The resonance drop is also clearly visible in all the plots. Note that in Fig. 3.19, there are some discontinuities in the plots arising from singularities in solving Eq. 3.43 and Eq. 3.44 in Mathematica and contains no physics at all. After finding the freeze-out

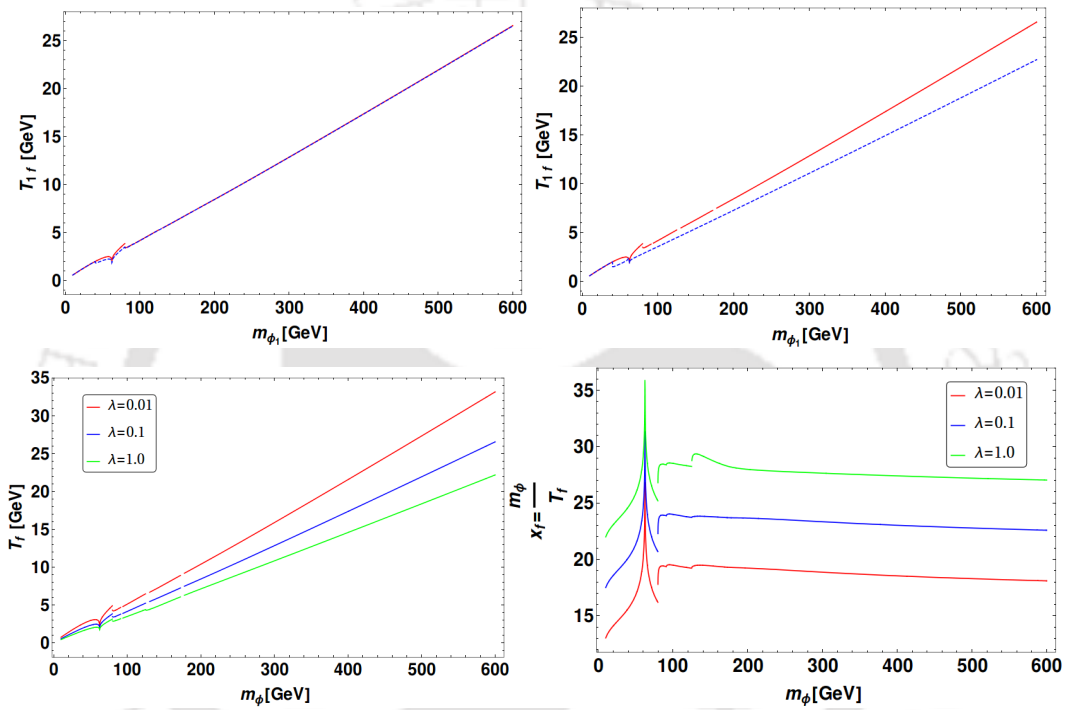

Figure 3.19: Top left: Freeze-out temperature of ϕ_1 (T_{1f}) as obtained from analytical solution is plotted as a function of DM mass m_{ϕ_1} for two cases: In absence of the second component ϕ_2 (red) and in presence of ϕ_2 and with DM-DM interaction (blue dotted) for $\{\lambda_1, \lambda_2, \lambda_3, m_{\phi_2}\} = \{0.1, 0.1, 0.0, 40\}$; Top right: Same as top left with $\{\lambda_1, \lambda_2, \lambda_3, m_{\phi_2}\} = \{0.1, 0.1, 1.0, 40\}$; Bottom left: Freeze-out temperature (T_f) of single component DM is shown for different choices of coupling $\lambda_1 = \{0.01, 0.1, 1.0\}$ (red, blue and green respectively); Bottom right: x_f versus m_ϕ in the single component case with same choices of λ_1 as in bottom left. All masses are in GeVs.

conditions of the DMs, the next goal is to find the respective relic densities. For that, we need to consider the epoch at $x \gg x_i^f$. For $x \gg x_i^f$: $y_i^{EQ} \to 0$ and evidently $\Delta_i \to y_i$. Then BEQs read

$$\begin{aligned} \frac{d\Delta_1}{dx} &= -\frac{1}{x^2}[(\sigma_1 + \sigma_{12})\Delta_1^2] \\ \frac{d\Delta_2}{dx} &= -\frac{1}{x^2}[\sigma_2\Delta_2^2 - \sigma_{12}\Delta_1^2] \end{aligned} \tag{3.47}$$

Integrating the equations, we get

$$\begin{aligned}\int_{\Delta_1(x_{1f})}^{\Delta_1(\infty)} -\frac{d\Delta_1}{\Delta_1^2} &= (\sigma_1+\sigma_{12})\int_{x_{1f}}^{\infty}\frac{dx}{x^2} \\ \Delta_1(\infty) &= \frac{1}{\frac{1}{\Delta_1(x_{1f})}+(\sigma_1+\sigma_{12})\frac{1}{x_{1f}}}\end{aligned} \tag{3.48}$$

$\Delta_1(x_{1f})$ can be found easily by putting $x = x_{1f}$ in above equations as,

$$\Delta_1(x_{1f}) = \frac{\frac{\mu}{m_{\phi_1}}(x_{1f}^2 - \frac{3}{2}x_{1f})}{(\sigma_1+\sigma_{12})} \tag{3.49}$$

So that we finally obtain the yield at a large $x \to \infty$ as

$$y_1(\infty) \equiv \Delta_1(\infty) = \frac{1}{(\sigma_1+\sigma_{12})\frac{m_{\phi_1}}{\mu}[\frac{2}{x_{1f}{}^2-\frac{3}{2}x_{1f}}+\frac{1}{x_{1f}}]} \tag{3.50}$$

The relic density can then easily be found using Eq. 3.31. The approximate solution thus obtained for ϕ_1 is then compared to the numerical solution obtained using Mathematica and is shown in Fig. 3.20. For approximate solution we choose two different values of the proportionality constant $c_1(c_1+1) \to 2$ (green dashed line), 10 (blue dashed line) and numerical solution is shown in red and what we see is a good agreement which shows the robustness of the solution obtained here. However, solving the

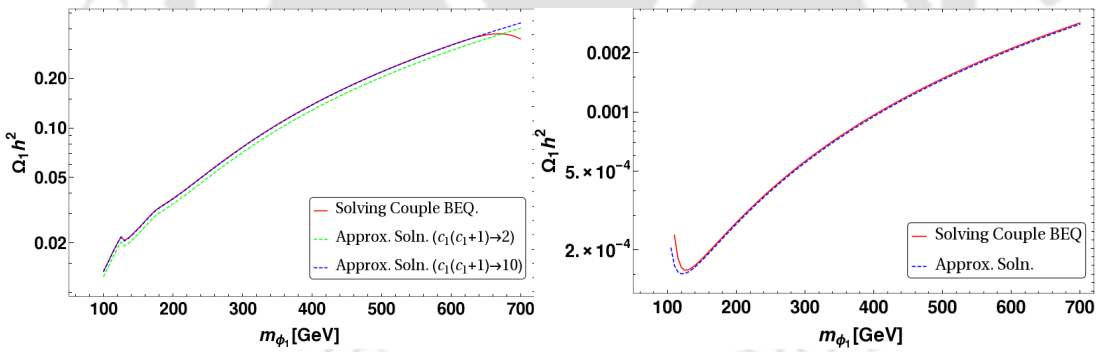

Figure 3.20: Relic density of the first DM component ϕ_1 ($\Omega_1 h^2$) obtained from numerical solution (solid red line) and approximate analytic solution with different values of the factor of proportionality constant $c_1(c_1+1) \to 2$ (green dashed line), 10 (blue dashed line) are compared. The parameters chosen here are $\{\lambda_1, \lambda_2, \lambda_3, m_{\phi_2}\}$: $\{0.1, 0.1, 0.0, 100\}$(left) and $\{0.1, 0.1, 2.0, 100\}$(right). Masses are in GeVs.

equation for second DM component ϕ_2 is more tricky. In this case first DM component freeze-out before; so that $x_{1f} < x_{2f}$. Hence, here we can consider $\Delta_1(x) \to \Delta_1(x_{1f})$ as the region x where we seek the freeze out of the second component lies beyond the freeze-out of the first component. BEQ for ϕ_2 in such a case is

$$\frac{d\Delta_2}{dx} = -\frac{1}{x^2}[\sigma_2\Delta_2^2 - \sigma_{12}\Delta_1^2(x_{1f})] \tag{3.51}$$

Integrating above equation we get

$$\begin{aligned}\int_{\Delta_2(x_{2f})}^{\Delta_2(\infty)} \frac{d\Delta_2}{\Delta_2^2 - a^2} &= -\sigma_2 \int_{x_{2f}}^{\infty} \frac{dx}{x^2} \\ y_2(\infty) \to \Delta_2(\infty) &= a \left[\frac{1 + \frac{\Delta_2(x_{2f})-a}{\Delta_2(x_{2f})+a} e^{-\frac{2a\sigma_2}{x_{2f}}}}{1 - \frac{\Delta_2(x_{2f})-a}{\Delta_2(x_{2f})+a} e^{-\frac{2a\sigma_2}{x_{2f}}}} \right] \end{aligned} \tag{3.52}$$

where $a = \sqrt{\frac{\sigma_{12}}{\sigma_2}}\Delta_1(x_{1f})$ and $\Delta_2(x_{2f}) = \frac{\frac{\mu}{m_{\phi_2}}(x_{2f}^2 - \frac{3}{2}x_{2f})}{\sigma_2}$. Now, for $m_{\phi_2} \ll m_{\phi_1}$ (i.e $\frac{\mu}{m_{\phi_2}} \to 1$) and $\sigma_2 \gg \sigma_{12}$: the terms $a = \sqrt{\frac{\sigma_{12}}{\sigma_2}}\Delta_1(x_{1f}) \ll 1$. For this limit Eq. 3.52 becomes

$$\begin{aligned} y_2(\infty) \to \Delta_2(\infty) &= a \left[\frac{(\Delta_2(x_{2f}) + a) + (\Delta_2(x_{2f}) - a)(1 - \frac{2a\sigma_2}{x_{2f}})}{(\Delta_2(x_{2f}) + a) - (\Delta_2(x_{2f}) - a)(1 - \frac{2a\sigma_2}{x_{2f}})} \right] \\ &\approx \frac{1}{\frac{1}{\Delta_2(x_{2f})} + \frac{\sigma_2}{x_{2f}}} \approx \frac{1}{\sigma_2\left(\frac{1}{{x_{2f}}^2} + \frac{1}{x_{2f}}\right)} \end{aligned} \tag{3.53}$$

Which exactly mimics the single component solution justifiably. It is good to remind the readers that the relic density of DM components in terms of the modified yield obtained using approximation solution can be written as:

$$\Omega_i h^2 = \frac{854.45 \times 10^{-13}}{\sqrt{g_*}} \frac{m_{\phi_i}}{\mu} y_i(\infty) \tag{3.54}$$

The approximate analytical solution for the second component ($\Omega_2 h^2$) is compared

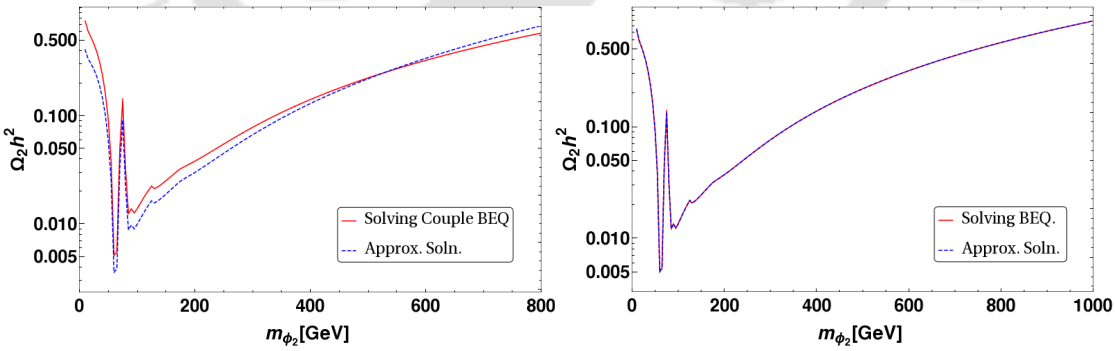

Figure 3.21: Left: Relic density of ϕ_2 ($\Omega_2 h^2$) obtained from numerical solution (solid red line) and approximate analytic solution (blue dashed line following Eq. 3.52) are compared in two component scenario. The parameters chosen here are: $\{\lambda_1, \lambda_2, \lambda_3, m_{\phi_1}\} : \{0.1, 0.1, 0.0, 800\}$. Right: Same in single component case is depicted following Eq. 3.53. We chose $\lambda_2 = 0.1$ for illustration. Masses are in GeVs.

with the numerical solution obtained using Mathematica and is shown in Fig. 3.21. In the left panel we show the comparison for two component case, while on the right panel, we show the limit in which it behaves like a single component DM.

3.6 Direct Detection

Scattering of scalar singlet DM with the detector nuclei originates from the Higgs-portal interaction. The quark level interaction in our model occurs via t channel diagram through Higgs exchange as shown in Fig. 3.22. Two interaction vertices are $\frac{1}{2}\lambda_i v h\phi_i\phi_i$ and $\frac{m_q}{v}h\bar{q}q$, where $i = 1, 2$. Effective Lagrangian for direct search process can be written as [88, 89]

$$\begin{aligned}\mathcal{L}_{eff} &= (\frac{1}{2}\lambda_i v)(\frac{m_q}{v})\frac{1}{m_h^2}\phi_i\phi_i\bar{q}q \\ &= \alpha_q\phi_i\phi_i\bar{q}q \end{aligned} \tag{3.55}$$

The matrix element of DM-quark elastic scattering in the limit of zero momentum transfer is $(Q \to 0)$

$$\mathcal{M}_{\phi_i q} = \sum_q \alpha_q\langle(\phi_i)_f|\phi_i\phi_i|(\phi_i)_i\rangle\langle q_f|\bar{q}q|q_i\rangle \tag{3.56}$$

One can convert the quark level interaction $\Rightarrow$ neucleon level interaction as

$$\sum_q \alpha_q\langle(\phi_i)_f|\phi_i\phi_i|(\phi_i)_i\rangle\langle q_f|\bar{q}q|q_i\rangle \Rightarrow \alpha_n\langle(\phi_i)_f|\phi_i\phi_i|(\phi_i)_i\rangle\langle n_f|\bar{n}n|n_i\rangle \tag{3.57}$$

where

$$\begin{aligned}\alpha_n &= m_n\sum_{u,d,s} f_{T_q}^{(n)}\frac{\alpha_q}{m_q} + \frac{2}{27}f_{T_g}^{(n)}\sum_{q=c,t,b}\frac{\alpha_q}{m_q} \\ &= m_n\sum_{u,d,s} f_{T_q}^{(n)}\frac{\alpha_q}{m_q} + \frac{2}{27}(1-\sum_{u,d,s} f_{T_q}^{(n)})\sum_{q=c,t,b}\frac{\alpha_q}{m_q} \\ &= \frac{m_n\lambda_i}{m_h^2}[(f_{T_u}^{(n)} + f_{T_d}^{(n)} + f_{T_s}^{(n)}) + \frac{2}{9}(f_{T_u}^{(n)} + f_{T_d}^{(n)} + f_{T_s}^{(n)})]\end{aligned} \tag{3.58}$$

where nucleon n stands for both proton and neutron. For proton : $f_{T_u}^p = 0.0153$, $f_{T_d}^p = 0.0191$, $f_{T_s}^p = 0.0447$ [90, 91]. Hence, spin independent cross section of DM-Neucleon scattering reads[79]:

$$\sigma_{n_i}^{SI} = \frac{\alpha_n^2\mu_n^2}{4\pi m_{\phi_i}^2} \tag{3.59}$$

where $\mu_n = \frac{m_n m_{\phi_i}}{m_n + m_{\phi_i}}$

For Two component DM case, the DM-nucleon cross-section has to be even further modified by the fraction of the particular component present in the universe as [47]:

$$\sigma_{eff}^{SI}(n_i) = (\frac{\Omega_i}{\Omega_T})\sigma_{n_i}^{SI} = \frac{\Omega_i}{\Omega_T}\frac{\alpha_n^2\mu_n^2}{4\pi m_{\phi_i}^2} \qquad (i = 1, 2) \tag{3.60}$$

A more rigorous way of achieving the correct direct search limit on the individual DM components can be achieved via the total recoil rate of the nucleus, which we will illustrate in the summary of the thesis.

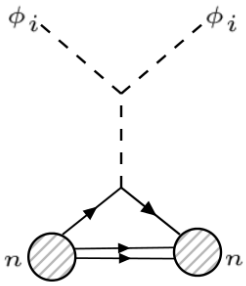

Figure 3.22: Feynman diagram for direct detection of scalar singlet DM.

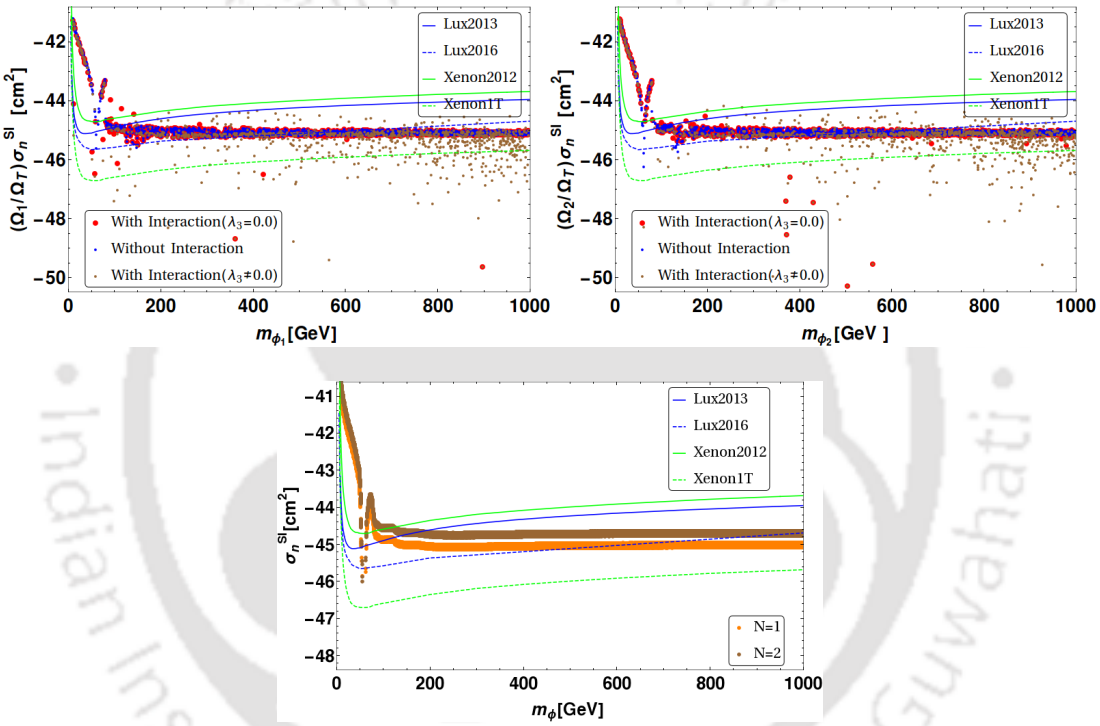

Figure 3.23: Spin-independent DM-nucleon effective cross-section (in Log scale) for relic density allowed points as a function of DM mass in $\mathcal{Z}_2 \times \mathcal{Z}_2^{'}$ model. Top Left: The case for ϕ_1 is shown in $m_{\phi_1} - \frac{\Omega_1}{\Omega_T}\sigma_n^{SI}$ plane; Top Right: The case for ϕ_2 is shown in $m_{\phi_2} - \frac{\Omega_2}{\Omega_T}\sigma_n^{SI}$ plane. Three different situations are indicated as follows: no DM-DM interactions by blue dots, DM interaction with $\lambda_3 = 0$ through red dots and DM interaction with $\lambda_3 \neq 0$ by grey dots. Bottom: Single component DM framework and two component case with $\mathcal{O}(2)$ are shown for comparison. Limits from XENON 2012, LUX and LUX 2016 data have been indicated while the predictions of XENON1T is also provided.

It is of great importance to see how much of relic density allowed DM parameter space of $\mathcal{Z}_2 \times \mathcal{Z}_2^{'}$ model is allowed by the spin independent direct search constraints by XENON2012 [42, 43], and updated LUX data [40, 41]. This is what is presented in Fig. 3.23. The scattered points show DM-nucleon spin-independent cross-section (σ_n^{SI}) multiplied by effective scaling $\frac{\Omega_i}{\Omega_T}$ (as in Eq. 4.32) as a function of DM mass for relic density allowed points. The case for ϕ_1 is shown in left while for ϕ_2 is in the right side of Fig. 3.23. The cases for no DM-DM interaction (Blue), DM-DM interaction with $\lambda_3 = 0$ (Red) and DM-DM interaction with $\lambda_3 \neq 0$ (Grey) are separately shown. One

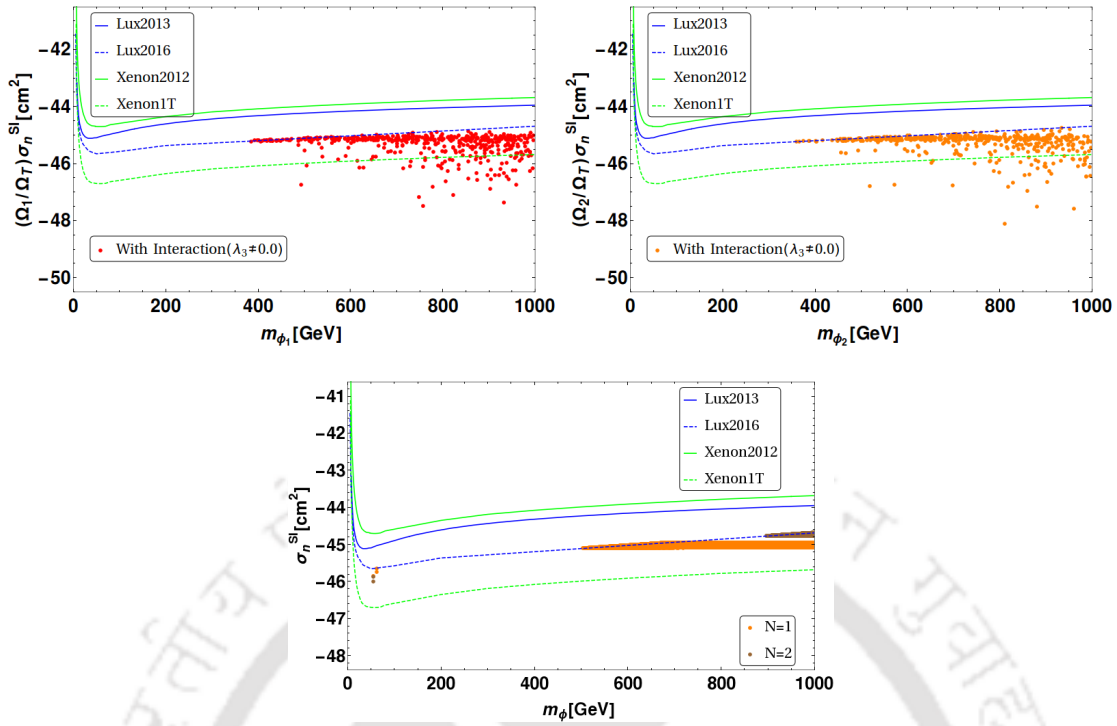

Figure 3.24: Points in $\mathcal{Z}_2 \times \mathcal{Z}_2^{'}$ model that satisfy relic density and direct search constraint for both ϕ_1 and ϕ_2 by LUX data in presence of DM-DM interactions with $\lambda_3 \neq 0$. Top left: Points in $m_{\phi_1} - \frac{\Omega_1}{\Omega_T}\sigma_n^{SI}$ plane; Top right: Same points in $m_{\phi_2} - \frac{\Omega_2}{\Omega_T}\sigma_n^{SI}$ plane. Bottom: Single component and two component DM in $\mathcal{O}(2)$ cases are illustrated.

can clearly see that the blue dots are placed below the LUX line but a significant part of them is discarded by the updated LUX data indicating that the model without DM-DM interaction is discarded in the low mass region excepting for the Higgs resonance $m_{\phi_1} \sim m_h/2$. Although there are blue points allowed above ~ 600 GeVs, we will show that they are not simultaneously present for both ϕ_1 and ϕ_2. On the contrary, there are several points in red and grey which yields much smaller DM-nucleon cross-section that are placed below the updated LUX data and can be even delayed upto XENON1T. Hence, the multipartite model may live longer in presence of DM-DM interaction. This feature of multipartite DM models seems very interesting and hasn't been pointed out in analysis recent past. The reason for obtaining small DM-nucleon cross-section in presence of DM-DM interactions can be understood as follows: DM conversion helps heavier component to acquire small relic density (through larger annihilations due to DM conversion) without enhancing the coupling to SM (λ_1 or λ_2); thus yielding DM-nucleon cross-section smaller than what one can achieve without having DM-DM interactions. What about the lighter component then ? It is easy to appreciate that it has to possess a larger density to account for correct abundance and hence requires smaller annihilation cross-section. In presence of DM-DM interaction, lighter component is also produced by the heavier ones requiring the annihilations of the lighter component to SM even smaller; hence, smaller becomes DM-SM coupling and direct search cross-section. Effective DM-nucleon cross-section can also get smaller by reducing the factor $\frac{\Omega_{1,2}}{\Omega_T}$. However, if one ratio is small, the other one must be large or close to one, which may not justify to keep both components on board. In Fig. 3.23, there is no correlation between the points in left and right. Here, we have

plotted all the points allowed by relic density in both figures not bothering about one particular point in one picture correspond to what in the other. This is what we do systematically in the following scans. It is also very important to note the status of the single component framework of the scalar singlet DM and the two-component framework of $\mathcal{O}(2)$ model as shown in the bottom panel of Fig. 3.23. We see that for the single component case, the DM is ruled out to approximately 500 GeV while for the two component DM in $\mathcal{O}(2)$ case, $m_{DM} \geq 800$ GeV.

A correlated scan with $\lambda_3 \neq 0$ is shown in Fig. 3.24. We plot relic density allowed points that satisfy LUX bounds for both ϕ_1 and ϕ_2. It turns out that now there are points even below XENON1T. This indicates that discovery of at least one component can get delayed even beyond XENON1T. The reason for such a phenomena to occur is easy to appreciate. In presence of λ_3, the DM abundance is within limit without having a large λ_1, λ_2 even without compromising for one component to make up the whole relic density, thus having the effective DM-nucleon cross-section reduced for both the cases. The outcome also means, that the model yields a possibility of detecting one component in near future, while the other might be delayed beyond XENON1T. It is also important to note here that there are no points where both ϕ_1 and ϕ_2 direct search cross-section goes beyond XENON1T indicating that if nothing is seen till the sensitivity of XENON1T, the two component framework with $\mathcal{Z}_2 \times \mathcal{Z}_2^{'}$ is most likely discarded. In the bottom panel of Fig. 3.24, we again compare the single component and two component $\mathcal{O}(2)$ cases. This also shows that for the fate of lighter component of the two-component interacting DM scenario is nothing significantly different from the single component framework.

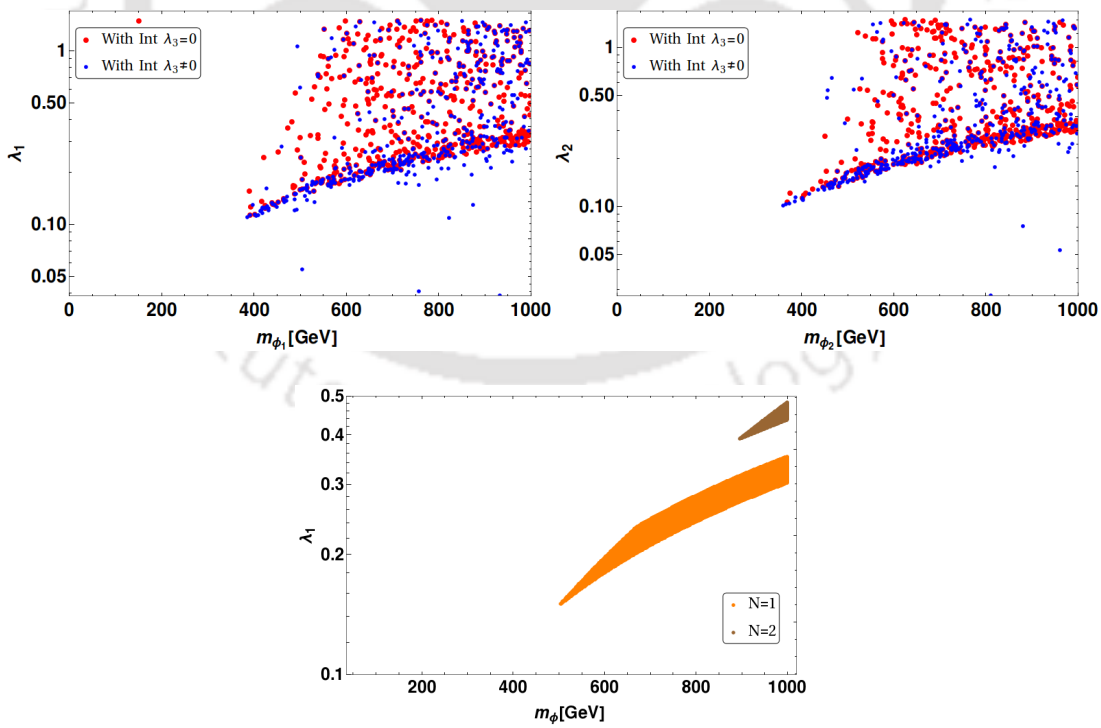

Figure 3.25: Points in $\mathcal{Z}_2 \times \mathcal{Z}_2^{'}$ model that satisfy relic density and direct search from updated LUX bound for both ϕ_1 and ϕ_2 is projected in $m_{\phi_1} - \lambda_1$ plane (top left) and in $m_{\phi_2} - \lambda_2$ (top right) plane. The case with $\lambda_3 = 0$ is shown in red and $\lambda_3 \neq 0$ is shown in blue. The cases of single component and two component $\mathcal{O}(2)$ framework are shown in the bottom panel in orange and brown respectively.

Relic density and direct search (LUX) allowed points for both ϕ_1 and ϕ_2, for the case of $\lambda_3 = 0$ (red) and $\lambda_3 \neq 0$ (blue) are shown in $m_{\phi_1} - \lambda_1$ plane (top left) and $m_{\phi_2} - \lambda_2$ plane (top right) of Fig. 3.25. Again, those in single component and two component non-interacting cases are shown in the bottom panel for comparison. Required DM mass for both the components ~ 300 GeV for $\mathcal{Z}_2 \times \mathcal{Z}_2^{'}$ model which is not drastically different from that of the single component case. However, the flexibility in two component set up allows a larger region of DM-SM couplings (λ_1, λ_2). Secondly, the two scenarios of DM-DM interactions with $\lambda_3 = 0$ and $\lambda_3 \neq 0$ distinguishes themselves at small values of λ_1, λ_2 as has lready been discussed.

Benchmark Points	$\{\lambda_1, \lambda_2, \lambda_3, m_{\phi_1}, m_{\phi_2}\}$	$\Omega_1 h^2$	$\Omega_2 h^2$	$\frac{\Omega_1}{\Omega_T}(\%)$	$\frac{\Omega_2}{\Omega_T}(\%)$	$\sigma_{1_{eff}}^{SI}$ $(10^{-46} cm^2)$	$\sigma_{2_{eff}}^{SI}$ $(10^{-46} cm^2)$
BP1	$\{0.4, 0.3, 0.0, 815, 715\}$	0.04	0.06	40	60	7.7	8.4
BP2	$\{0.15, 0.3, 0.0, 390, 572\}$	0.06	0.04	60	40	7.8	7.3
BP3	$\{0.3, 0.8, 0.0, 960, 850\}$	0.10	0.01	91	9	7.0	6.3
BP4	$\{0.36, 0.38, 0.7, 890, 895\}$	0.06	0.06	50	50	6.2	7.4
BP5	$\{0.31, 0.46, 0.82, 940, 915\}$	0.05	0.06	45	55	4.3	1.0
BP6	$\{0.6, 0.1, 1.6, 775, 370\}$	0.003	0.117	2	98	2.8	7.2

Table 3.1: Some benchmark points in $\mathcal{Z}_2 \times \mathcal{Z}_2^{'}$ model allowed by relic density and direct search. The input parameters, relic density of individual components and direct search cross-sections mentioned. All the masses are in GeV.

Finally some benchmark points have been mentioned for $\mathcal{Z}_2 \times \mathcal{Z}_2^{'}$ model in Tab. 3.1 (BP1-BP6) where all the input parameters, individual relic densities and spin independent direct search effective cross-sections are mentioned. We choose examples of one component dominating over the other as well as the case where they contribute equally to relic density.

However, there is an important caveat to what we have discussed above in context of direct search of non-degenerate multicomponent DM model. Direct search of DM depends on the nuclear recoil of the detector. The rate of nuclear recoil is very less sensitive to DM mass above $\sim$400 GeV (as the allowed parameter space suggests here). For example, a DM of 400 GeV and 700 GeV yield similar rate so that they can hardly be distinguished. The effective recoil is then a sum of both the components interacting with the detector. In that circumstances, one needs to add the individual direct search effective cross-sections to evaluate the limit on the available parameter space of the model. Here, we assume that DMs with mass difference of ≤ 300 GeV are indistinguishable. This is a simplified choice, the detailed analysis lies beyond the scope of the draft. Then, we choose the set of parameter space $\{\lambda_1, \lambda_2, \lambda_c, m_{\phi_1}, m_{\phi_2}\}$ which obeys relic density constraint for $|\Delta m = m_{\phi_1} - m_{\phi_2}| \leq 300$ GeV. We then add the individual direct search effective rates together to find the limit on ϕ_1 as $\sigma_T^{SI} = \frac{\Omega_1}{\Omega_T}\sigma_1^{DD} + \frac{\Omega_2}{\Omega_T}\left(\frac{m_{\phi_1}}{m_{\phi_2}}\right)\sigma_2^{DD}$. This follows from a simple derivation. The recoil rate in direct search [92] is given by:

$$\begin{aligned} R &= n_t \langle v \rangle n_\phi \sigma^{DD} \\ &= \left(\frac{n_t \langle v \rangle \rho_c}{m_\phi}\right) \Omega_\phi \sigma^{DD} \end{aligned} \tag{3.61}$$

where $n_t = \frac{N}{A}$ with N is Avogadro number and A is atomic mass of the target; rest of

the variables are self explanatory. Then for the two component case:

$$
\begin{aligned}
R = \left(\frac{n_t\langle v\rangle\rho_c}{m_\phi}\right)\Omega_T\sigma_T^{SI} &= \left(\frac{n_t\langle v\rangle\rho_c}{m_{\phi_1}}\right)\Omega_1\sigma_1^{DD} + \left(\frac{n_t\langle v\rangle\rho_c}{m_{\phi_2}}\right)\Omega_2\sigma_2^{DD} \\
&= \left(\frac{n_t\langle v\rangle\rho_c}{m_{\phi_1}}\right)[\Omega_1\sigma_1^{DD} + \frac{m_{\phi_1}}{m_{\phi_2}}\Omega_2\sigma_2^{DD}] \\
\therefore \qquad \sigma_T^{SI} &= \frac{\Omega_1}{\Omega_T}\sigma_1^{DD} + \frac{\Omega_2}{\Omega_T}\left(\frac{m_{\phi_1}}{m_{\phi_2}}\right)\sigma_2^{DD}
\end{aligned}
\tag{3.62}
$$

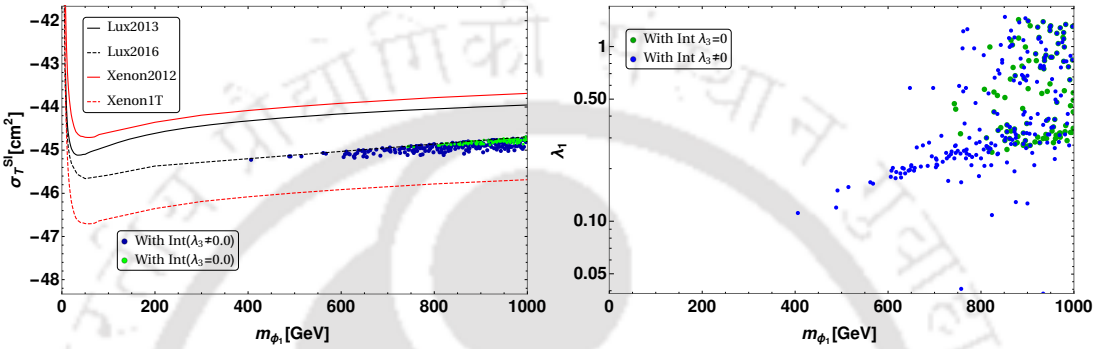

Figure 3.26: Direct search constraints on the two component model when $|\Delta m = m_{\phi_1} - m_{\phi_2}| \leq 300$ GeV behaves as degenerate DM scenario due to insensitivity of the detector. Left: Relic density allowed points in $\sigma_T^{SI} - m_{\phi_1}$ plane satisfying LUX data; Right: Same points in $m_{\phi_1} - \lambda_1$ plane. Blue points depict interacting scenario with $\lambda_c \neq 0$, while the green points depict the case of $\lambda_c = 0$.

We plot σ_T^{SI} it with respect to m_{ϕ_1} in the left panel of Fig. 3.26 to evaluate the direct search allowed region of parameter space. Blue points depict interacting scenario with $\lambda_c \neq 0$, while the green points depict the case of $\lambda_c = 0$. On the right panel of Fig. 3.26, we show the same in $m_{\phi_1} - \lambda_1$ plane. What we see that still with non-zero DM-DM interactions, one achieves a larger region of allowed parameter space than the single component set up assuming that a large mass gap of the DMs is insensitive to the detector, while the case for $\lambda_c = 0$ actually behaves like a degenerate two component scenario ($\mathcal{O}_2$) for obvious reasons. The lower DM mass limit evaluated before is now shifted slightly to a higher value, so that points like BP2 may already be ruled out by LUX constraint.

3.7 Higgs Invisible Decay Constraint in Two-Component set up

If DM masses are smaller than the Higgs mass as $m_{\phi_i} < m_h/2$, then Higgs can decay to two DMs through the same vertex $h \to \phi_i\phi_i$ and will yield invisible decay width. There is a strong constraint on such a process, which in turn puts a constraint on DM-Higgs coupling for $m_{DM} < m_h/2$.

The decay width of Higgs to one DM component (ϕ) is given by [70, 79]:

$$
\Gamma_{h\to\phi\phi} = \frac{\lambda^2 v^2}{32\pi m_h^2}(m_h^2 - 4m_\phi^2)^{1/2}. \tag{3.63}
$$

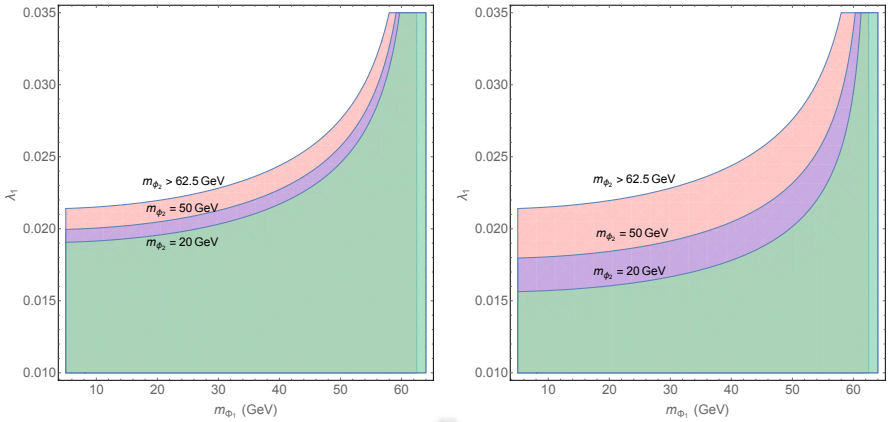

Figure 3.27: Constraints from invisible Higgs decay width on $\mathcal{Z}_2 \times \mathcal{Z}_2^{'}$ model in $m_{\phi_1} - \lambda_1$ plane for $\lambda_2 = 0.01$ (left) and $\lambda = 0.015$ (right) for $m_{\phi_2} = 20,\ 50$ GeV and for $\mathrm{m}_{\phi_2} > 62.5$ GeV. For $m_{\phi_2} = 20$ GeV only the green region is allowed. For $m_{\phi_2} = 50$ GeV the lilac and green both are allowed and for $m_{\phi_2} > 62.5$ GeV, orange, lilac and green regions are allowed.

For the two component DM scenario in $\mathcal{Z}_2 \times \mathcal{Z}_2^{'}$ model, the total width will be

$$\begin{aligned} \Gamma_{h\to inv} &= \Gamma_{h\to\phi_1\phi_1} + \Gamma_{h\to\phi_2\phi_2} \\ &= \frac{\lambda_1^2 v^2}{32\pi m_h^2}\sqrt{m_h^2 - 4m_{\phi_1}^2} + \frac{\lambda_2^2 v^2}{32\pi m_h^2}\sqrt{m_h^2 - 4m_{\phi_2}^2}. \end{aligned} \tag{3.64}$$

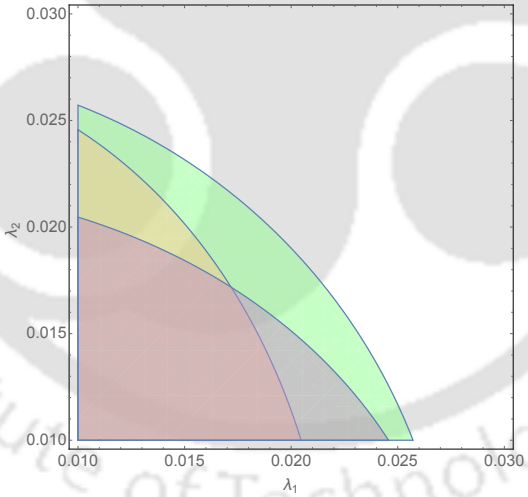

Figure 3.28: Constraints from invisible Higgs decay width on $\mathcal{Z}_2 \times \mathcal{Z}_2^{'}$ model in $\lambda_1 - \lambda_2$ plane for $\{m_{\phi_1}, m_{\phi_2}\} = \{50, 50\}$ (Green and below), $\{20, 50\}$ (Yellow and below), $\{50, 20\}$ (Grey and below). All masses are in GeVs.

From recent analysis at Large Hadron Collider (LHC), constraint on the invisible branching fraction of Higgs has become tighter $Br(h \to inv) \leq 0.35$ [70, 93]. Higgs decay width on the other hand is measured rather accurately at LHC and is given by $\Gamma_{h\to SM} = 4.07$ MeV for Higgs mass $m_h = 125$ GeV. For the two component set up this then indicates

$$\begin{aligned} Br(h \to \phi_1\phi_1) + Br(h \to \phi_2\phi_2) &\leq 0.35 \\ \Rightarrow \Gamma_{h\to\phi_1\phi_1} + \Gamma_{h\to\phi_2\phi_2} &\leq 2.2 \text{ MeV} \end{aligned}$$

Clearly the constraints on individual DM-SM coupling is tighter in two component framework than the single component one. The constraint in $\mathcal{Z}_2 \times \mathcal{Z}_2^{'}$ model is presented in Fig. 3.27 in the plane of $m_{\phi_1} - \lambda_1$ for specific choices of $\lambda_2 = 0.01$ (left), 0.015 (right) and $m_{\phi_2} = 20,\ 50$ GeV and for $m_{\phi_2} > 62.5$ GeV. For $m_{\phi_2} = 20$ GeV, only the green region is allowed. For $m_{\phi_2} = 50$ GeV the lilac and green both are allowed indicating that the constraint is slightly loose on λ_1. For $m_{\phi_2} > 62.5$ GeV, it effectively boils down to a single component scenario and all the regions below the curve is allowed. With larger λ_2, the constraints on λ_1 is tighter as is clear from the RHS of Fig. 3.27. Another possible representation of the invisible decay width constraint on $\mathcal{Z}_2 \times \mathcal{Z}_2^{'}$ model will be in $\lambda_1 - \lambda_2$ plane for different combinations of m_{ϕ_1}, m_{ϕ_2} as shown in Fig. 3.28. Here, we have chosen three different combinations of DM masses $\{m_{\phi_1}, m_{\phi_2}\} = \{50, 50\}$ (Green and below), $\{20, 50\}$ (Yellow and below), $\{50, 20\}$ (Grey and below) showing that smaller the DM mass is, tighter is the corresponding coupling.

To summarise, invisible Higgs decay constraint is tighter on multipartite DM models than the single component one as the invisible Higgs decay width to individual components get narrower if the DM component have masses $m_{\phi_i} < m_h/2$. Such constraints are very important to take into account when we look into the Higgs resonance region and below ($m_{\phi_i} \leq m_h/2$). What we conclude is that the invisible decay of Higgs rules out a viable DM for ($m_{\phi_i} < m_h/2$), as the DM relic density allowed DM-SM couplings need to be much larger than what the invisible decay predicts.

3.8 Conclusions

We have analysed the two-component scalar singlet DM scenarios coupled to SM with Higgs portal coupling, in particular with $\mathcal{Z}_2 \times \mathcal{Z}_2^{'}$ symmetry in the light of relic density and direct search constraints. We point out that DM-DM interaction plays a crucial role and yields a much larger region of parameter space from relic density constraints. We also demonstrate the effect of DM-DM interaction in the freeze out of DM components and in particular how it alters the DM density from the non-interacting or single component scenario. A generic feature of interacting multicomponent DM framework turns out to be reducing the required DM-SM coupling compared to the non-interacting or single component cases, as has been demonstrated for a two component scenario. With more than two DM components, the changes in the available parameter space will be in regions where the DM components contribute equally. However, the lowest DM-SM coupling for one DM component that can be achieved is determined by two component framework itself.

On the other hand, direct search bound from updated LUX data constraints single component scalar singlet DM scenario upto DM mass $\sim$ 500 GeV and the two component case with $\mathcal{O}(2)$ symmetry upto $\sim$ 800 GeV excepting for Higgs resonance region. It is through multipartite models such as $\mathcal{Z}_2 \times \mathcal{Z}_2^{'}$, scalar singlet DM can still survive in a large parameter space. The presence of non-zero DM-DM interaction coupling λ_3 can delay the direct detection of one component upto XENON1T while the other (lighter component) is expected to be unravelled soon. DM masses larger than 400 GeV seems to be allowed in $\mathcal{Z}_2 \times \mathcal{Z}_2^{'}$ case. Other mechanisms of hiding DM from direct search bound includes co-annihilation, semi-annihilation etc., which we will elaborate in other draft. Here, we also discuss approximate analytical solution for the $\mathcal{Z}_2 \times \mathcal{Z}_2^{'}$ case which closely agree to the numerical solutions in the moderate

DM-DM interaction regions.

We propose a few benchmark points allowed by relic density and direct search for discovery potential at LHC. It is indeed important to study constraints coming from non-observation of missing energy signatures of such DM models at the LHC. The common notion is that the limits from collider are still weaker than the one from direct search, particularly for Higgs portal interactions. However one needs to carefully study the multicomponent framework in context of LHC and see if any new feature or correlation emerges. Such a study lies beyond the scope of this chapter, and will be taken up in next chapters. Indirect search also plays a crucial role constraining the dark matter models, but again less constraining to multicomponent frameworks.

It is important at the end to ask whether it is possible to unravel a multicomponent DM scenario in future experiments and how. We argued that the very existence of a scalar singlet DM in future detection will hint towards a multipartite framework or with extended beyond the SM scenario. Given the knowledge of one DM mass and coupling with SM, one can loosely predict the other DM mass and coupling as seen from the benchmark points to account for correct relic density and direct search bound. We of course plan to elaborate more in this direction in future, both in context of signatures at the LHC and that of direct search.

Chapter 4

Multipartite Dark Matter with Scalar and Fermions

Contents

4.1 Introduction

Present chapter investigates one of the simplest multipartite DM frameworks with scalar and fermion, which has detectability in upcoming direct and collider searches. We assume the presence of two DM components: one scalar (S) and a fermion (N_1). While both DMs have been studied as individual components [67, 94–96], we study the interplay of DM-DM interactions when they are present together. In order to enhance such interactions, we insert an additional singlet fermion field (χ_2), which works as a mediator and carries the interaction through a Yukawa term. We thereafter demonstrate that a large parameter space becomes available to each DM components, whichever is heavy, saved from direct search bound thanks to enhanced DM-DM interactions. The lighter DM component however, has the fate similar to that of a single component case, particularly when direct search is concerned. This shows that scalar DM can only be present in the vicinity of Higgs resonance ($m_S \sim m_h/2$) when it is lighter than fermion DM. The presence of an additional heavy scalar (S_H) in the model can however yield a larger parameter space for the scalar DM (even when it is lighter than fermion DM). Efforts have already been made to accommodate scalar and fermion DM together in a single framework [48, 51], but most often the role of

DM-DM interactions have been subdued and the outcome is predictive and severely constrained.

Collider signatures of both the DM components have also been addressed before (see for example, [97, 98]). Unfortunately, it turns out that neither the scalar nor the fermion DM (in their single component realisation) has a possibility of producing signal excess over SM background in near future run of Large Hadron Collider (LHC)[1], while satisfying relic density and direct search constraints. We however demonstrate here, the presence of a lighter scalar DM component helps in identifying hadronically quiet dilepton signal (a characteristic signature for the charged lepton components present in the fermion dark sector) at LHC, which was otherwise impossible due to unsurpassable SM background contribution. This is accessible due to the freedom of utilising a larger missing energy cut, resulting from a larger allowed mass difference between the fermion DM and its charge companions, thanks to the presence of a lighter DM component and non-negligible DM-DM interactions in the set up to satisfy relic density and direct search bounds.

The chapter is organised as follows. We first introduce the model framework (in Section 5.2). After reviewing relic density and direct search constraints on the individual DM components for single component frameworks (in Section 4.3), we discuss in details the case of two-component set up poised with DM-DM conversion (in Section 4.4). We also point out to the possibilities of having an additional heavy scalar in the framework (in Section 4.5). We then elucidate signatures of fermion dark sector at LHC accessible through two component set up (in Section 4.6). We also briefly discuss possible cosmological effect on DM particles due to early universe inflation and reheating (in Section 4.7). Finally we summarise and conclude (in Section 4.8). Some illustrative features of fermion DM.

4.2 The Model

The model addressed here, accommodates two single component DM frameworks together: (i) a real scalar singlet DM (S), connected to SM through Higgs portal [22, 67, 94, 95] and (ii) a fermion DM arising out of the admixture of vectorlike fermion (VF) doublet, $N = \begin{pmatrix} N^0 & N^- \end{pmatrix}^T$ and a vectorlike fermion singlet χ_1 [96, 97, 99], where lightest component becomes a DM. Stability of a single DM can be ensured by an additional discrete $\mathcal{Z}_2$ symmetry, under which the DM transforms nontrivially. However, when two DMs are present together, the stability of both components can be ensured by enhancing the symmetry to $\mathcal{Z}_2 \times \mathcal{Z}_2'$, where two DMs transform differently under the symmetry as we will illustrate shortly. Two-component DM frameworks are naturally disfavoured from direct search as each DM component acquires smaller relic density resulting enhanced annihilation cross-section to SM for freeze out. This enhances direct search cross-sections for both the DM components (resulting from same interaction vertices). This is the reason that most of the existing scalar-fermion DM scenarios have been severely discarded by stringent direct search limits [48, 51]. However, DM-DM interactions may come to rescue as the freeze-out of the heavier component will then be additionally driven by its annihilation to lighter DM component, which do not contribute to direct search cross-section of that compo-

[1]Fermion DM with singlet-doublet mixing may however yield a displaced vertex signature [97].

nent. In order to enhance such interplay, we have introduced an additional vectorlike singlet fermion χ_2, which behaves like a messenger between the two DM components. The interaction between the two DM components and their individual connection to the visible sector (SM) are shown by a schematic diagram in Fig. 4.1. Under the $\mathcal{Z}_2 \times \mathcal{Z}_2'$ symmetry, additional dark fields transform as: N $[-,+]$, χ_1 $[-,+]$, χ_2 $[+,-]$ and S $[-,-]$, where all SM fields remain invariant: SM $[+,+]$. The quantum numbers under the SM gauge group $SU(3)_C \times SU(2)_L \times U(1)_Y$ and $\mathcal{Z}_2 \times \mathcal{Z}'_2$ symmetry for these additional fields are shown in the Table 4.1. It is remarkable that these additional fermions χ_1, χ_2 and N are verctor-like and hence they don't introduce any extra anomalies. This is easy to see through the chiral gauge anomaly free condition coming from the one loop triple gauge boson vertex, which reads [100]:

$$\sum_{rep} Tr[\{T_L^a, T_L^b\}T_L^c - \{T_R^a, T_R^b\}T_R^c] = 0. \tag{4.1}$$

Here, T denotes the generators for the SM gauge group and L, R denotes the interactions of left or right chiral fermions with the gauge bosons. It is straightforward to see, that while the SM satisfies the anomaly free condition because of the presence of a quark family to each lepton family [100, 101], the additional vector like fermions introduced here, have the left chiral components transforming similarly to the right chiral ones under the SM gauge symmetry. Therefore, the model is anomaly free.

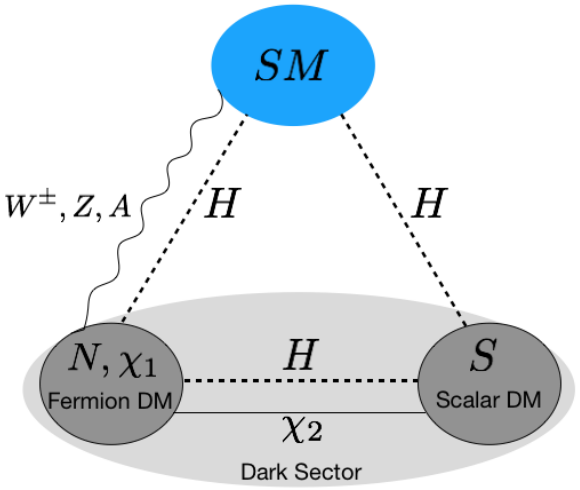

Figure 4.1: Schematic diagram showing the interactions between scalar and fermion DM components and that to SM particles.

In Table 4.1, we note that N and χ_1 have similar $\mathcal{Z}_2 \times \mathcal{Z}'_2$ charges. Hence they mix with each other after the SM Higgs acquires a vacuum expectation value (vev), while the other fermion χ_2 does not. The lightest of such singlet-doublet admixture can be one fermion DM component of this model. The scalar singlet S also have different charge assignment from that of all the other fermion fields, allowing it to be stabilized to form another DM component. The key feature of this model is the possibility of writing a Yukawa interaction between χ_1, χ_2, and S by the assigned $\mathcal{Z}_2 \times \mathcal{Z}'_2$ charges, which adds to the possible DM-DM interactions as we explain below. This particular feature segregates this model from earlier attempts of two component

Dark Fields	$\underbrace{SU(3)_C \times SU(2)_L \times U(1)_Y}\times \mathcal{Z}_2 \times \mathcal{Z}'_2$				
$N = \begin{pmatrix} N^0 \\ N^- \end{pmatrix}$	1	2	-1	-	+
χ_1	1	1	0	-	+
χ_2	1	1	0	+	-
S	1	1	0	-	-

Table 4.1: Dark sector fields and their corresponding quantum numbers under $\mathcal{G} \equiv SU(3)_C \times SU(2)_L \times U(1)_Y \times \mathcal{Z}_2 \times \mathcal{Z}'_2$.

scalar-fermion DM set-up like in [48, 51], where DM-DM interactions were small, so the model becomes strongly constrained by direct search or from the case where fermion DM doesn't have an interaction with visible sector (excepting at the loop level) to credit a large share of relic density to it and thus constraining the model to a particular possibility.

Let us now describe the Lagrangian for the model, which can be segregated into three parts, constituting the vector like fermion sector, scalar sector and the interaction between the fermion and scalar sector as follows:

$$\mathcal{L} \supset \mathcal{L}^{VF} + \mathcal{L}^{Scalar} + \mathcal{L}^{VF+Scalar}, \tag{4.2}$$

where,

$$\begin{aligned} \mathcal{L}^{VF} &= \overline{N}\left[i\gamma^\mu(\partial_\mu - ig\frac{\sigma^a}{2}W^a_\mu - ig'\frac{Y'}{2}B_\mu) - m_N\right] N \\ &\quad + \overline{\chi_1}\left(i\gamma^\mu\partial_\mu - m_{\chi_1}\right)\chi_1 - (Y_1\overline{N}\widetilde{H}\chi_1 + h.c) \\ &\quad + \overline{\chi_2}\left(i\gamma^\mu\partial_\mu - m_{\chi_2}\right)\chi_2, \end{aligned} \tag{4.3}$$

$$\mathcal{L}^{Scalar} = \frac{1}{2}\partial^\mu S\partial_\mu S - \frac{1}{2}m_S^2S^2 - \frac{1}{4!}\lambda_S S^4 - \frac{1}{2}\lambda_{SH}\left(H^\dagger H - \frac{v^2}{2}\right)S^2, \tag{4.4}$$

and

$$\mathcal{L}^{VF+Scalar} = -Y_2(\overline{\chi_1}\chi_2 S + h.c). \tag{4.5}$$

There are two Yukawa interactions present in this model. We will focus on the first in Eqn. 4.3. Electroweak symmetry breaking (EWSB) occurs as the SM Higgs acquires a vacuum expectation value: $H = \begin{pmatrix} 0 & \frac{1}{\sqrt{2}}(v+h) \end{pmatrix}^T$ where $v = 246$ GeV. The Yukawa $Y_1\overline{N}\widetilde{H}\chi_1$ term in the Lagranigan (Eqn. 4.3) mixes N^0 and χ_1. Mass terms of the vector like fermions in $\mathcal{L}^{VF}$ then take the following form:

$$
\begin{aligned}
-\mathcal{L}^{VF}_{mass} &= m_N\overline{N^0}N^0 + m_N N^+N^- + m_{\chi_1}\overline{\chi_1}\chi_1 + \frac{Y_1 v}{\sqrt{2}}\overline{N^0}\chi_1 + \frac{Y_1 v}{\sqrt{2}}\overline{\chi_1}N^0 \\
&= \overline{\begin{pmatrix}\chi_1 & N^0\end{pmatrix}}\begin{pmatrix} m_{\chi_1} & \frac{Y_1 v}{\sqrt{2}} \\ \frac{Y_1 v}{\sqrt{2}} & m_N\end{pmatrix}\begin{pmatrix}\chi_1 \\ N^0\end{pmatrix} + m_N N^+N^- \\
&= \overline{\begin{pmatrix}N_1 & N_2\end{pmatrix}}\begin{pmatrix} m_1 & 0 \\ 0 & m_2\end{pmatrix}\begin{pmatrix}N_1 \\ N_2\end{pmatrix} + m_N N^+N^-, \qquad (4.6)
\end{aligned}
$$

where in the last step, the unphysical basis, $\begin{pmatrix}\chi_1 & N^0\end{pmatrix}^T$ is related to physical basis, $\begin{pmatrix}N_1 & N_2\end{pmatrix}^T$ through the following unitary transformation:

$$
\begin{pmatrix}\chi_1 \\ N^0\end{pmatrix} = \mathcal{U}\begin{pmatrix}N_1 \\ N_2\end{pmatrix} = \begin{pmatrix}\cos\theta & -\sin\theta \\ \sin\theta & \cos\theta\end{pmatrix}\begin{pmatrix}N_1 \\ N_2\end{pmatrix}, \qquad (4.7)
$$

where the mixing angle

$$
\tan 2\theta = -\frac{\sqrt{2}Y_1 v}{m_N - m_{\chi_1}}. \qquad (4.8)
$$

The mass eigenvalues of the physical states N_1 and N_2, for small $\sin\theta$ ($\sin\theta \to 0$) limit, can be expressed as:

$$
\begin{aligned}
m_{N_1} &\simeq m_{\chi_1} + \frac{Y_1 v}{\sqrt{2}}\sin 2\theta \equiv m_{\chi_1} - \frac{(Y_1 v)^2}{(m_N - m_{\chi_1})}, \\
m_{N_2} &\simeq m_N - \frac{Y_1 v}{\sqrt{2}}\sin 2\theta \equiv m_N + \frac{(Y_1 v)^2}{(m_N - m_{\chi_1})}. \qquad (4.9)
\end{aligned}
$$

Here we have considered $Y_1 v/\sqrt{2} < m_{\chi_1} < m_N$. Hence $m_{N_1} < m_{N_2}$. Therefore N_1 becomes the stable DM candidate (with a small kinematic caveat as we discuss shortly). Using Eqn. 4.8, one can find:

$$
\begin{aligned}
Y_1 &= -\frac{\Delta m \sin 2\theta}{\sqrt{2}v}, \\
m_N &= m_{N_1}\sin^2\theta + m_{N_2}\cos^2\theta. \qquad (4.10)
\end{aligned}
$$

where $\Delta m = m_{N_2} - m_{N_1}$ is the mass difference between the two mass eigenstates and m_N is the mass of electrically charged component of vectorlike fermion doublet $N^{\mp}$. This serves as an important parameter for the phenomenology of the model as we illustrate. Note again that due to a different $\mathcal{Z}_2 \times \mathcal{Z}'_2$ charge, χ_2 do not mix with N and χ_1.

Vector like fermion DM has gauge interactions to SM due to the inclusion of doublet in the model. Expanding the covariant derivative in $\mathcal{L}^{VF}$, one can find:

$$
\begin{aligned}
\mathcal{L}^{VF}_{int} &= \overline{N}i\gamma^\mu(-ig\frac{\sigma^a}{2}W^a_\mu + i\frac{g'}{2}B_\mu)N \\
&= \left(\frac{e_0}{2\sin\theta_W\cos\theta_W}\right)\overline{N^0}\gamma^\mu Z_\mu N^0 + \frac{e_0}{\sqrt{2}\sin\theta_W}\overline{N^0}\gamma^\mu W^+_\mu N^- + \frac{e_0}{\sqrt{2}\sin\theta_W}N^+\gamma^\mu W^-_\mu N^0 \\
&\quad -e_0 N^+\gamma^\mu A_\mu N^- - \left(\frac{e_0}{2\sin\theta_W\cos\theta_W}\right)\cos 2\theta_W N^+\gamma^\mu Z_\mu N^- \qquad (4.11)
\end{aligned}
$$

where $g = e_0/\sin\theta_W$ and $g' = e_0/\cos\theta_W$ with e_0 being the electromagnetic coupling constant and θ_W being the Weinberg angle. One can therefore express the gauge and the Yukawa interactions of $\mathcal{L}^{VF}$ in mass basis of N_1 and N_2 as:

$$\begin{aligned}
\mathcal{L}_{int}^{VF} &= \Big(\frac{e_0}{2\sin\theta_W\cos\theta_W}\Big)\Big[\sin^2\theta\overline{N_1}\gamma^\mu Z_\mu N_1 + \cos^2\theta\overline{N_2}\gamma^\mu Z_\mu N_2 \\
&\qquad + \sin\theta\cos\theta(\overline{N_1}\gamma^\mu Z_\mu N_2 + \overline{N_2}\gamma^\mu Z_\mu N_1)\Big] \\
&+ \frac{e_0}{\sqrt{2}\sin\theta_W}\sin\theta\overline{N_1}\gamma^\mu W_\mu^+ N^- + \frac{e_0}{\sqrt{2}\sin\theta_W}\cos\theta\overline{N_2}\gamma^\mu W_\mu^+ N^- \\
&+ \frac{e_0}{\sqrt{2}\sin\theta_W}\sin\theta N^+\gamma^\mu W_\mu^- N_1 + \frac{e_0}{\sqrt{2}\sin\theta_W}\cos\theta N^+\gamma^\mu W_\mu^- N_2 \\
&- e_0 N^+\gamma^\mu A_\mu N^- - \Big(\frac{e_0}{2\sin\theta_W\cos\theta_W}\Big)\cos 2\theta_W N^+\gamma^\mu Z_\mu N^- \\
&- \frac{Y_1}{\sqrt{2}}h\Big[\sin 2\theta(\overline{N_1}N_1 - \overline{N_2}N_2) + \cos 2\theta(\overline{N_1}N_2 + \overline{N_2}N_1)\Big]
\end{aligned} \tag{4.12}$$

Let us now focus into the other Yukawa interaction between different DM particles as introduced in $\mathcal{L}^{VF+Scalar}$ (Eqn. 4.5). In the physical basis it reads:

$$\mathcal{L}_{int}^{VF+Scalar} = -Y_2(\cos\theta\overline{N_1}\chi_2 S - \sin\theta\overline{N_2}\chi_2 S + \cos\theta\overline{\chi_2}N_1 S - \sin\theta\overline{\chi_2}N_2 S). \tag{4.13}$$

The scalar field S do not acquire any vev and thus retains the $\mathcal{Z}_2 \times \mathcal{Z}'_2$ symmetry intact and is eligible as a possible DM candidate of the model. The interaction terms involving S of $\mathcal{L}^{Scalar}$ after EWSB turns out to be:

$$\mathcal{L}_{int}^{Scalar} = -\frac{\lambda_{SH}v}{2}hS^2 - \frac{\lambda_{SH}}{4}h^2S^2. \tag{4.14}$$

Following $\mathcal{L}^{Scalar}$ (Eqn. 4.4), the full scalar potential including SM Higgs can be written as:

$$V(H,S) = -{\mu_H}^2(H^\dagger H) + \lambda_H(H^\dagger H)^2 + \frac{1}{2}m_S^2S^2 + \frac{\lambda_S}{4!}S^4 + \frac{\lambda_{SH}}{2}\Big(H^\dagger H - \frac{v^2}{2}\Big)S^2. \tag{4.15}$$

It is important now to identify the key parameters of the model which control relevant phenomenology of the model. Mainly six independent parameters do the job including two DM masses, mass of the mediator, mixing angle of singlet-doublet fermion, Yukawa coupling denoting DM-DM interactions and the Higgs portal coupling of the scalar DM:

$$\{\, m_{N_1},\ \Delta m,\ m_S,\ m_{\chi_2},\ \sin\theta,\ \lambda_{SH}\} \tag{4.16}$$

4.2.1 Constraints on the model parameters

Before evaluating the constraints on the model parameters given in Eqn. 4.16, from DM and collider analysis, we would like to go through the constraints coming from stability of the potential, perturbativity of the parameters and invisible decay widths of Z and H to determine the broad parameter space available for our numerical scan.

- **Stability of potential**: For the tree-level vacuum stability of the scalar potential as in Eqn. (4.15), one requires to satisfy the following co-positivity conditions [76]:

$$\lambda_H \geq 0, \quad \lambda_S \geq 0, \quad \text{and} \quad \lambda_{\rm SH} + \sqrt{\frac{2}{3}\lambda_{\rm H}\,\lambda_{\rm S}} \geq 0\ . \tag{4.17}$$

  This essentially means, we satisfy the constraints if we assume $\lambda_H, \lambda_S, \lambda_{SH} \geq 0$ throughout the scan.

- **Perturbativity**: The upper limit of perturbativity bound on quartic and Yukawa couplings of the model are given by,

$$\begin{aligned} |\lambda_S|,\ |\lambda_{SH}| &< 4\pi, \\ \text{and} \quad |{\rm Y}_1|,\ |{\rm Y}_2| &< \sqrt{4\pi}\ . \end{aligned} \tag{4.18}$$

- **Invisible decay width of Higgs** : When masses of DMs are smaller than the Higgs mass i.e. $m_{DM} < m_h/2$, then Higgs can decay to DM (invisible particles) and will contribute to invisible decay width. LHC data puts strong constraint on the invisible branching fraction of Higgs as $Br(h \to inv) < 0.24$ [102]. This can be interpreted as follows:

$$\begin{aligned} Br(h \to inv.) &< 0.24 \\ \frac{\Gamma(h \to inv.)}{\Gamma(h \to SM) + \Gamma(h \to inv.)} &< 0.24, \end{aligned} \tag{4.19}$$

  where $\Gamma(h \to SM) = 4.2$ MeV for SM Higgs (with mass $m_h = 125.09$ GeV) is measured at LHC [102]. This then yields,

$$\Gamma(h \to inv.) < 1.32 \ \ \text{MeV}\ . \tag{4.20}$$

  In our two component DM scenario, the invisible decay may have two contributions if both $m_{N_1},\ m_S < m_h/2$:

$$\Gamma(h \to inv.) = \Gamma(h \to \overline{N_1} N_1) + \Gamma(h \to S\ S). \tag{4.21}$$

  The decay width of Higgs to S and $\rm N_1$ can easily be calculated as:

$$\begin{aligned} \Gamma_{h \to S\ S} &= \frac{\lambda_{SH}^2 v^2}{32\pi m_h^2}\sqrt{m_h^2 - 4m_S^2}\ \ \Theta(m_h - 2m_S), \\ \Gamma_{h \to \overline{N_1} N_1} &= \frac{1}{16\pi}\Big(Y_1 \sin 2\theta\Big)^2 m_h\ \ \Big(1 - \frac{4m_{N_1}^2}{m_h^2}\Big)^{\frac{3}{2}}\ \ \Theta(m_h - 2m_{N_1}). \end{aligned} \tag{4.22}$$

  Invisible Higgs decay constraint from Eq. 4.20 together with Eq. 4.21 and Eq. 4.22 is shown in Fig. 4.2. In top left panel of Fig. 4.2, the constraint is shown in $m_S - \lambda_{SH}$ plane. Here, the green region is allowed from Higgs invisible decay while grey region excluded for a fixed $\sin\theta = 0.01$. The allowed (or excluded)

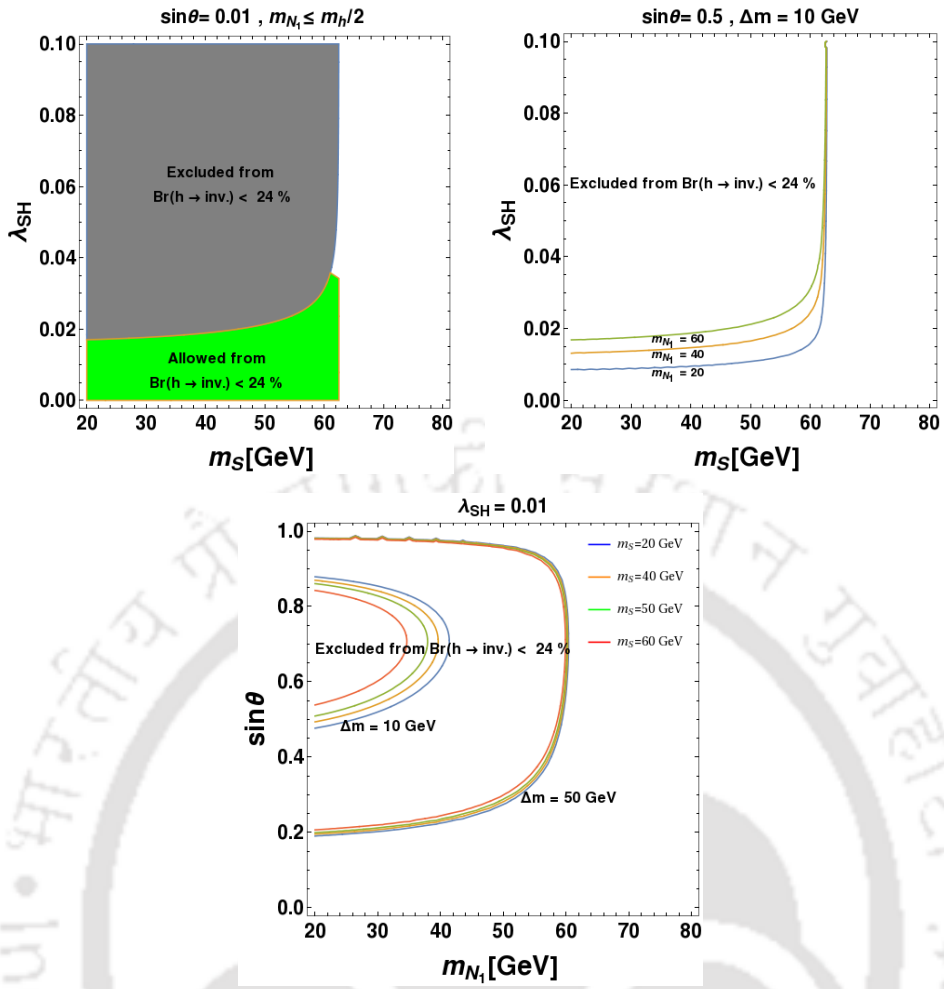

Figure 4.2: Constraints on scalar and fermion DM from Higgs invisible branching ratio $Br(h \to inv.) < 0.24$ [102] in $m_S - \lambda_{SH}$ plane (top panel) and $m_{N_1} - \sin\theta$ plane (bottom panel) keeping other parameter fixed (mentioned in the figure inset).

region remains almost unchanged for any fermion DM mass ($m_{N_1} < m_h/2$) and Δm for the small $\sin\theta$ due to negligible contribution of $\Gamma(h \to \overline{N_1} N_1)$. In the top right panel we consider larger mixing angle, $\sin\theta = 0.5$. As the contribution the contribution of $\Gamma(h \to \overline{N_1} N_1)$ plays a important role to $\Gamma(h \to inv.)$. And therefore, choices of other parameters like $m_{N_1}, \Delta m$ becomes relevant. The inner region of each contour in $m_S - \lambda_{SH}$ plane (top right panel) is excluded from Higgs invisible decay constraint [102]. Note here however that such large $\sin\theta (= 0.5)$ is disfavoured from direct search bounds [103, 104]. In the bottom panel we have shown excluded region in $m_{N_1} - \sin\theta$ plane keeping other parameters, m_S, λ_{SH} and Δm fixed. Similarly here the inner region of each contour line (which corresponds to different fixed values of Δm and scalar DM mass (m_S), depicted in the figure) is excluded from Higgs invisible decay [102].

- **Invisible decay width of Z** : As the fermion DM has a doublet component in it, it has Z mediated interaction. Hence, if fermion DM mass is below $m_Z/2$, then Z can invisibly decay to dark particles. From current observation, invisible decay width of Z is strongly constrained. The upper limit of invisible Z decay

width is following [102]:

$$\Gamma(Z \to inv.) \leq 499.0 \pm 1.5 \quad \text{MeV}, \tag{4.23}$$

where in our model,

$$\begin{aligned}\Gamma(Z \to inv.) &= \Gamma(Z \to \overline{N_1} N_1) \\ &= \frac{1}{48\pi}\Big(\frac{g\ \sin^2\theta}{\cos\theta_W}\Big)^2 m_Z \ \Big(1+\frac{2m_{N_1}^2}{m_Z^2}\Big)\sqrt{1-\frac{4m_{N_1}^2}{m_Z^2}}\ \Theta(m_Z - 2m_{N_1})\ .\end{aligned} \tag{4.24}$$

Invisible decay of Z mainly depend on mixing angle $\sin\theta$. Choice of small mixing angle, with $\sin\theta < 0.1$ is preferable from direct search bound in which all fermion DM mass $m_{N_1} < m_Z/2$ is allowed from invisible decay width of Z [23]. We note that as the scalar DM component is a gauge singlet, it doesn't have a Z mediated interaction and therefore no constraint from invisible Z decay applies to it.

4.2.2 Possible multipartite DM scenarios

We have four electromagnetic charge neutral particles in the model: N^0, χ_1, χ_2 and S. Given the same charge of N^0 and χ_1 under $\mathcal{Z}_2 \times \mathcal{Z}_2'$, they mix and the lighter eigenstate N_1 (with $m_{N_1} < m_{N_2}$) can not decay to SM, while N_2 decays to N_1. Then, we are left with three possible DM candidates, i.e. N_1, χ_2 and S. However, the absolute stability will be dictated by other Yukawa coupling present in dark sector $Y_2\overline{\chi_1}\chi_2 S \to Y_2\overline{N_1}\chi_2 S$ (as in Eqn. 4.13). Evidently, if one of the physical states is heavier than the other two, then it can decay to the other two lighter particles and become unstable. As a result, the two lighter physical states will be the viable DM candidates. Therefore, depending on the mass hierarchy, the model offers four different types of multipartite DM scenarios as illustrated in Fig. 4.3.

- Type-I : $m_{\chi_2} > m_{N_1} + m_S$: N_1 and S are the stable DM components.
- Type-II: $m_S > m_{N_1} + m_{\chi_2}$: N_1 and χ_2 are stable DM components.
- Type-III: $m_{N_1} > m_S + m_{\chi_2}$: S and χ_2 are stable DM components.
- Type-IV: If $m_{\chi_2} < m_{N_1} + m_S$, $m_S < m_{N_1} + m_{\chi_2}$ and $m_{N_1} < m_S + m_{\chi_2}$, then all three particles N_1, χ_2 and S are stable and will yield a three-component DM scenario.

In this paper, we focus mostly on Type-I scenario (green region in Fig. 4.3). This gives us an opportunity to compare with the single component cases of the corresponding DM components (N_1 and S), which are very well studied, and indicate the effects of DM-DM conversion employed in this set-up.

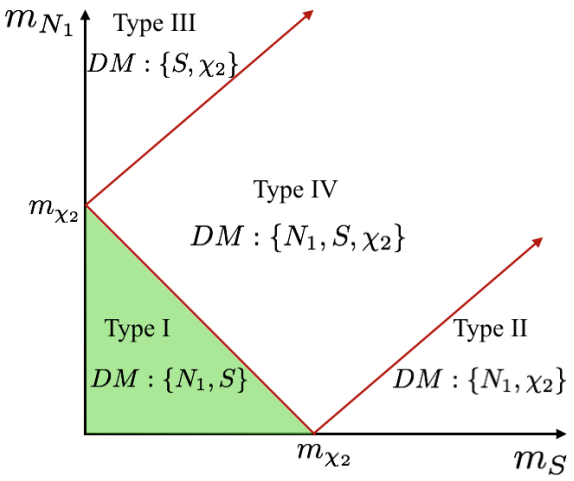

Figure 4.3: Different types of multicomponent DM scenarios that can be realised in the model depicted in $m_{N_1} - m_S$ plane, given that a hierarchy among m_{N_1}, m_S, m_{χ_2}. Type-I scenario (coloured in green) is analysed in this paper.

4.3 Review of single component DM frameworks with N_1 and S

Before we discuss the two component DM set up (of Type-I) as advocated above, we need to know the fate of the individual DMs in single component frameworks. We review relic density and direct search allowed parameter space for both vectorlike fermion DM (N_1) and singlet scalar DM (S) in the next two consecutive subsections.

4.3.1 Single component fermion DM (N_1)

The presence of vector-like fermion singlet (χ_1) and a doublet (N) can give rise to a fermion DM [96], where both transform under a $\mathcal{Z}_2$ symmetry. The relevant Lagrangian is still given by $\mathcal{L}^{VF}$ as in Eq. 4.3. As described above, the singlet and the neutral component of the doublet mix after EWSB, and the lightest component of the neutral physical states N_1 becomes a stable single component DM.

We note here that the freeze-out abundance of N_1 DM is controlled by the annihilation and co-annihilation channels as detailed in Appendix C (Fig. C.1, C.2 and C.3). Therefore, the important parameters which decide the relic abundance of N_1 are

$$\{m_{N_1},\ \Delta m,\ \sin\theta\}.$$

Due to singlet-doublet mixing, the DM in direct search experiments can scatter off the target nucleus via both Z and Higgs mediated processes (shown in top pannel of Fig. 4.10).

The relic density and direct search allowed parameter space for N_1 DM is shown in Fig. 4.4. This is shown in $m_{N_1} - \Delta m$ plane for small values of $\sin\theta$. It has already been noted [96] that due to Z mediation, $\sin\theta$ is limited to very small values $\lesssim 0.1$ by the non-observation of DM in direct search experiments. We therefore choose only such small mixing regions for illustration in Fig. 4.4. Essentially, the whole relic density allowed plane is also allowed by direct search constraints (XENON1T [104], XENON

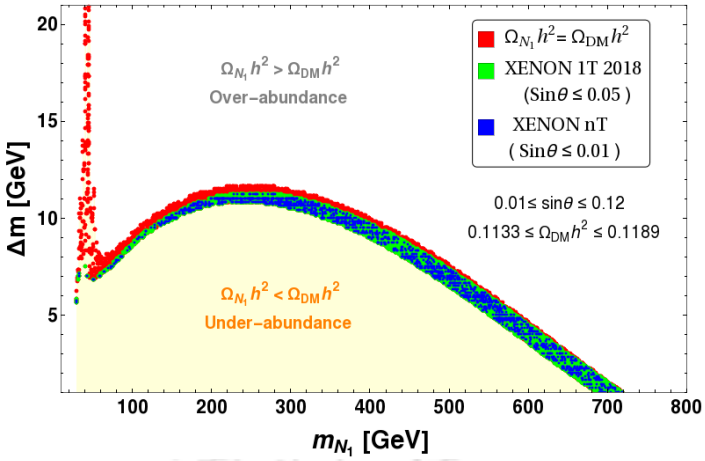

Figure 4.4: Relic density allowed (red points) and direct detection {XENON 1T (green region), XENON nT (blue points)} allowed parameter space for single component fermion DM (N_1) is shown in $m_{N_1} - \Delta m$ plane. Under abundance ($\Omega_{N_1}h^2 < \Omega_{DM}h^2$) (yellow region below the red patch) and over-abundance ($\Omega_{N_1}h^2 > \Omega_{DM}h^2$) (the region above the red patch) are also shown for reference.

nT [105] as shown in the Fig. 4.4). The under and over abundant regions are also indicated, which will be more useful for discussing the two component framework. The important message from this graph is that for small $\sin\theta$, Δm has to be small ($\lesssim 12$ GeV) to satisfy relic density, except for those low DM mass resonance regions ($\sim m_Z/2,\ m_h/2$). For under abundance, the DM has to obtain even higher annihilation cross-section. For small $\sin\theta$ to satisfy direct search, the only way to probe under abundant regions is to have even smaller Δm to enhance co-annihilation effects. Therefore, when we embed the fermion DM in a non-interacting two component DM framework, the under abundant regions (as indicated in Fig. 4.4) are going to be allowed. However, the situation alters in presence of an interacting two-component framework as we will demonstrate in Section 4.4.

4.3.2 Single component scalar DM (S)

The Lagrangian $\mathcal{L}^{Scalar}$ in Eqn. 4.4, describes the case of single component scalar DM S. The relevant parameters describing the scalar DM interaction with SM is given by

$$\{m_S, \lambda_{SH}\}.$$

The annihilation process which controls the freeze-out of S are shown in Fig. 4.5.

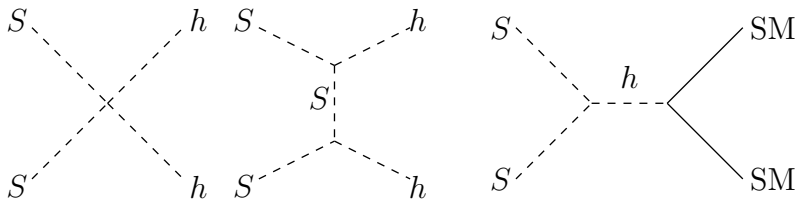

Figure 4.5: Feynman diagrams of Scalar DM S annihilation to SM particles i.e $S\ S \to \text{SM}\ \ \text{SM}$.

The relic density allowed parameter space for the scalar DM is well studied [22, 23, 67, 94, 95] and is summarised in Fig. 4.6, in terms of DM mass (m_S) and Higgs

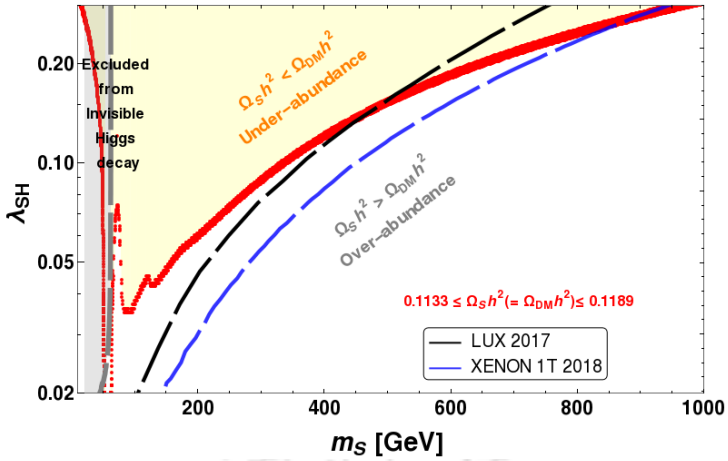

Figure 4.6: Relic density allowed ($\Omega_S h^2 = \Omega_{DM} h^2$) (red region) parameter space for scalar DM (S) is shown in $m_S - \lambda_{SH}$ plane. LUX [103] (black dashed) and XENON 1T [104] (blue dashed) exclusion limits are also shown. The region 'above' the red patch (in yellow) corresponds to under abundance ($\Omega_S h^2 < \Omega_{DM} h^2$) and the one below corresponds to over abundance ($\Omega_S h^2 > \Omega_{DM} h^2$). Exclusion limit from invisible Higgs decays is shown by grey region.

portal coupling (λ_{SH}). Direct search sensitivities of LUX [103] and XENON 1T [104] from null detection are also shown in the same graph for S which only has a t-channel Higgs mediation with nucleus (shown in bottom pannel of Fig. 4.10). This essentially shows that if S contributes to the full DM relic density, it lives either in resonance region ($m_S \sim m_h/2$) or in high DM mass regions ($m_S \gtrsim 900$ GeV) to satisfy null observations from direct search experiments. Under abundance for S can only be achieved with larger annihilation cross-section, that can only occur with larger Higgs portal coupling (λ_{SH}) and that is even more constrained from direct search data. If the scalar DM is embedded in an non-interacting multi-component DM framework, it is further restricted by direct search, discarding m_S upto TeV or more. We will show in Section 4.4, that the situation alters in presence of an additional DM component, with which the scalar DM has non-negligible interactions. We also point out that the presence of a heavy scalar S_H (also a SM singlet) having same $\mathcal{Z}_2$ charge as of S, can change the conclusion significantly allowing a larger parameter space through co-annihilation (in Section 4.5).

4.4 Two Component DM with N_1 and S

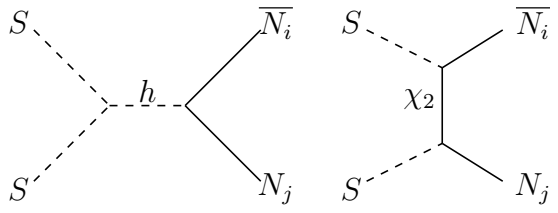

Figure 4.7: Diagrams contributing to DM-DM conversion ($i = 1, 2$) between fermion (N_i) and scalar DM (S) components.

As already discussed in Section 4.2.2, we choose Type-I case for illustrating a two-

component interacting DM model with $m_{\chi_2} > m_{N_1} + m_S$, where N_1 froms a vectorlike fermion DM component and S forms a scalar DM component. The heaviest field χ_2 in the dark sector, which can decay to N_1 and S, act as a mediator between the two DM components through the Yukawa interaction: $Y_2\overline{\chi_2}\chi_1 S$. These DMs can also interact with each other through Higgs portal couplings: $Y_1\overline{N}\widetilde{H}\chi_1$ and $\lambda_{SH}(H^\dagger H)S^2$. The DM-DM interactions of this model is shown by the Feynman diagrams in Fig. 4.7. DM-DM conversion diagrams will dominantly help the heavier DM component to annihilate into the lighter one and therefore contribute to its thermal freeze-out and relic density. Apart from DM masses and mediator mass (m_{χ_2}), the DM-DM conversion is a function of the following couplings

$$\{Y_1, Y_2, \lambda_{SH}\}.$$

However, the Higgs portal couplings Y_1 (as a function of Δm and $\sin\theta$, see in Eqn. 4.10) and λ_{SH} are strongly constrained from direct detection bound (already discussed in section 4.3). Therefore, DM-DM interaction through Higgs mediation will be negligible in relic density and direct search allowed parameter space of the two component model and can be identified with $Y_2 = 0$ situation. We will show that in such a case, the two DMs are almost decoupled and behave like single component cases to occupy the under abundant regions of their corresponding DM parameter space. Here lies the importance of assuming the presence of a heavy mediator χ_2 in this model to carry out DM-DM interactions through Yukawa coupling Y_2.

4.4.1 Coupled Boltzmann Equations

The thermal freeze-out of two component DM framework is described by a coupled Boltzmann equations (BEQs) and can be written as a function of reduced x, where $x = \mu/T$, with $\frac{1}{\mu} = \frac{1}{m_{N_1}} + \frac{1}{m_{N_2}} + \frac{1}{m_S}$ [23, 34, 54]. The one here reads:

$$\begin{aligned}
\frac{dY_{N_i}}{dx} &= -0.264 M_{Pl}\sqrt{g_*}\frac{\mu}{x^2}\Bigg[\sum_j \Bigg\{\langle\sigma v_{\overline{N_i}N_j\to SM}\rangle\Big(Y_{N_i}Y_{N_j} - Y_{N_i}^{EQ}Y_{N_j}^{EQ}\Big) \\
&\quad + \langle\sigma v_{\overline{N_i}N_j\to SS}\rangle\Big(Y_{N_i}Y_{N_j} - \frac{Y_{N_i}^{EQ}Y_{N_j}^{EQ}}{Y_S^{EQ^2}}Y_S^2\Big)\Theta(m_{N_i}+m_{N_j}-2m_S) \\
&\quad - \langle\sigma v_{SS\to\overline{N_i}N_j}\rangle\Big(Y_S^2 - \frac{Y_S^{EQ^2}}{Y_{N_i}^{EQ}Y_{N_j}^{EQ}}Y_{N_i}Y_{N_j}\Big)\Theta(2m_S - m_{N_i} - m_{N_j})\Bigg\} \\
&\quad + \langle\sigma v_{\overline{N_i}N^\pm\to SM}\rangle\Big(Y_{N_i}Y_{N^\pm} - Y_{N_i}^{EQ}Y_{N^\pm}^{EQ}\Big)\Bigg], \\
\frac{dY_S}{dx} &= -0.264 M_{Pl}\sqrt{g_*}\frac{\mu}{x^2}\Bigg[\langle\sigma v_{SS\to SM}\rangle\Big({Y_S}^2 - Y_S^{EQ^2}\Big) \\
&\quad + \sum_{i,j}\Bigg\{ - \langle\sigma v_{\overline{N_i}N_j\to SS}\rangle\Big(Y_{N_i}Y_{N_j} - \frac{Y_{N_i}^{EQ}Y_{N_j}^{EQ}}{Y_S^{EQ^2}}Y_S^2\Big)\Theta(m_{N_i}+m_{N_j}-2m_S) \\
&\quad + \langle\sigma v_{SS\to\overline{N_i}N_j}\rangle\Big(Y_S^2 - \frac{Y_S^{EQ^2}}{Y_{N_i}^{EQ}Y_{N_j}^{EQ}}Y_{N_i}Y_{N_j}\Big)\Theta(2m_S - m_{N_i} - m_{N_j})\Bigg],
\end{aligned} \tag{4.25}$$

where the subscripts $i, j = 1, 2$ describes the fermion DM and the heavy neutral fermion component of the model respectively. In the above equations, we note that

the annihilation contribution of N_i to S or otherwise depending on the mass hierarchy is included. The equilibrium distributions now recast in terms of μ takes the form:

$$Y_{N_i}^{EQ}(x) = 0.145\frac{g}{g_*}x^{\frac{3}{2}}\left(\frac{m_i}{\mu}\right)^{\frac{3}{2}}e^{-x\left(\frac{m_i}{\mu}\right)}$$
$$Y_S^{EQ}(x) = 0.145\frac{g}{g_*}x^{\frac{3}{2}}\left(\frac{m_S}{\mu}\right)^{\frac{3}{2}}e^{-x\left(\frac{m_S}{\mu}\right)} \tag{4.26}$$

The relic density allowed parameter space of the two-component framework is then given by the solution of the above Boltzmann equations, that determine the freeze-out of the individual components depending on annihilations plus co-annihilations and DM-DM interactions. Obviously, total DM relic density for the two component case will be the sum of individual relic density as:

$$\Omega_T h^2 = \Omega_{N_1} h^2 + \Omega_S h^2, \tag{4.27}$$

which should satisfy combined WMAP and PLANCK limit $0.1133 \leq \Omega_T h^2\ (= \Omega_{DM} h^2) \leq 0.1189$ [11]. Individual relic density in interacting multipartite DM case can be found out by numerical solution to the coupled Boltzmann equations or approximate analytical solution of coupled BEQ [23] and that of the i-th DM candidate is given by:

$$\Omega_i h^2 = \frac{854.45 \times 10^{-13}}{\sqrt{g_*}} \frac{x_f^i}{\langle\sigma v\rangle_i^T}, \tag{4.28}$$

where $\langle\sigma v\rangle_i^T$ is the total effective annihilation cross-section and x_f^i corresponds to freeze-out temperature of the ith DM component. Note however, for the ease of the analysis, we are not using the approximate solution here; relic density and direct search cross-sections for both the DM components are obtained numerically by inserting the model in `MicrOmegas` package [84].

If fermion DM is heavier than scalar DM ($m_{N_1} > m_S$), then heavier DM component (N_1) can annihilate to lighter component (S) following processes as in Fig. 4.7. Such DM-DM conversion affects the freeze out of heavier DM component and hence its relic density [23]. The lighter DM candidate on the other hand, have no new channel to deplete its number density and behave almost like single component DM. Then $\langle\sigma v\rangle_{N_1}^T$ for fermionic DM assuming $m_{N_1} > m_S$ will be given by:

$$\langle\sigma v\rangle_{N_1}^T \simeq \langle\sigma v\rangle_{N_1}^{eff} + \langle\sigma v\rangle_{\bar{N}_1 N_1 \to SS} + 2\langle\sigma v\rangle_{\bar{N}_1 N_2 \to SS}(1+\frac{\Delta m}{m_{N_1}})^{3/2} e^{\frac{-\Delta m}{T}}, \tag{4.29}$$

where $\langle\sigma v\rangle_{N_1}^{eff}$ is the annihilation plus co-annihilation cross-section of fermion DM to SM given by Eq. C.1. The last term in the above equation represents co-annihilation to scalar DM component and is therefore aided by the Boltzmann factor along with a symmetry factor of 2 (assuming $m_{N_1} \simeq m_{N_2}$). In this limit of $m_{N_1} > m_S$, the annihilation cross-section for scalar DM (S) only captures the annihilations to SM as in a single component framework:

$$\langle\sigma v\rangle_S^T = \langle\sigma v\rangle_{SS\to SM\ SM}\ . \tag{4.30}$$

Evidently, for the opposite hierarchy, $m_S > m_{N_1}$:

$$\begin{aligned}\langle\sigma v\rangle_{N_1}^T &= \langle\sigma v\rangle_{N_1}^{eff},\\ \langle\sigma v\rangle_S^T &= \langle\sigma v\rangle_{SS\to SMSM} + \langle\sigma v\rangle_{SS\to\overline{N_i}N_j}.\end{aligned} \tag{4.31}$$

We would like to again remind here that the parameter space scan performed in the subsequent analysis does not use above approximate solutions to the coupled BEQs. However, the relic density of the individual DM components depend very much on this basic idea of DM-DM conversion advocated above.

4.4.2 Relic density and direct search outcome

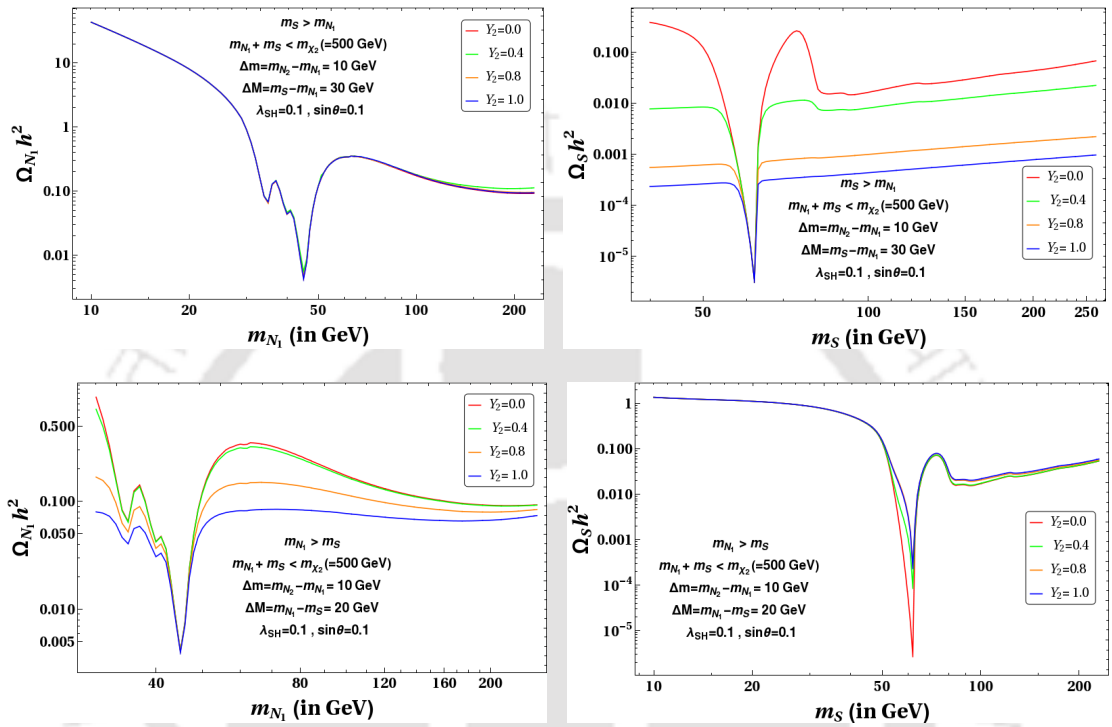

Figure 4.8: Relic densities ($\Omega_{N_1} h^2$ and $\Omega_S h^2$) of the individual components as a function of respective DM masses (m_{N_1} and m_s). Two possible mass hierarchies are shown: $m_S > m_{N_1}$ (top panel) and $m_{N_1} > m_S$ (bottom panel). Different values of $Y_2 = 0.0$ (red) , 0.4 (green) , 0.8 (orange) , 1.0 (blue) are chosen keeping other parameters fixed (as mentioned in the plots) to decipher DM-DM interactions.

We first study the variation of individual relic densities with corresponding DM masses as shown in Fig. 4.8. Two possible mass hierarchies are shown; in top we choose $m_S > m_{N_1}$ and in the bottom panel we have $m_S < m_{N_1}$. Relic density of fermion DM (N_1) is shown in the left panel and that of the scalar (S) is shown in the right panel. We see that for $m_S > m_{N_1}$ (top left panel of Fig. 4.8), $\Omega_{N_1} h^2$ do not change with different choices of Yukawa coupling Y_2. However with same hierarchy ($m_S > m_{N_1}$) for S, relic density is steadily reduced with larger choice of Y_2 (top right panel). It is exactly the other way round, when we have $m_S < m_{N_1}$ (bottom panel of Fig. 4.8). In such a case, relic density for N_1 decreases with larger Y_2, while it remains unaltered for S. This follows from the analytic solution of the effective annihilation cross sections as mentioned in Eqs. 4.29, 4.30, 4.31 showing the importance of DM-DM conversion. In this plot we have kept other parameters fixed as mentioned in the plot, particularly with a moderate value of the mediator mass fixed at $m_{\chi_2} = 500$ GeV.

The sensitivity of individual relic densities to DM-DM conversion as a function of mediator mass (m_{χ_2}) is shown in Fig. 4.9. Evidently, we demonstrate it for the heavier component (N_1 on the left and S on the right) with different choices of mediator masses:

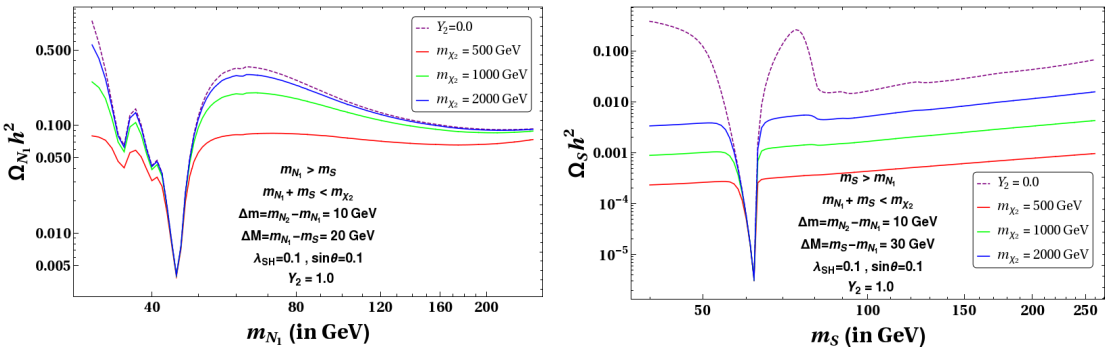

Figure 4.9: Sensitivity of mediator mass (m_{χ_2}) to DM-DM conversion and that to relic density of the heavier component is demonstrated. [Left] $\Omega_{N_1}h^2$ as a function of m_{N_1} for different values of $m_{\chi_2} = 500$ (red) , 1000 (green) , 2000 GeV (blue) assuming $m_{N_1} > m_S$. [Right] $\Omega_S h^2$ as a function of m_S for $m_S > m_{N_1}$. Other parameters kept fixed at different values are mentioned in the plot along with $Y_2 = 1.0$ and $\lambda_{SH} = 0.1$. Purple dotted line in both graphs correspond to $Y_2 = 0$ case, shown for comparison.

m_{χ_2}: 500 (red), 1000 (green) and 2000 (blue) GeV, keeping $Y_2 = 1.0$ and $\lambda_{SH} = 0.1$ fixed. In the same Fig. 4.9, we have also demonstrated the case of $Y_2 = 0$ (purple dotted line), when χ_2 does not take part in the DM-DM conversions. It is evident that with large m_{χ_2}, DM-DM conversion becomes feeble and closely resembles $Y_2 = 0$ (purple dotted line) case. Therefore, large Yukawa Y_2 can play an important role in relic density, but with not-so-heavy mediator mass (m_{χ_2}). The lighter DM component is again mostly unaffected by DM-DM conversion as has already been discussed. One important point to note is the difference between $Y_2 = 1.0$ and $\lambda_{SH} = 0.1$ chosen for illustration. This is because Y_2 remains unconstrained (excepting for large perturbative limit $\leq \sqrt{4\pi}$), while λ_{SH} is highly restricted by direct search (recall Fig. 4.6). We can also see that $m_{\chi_2} = 2$ TeV closely mimic $Y_2 = 0$ case for fermion DM, while it does not completely do so for Ω_S. This is because of very small annihilation cross-section of the scalar DM to SM compared to DM-DM conversion due to the choice of small λ_{SH}.

Let us now turn to direct search constraints of this two component DM set up. Feynman graphs for direct search contribution of the DM components are shown in Fig. 4.10. Fermion DM (N_1) has both Z and Higgs mediated interaction, while the scalar (S) interacts only through Higgs mediation. Direct search cross-sections for individual components are well known; however in two-component set up, the direct search cross-section for each component is folded by their fraction of relic density as[2]:

$$\sigma^{SI}_{eff}(S) = \left(\frac{\Omega_S h^2}{\Omega_T h^2}\right)\sigma^{SI}_S, \tag{4.32}$$

and

$$\sigma^{SI}_{eff}(N_1) = \left(\frac{\Omega_{N_1} h^2}{\Omega_T h^2}\right)\sigma^{SI}_{N_1}. \tag{4.33}$$

Spin independent direct search cross-sections for both DM components (σ^{SI}_S and $\sigma^{SI}_{N_1}$) are obtained from inserting the model into the code `MicrOmegas` [84]. No signal

[2]The actual limit from direct search on multipartite DM scenarios need to account for mass sensitivity on the nuclear recoil, the details can be found here [23, 54].

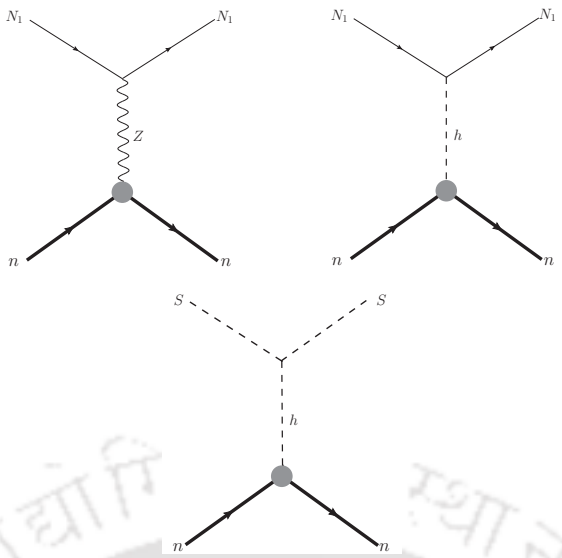

Figure 4.10: Feynman diagrams of spin independent (SI) direct detection of fermion DM (top panel) and scalar DM (bottom panel).

for DM in direct search experiments like LUX [103], XENON 1T [104] so far put a strong constraint on the WIMP-like DM scenarios as we have here. Recall that scalar DM lives only in the high mass region (≥ 900 GeV) except for resonance ($\sim m_h/2$) and fermion DM lives in $\sin\theta \leq 0.1$ region with a small Δm in their single component set up. The question is how much the above conclusions get relaxed in a two component set up with large DM-DM conversion as adopted here.

Case I: Feeble DM-DM interactions with $Y_2 = 0$

Let us now turn to relic density ($0.1133 \leq \Omega_T h^2 \leq 0.1189$) and SI direct search allowed parameter space of this two component model. We will first study the case for negligible DM-DM interactions with $Y_2 = 0$. The results are summarised in Fig. 4.11. We show the relic density allowed parameter space in upper panel, in the left for N_1 and in the right for S. With $Y_2 = 0$, the two DM-components behave as if they are decoupled and the allowed parameter space only opens up in the under-abundant regions of those individual DMs (compare the single component cases as demonstrated before in Fig. 4.4 and Fig. 4.6). Different colour codes indicate the percentage of the individual DM density as indicated in the figure inset. It is understood that given a certain percentage of one DM, rest of DM relic density is composed of the other component. So any combination is essentially possible by relic density constraint. In the bottom panel of Fig. 4.11, we show the allowed parameter space after direct search constraints from PANDA where both DMs simaltaneously satisfy direct seach bound from PANDA [46]. Note here that there are no parameter space where effective DD cross-section (in Eqs. 4.32, 4.33) of both N_1 and S DM simaltaneously goes beyond recent XENON-1T limit [105]. For fermion DM, direct search allowed parameter space spans the whole of under-abundant parameter space as it doesn't constrain the small Δm region further with small singlet-doublet mixing $\sin\theta \leq 0.05$, as we have chosen for the scan. We have already explained that for fermion DM, direct search crucially controls $\sin\theta$ only, which is well below the required cut-off. On the other hand, scalar DM is severely constrained by direct search constraint in $m_S - \lambda_{SH}$ plane, which leaves

Higgs resonance (not shown in the plot) and heavy Scalar DM mass region ($m_S \geq 900$ GeV) only. In the heavy scalar mass region, the relic density is $\gtrsim 80\%$, therefore allowing only a tiny fraction of fermion DM. The whole analysis at $Y_2 = 0$ also shows that the presence of s-channel Higgs mediated DM-DM interactions to be very feeble to alter the freeze-out of any of the DM component as mentioned earlier.

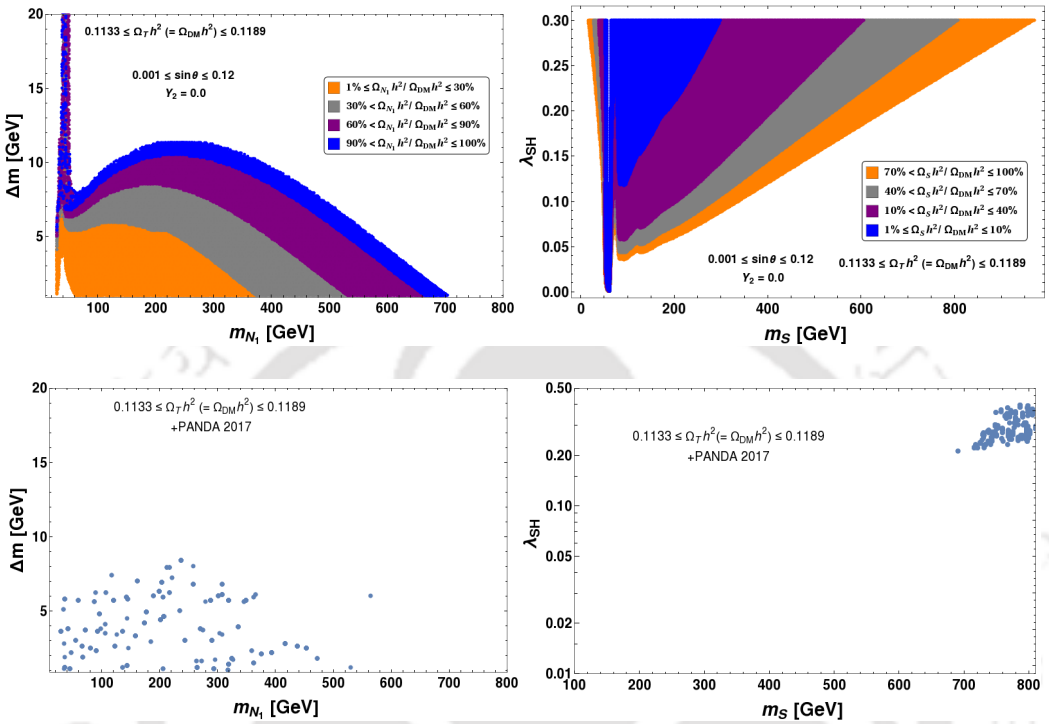

Figure 4.11: [Top Panel] Relic density allowed regions of two component DM scenario $\{N_1, S\}$ in $m_{N_1} - \Delta m$ (top left) and $m_S - \lambda_{SH}$ (top right) for $Y_2 = 0$. Different colour codes indicate the fraction of individual relic density $\frac{\Omega_i}{\Omega_T}$ varied in different ranges as mentioned in inset. [Bottom Panel] Relic density and direct detection (PANDA 2017 [46]) allowed parameter space in $m_{N_1} - \Delta m$ (bottom left) and $m_S - \lambda_{SH}$ (bottom right) planes.

Case II: The case of DM-DM interactions with $Y_2 \neq 0$

In Fig. 4.12, we show the relic density and direct search allowed parameter space of the model with a non-zero Yukawa coupling ($Y_2 \neq 0$, $0.1 \leq Y_2 \leq 1.6$). Relic density allowed parameter space is shown in the upper panel for N_1 (in $m_{N_1} - \Delta m$ plane) on left and for S (in $m_S - \lambda_{SH}$ plane) on right. Both possible mass hierarchies are studied and depicted; (i) $m_{N_1} > m_S$ by orange and (ii) $m_S > m_{N_1}$ by blue points. We see that when $m_S > m_{N_1}$, the whole $m_S - \lambda_{SH}$ parameter space is allowed (blue points in top right plot), where smaller λ_{SH} is substituted by larger Y_2 appropriately. On the other hand, N_1 DM has the fate of single component DM with under abundance adjusted to the other component when $m_S > m_{N_1}$ (blue points in top left plot). This is exactly the other way round, when we choose $m_S < m_{N_1}$; the whole $m_{N_1} - \Delta m$ plane becomes allowed (orange points in top left plot) and S has the fate of single component DM filling the under abundance region (orange points in top right plot). This is possible because of DM-DM conversion that we introduced in this model through the heavy

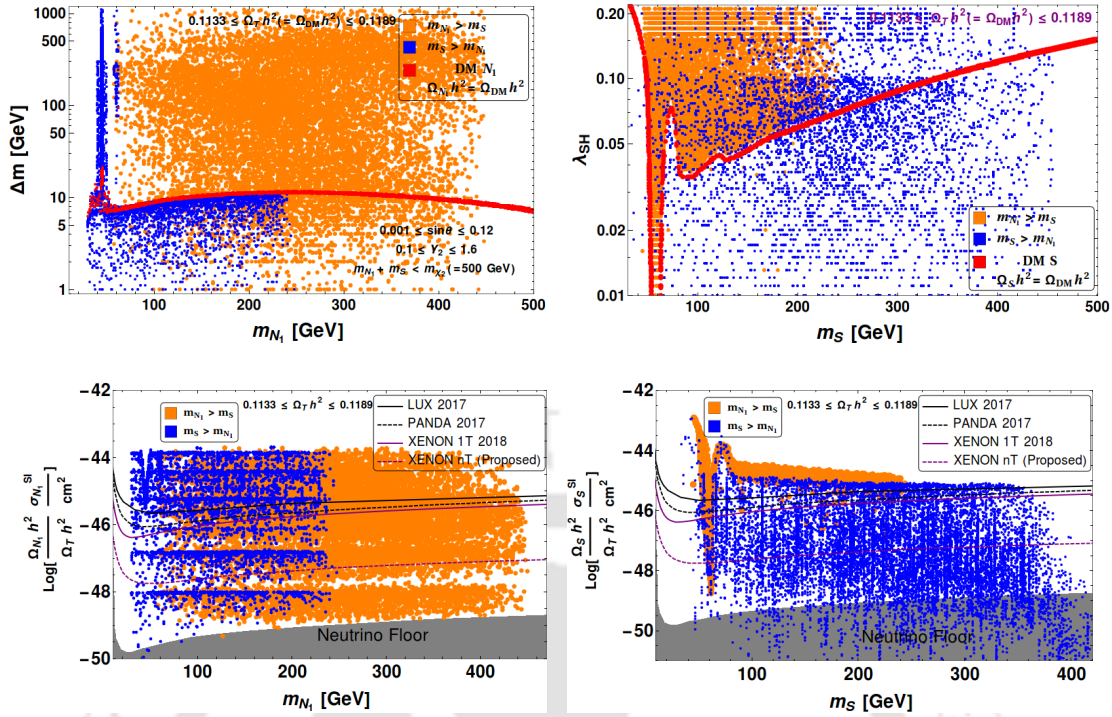

Figure 4.12: [Top Panel] Relic density allowed parameter space ($0.1133 \leq \Omega_T h^2 \leq 0.1189$) for two component DM model in $m_{N_1} - \Delta m$ (top left) and $m_S - \lambda_{SH}$ (top right) planes. Two mass hierarchies : $m_{N_1} > m_S$ (orange points) and $m_S > m_{N_1}$ (blue points) are shown in both plots. Red points depict the case of single component DM scenarios, for N_1 on the left and for S on the right panel. [Bottom Panel] Relic density allowed points are shown in DM mass vs effective SI DM-nucleon cross-section planes; $\left(\frac{\Omega_{N_1}h^2}{\Omega_T h^2}\right)\sigma^{SI}_{N_1} - m_{N_1}$ in bottom left and $\left(\frac{\Omega_S h^2}{\Omega_T h^2}\right)\sigma^{SI}_{S} - m_S$ in bottom right. Limits from different DD experiments, LUX [103](black solid line), recent PANDA [46] (black dashed), XENON 1T [104] (purple solid line) and predicted XENON nT [105] (purple dotted line) are also indicated in the figures. Shadded region correspond to Neutrino floor where DM signal cannot be distinguish from neutrino background.

mediator χ_2 with Y_2 Yukawa interaction. With $m_{N_1} > m_S$, the effective annihilation required for fermion DM to acquire required relic density ($\Omega_{N_1}h^2 < \Omega_{DM}h^2$) in small $\sin\theta$ region no longer depends on small Δm through co-annihilation because of additional annihilation channel to scalar DM. We will focus on this particular case for collider signatures of this model at the LHC. In the bottom panel of Fig. 4.12, we show the effective SI direct search cross-section for both DM components at relic density allowed points ($\Omega_i h^2 < \Omega_{DM}h^2$) for both the mass hierarchies. The limits from LUX [103], PANDA [46], XENON 1T [104] and XENON nT [105] are shown. The plots in the bottom panel point out to a larger available parameter space for the heavier DM component. This is simply due to freeze-out of the heavier component being governed by DM-DM conversion, not affecting direct search significantly. The scans in Fig. 4.12 are limited to DM mass within $\lesssim$ 500 GeV as it has been done for a mediator mass $m_{\chi_2} = 500$ GeV to satisfy $m_{N_1} + m_S < m_{\chi_2}$.

The outcome of relic density and direct search (XENON 1T limits [104] from the bottom panel of Fig. 4.12) constraints put together yield Fig. 4.13. The constraints on fermion DM in $m_{N_1} - \Delta m$ plane (left) is obviously less restrictive as we choose small $\sin\theta \lesssim 0.05$ for the scan, thus allowing the whole parameter space with upto

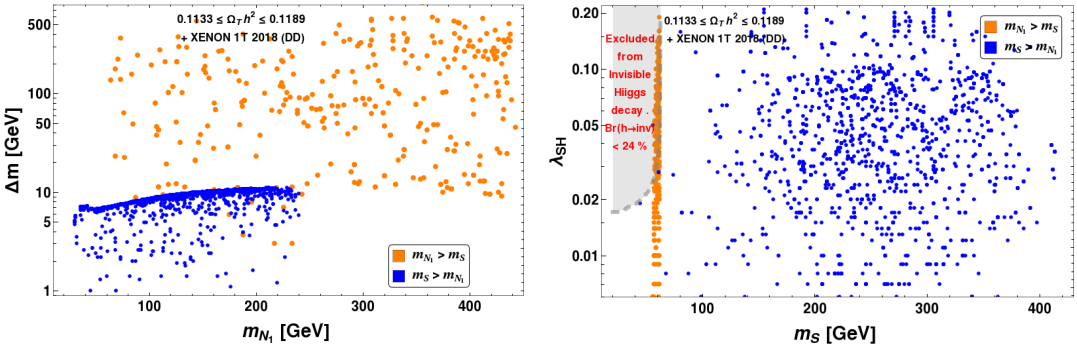

Figure 4.13: Relic density and direct search (XENON 1T data [104]) allowed parameter space is shown for both N_1 and S components in $m_{N_1} - \Delta m$ (left) and $m_S - \lambda_{SH}$ (right) plane. Two possible mass hierarchies: $m_{N_1} > m_S$ (orange points) and $m_S > m_{N_1}$ (blue points) are indicated in both planes. Invisible Higgs branching constraint is also shown in the right panel which discards a significant part of $m_S < m_h/2$ region.

$\Delta m \gtrsim 500$ or more for $m_{N_1} > m_S$ (orange points in left plot) thanks to conversion to the scalar DM. This feature serves as the most interesting phenomenological outcome of this model, as we discuss in collider section. For $m_{N_1} > m_S$, the scalar DM however is allowed only in the resonance region ($m_S \sim m_h/2$) as can be seen by orange points in the right plot of Fig. 4.13. This is already expected as direct search tames down the relic density allowed scalar DM parameter space absent DM-DM conversion. For the reverse hierarchy $m_{N_1} < m_S$ (blue points), fermion DM is allowed only in the under-abundant regions of its single component manifestation, whereas it allows a larger mass range of scalar DM, thanks again to the possible DM-DM conversion with a lighter N_1. Invisible Higgs branching ratio $Br(h \to \text{inv}) < 0.24$ [102], puts a significant constraint for the scalar DM with $m_S < m_h/2$. But for fermion DM, this doesn't discard any parameter space given the small values of $\sin\theta$ chosen for the scan.

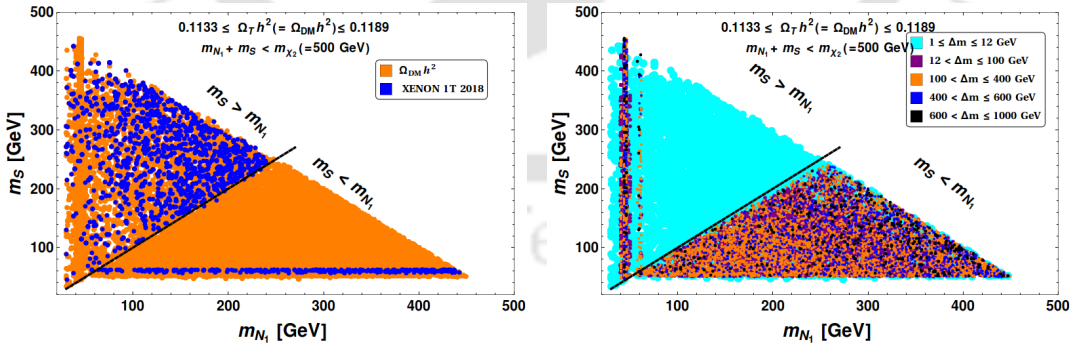

Figure 4.14: Mass correlation of the two DM components in $m_{N_1} - m_S$ plane. [Left Panel] Relic density allowed parameter space is shown by orange points and direct search constraint from XENON 1T [104] on both N_1 and S is shown by blue points. Black solid line corresponding to $m_{N_1} = m_S$ segregates the two possible hierarchies: the one above corresponds to $m_S > m_{N_1}$ and the region below has $m_S < m_{N_1}$. [Right Panel] Relic density allowed points for different ranges of Δm shown with different colour codes.

A possible mass correlation of these two DM components is studied next and depicted in Fig. 4.14 in $m_{N_1} - m_S$ plane for satisfying relic density and direct search

constraints. On the left panel, we show that the whole triangle designated by the kinematic limit $m_{N_1} + m_S < m_{\chi_2}$, with $m_{\chi_2} = 500$ GeV chosen for the scan is allowed by relic density constraint. However direct search (XENON1T data [104]) restricts it significantly for $m_{N_1} > m_S$, allowing only scalar DM to lie in resonance $m_h/2$, while it is not that restrictive for the other hierarchy $m_{N_1} < m_S$, as shown by the spread of blue points filling almost entirely the upper part of the triangle. The thick black line depicting $m_{N_1} = m_S$ separates these two heirarchies. The plot on the right panel shows the allowed points in $m_{N_1} - m_S$ plane to satisfy relic density for different ranges of Δm. It shows that small $1 \leq \Delta m \leq 12$ GeV is allowed throughout the parameter space while large Δm is restricted to $m_{N_1} > m_S$ as we already discussed. For $m_{N_1} < m_S$, one can have larger Δm allowed only in the resonance region $m_{N_1} \sim m_h/2$ and $\sim m_Z/2$.

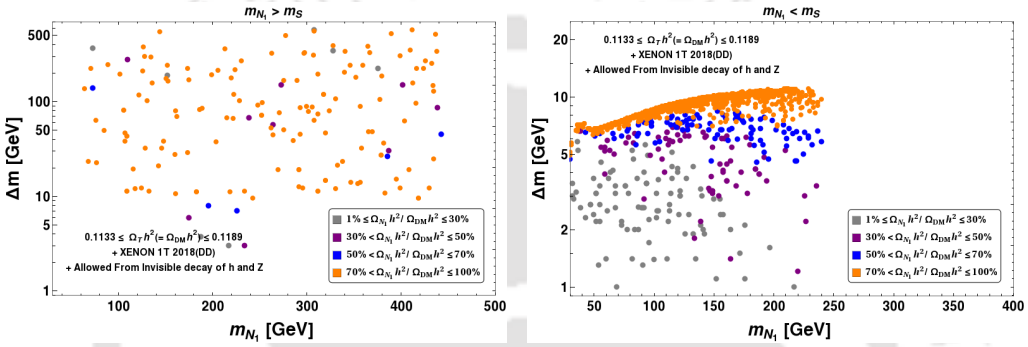

Figure 4.15: Relic density, direct search (XENON 1T [104]) and invisible decay constrain of Higgs and Z boson [102] allowed parameter space of the two component model (with $Y_2 \neq 0$) in $m_{N_1} - \Delta m$ plane. Percentage of fermion DM component in total relic density within different ranges are shown by different coloured points as detailed in the figure inset. Two different hierarchies $m_S < m_{N_1}$ and $m_S > m_{N_1}$ are shown separately in left and right panel respectively.

Another important question is to know the percentage of fermion or scalar DM component present in the allowed parameter space of this two component model. We show the outcome of this exercise in Fig. 4.15, for fermion DM in $m_{N_1} - \Delta m$ plane. The other component (S) just fills the rest of it and can be gauged from this figure itself. Two possible mass hierarchies $m_S < m_{N_1}$ and $m_S > m_{N_1}$ are shown separately in left and right panel respectively. Fermion DM content in total relic density (for different ranges in percentage) is shown by different colour codes mentioned in the figure inset. All the points also additionally satisfy direct search constraint from XENON1T data [104] and invisible decay constraint of Higgs and Z [102]. The bottom line is that for $m_{N_1} > m_S$, the larger share of DM density is carried by fermion DM with $\Delta m \gg 12$ GeV as it becomes enough to bring the annihilation in the right ballpark through conversion to the scalar DM component (with small $\sin\theta$), while the scalar DM anyway has a large annihilation cross section (and therefore smaller relic density) as it requires to be in the Higgs resonance region ($m_S \sim m_h/2$) to address direct search bound. For the other hierarchy $m_{N_1} < m_S$, under abundant regions of the single component fermion DM is filled up with different percentage as the scalar DM has the freedom to adjust its relic density through its annihilation to SM plus fermion DM.

So far we have discussed the allowed DM parameters space for the model with a moderate choice of mediator mass, $m_{\chi_2} = 500$ GeV. Now we choose a higher value of

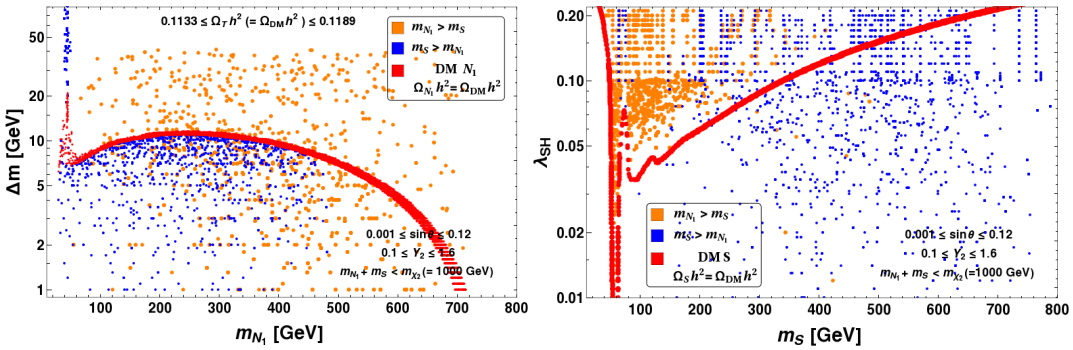

Figure 4.16: Total relic density allowed regions of two component DM model in $m_{N_1} - \Delta m$ (left panel) and $m_S - \lambda_{SH}$ plane (right panel) with $Y_2 \neq 0$ for mediator mass $m_{\chi_2} = 1000$ GeV. Two mass hierarchies are shown in different colour codes: $m_{N_1} > m_S$ (orange points) and $m_S > m_{N_1}$ (blue points). Red points correspond to the case of single component DM scenarios for N_1 on left and for S on right panel.

BPs	$\{ m_{N_1}, m_S, \lambda_{SH}, Y_2, \sin\theta \}$	Δm	$\Omega_{N_1}h^2$	$\Omega_S h^2$	$\left(\frac{\Omega_{N_1}h^2}{\Omega_{DM}h^2}\right)\sigma_{N_1}^{SI}$ (in cm^2)	$\left(\frac{\Omega_S h^2}{\Omega_{DM}h^2}\right)\sigma_S^{SI}$ (in cm^2)
BPA1	$\{ 79, 256, 0.029, 0.2, 0.02 \}$	6.1	0.0546	0.0641	6.8×10^{-48}	5.9×10^{-47}
BPA2	$\{ 276, 58, 0.010, 0.9, 0.02 \}$	50	0.1092	0.0054	1.5×10^{-48}	1.5×10^{-47}
BPA3	$\{ 131, 61, 0.026, 0.9, 0.01 \}$	101	0.1171	0.0012	1.0×10^{-48}	1.5×10^{-47}
BPA4	$\{ 102, 62, 0.010, 0.9, 0.02 \}$	193	0.1144	0.0010	1.8×10^{-47}	2.0×10^{-48}
BPA5	$\{ 135, 58, 0.004, 1.0, 0.02 \}$	295	0.0840	0.0313	1.5×10^{-47}	1.0×10^{-47}
BPA6	$\{ 127, 62, 0.020, 0.9, 0.01 \}$	377	0.1136	0.0004	1.4×10^{-48}	3.0×10^{-48}
BPA7	$\{ 144, 62, 0.032, 0.9, 0.02 \}$	541	0.1152	0.0002	2.7×10^{-47}	4.2×10^{-48}

Table 4.2: Some benchmark points allowed by relic density, direct search and invisible Higgs and Z decay limit for mediator mass, $m_{\chi_2} = 500$ GeV. DM masses, couplings, relic density of individual components and effective SI direct search cross-sections are mentioned. All the masses are in GeVs. We mainly focus on $m_{N_1} > m_S$ excepting for BPA1.

χ_2 mass, $m_{\chi_2} = 1000$ GeV to depict relic density allowed limit in $m_{N_1} - \Delta m$ plane (left) and $m_S - \lambda_{SH}$ plane (right) of Fig. 4.16. Allowed parameter space in $m_{N_1} - \Delta m$ plane becomes more restrictive (Δm spanning roughly upto ~ 50 GeV compared to 500 GeV with $m_{\chi_2} = 500$ GeV) even with $m_{N_1} > m_S$ due to suppressed t-channel DM-DM conversion $\overline{N_i} N_j \to SS$ due to the heavy mediator (m_{χ_2}). Comparatively, larger parameter space is available for scalar DM S as shown in right panel of Fig. 4.16 in $m_S - \lambda_{SH}$ plane. This is possible as $SS \to \overline{N_i} N_j$ with ($Y_2 \neq 0.0$) still dominate over scalar DM annihilation to SM (controlled by portal coupling λ_{SH}) even with a heavy mediator mass. This feature has already been pointed out while discussing the outcome of DM-DM conversion cross-sections in Fig. 4.9.

Finally, to summarise the main outcome of the DM analysis is to see that heavier DM component enjoys annihilation to lighter DM for thermal freeze out, relaxing its interaction to visible sector and thus reducing the constraints from direct search cross-sections. Specifically for the two-component case, when scalar DM is heavier than the fermion DM, the Higgs portal coupling can be reduced significantly allowing the scalar DM to be allowed through the entire DM mass plane. On the other hand, when the fermion DM is heavier than the scalar DM, it relaxes the mass difference with the

charge companion, allowing larger Δm. No relaxation is possible however for $\sin\theta$ as larger values of mixing is still discarded by Z mediated direct search. The relaxation of Δm plays a crucial role in achieving collider signatures of fermion DM as we illustrate next. We choose a set of benchmark points allowed by relic density and direct search in Table 4.2 for performing collider analysis, where above features are apparent.

4.5 Two Component DM in presence of additional heavy scalar

In the two component DM set up, lighter DM component behaves almost as a single component candidate, due to the absence of additional channels for annihilation, thus occupying only under abundant regions accessible from relic density. For $m_{N_1} > m_S$, a large mass splitting Δm can be achieved for a moderated value of mediation mass $m_{\chi_2} \sim 500$ GeV. But at the same time, the scalar DM can only be accommodated at the resonance region, $m_S \approx \frac{m_h}{2}$ (see Fig. 4.13 and Table 4.2). This is predictive and restrictive at the same time. This situation however alters significantly if the scalar sector is enlarged with a heavy real scalar S_H which has same charge like S under $\mathcal{Z}_2 \times \mathcal{Z}_2'$ as: S $[-,-]$ and $\mathrm{S_H}$ $[-,-]$ [94, 106]. We briefly discuss such a possibility here. The relevant interacting scalar potential is given by:

$$\begin{aligned} V(S,S_H) \supset\ & \frac{1}{2}m_S^2 S^2 + \frac{1}{2}m_{S_H}^2 S_H^2 + \frac{\lambda_{SH}}{2}\Big(H^\dagger H - \frac{v^2}{2}\Big)(S^2+S_H^2) \\ & + \lambda_{CH}\Big(H^\dagger H - \frac{v^2}{2}\Big) S S_H, \end{aligned} \tag{4.34}$$

where m_{S_H} is the heavy scalar mass and λ_{CH} is additional (co-annihilation type) Higgs portal coupling. Due to the presence of this interaction, $\lambda_{CH}\Big(H^\dagger H\Big) S S_H$, a new co-annihilation channel, $S\ S_H \to SM\ SM$ opens up. S_H having same charge as of S, is not stable and therefore is not a DM. But the possibility of co-annihilation provides additional channel for scalar DM to freeze out, while it does not contribute to direct search. This is similar to the co-annihilation processes already present in the fermion DM sector. With this, even for $m_{N_1} > m_S$, the scalar DM can be allowed in a large parameter space beyond resonance. Presence of this heavy scalar, also augments dark sector Yukawa interaction providing additional contribution to DM-DM conversion:

$$\mathcal{L_{DM}}^{Yuk} = -Y_2(\overline{\chi_1}\chi_2 S + h.c) - Y_2^{'}(\overline{\chi_1}\chi_2 S_H + h.c). \tag{4.35}$$

In our numerical analysis, we assume $Y_2 = Y_2^{'}$ for simplicity.

The first outcome of this extended two component framework is to show a large parameter space available to the scalar DM through relic density and direct search bounds with the hierarchy $m_{N_1} > m_S$. This is illustrated in Fig. 4.17. The direct search cross-section for fermion DM in relic density allowed points is shown on the left plot, while that for the scalar is shown in the right panel. We see in the right plot that orange points now span allover the plane with a huge number below the direct search limit unlike being only available in resonance region with the previous case (compare bottom right plot of Fig. 4.12).

A mass correlation for two DM components is shown in Fig. 4.18 and compared between the original framework (left) to that in presence of an additional heavy scalar

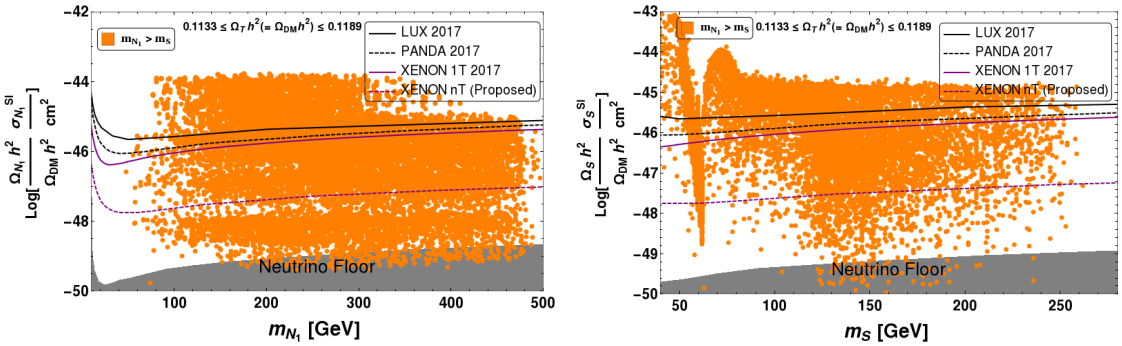

Figure 4.17: Relic density allowed points plotted in DM mass vs effective SI DM-nucleon cross-section plane: $\left(\frac{\Omega_{N_1} h^2}{\Omega_{DM} h^2}\right)\sigma_{N_1}^{SI} - m_{N_1}$ plane (left) and $\left(\frac{\Omega_S h^2}{\Omega_{DM} h^2}\right)\sigma_S^{SI} - m_S$ plane (right) in presence of heavy scalar S_H. Upper bounds on SI DM-nucleon cross-section from LUX [103] (black solid line), recent PANDA [46] (black dashed), XENON 1T [104] (purple solid line) and predicted XENON nT [105] (purple dotted line) are also indicated in the figures. We have chosen the mass hierarchy: $m_{N_1} > m_S$ and the mediator mass $m_{\chi_2} = 500$ GeV.

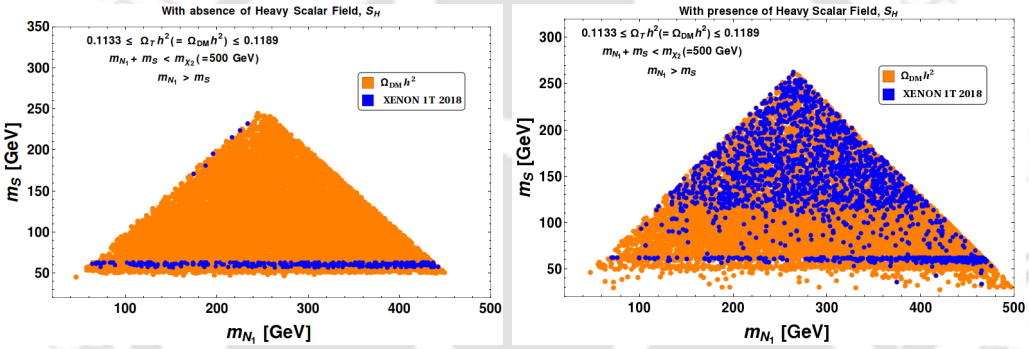

Figure 4.18: Allowed region of parameters space in $m_{N_1} - m_S$ plane, which satisfy relic density (Orange points) and direct search constraints for both N_1 and S by XENON1T data (blue points) for $m_{N_1} > m_S$. In left panel, we show the original two component scenario in absence of heavy scalar (S_H) and in the right panel, we show it in presence of additional heavy scalar S_H.

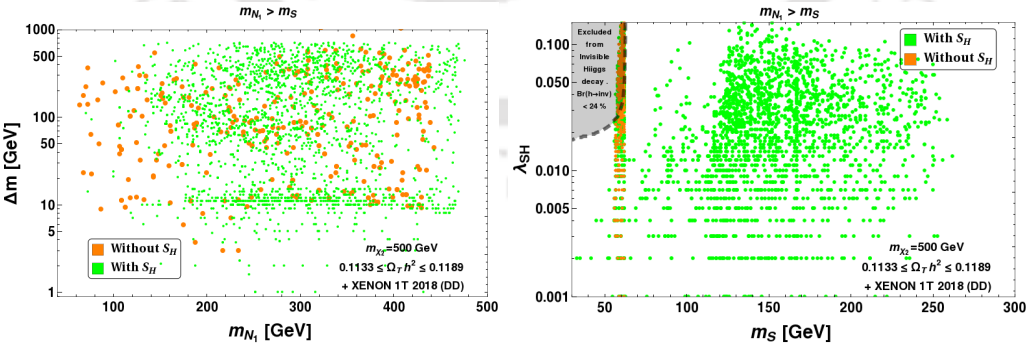

Figure 4.19: Relic density and direct search (XENON 1T [104]) allowed parameter space of the two component model compared between two cases: (i) original model, in absence of the heavy scalar (S_H) (orange points) and (ii) in presence of a heavy scalar (S_H) (green points) in $m_{N_1} - \Delta m$ plane (left) and $m_S - \lambda_{SH}$ plane (right).

(right). We show that with $m_{N_1} > m_S$, presence of co-annihilation in the scalar sector allows the scalar DM to be present in a larger parameter space after satisfying direct

search constraints (plot on the right panel).

Finally, we compare relic density and direct search (XENON 1T [104]) allowed parameter space of the two component model in presence of S_H (green points) to that in absence of S_H (orange points) for both fermion DM and scalar DM components in Fig.4.19. As expected, we see that for fermion DM, in $m_{N_1} - \Delta m$ plane (on left panel), there is no difference between these two cases, while for the scalar DM S, the presence of the heavy scalar S_H allows almost all of the plotted parameter space (green points on the right panel) due to coannihilation. A few benchmark points are indicated in Table 4.3 to show the effect of relaxing the case for scalar DM in presence of S_H for $m_{N_1} > m_S$. They should be contrasted with those in Table 4.2.

BPs	$\{m_{N_1}, m_S, m_{S_H}, \lambda_{SH}, \lambda_{CH}, Y_2, \sin\theta\}$	Δm	$\Omega_{N_1}h^2$	$\Omega_S h^2$	$\left(\frac{\Omega_{N_1}h^2}{\Omega_{DM}h^2}\right)\sigma_{N_1}^{SI}$ (in cm^2)	$\left(\frac{\Omega_S h^2}{\Omega_{DM}h^2}\right)\sigma_S^{SI}$ (in cm^2)
BPB1	$\{200,\ 150,\ 205, 0.006,\ 0.8,\ 0.7, 0.01\}$	50	0.1144	0.0030	9.7×10^{-49}	3.3×10^{-49}
BPB2	$\{202,\ 118,\ 131, 0.002,\ 0.3,\ 0.9, 0.04\}$	101	0.0303	0.0838	7.2×10^{-47}	1.5×10^{-48}
BPB3	$\{183,\ 113,\ 135, 0.009,\ 0.8,\ 0.8, 0.04\}$	201	0.0462	0.0680	1.2×10^{-46}	3.0×10^{-47}
BPB4	$\{310,\ 153,\ 203, 0.052,\ 0.6,\ 0.7, 0.02\}$	300	0.1112	0.0100	2.0×10^{-47}	5.8×10^{-47}
BPB5	$\{424,\ 91,\ 109, 0.004,\ 0.6,\ 1.1, 0.03\}$	503	0.0238	0.0945	2.7×10^{-47}	1.1×10^{-47}

Table 4.3: Benchmark points allowed by relic density, direct search and invisible Higgs decay limit in presence of a heavy scalar S_H. Input parameters (masses and couplings), relic densities of individual components and direct search cross-sections are mentioned. All the masses are in GeVs.

4.6 Collider searches at LHC

Collider signature of this model includes searches for scalar and fermion DM. The scalar DM sector doesn't give any novel signature being comprised only of a singlet. Only possible signature can be the production of S through Higgs portal coupling associated with initial state radiation (ISR), yielding mono jet/mono-X signal (higher jet multiplicity can occur suppressed by further jet radiation) plus missing energy [65]. Given the limit on the Higgs portal coupling (λ_{SH}) and DM mass set by the relic density and direct search bound of the model, even in the two component set up, the signal cross-section is very weak to probe anything at near future run of LHC given a huge SM background for such final states[3]. On the other hand, fermion DM consisting of an admixture of vector-like singlet and doublet leptons, has better prospect of getting unravelled at LHC. This is of particular interest due to the possibility of producing the charged companions of fermion doublet (N^+N^-) at LHC. They eventually decay to DM with off/on- shell W mediation to leptonic final states to yield opposite sign dilepton plus missing energy as pointed out in the left side of Fig. 4.20. Therefore our interest lies in :

$$\text{Signal} : \ell^+\ell^- + (\not{E}_{\rm T}),$$

where ℓ includes electrons and muons[4]. However, the detectability of such a signal depends on the effective reduction of corresponding SM background contribution. We

[3]Even though the presence of a heavy scalar S_H adds to the freedom of choosing a larger span of scalar DM mass, the strength of the cross-section still is determined by the small λ_{SH}.

[4]Tau detection is harder due to hadronic decay modes.

will discuss below how the presence of a second (lighter) DM component as considered in this model framework, enhance the possibility of detecting such signals at LHC. Similar signal events appear for different other models, see for example [59, 107].

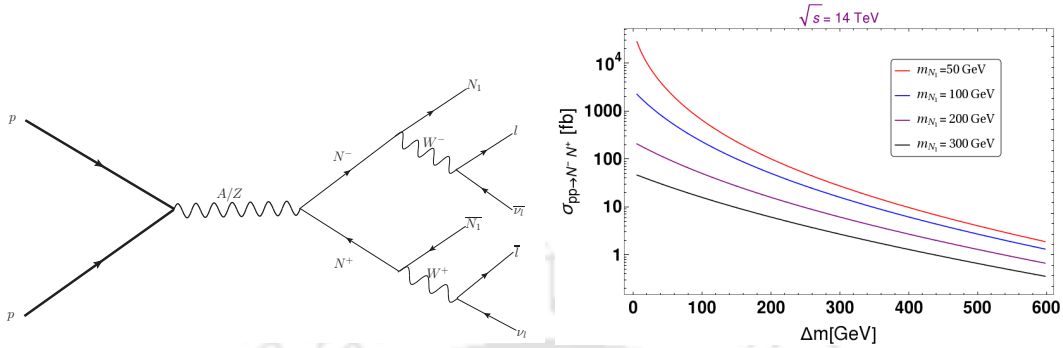

Figure 4.20: [Left] Feynman diagram for signal process $pp \to N^+N^-$, resulting in hadronically quiet opposite sign dilepton plus missing energy ($\ell^+\ell^- + (\not{E}_T)$) events. [Right] Variation in production cross section, $\sigma_{pp\to N^+N^-}$ with Δm ($= m_{N^\pm} - m_{N_1}$) for different values of DM mass m_{N_1} [mentioned at figure inset] for centre-of-mass energy $\sqrt{s} = 14$ TeV at LHC.

Signal strength is mainly dictated by the production cross-section for $pp \to N^+N^-$ at LHC. This cross-section is essentially a function of $m_{N^\pm}$ and is independent of mixing angle $\sin\theta$. Therefore, one can recast the cross-section as a function of Δm for a fixed DM mass (Given $m_{N^\pm} = m_N + \Delta m$). This is shown in the right panel of Fig. 4.20 for some different fixed DM masses (mentioned in the figure inset) with centre-of-mass-energy $\sqrt{s} = 14$ TeV. Essentially, this is to show that production cross-section is a falling function of charged fermion masses, but, as Δm plays a crucial role in further decay of the produced charged fermions, we have chosen such parametrisation. We already elaborated that even in the two component set up, direct search crucially tames $\sin\theta \leq 0.1$, it is important to choose a process which is not suppressed by small mixing angle. Therefore, this is the only process of interest. However, also note that, we do not consider the production of heavy neutral fermion N_2 in this analysis (although some of the processes like $N^\pm N_2$ are not suppressed by small $\sin\theta$), which decays through neutral current (Z mediation) interaction to DM N_1 with 100 percent branching ratio. But such signals will be completely washed out by the invariant mass-cut of the leptons not to lie within Z-mass window, that we must apply to suppress SM background (as explained shortly). There are two kinematic constraints that we obey for characteristic collider signal that we discuss here: (i) $m_{\chi_2} > m_{N_1} + m_S$ and (ii) $m_{N_1} > m_S$. The second constraint allows us to choose a large Δm as explained earlier and plays an important role in separating the signal from SM background. Most of the benchmark points in Table 4.2 and all in Table 4.3, follow the characteristics mentioned above. We will analyse signal strength for some such benchmark points. Although, we use benchmark points from Table 4.2 here, they can also be thought as similar points (with same Δm) from Table 4.3, where we have further relaxation on scalar DM mass (which do not play a role in the collider signature for fermion DM).

Before getting into the collider analysis, let us briefly explain the experimental environment of LHC, which mainly involves identification of leptons, jets and unclustered objects. Some important variables are also used in the analysis such as missing energy, invariant mass of the dilepton in the final state and scalar sum of the transverse

momentum of all the visible objects in the final state. They are identified as follows:

- *Lepton ($l = e, \mu$):* Leptons are identified with a minimum transverse momentum $p_T > 20$ GeV and pseudorapidity $|\eta| < 2.5$. Although the present sensitivity of the detector allows further soft leptons to be identified, we find that such a p_T cut also helps to tame SM background. Leptons require to be isolated if their mutual distance in the $\eta - \phi$ plane is $\Delta R = \sqrt{(\Delta\eta)^2 + (\Delta\phi)^2} \geq 0.2$, while the separation with a jet requires $\Delta R \geq 0.4$.

- *Jets (j):* Jets are formed for simulated signal and background events using cone algorithm `PYCELL` inbuilt in `Pythia` event generator. All the partons within $\Delta R = 0.4$ from the jet initiator cell are included to form the jets. We require $p_T > 20$ GeV for a clustered object to be identified as jets in hadron calorimeter (HCAL). Jets are isolated from unclustered objects with $\Delta R > 0.4$. Note here, that although jets are not present in the final state, we require a specific jet identification criteria to demand the final state has zero jets.

- *Unclustered Objects:* All the final state objects with low p_T, which are neither clustered to form jets, nor passes through the identification criteria to become isolated leptons, belong to such category. Hence all particles with $0.5 < p_T < 20$ GeV and $2.5 < |\eta| < 5$, are considered as unclustered objects. They only contribute to missing energy.

- *Missing Energy ($\not{E}_T$):* The transverse momentum of all those electromagnetic charge neutral particles not registered in the detector, can be estimated form the momentum imbalance in the transverse direction associated to the visible particles. Thus missing energy (MET) is defined as:

$$\not{E}_T = -\sqrt{(\sum_{\ell,j,unc.} p_x)^2 + (\sum_{\ell,j,unc.} p_y)^2}, \tag{4.36}$$

  where the sum runs over all visible objects that include the leptons and jets, and the unclustered components. Missing energy is the most significant variable to identify DM at collider.

- *Effective Mass (H_T):* Effective mass of an event is identified here with the scalar sum of the transverse momentum of detectable objects in an event, namely lepton and jets as follows:

$$H_T = \sum_{\ell,j} \Big(p_T\Big)_{\ell,j} \,. \tag{4.37}$$

  Effective mass usually also includes missing energy as a component added in the scalar sum. However, here we use H_T without including $\not{E}_T$, as we will use $\not{E}_T$ as a separate variable in combination of H_T cut anyway to segregate signal from SM background.

- *Invariant mass ($m_{\ell\ell}$):* Invariant mass of opposite sign dilepton is an important variable to segregate SM background from the signal, as it hints to the parent particle mass from which the leptons have been produced. This is defined as:

$$m_{\ell\ell} = \sqrt{(\sum_{\ell} p_x)^2 + (\sum_{\ell} p_y)^2 + (\sum_{\ell} p_z)^2}. \tag{4.38}$$

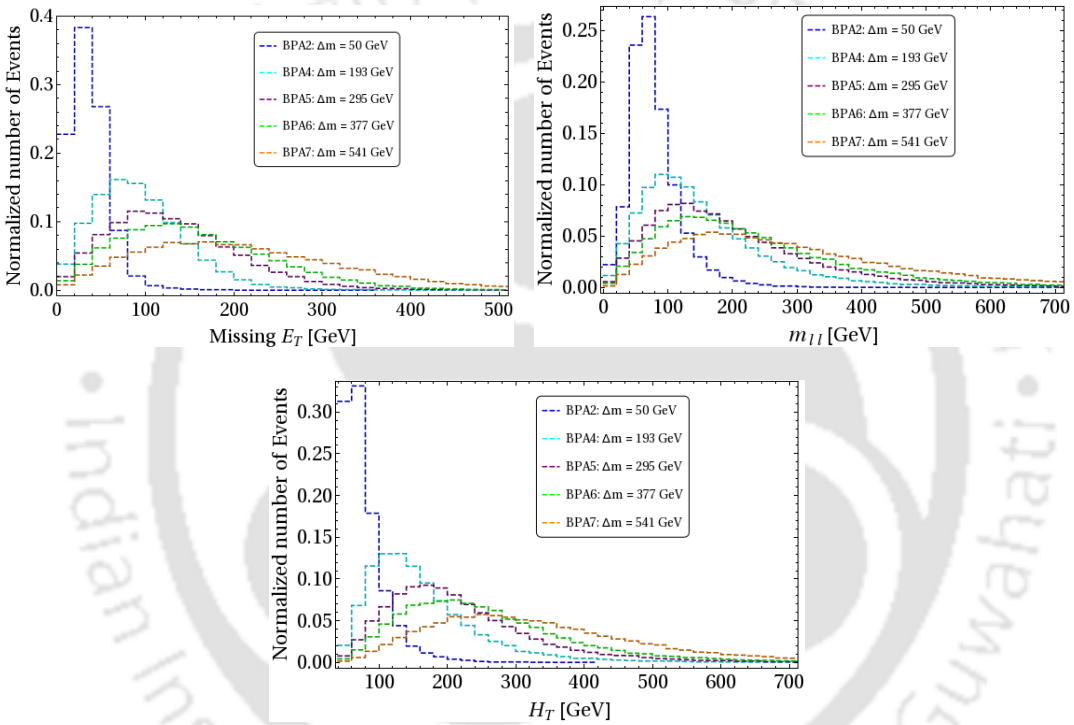

Figure 4.21: Missing energy ($\not{E}_T$), invariant mass of dilepton ($m_{\ell\ell}$) and effective mass (H_T) distributions of $\ell^+\ell^- + (\not{E}_T)$ events from signal at LHC are shown at $\sqrt{s} = 14$ TeV. We have chosen different values of Δm corresponding to different benchmark points as indicated in Table 4.2.

We inserted the model in `Feynrules` [108] and passed to `Madgraph` [109] to generate signal events, which were further analysed in `Pythia` [110] to reconstruct leptons, jets and other variables discussed above. The dominant SM backgrounds have been generated in `Madgraph` [109] and then showered through `Pythia` [110]. We have identified dominant SM backgrounds for hadronically quiet opposite sign dilepton events as the production of: $t\bar{t}$, W^+W^-, $W^\pm Z$, ZZ, W^+W^-Z and $Drell - Yan$. We have also used appropriate K-factors to incorporate the Next-to-Leading order (NLO) cross section for the backgrounds. The K-factors chosen are as [111] for $t\bar{t}$: $K = 1.47$, WW : $K = 1.38$, WZ : $K = 1.61$, ZZj : $K = 1.33$, $Drell\text{-}Yan$: $K = 1.2$. We have used `CTEQ 6L` [112] parton distribution function and subprocess centre-of-mass-energy ($\sqrt{\hat{s}}$) as jet energy scale for the analysis.

BPs	Δm (GeV)	$\sigma_{pp\to N^+N^-}$ (fb)	$\not{E}_T$ (GeV)	H_T (GeV)	$\sigma^{\rm OSD}$(fb)	$N_{\rm eff}^{\rm OSD}$
BPA2	50	1.73	>100	>100	0.002	< 1
				>200	0.001	< 1
				>300	0.00	0
BPA3	101	6.23	>100	>100	0.155	15
				>200	0.045	4
				>300	0.013	1
			>200	> 100	0.006	1
				>200	0.005	< 1
				>300	0.004	< 1
BPA4	193	2.47	>100	>100	0.305	30
				>200	0.138	14
				>300	0.044	4
			>200	> 100	0.032	3
				>200	0.031	3
				>300	0.017	2
BPA5	295	0.54	>100	>100	0.113	11
				>200	0.075	7
				>300	0.031	3
			>200	> 100	0.032	3
				>200	0.031	3
				>300	0.016	2
			>300	> 100	0.006	1
				>200	0.006	1
				>300	0.005	< 1
BPA6	377	0.27	>100	>100	0.067	7
				>200	0.052	5
				>300	0.027	3
			>200	> 100	0.027	3
				>200	0.027	3
				>300	0.016	2
			>300	> 100	0.007	1
				>200	0.007	1
				>300	0.006	1
BPA7	541	0.06	>100	>100	0.017	2
				>200	0.015	1
				>300	0.011	1
			>200	> 100	0.011	1
				>200	0.010	1
				>300	0.008	1

Table 4.4: Signal events for few selected benchmark points (BPA2-BPA7, see Table 4.2) with $\sqrt{s}$ = 14 TeV at the LHC for the luminosity $\mathcal{L} = 100\ fb^{-1}$ after $\not{E}_T$, H_T and $m_{\ell\ell}$ cuts.

Most important outcome of this analysis is summarised in Fig. 4.21, where the

distribution of the signal events with respect to $\not{E}_T$, $m_{\ell\ell}$ and H_T are shown in top left, top right and bottom panel. We have chosen different Δm (from the benchmark points as in Table 4.2) upto as large as ∼500 GeV allowed by relic density and direct search for illustration. In top left figure, we see that with larger Δm, missing energy distribution becomes flatter and the peak shifts to a higher value. When this is contrasted with the same distributions from those of SM background contributions as pointed out in Fig. 4.22, we see that the separation of signal events from those of the background becomes easier at high Δm. Therefore, for signal events with large Δm can survive a large $\not{E}_T$ cut while reducing the SM background significantly. This should be contrasted with low Δm ($\sim$ 50 GeV, BPA2 case), where the peak of missing energy falls within the same ballpark as those of SM backgrounds and therefore can not be separated. Therefore even if the signal cross-section is higher for such cases (as in the single component fermion DM case), the events are submerged into SM background. This feature is not very difficult to understand. With $\Delta m < m_W$, the W decay is off-shell and $N^{\pm}$ momenta is shared amongst all the final state particles yielding a missing energy peak at lower value. For $\Delta m > m_W$, W is produced on-shell and dominant momenta is carried by the dark matter (N_1) as $m_{N_1} > m_W$. The higher the Δm is, the higher is the available momenta for DM. This therefore yields missing energy peak at larger values with larger mass splitting Δm. We also note that such distinction is also possible with H_T distribution. Again, the larger the Δm, the larger will be the available momenta for the leptons as well. Therefore, large H_T cut can also reduce SM background retaining signals particularly for benchmark points with higher Δm. On the other hand, invariant mass cut can effectively reduce SM background events coming from ZZ and WZ background, when a cut is applied within the Z mass window where the peak of the distribution lies. Therefore, to eliminate SM background from the signal event, we further employ some combination of the following cuts:

- $m_{\ell\ell} < |m_z - 15|$ and $m_{\ell\ell} > |m_z + 15|$,
- $H_T > 100,\ 200,\ 300$ GeV,
- $\not{E}_T > 100,\ 200,\ 300$ GeV.

Signal events with $\Delta m = \{50, 101, 193, 295, 377, 541\}$ GeV corresponding to benchmark points BPA2, BPA4-BPA7 (as in Table 4.2), are summarised in Table 4.4, where the cut flow with different H_T and $\not{E}_T$ are furnished. The final state event rates (N_{eff}) at a desired luminosity $\mathcal{L}$ is computed by:

$$N_{eff} = \frac{\sigma_p\ n}{N} \times \mathcal{L}, \tag{4.39}$$

where N is the simulated number of events and n is the obtained final state events corresponding to production cross-section of σ_p. We see that although with larger Δm, the production cross-sections get diminished by the phase space suppression (as already pointed out in RHS of Fig. 4.20), the shift in the peak of the distribution compensates it to ensure the survival of more number of signal events for such cases. With $\Delta m = 101$ GeV, the combination of $\not{E}_T > 200$ GeV and $H_T > 100$, leaves with a very few events to be observed. $\mathcal{L} = 100$ fb^{-1} turns out to be rather low to see the signals from such events and we need higher luminosity. The main take however is to

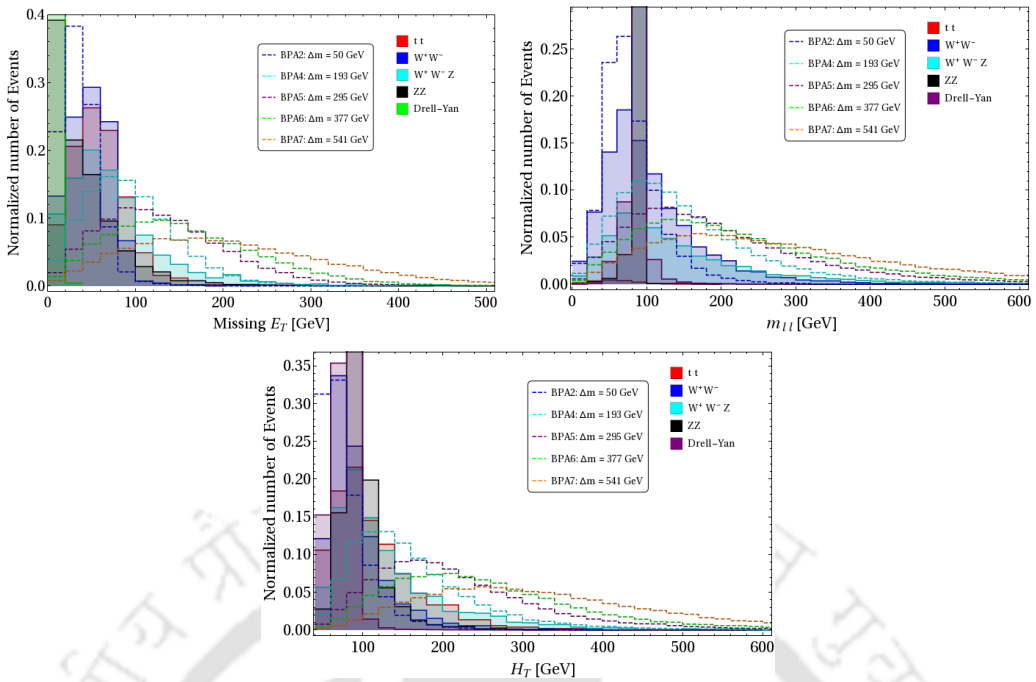

Figure 4.22: Missing energy ($\not{E}_T$), invariant mass of dilepton ($m_{\ell\ell}$) and effective mass (H_T) distributions of $\ell^+\ell^- + (\not{E}_T)$ events from signal (Benchmark points as in Table 4.2) and dominant SM background events at LHC with $\sqrt{s} = 14$ TeV .

note that only those cases where Δm is large, has a prospect of discovery by reducing SM background through effective cuts, while those with small Δm as in the single component framework is almost hopeless. The signal event rates can be contrasted with the SM background events with similar cut flow at 14 TeV at LHC as detailed in Table 5.8. We also note that the limitation in warranting any final state event with number of simulated points yield a limit on the effective background cross-section as indicated in the Table. We see that the dominant SM backgrounds can be tamed down significantly with a combination of $\not{E}_T$ and H_T cut. The reach of the signal significance $\sigma = \frac{S}{\sqrt{S+B}}$ is plotted with integrated luminosity $\mathcal{L}$ for selected benchmark points with two different combinations of $\not{E}_T$ and H_T cut in left and right panel of Fig. 4.23. It shows that 5σ significance can be reached with luminosity as high as $\sim 10^4\ fb^{-1}$.

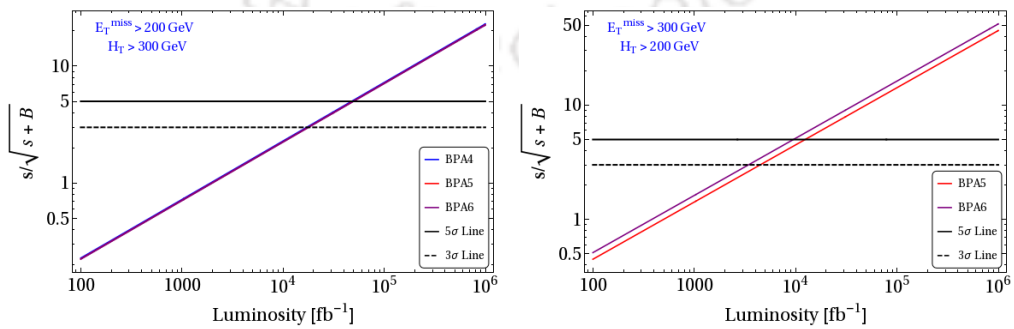

Figure 4.23: Signal significance $\sigma = \frac{S}{\sqrt{S+B}}$ of OSD events for select few benchmark points (see Table 4.2) at LHC with $E_{CM} = 14$ TeV as a function of integrated luminosity. Different combinations of $\not{E}_T$, H_T cuts are chosen in left and right panel (mentioned in inset). 3σ (black dashed) and 5σ (black thick) lines are indicated as references.

SM Backgrounds	$\sigma_{p\ p\to SM}$ (fb)	$\not{E}_T$ (GeV)	H_T (GeV)	$\sigma^{\rm OSD}$(fb)	$N_{\rm eff}^{\rm OSD}$
$t\,\bar{t}$	814.78×10^3	>100	>100	17.11	1711
			>200	2.44	244
			>300	< 0.81	< 1
		>200	> 100	< 0.81	< 1
			>200	< 0.81	< 1
			>300	< 0.81	< 1
		>300	> 100	< 0.81	< 1
			>200	< 0.81	< 1
			>300	< 0.81	< 1
$W^+\,W^-$	100.06×10^3	>100	>100	20.51	2051
			>200	10.01	1001
			>300	2.00	200
		>200	> 100	2.00	200
			>200	2.00	200
			>300	0.50	50
		>300	> 100	< 0.50	< 1
			>200	< 0.50	< 1
			>300	< 0.50	< 1
$Z\,Z$	14.03×10^3	>100	>100	0.21	21
			>200	0.14	14
			>300	0.07	7
		>200	> 100	< 0.07	< 1
			>200	< 0.07	< 1
			>300	< 0.07	< 1
		>300	> 100	< 0.07	< 1
			>200	< 0.07	< 1
			>300	< 0.07	< 1
$W^+\,W^-\,Z$	0.16×10^3	>100	>100	0.17	17
			>200	0.09	9
			>300	0.03	3
		>200	> 100	0.04	4
			>200	0.04	4
			>300	0.02	2
		>300	> 100	0.01	1
			>200	0.01	1
			>300	0.01	1

Table 4.5: Dominant SM background contribution to $\ell^+\ell^- + (\not{E}_T)$ signal events with $\sqrt{s} = 14$ TeV at the LHC for luminosity $\mathcal{L} = 100\ fb^{-1}$ after $\not{E}_T$, H_T and $m_{\ell\ell}$ cuts. The variation of effective number of final state background events with cut-flow are also tabulated.

We also note here that small Δm along with small $\sin\theta$ predicts a delay in the decay of the charged fermion, yielding displaced vertex or stable charge track signature and

serves as a characteristic signal for the fermion dark sector with singlet-doublet mixing, as has already been noted in ref. [97]. However, in that case, signal excess in dilepton channel can not be seen. On the contrary, with large Δm, when excess in opposite sign dilepton events can be seen, the decay of the charged fermion is quick and therefore no displaced vertex signature can be observed. Therefore the signal of singlet-doublet fermion DM in presence of a second lighter DM component has a complementarity to that of the same DM in a single component framework as far as collider search is concerned. The presence of a heavy scalar (as illustrated in Sec. 4.5) doesn't of course change the fermion DM signal discussed here, but allows one to choose the scalar DM in a large mass range.

4.7 Possible implications to Inflation and Reheating

In this section, we comment briefly on the possibility of production of dark sector particles in the early Universe. It is usually assumed that the early Universe has gone through a period inflation driven by a scalar field, the so called inflaton. Subsequently the inflaton decays perturbatively (nonperturbatively) to bring back a thermal bath, the so called reheating (preheating) phase, with a temperature $T_R > 4$ MeV to pave a path for Big-Bang nucleosynthesis (BBN). See for a review [113, 114]. During the reheating (preheating) phase all the elementary particles, including dark sector, are assumed to be produced. The process of reheating is quite model dependent and accordingly the temperature T_R of thermal bath is set in a large range.

It has been pointed out that during Inflation, the SM Higgs boson may develop a non-zero and large vev $h_I \sim H_I$ [115], where H_I is the Hubble scale at the end of inflation. Therefore, the particles which couple to the Higgs will also acquire very high mass during this period. This may result in a kinematic blocking of the inflaton decay if the mass of the inflaton is lighter that than the decay products induced by the non-zero Higgs vev[115]. The phenomena is involved and model dependent. We just provide a brief sketch of the main idea. The presence of the scalar DM which couples to Higgs in our scenario through Higgs portal, may add to the phenomena. A simple illustration of the above situation can be made by looking into the perturbative inflaton decay neglecting backreaction. If we assume a simple inflaton (ϕ) potential given by $V_\phi = m_\phi^2\phi^2/2$, the perturbative reheating temperature (T_R) is obtained through the solution of the following coupled Boltzmann Equations:

$$\begin{aligned} \dot{\rho_\phi} + 3H\rho_\phi &= -\Gamma_\phi\rho_\phi, \\ \dot{\rho_R} + 3H\rho_R &= \Gamma_\phi\rho_\phi, \end{aligned} \tag{4.40}$$

where ρ_ϕ is the density of the inflaton and ρ_R is the density of radiation resulting from the decay of the inflaton with decay width Γ_ϕ. H is the Hubble constant with $H^2 = \frac{8\pi}{3}(\rho_\phi + \rho_R)$. In presence of the DM, the inflaton also decays to DM in addition to SM particles and the total decay width is given by:

$$\Gamma_\phi = \Gamma_0 \left(1 - \frac{4m_f^2}{m_\phi^2}\right)^{3/2} \Theta(m_\phi^2 - 4m_f^2) + \Gamma_0 \left(1 - \frac{4m_s^2}{m_\phi^2}\right)^{3/2} \Theta(m_\phi^2 - 4m_s^2). \tag{4.41}$$

In above equation, for simplicity, we just incorporate the decay to SM fermions (f) and to the scalar DM S. Γ_0 denotes the decay width at zero mass limit. The mass

term for the SM fermion and DM are generated from Yukawa interactions (y and λ_{SH}) followed by the large vev (h_I) that Higgs acquires during inflation and will be given by:

$$m_f^2 = \frac{1}{2}y^2 h_I^2;\ m_S^2 = \frac{1}{2}\lambda_{SH}^2 h_I^2. \tag{4.42}$$

The Θ function in Eq.4.41 denotes the phase space blocking. Depending on whichever is lighter between m_f and m_S, the effective blocking condition for the inflaton decay (assuming $m_S < m_f$) reads:

$$\frac{h_I^2}{m_\phi^2} > \frac{1}{2\lambda_{SH}^2}. \tag{4.43}$$

As a result the reheating temperature T_R can drop significantly and can be even be less than the Higgs mass depending on the coupling and vev. The delay in reheating may alter the CMB spectrum in terms of the spectral index of density perturbation (n_s) and tensor-to-scalar ratio (r) or affect the heavy particle production. However, one should note here that the maximum temperature $T_{\rm max}$ during reheating can be much larger than reheating temperature T_R. During reheating, the temperature rises to T_{max} and then falls to T_R, see for example, [116]:

$$T_{max} = 0.6 g_*^{-1/4} (\Gamma_\phi M_{Pl})^{1/4} M_I^{1/2}, \tag{4.44}$$

where $M_I = V_I^{1/4}$, V_I depicts the energy density at t_{osc}. Depending on the model, maximum temperature can be as high as $T_{max} \sim 10^3 T_R$. As a result, the heavy particles (including dark sector particles χ_1, χ_2, N, S *etc.*) in general can be produced during reheating phase itself. Once these particles are produced, irrespective of their initial number density, they can easily thermalise due to their coupling with the SM Higgs and other SM particles. For instance in our case N is a doublet. So it can be easily thermalise due to its gauge coupling. On the other hand, χ_1 and χ_2 are singlets under the SM gauge group. However, these particles couple to the SM Higgs through (large) Yukawa interaction. Therefore, the dark sector particles in our case are no more in danger being over produced even if the kinematic blocking effects in a lower reheat temperature as discussed above.

4.8 Summary

The dark sector of the universe is still a mystery to us. In this work, we have discussed a possible two component (WIMP-like) DM scenario with a vector like fermion (an admixture of a singlet and a doublet) and a scalar singlet stabilised by $\mathcal{Z}_2 \times \mathcal{Z}_2'$ symmetry. The proposed scenario crucially addresses the possibility of DM-DM interaction between fermion and scalar DM candidates through another heavy vectorlike fermion singlet which acts as mediator. We show that in absence of the mediator (which means the absence of t- channel heavy fermion mediated DM-DM interaction), both fermion and scalar DM components behave like two decoupled single component DMs. This is due to suppressed s-channel Higgs mediated interaction between the DM components. In such a situation, both of the sector turns out to fill up the corresponding under-abundant regions to add to the observed relic density. Although such a non interacting

situation satisfy observed DM relic density, the direct search limit (XENON1T) rules-out most of the parameter space, particularly for the scalar DM to a very heavy mass $\gtrsim 1$ TeV. For fermion DM, the necessity of co-annihilation contribution limits the mass difference with the charged doublet component to a small value ($\lesssim 12$ GeV).

However, in presence of a heavy fermion mediated t-channel DM-DM conversion, with moderate values of mediator mass ~ 500 GeV, the freeze out and relic density of DM components get affected significantly. The change is observed mostly in the relic density of the heavier DM component, which has the liberty of annihilating to the lighter DM, unconstrained by direct search limit; while lighter DM component behaves mostly as in single component framework. So, by allowing DM-DM conversion in the interacting picture, we open up large parameter space allowed by both relic density and direct search bounds which otherwise yields over-abundance in non-interacting cases. For fermion DM (when it is heavier than scalar DM), large Δm regions become allowed, but scalar DM is restricted to the Higgs resonance region. In presence of a heavy scalar, which helps co-annihilating the scalar DM component, allow a larger mass range for scalar DM even when it is lighter than fermion DM. On the other hand, when scalar DM is heavier than fermion DM, DM-DM conversion allows the presence of smaller Higgs portal couplings, hiding the scalar DM from direct search to allow a larger mass range upto TeV and beyond.

The work also demonstrates the importance of DM-DM conversion in seeing signals of a dark sector at LHC in relic density and direct search allowed parameter space. In the model, fermion dark sector is composed of a doublet and a singlet. Hence, the charged companions can be produced at LHC which yields hadronically quiet oppsite sign dilepton events plus missing energy through their decays to fermion DM. However, in a single component framework, relic density and direct search constraints restrict the fermion DM to have a small mass difference with the charged companion (Δm), which makes the signal submerged into SM background. On the contrary, in presence of a lighter DM component and an effective DM-DM conversion, Δm can be large, which can segregate the signal from SM background by a combination of large missing energy and effective mass cuts as detailed in the analysis. The discovery limit of such a signal still might be delayed to an integrated luminosity $\sim 10^4$ fb^{-1}.

Chapter 5

Multipartite Dark Matter with Scalar and inert Higgs doublet

Contents

5.1 Introduction

Our model under scrutiny in this chapter addresses three major issues, namely DM, neutrino masses and Higgs vacuum stability. We address a multipartite dark sector consisting of a $SU(2)_L$ doublet scalar (the IDM) and a scalar singlet, both stabilized by additional $\mathcal{Z}_2 \times \mathcal{Z}_2^{'}$ symmetry (for an earlier effort, see [49]) and provide a two component DM set up. The presence of DM-DM interactions enlarge the available parameter space significatly, while the inert DM can also produce leptonic collider signature at LHC. We augment the model with heavy RH neutrinos to address neutrino masses. However, the presence of RH neutrino Yukawa coupling tends to destabilze the EW vacuum while the additional scalars tend to stabilize them[117–129]. So, we take up an interesting exercise of validating the model from DM constraints, neutrino masses and high scale validity (absolute stability of the Higgs vacuum and perturbativity). This analysis provides some important conclusions, which are phenomenologically viable at LHC.

Let us finally discuss the plan of the chapter. In section 5.2, we discuss the model construct in details. Section 5.3 presents possible theoretical and experimental constraints on the model parameters. Then in sections 5.4,5.5 and 5.6 subsequently, we discuss DM phenomenology. In section 5.7, we investigate the high scale validity of the model. Section 5.8 summarises collider signature(s) in context of the proposed set up. Finally we conclude in section 5.9. Tree level unitarity condition is elaborated in Appendix D.

5.2 The Model

The model is intended to capture the phenomenology of two already established DM frameworks involving that of a singlet scalar and that of an inert scalar doublet together with right handed neutrinos to address neutrino mass under the same umbrella. Therefore, we extend SM by an inert doublet scalar (Φ) and a real scalar singlet (ϕ) and include three RH Majorona neutrinos $N_i (i = 1, 2, 3)$ in the set up. The lightest neutral scalar mode of the IDM and ϕ are the DM candidates provided an appropriate symmetry in addition to that of SM stabilizes both of them. This is minimally possible by introducing an additional $\mathcal{Z}_2 \times \mathcal{Z}'_2$ discrete symmetry under which all SM fields along with the right handed neutrinos transform trivially and the other additional fields transform non-trivially as tabulated in the Table 5.1. We also note the charges of SM Higgs (H) explicitly in Table 5.1, as it will be required to form the scalar potential of the model. Note here, that charges of the two DM candidates (Φ and ϕ) are complementary, i.e. odd under either $\mathcal{Z}_2$ or $\mathcal{Z}'_2$ for their stability. We also point out

BSM and SM Higgs Fields	$SU(3)_C \times SU(2)_L \times U(1)_Y \times \mathcal{Z}_2 \times \mathcal{Z}'_2 \equiv \mathcal{G}$				
$\Phi \equiv \begin{pmatrix} H^+ \\ \frac{1}{\sqrt{2}}(H^0 + iA^0) \end{pmatrix}$	1	2	+1	-	+
ϕ	1	1	0	+	-
N_i $(i = 1, 2, 3)$	1	1	0	+	+
$H \equiv \begin{pmatrix} w^+ \\ \frac{1}{\sqrt{2}}(h + v + iz) \end{pmatrix}$	1	2	+1	+	+

Table 5.1: Charge assignments of the BSM fields assumed in the model under $\mathcal{G}$ as well as that of SM Higgs. The $U(1)_Y$ hypercharge is chosen as $Q = T_3 + Y/2$.

that the $U(1)_Y$ hypercharge assignment of Φ is identical to SM doublet H. Therefore the only $SU(2)_L \times U(1)_Y$ invariant terms are $H^\dagger H$, $\Phi^\dagger \Phi$, $H^\dagger \Phi$ and its conjugate.

The scalar Lagrangian reads as :

$$\begin{aligned}\mathcal{L}_{scalar} &= |D^\mu H|^2 + |D^\mu \Phi|^2 + \frac{1}{2}(\partial^\mu \phi)^2 - V(H,\Phi,\phi), \\ \text{where } D^\mu &= \partial^\mu - ig_2\frac{\sigma^a}{2}W^{a\mu} - ig_1\frac{Y}{2}B^\mu\end{aligned} \tag{5.1}$$

and g_2, g_1 denote $SU(2)_L$ and $U(1)_Y$ coupling respectively.
The most relevant renormalizable scalar potential in this case is given by,

$$V(H,\Phi,\phi) = -\mu_H^2(H^\dagger H) + \lambda_H(H^\dagger H)^2 + V(H,\Phi) + V(H,\phi) + V(\Phi,\phi), \tag{5.2}$$

where,

$$\begin{aligned}V(H,\Phi) &= \mu_\Phi^2(\Phi^\dagger\Phi) + \lambda_\Phi(\Phi^\dagger\Phi)^2 + \lambda_1(H^\dagger H)(\Phi^\dagger\Phi) \\ &\quad +\lambda_2(H^\dagger\Phi)(\Phi^\dagger H) + \frac{\lambda_3}{2}[(H^\dagger\Phi)^2 + h.c.],\end{aligned} \tag{5.3}$$

$$V(H,\phi) = \frac{1}{2}\mu_\phi^2\phi^2 + \frac{\lambda_\phi}{4!}\phi^4 + \frac{1}{2}\lambda_{\phi h}\phi^2(H^\dagger H), \tag{5.4}$$

$$V(\Phi,\phi) = \frac{\lambda_c}{2}(\phi^2)\Big(\Phi^\dagger\Phi\Big). \tag{5.5}$$

The Lagrangian involving right handed neutrinos can be written as,

$$\mathcal{L}^\nu = -(Y_\nu)_{ij}\bar{l}_{L_i}\widetilde{H}N_j - \frac{1}{2}M_{N_{ij}}\overline{N_i^C}N_j, \tag{5.6}$$

where $\tilde{H} = i\sigma_2 H^*$. We have considered three generations of RH neutrinos with $\{i,j\} = 1,2,3$, which can acquire Majorana masses and can possess Yukawa interactions with SM lepton doublet l_L. Note here, that the charge assignment of the N fields then aid us to obtain neutrino masses through standard Seesaw-I [130, 131] mechanism (as detailed later), while it also prohibits the operator like $\bar{l_L}\Phi N$ due to $\mathcal{Z}_2$ charge assignment, and hence discards the possibility of generating the light neutrino mass radiatively. The ingredients and interactions of the model set up is described in the cartoon as in Fig. 5.1.

After spontaneous symmetry breaking, SM Higgs doublet acquires non-zero vacuum expectation value (VEV) as $H = (0\ \frac{v+h}{\sqrt{2}})^T$ with v=246 GeV. Also note that neither of the added scalars acquire VEV to preserve $\mathcal{Z}_2\times\mathcal{Z}'_2$ and act as DM components. After minimizing the potential $V(H,\Phi,\phi)$ along different field directions, one can obtain the following relations between the physical masses and the couplings involved:

$$\begin{aligned}\mu_H^2 &= \tfrac{m_h^2}{2}, \quad \mu_\Phi^2 = m_{H^0}^2 - \lambda_L v^2, \quad \lambda_3 = \tfrac{1}{v^2}(m_{H^0}^2 - m_{A^0}^2), \\ \lambda_2 &= \tfrac{1}{v^2}(m_{H^0}^2 + m_{A^0}^2 - 2m_{H^\pm}^2) \text{ and } \lambda_1 = 2\lambda_L - \tfrac{2}{v^2}(m_{H^0}^2 - m_{H^\pm}^2)\ ,\end{aligned} \tag{5.7}$$

where $\lambda_L = \frac{1}{2}(\lambda_1 + \lambda_2 + \lambda_3)$ and m_h, m_{H^0}, m_{A^0} are the mass eigenvalues of SM-like neutral scalar found at LHC (m_h = 125.09 GeV), heavy or light additional neutral scalar and the CP-odd neutral scalar respectively. $m_{H^\pm}$ denotes the mass of charged scalar eigenstate(s). The mass for ϕ DM will be rescaled as $m_\phi^2 = \mu_\phi^2 + \frac{1}{2}\lambda_{\phi h}v^2$. The independent parameters of the model, those are used to evaluate the DM, neutrino mass constraints are as follows:

$$\text{Parameters}: \quad \{m_{H^0}, m_{A^0}, m_{H^\pm}, m_\phi, \lambda_L, \lambda_{\phi h}, \lambda_\Phi, \lambda_\phi, Y_{\nu_{ij}}, M_{N_{ij}}\}. \tag{5.8}$$

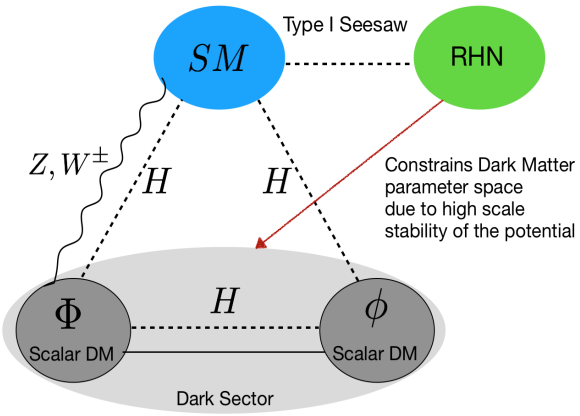

Figure 5.1: A schematic diagram illustrating the different sectors of the model and their connection to SM. The dotted lines represent Higgs portal coupling, wavy line indicate gauge coupling, while the thin solid line indicates direct DM-DM coupling through $\frac{\lambda_c}{2}\phi^2(\Phi^\dagger\Phi)$ term.

5.3 Theoretical and Experimental constraints

We would like to address possible theoretical and experimental constraints on model parameters here.

• **Stability:** In oder to get the potential bounded from below, the quartic couplings of the potential $V(H,\Phi,\phi)$ must have to satisfy following co-positivity conditions denoted as CPC$\{i\}$ [82, 132],

$$\begin{aligned}
\text{CPC}\{1,2,3\} &: \lambda_H(\mu) \geq 0, \quad \lambda_\Phi(\mu) \geq 0, \quad \lambda_\phi(\mu) \geq 0, \\
\text{CPC}\{4,5\} &: \Big(\lambda_1(\mu) + \lambda_2(\mu) \pm \lambda_3(\mu)\Big) + \sqrt{\lambda_H(\mu)\lambda_\Phi(\mu)} \geq 0, \\
\text{CPC}\{6,7\} &: \lambda_1(\mu) + 2\sqrt{\lambda_H(\mu)\lambda_\Phi(\mu)} \geq 0, \quad \lambda_{\phi h}(\mu) + \sqrt{\frac{2}{3}\lambda_H(\mu)\lambda_\Phi(\mu)} \geq 0, \\
&\text{CPC8} : \lambda_c(\mu) + \sqrt{\frac{2}{3}\lambda_\Phi(\mu)\lambda_\phi(\mu)} \geq 0\ , \qquad (5.9)
\end{aligned}$$

where μ is the running scale. The above conditions show that the model offers to choose even negative $\lambda_{1,2,3,\phi h}$ satisfying the above conditions. However, as demonstrated in Eqn. 5.8, we use λ_L and physical masses to be the parameters. Therefore, if we choose a specific mass hierarchy as: $m_{H^\pm} \geq m_{A^0} \geq m_{H^0}$ with positive λ_L, we are actually using λ_1 to be positive while $\lambda_{2,3}$ negative abiding by the above conditions (see Eqn. 5.7). The conditions CPC(i) as in Eqn. 5.9, will be used later in demonstrating stability of the potential in Sec. 5.7.

• **Perturbativity:** In oder to maintain perturbativity, the quartic couplings of the scalar potential $V(H,\Phi,\phi)$, gauge couplings $(g_{i=1,2,3})$ and neutrino Yukawa coupling

Y_ν should obey:

$$\begin{aligned} |\lambda_H(\mu)| < 4\pi, \quad |\lambda_\Phi(\mu)| < 4\pi, \quad |\lambda_\phi(\mu)| < 4\pi, \\ |\lambda_c(\mu)| < 4\pi, \quad |\lambda_{\phi h}(\mu)| < 4\pi, \\ |\lambda_1(\mu)| < 4\pi, \quad |\lambda_2(\mu)| < 4\pi, \quad |\lambda_3(\mu)| < 4\pi, \\ |g_{i=1,2,3}| < \sqrt{4\pi} \quad \text{and} \quad \left|\mathrm{Tr}\left[Y_\nu^\dagger(\mu) Y_\nu(\mu)\right]\right| < 4\pi \ . \end{aligned} \tag{5.10}$$

• **Tree Level Unitarity:** Next we turn to the constraints imposed by tree level unitarity of the theory, coming from all possible $2 \to 2$ scattering amplitudes as detailed in Appendix D follows as [133, 134]:

$$\begin{aligned} |\lambda_H| < 4\pi, \quad |\lambda_\Phi| < 4\pi, \\ |\lambda_c| < 8\pi, \quad |\lambda_{\phi h}| < 8\pi, \\ |\lambda_1| < 8\pi, \quad |\lambda_1 + 2(\lambda_2 + \lambda_3)| < 8\pi \\ |\lambda_1 + \lambda_2 + \lambda_3| < 8\pi, \quad |\lambda_1 - \lambda_2 - \lambda_3| < 8\pi, \\ |(\lambda_\Phi + \lambda_H) \pm \sqrt{(\lambda_2 + \lambda_3)^2 + (\lambda_H - \lambda_\Phi)^2}| < 8\pi, \\ \text{and} \quad |x_{1,2,3}| < 16\pi \ . \end{aligned} \tag{5.11}$$

where $x_{1,2,3}$ be the roots of the cubic equation as detailed in Appendix D.

• **Electroweak precision parameters:** There exists an additional $SU(2)_L$ doublet (Φ) in our model in addition to a gauge singlet scalar (ϕ). As the vev of Φ is zero, it does not alter the SM predictions of electroweak ρ parameter [83]. However IDM, being an $SU(2)_L$ doublet makes a decent contribution to S and T parameters [135, 136] which we will identify as ΔS and ΔT. The experimental bound from the global electroweak fit results on ΔS and ΔT using $\Delta U = 0$ are given by:

$$\Delta S|_{\Delta U=0} = 0.06 \pm 0.09, \quad \Delta T|_{\Delta U=0} = 0.1 \pm 0.07, \tag{5.12}$$

at 1σ level with correlation coefficient 0.91 [137]. We show the constraint from ΔS

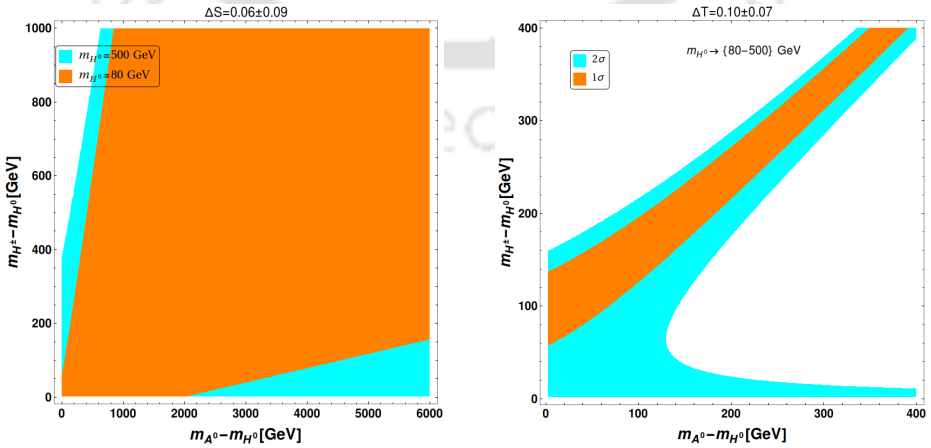

Figure 5.2: Constraints from ΔS (left) and ΔT (right) in $m_{A^0} - m_{H^0}$ and $m_{H^\pm} - m_{H^0}$ plane. For ΔS, we have taken 1σ limit for two different choices of $m_{H^0} = \{80, 500\}$ GeV. For ΔT scan, we show both 1σ and 2σ limits for a range of $m_{H^0} = \{80 - 500\}$ GeV.

and ΔT on the model parameter space in Fig. 5.2 using the standard formula as presented in [135, 136]. In left plot, we scan 1σ fluctuation on ΔS in $m_{A^0} - m_{H^0}$ versus $m_{H^\pm} - m_{H^0}$ plane for two different values of $m_{H^0} = \{80, 500\}$ GeV. We see that for smaller m_{H^0}, the constraint is larger. In right panel, we show 1σ and 2σ limits from ΔT in $m_{A^0} - m_{H^0}$ versus $m_{H^\pm} - m_{H^0}$ plane for a range of IDM mass $m_{H^0} = \{80 - 500\}$ GeV. We can clearly see, that ΔT constrains the mass splitting much more than ΔS.

• **Higgs invisible decay:** Whenever the DM particles are lighter than half of the SM Higgs mass, the Higgs can decay to DM and therefore it will contribute to Higgs invisible decay. Therefore, in such circumstances, we have to employ the bound on the invisible decay width of the 125.09 GeV Higgs as [38]:

$$\begin{aligned} Br(h \to \text{Inv}) &< 0.24 \\ \frac{\Gamma(h \to \text{Inv})}{\Gamma(h \to \text{SM}) + \Gamma(h \to \text{Inv})} &< 0.24\,. \end{aligned} \tag{5.13}$$

where

$$\Gamma(h \to \text{Inv}) = \Gamma(h \to H^0\ H^0) + \Gamma(h \to \phi\ \phi),\ \text{when}\ m_\phi, m_{H_0} < m_h/2 \sim 62.5\ \text{GeV};$$

and $\Gamma(h \to \text{SM}) = 4.2$ MeV [38]. In this analysis, we have mostly focused in the region where $m_\phi, m_{H_0} > m_h/2$, actually larger than W mass, i.e. $m_\phi, m_{H_0} \geq m_W$, so that the above constraint is not applicable.

• **Collider search constraints:** Experimental searches for additional charged scalars and pseudoscalar in LEP and LHC provide bound on IDM mass parameters and coupling coefficients of IDM with SM particles.
(i) Bounds from LEP: The observed decay widths of Z and W bosons from LEP data restrict the decay of gauge bosons to the additional scalars and therefore provide a bound on IDM mass parameters as $m_{A^0} + m_{H^0} > m_Z$, $2\ m_{H^\pm} > m_Z$ and $m_{H^\pm} + m_{H^0, A^0} > m_W$. In addition, neutralino searches at LEP-II, provides a lower limit on the pseudoscalar Higgs (m_{A^0}) to 100 GeV when $m_{H^0} < m_{A^0}$ [138]. The chargino search at LEP-II limits indicate a bound on the charged Higgs to $m_{H^\pm} > 70$ GeV [139].
(ii) Bounds from LHC: Due to the presence of SM Higgs and IDM interaction, charged scalars $H^\pm$ take part into the decay of SM Higgs to diphoton. Thus it contributes to Higgs to diphoton signal strength $\mu_{\gamma\gamma}$ which is defined as [140–143]

$$\mu_{\gamma\gamma} = \frac{\sigma(gg \to h \to \gamma\gamma)}{\sigma(gg \to h \to \gamma\gamma)_{\text{SM}}} \simeq \frac{\text{Br}(h \to \gamma\gamma)_{\text{IDM}}}{\text{Br}(h \to \gamma\gamma)_{\text{SM}}}. \tag{5.14}$$

Now when IDM particles are heavier than $m_h/2$, one can further write

$$\frac{\text{Br}(h \to \gamma\gamma)_{\text{IDM}}}{\text{Br}(h \to \gamma\gamma)_{\text{SM}}} = \frac{\Gamma(h \to \gamma\gamma)_{\text{IDM}}}{\Gamma(h \to \gamma\gamma)_{\text{SM}}}. \tag{5.15}$$

The analytic expression of $\Gamma(h \to \gamma\gamma)_{\text{IDM}}$ can be obtained as [140–143]:

$$\Gamma(h \to \gamma\gamma)_{\text{IDM}} = \left| \mathcal{A}_{\text{SM}} + \frac{\alpha_e m_h^{3/2}}{16\pi^{3/2}} \frac{\lambda_1 v}{m_{H^\pm}^2} F\left(\frac{m_h^2}{4m_{H^\pm}^2}\right) \right|^2, \tag{5.16}$$

where $\mathcal{A}_{\rm SM}$ represents pure SM contribution (see [140–143]). And $F(x) = -[x - f(x)]x^{-2}$ where

$$f(x) = \begin{cases} (\sin^{-1} x)^2, & x \leq 1 \\ -\frac{1}{4}\left[\ln\frac{1+\sqrt{1-x^{-1}}}{1-\sqrt{1-x^{-1}}} - i\pi\right]^2 & x > 1. \end{cases} \tag{5.17}$$

Therefore it turns out that IDM contribution to $\mu_{\gamma\gamma}$ is function of both mass of the

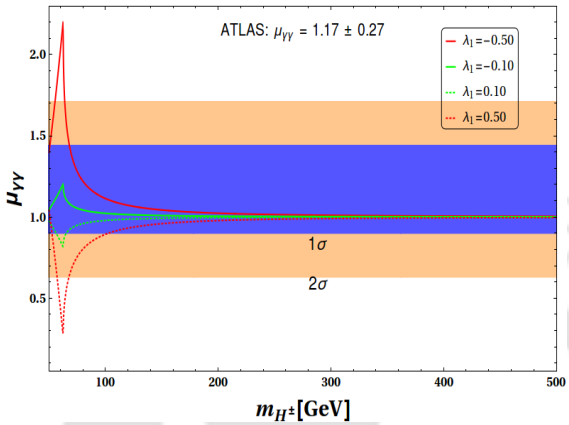

Figure 5.3: $\mu_{\gamma\gamma}$ as function of $m_{H^\pm}$ for different values of λ_1 as defined in the inset. 1σ and 2σ limits of $\mu_{\gamma\gamma}$ from ATLAS are also shown in blue and orange colours for comparison purpose.

charged Higgs ($m_{H^\pm}$) and the coefficient of the trilinear coupling hH^+H^- *i.e.* λ_1. The measured value of $\mu_{\gamma\gamma}$ are given by $\mu_{\gamma\gamma} = 1.17 \pm 0.27$ from ATLAS [144] and $\mu_{\gamma\gamma} = 1.14^{+0.26}_{-0.23}$ from CMS [145]. In Fig. 5.3, we show the variation of $\mu_{\gamma\gamma}$ as function of $m_{H^\pm}$ for different values of λ_1. We also present the experimental limits on $\mu_{\gamma\gamma}$ from ATLAS in Fig. 5.3. Excepting for the resonance at $m_{h/2}$, we see that our choice of λ_1 is consistent with experimental bound. The larger is $m_{H^\pm}$ GeV, $\mu_{\gamma\gamma} \to 1$ i.e. approches to SM value. Also, we see that $\lambda_1 > 0$ diminishes $\mu_{\gamma\gamma}$, while $\lambda_1 < 0$ tends to enhance it. In this analysis, we mostly consider $m_{H^\pm} > m_{h/2}$ and positive λ_1 within correct experimental limit.

• **Relic Density of DM:** The PLANCK experiment [146] provides the observed amount of relic abundance

$$0.1166 \leq \Omega_{\rm DM} h^2 \leq 0.1206\ . \tag{5.18}$$

Furthermore, strong constraints exist from direct DM search experiments. In our analysis we will consider the most recent bound on direct detection cross section provided by XENON 1T [27]. Relic density and direct search allowed parameter space of the model will be evaluated in details.

• **Neutrino observables:** The parameters associated to the neutrino sector should satisfy the bounds provided by different ongoing neutrino experiments. Limit on sum of light neutrino masses $\sum m_{\nu_i} \leq 0.12$ eV as provided by PLANCK data [146, 147] is incorporated. The present values of neutrino mass hierarchies and mixing angle can be found in [148, 149]. Due to the presence of RH neutrino in the set up, the constraint from lepton flavor violating decay (LFV) (dominantly from $\mu \to e\gamma$) will be applicable

[150–152]. LFV constraint can be successfully evaded for $M_N \gtrsim 10^{3.5}$ GeV [95, 153] even for neutrino Yukawa coupling of $\mathcal{O}(1)$. It is important to note that in our model, the IDM does not interact with SM leptons and thus plays no role in LFV.

5.4 Single component DM frameworks involving ϕ or H^0

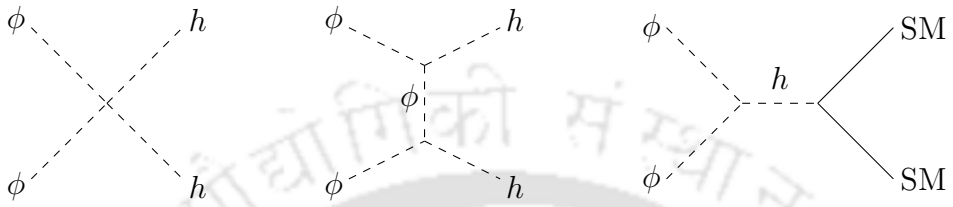

Figure 5.4: Annihilation processes of real scalar singlet DM (ϕ) to SM particles. SM in the last graph stands for $W^{\pm}, Z, h$ and SM fermions.

The model inherits two DM candidates: inert DM H^0 and singlet scalar DM ϕ. Both the DM components have been studied extensively in literature as individual candidates to satisfy relic density and direct search bounds. Let us first revisit the single component frameworks for these two cases here. The relic density of scalar singlet (ϕ) is obtained via thermal freeze out through annihilation to SM through the Feynman graphs shown in Fig. 5.4. The direct search constraint for ϕ comes from the t- channel Higgs portal interaction (turning the last graph of Fig. 5.4 upside down). The relevant parameters of the model are [22, 67, 94]:

$$\phi \text{ as single component DM} : \{m_\phi, \lambda_{\phi h}\}. \tag{5.19}$$

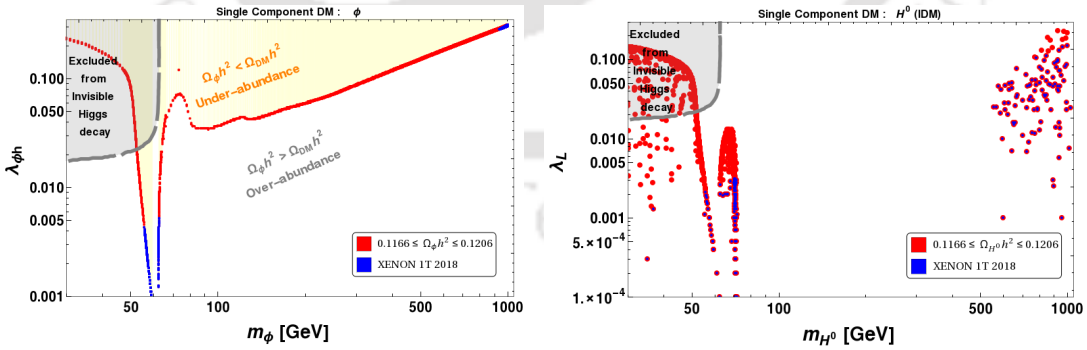

Figure 5.5: Relic density (red dots) and direct search/XENON1T (blue dots) allowed parameter space of the single component DM; scalar singlet (ϕ) on left (in $m_\phi - \lambda_{\phi h}$ plane) and IDM (H^0) on right (in $m_{H^0} - \lambda_L$ plane). For the right hand side plot, we have used: $0 \leq m_{A^0} - m_{H^0} \leq 200$ GeV, $1 \leq m_{H^\pm} - m_{H^0} \leq 400$ GeV, and $\lambda_\Phi = 0.001$.

The allowed parameter space of ϕ is depicted in left hand side (LHS) of Fig. 5.5 in $m_\phi - \lambda_{\phi h}$ plane by the red dots. Direct search allowed parameter space from XENON1T data [27, 44] using spin-independent DM-nucleon scattering cross section is shown by

the blue dots. We therefore see that the model can only survive either in the Higgs resonance region ($\sim m_h/2$) or at a very heavy mass $\gtrsim$ 900 GeV. The under abundant (shown in yellow) and over abundant regions are also indicated.

IDM (H^0) as a single component DM have annihilation and co-annihilation chan-

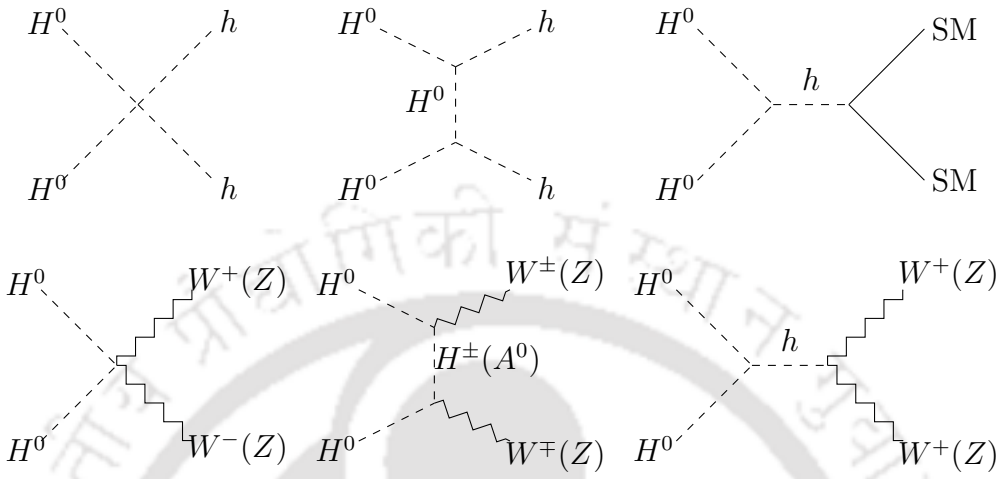

Figure 5.6: Annihilation processes of IDM (H^0) to SM particles. SM in the top right graph stands for $W^\pm, Z, h$ and SM fermions.

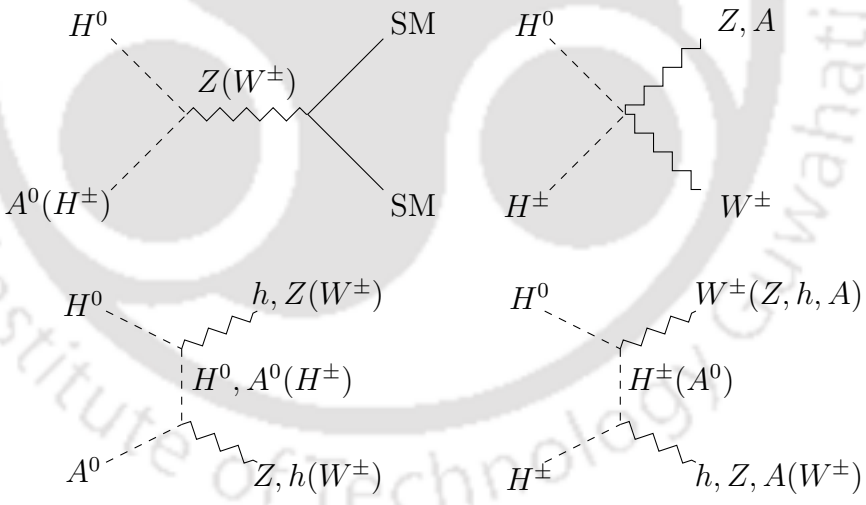

Figure 5.7: Co-annihilation processes of IDM (H^0) with A^0 and $H^\pm$ to SM particles. SM in the top left graph stands for $W^\pm, Z, h$ and SM fermions in suitable combination.

nels for freeze-out due to both gauge and Higgs portal interactions as shown by the Feynman graphs in Figs. 5.6 and 5.7. The parameters, which govern the IDM phenomenology are [154]:

$$H^0 \text{ as single component DM: } \{m_{H^0}, m_{A^0}, m_{H^\pm}, \lambda_L\}. \tag{5.20}$$

Relic density allowed parameter space for single component IDM is shown in right hand side (RHS) of Fig. 5.5 in $m_{H^0} - \lambda_L$ plane by red dots. Direct search (XENON1T data)

allowed points are shown by blue dots. The scan is obtained using $1 \leq m_{A^0} - m_{H^0} \leq 200$ GeV, $1 \leq m_{H^\pm} - m_{H^0} \leq 400$ GeV with self coupling $\lambda_\Phi = 0.001$ kept constant. Here we see again that allowed region from relic density and direct search constraint for IDM lies either in the small mass region $m_{H^0} \lesssim m_W \sim 80$ GeV or in the heavy mass region $m_{H^0} \gtrsim 550$ GeV. It is a well known result coming essentially due to too much annihilation and co-annihilation of IDM to SM through gauge interactions [154]. The disallowed region 80 GeV $< m_{H^0} <$ 550 GeV is often called desert region, which is obviously under abundant. Another important point of single component IDM is that the direct search allowed parameter space beyond resonance ($m_{H^0} \gtrsim 550$ GeV) have significant co-annihilation dependence with $m_{H^\pm} - m_{H^0} \lesssim 10$ GeV and $m_{A^0} - m_{H^0} \lesssim 10$ GeV.

5.5 Two component DM set-up with ϕ and H^0

5.5.1 Coupled Boltzmann Equations and Direct search

In presence of two DM components (ϕ and H^0) DM-DM conversion plays a crucial role. The heavier DM can annihilate to the lighter component and thus contribute to the freeze-out of heavier DM. The conversion processes are shown in Fig. 5.8, which shows that they are dictated by four point contact interactions as well as by Higgs portal coupling. It is clear that $H^\pm, A^0$ are not really DM, but belongs to dark sector, hence annihilation to them is broadly classified within DM-DM conversion. More importantly none of them contribute to direct search. The two component DM set up therefore requires following parameters for analysis:

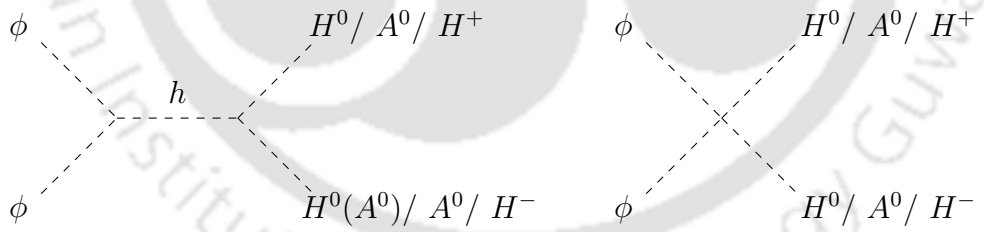

Figure 5.8: DM $\rightarrow$ DM conversion processes in a model with ϕ and H^0. We have assumed $m_\phi > m_{H^0}, m_{H^\pm}, m_{A^0}$ here. The reverse processes occur with reverse hierarchy.

$$\text{Two component DM}: \ \{m_{H^0}, m_{A^0}, m_{H^\pm}, m_\phi, \lambda_L, \lambda_{\phi h}\}. \tag{5.21}$$

There are two self interacting quartic couplings present in the model; namely λ_Φ and λ_ϕ, which do not play an important role in DM analysis, but appear in vacuum stability constraint that we discuss later.

When $m_\phi > m_{H^0}, m_{H^\pm}, m_{A^0}$, then ϕ can annihilate to all possible IDM components. The dominant s- wave DM-DM conversion cross-sections (σv) of ϕ in non-relativistic

approximation are given by:

$$\begin{aligned}
(\sigma v)_{\phi\ \phi\to H^0\ H^0} &= \frac{1}{64\pi {m_\phi}^2}\left[\lambda_c + \frac{2\lambda_L\lambda_{\phi h}v^2}{(4{m_\phi}^2 - m_h^2)}\right]^2\sqrt{1-\frac{4m_{H^0}^2}{4m_\phi^2}}\ \Theta(m_\phi - m_{H^0}) \\
(\sigma v)_{\phi\ \phi\to A^0\ A^0} &= \frac{1}{64\pi m_\phi^2}\left[\lambda_c + \frac{2\lambda_S\lambda_{\phi h}v^2}{(4{m_\phi}^2 - m_h^2)}\right]^2\sqrt{1-\frac{4m_{A^0}^2}{4m_\phi^2}}\ \Theta(m_\phi - m_{A^0}) \\
(\sigma v)_{\phi\ \phi\to H^+\ H^-} &= \frac{1}{32\pi m_\phi^2}\left[\lambda_c + \frac{\lambda_1\lambda_{\phi h}v^2}{(4{m_\phi}^2 - m_h^2)}\right]^2\sqrt{1-\frac{4m_{H^\pm}^2}{4m_\phi^2}}\ \Theta(m_\phi - m_{H^\pm})
\end{aligned} \tag{5.22}$$

where $\lambda_S = \frac{1}{2}(\lambda_1 + \lambda_2 - \lambda_3)$. On the other hand, when $m_\phi < m_{H^0}$, the conversion process will be as $H^0H^0(A^0) \to \phi\phi$ or $H^+H^- \to \phi\phi$. The corresponding cross-sections can easily be gauged from Eqn. 5.22.

The evolution of DM number density for both components (ϕ and H^0) in early universe as a function of time is obtained by coupled Boltzmann equations (CBEQ) as described in Eqn. 5.23:

$$\begin{aligned}
\frac{dn_{H^0}}{dt} + 3Hn_{H^0} = &-\sum_X \langle\sigma v\rangle_{H^0\ X\to SM\ SM}\left(n_{H^0}n_X - n_{H^0}^{eq}n_X^{eq}\right)\ \Theta(m_{H^0} + m_X - 2\ m_{SM}), \\
&-\sum_X \langle\sigma v\rangle_{H^0\ X\to\phi\phi}\left(n_{H^0}n_X - \frac{n_{H^0}^{eq}n_X^{eq}}{n_\phi^{eq2}}{n_\phi}^2\right)\ \Theta(m_{H^0} + m_X - 2\ m_\phi), \\
&+\sum_{X,Y} \langle\sigma v\rangle_{\phi\phi\to X\ Y}\left({n_\phi}^2 - \frac{n_\phi^{eq2}}{n_X^{eq}n_Y^{eq}}n_Xn_Y\right)\ \Theta(2m_\phi - m_X + m_Y); \\
\frac{dn_\phi}{dt} + 3Hn_\phi = &-\langle\sigma v\rangle_{\phi\phi\to SM\ SM}\left({n_\phi}^2 - n_\phi^{eq2}\right)\ \Theta(m_\phi - \ m_{SM}), \\
&-\sum_{X,Y} \langle\sigma v\rangle_{\phi\phi\to X\ Y}\left({n_\phi}^2 - \frac{n_\phi^{eq2}}{n_X^{eq}n_Y^{eq}}n_Xn_Y\right)\ \Theta(2m_\phi - m_X + m_Y), \\
&+\sum_X \langle\sigma v\rangle_{H^0\ X\to\phi\phi}\left(n_{H^0}n_X - \frac{n_{H^0}^{eq}n_X^{eq}}{n_\phi^{eq2}}{n_\phi}^2\right)\ \Theta(m_{H^0} + m_X - 2\ m_\phi)
\end{aligned} \tag{5.23}$$

where $\{X, Y\} = \{H^0, A^0, H^\pm\}$. We can clearly spot DM-DM conversion contributions in second and third lines of each equation, which actually make the two equations 'coupled'. The freeze-out of two component DM is therefore obtained by numerically solving the above CBEQ and yields relic density (for a detailed discussion see for example [23]). The total relic density (Ω_{DM}) will then have contributions from both DM components as:

$$\Omega_{DM}h^2 = \Omega_{H^0}h^2 + \Omega_\phi h^2. \tag{5.24}$$

Now let us turn to direct search of two component DM set up. Both the DM candidates can be detected through the spin independent (SI) direct detection (DD) processes through t-channel Higgs mediation as depicted in Fig. 5.9. The SI DD cross section for H^0 (σ_{H^0}) and for ϕ (σ_ϕ) turn out to be [22, 23]:

$$\sigma_{H^0}^{eff} = \left(\frac{\Omega_{H^0}h^2}{\Omega_{DM}h^2}\right)\frac{\lambda_L^2 f_N^2}{\pi}\frac{\mu_{H^0,N}^2 m_N^2}{m_h^4 m_{H_0}^2}, \quad \sigma_\phi^{eff} = \left(\frac{\Omega_\phi h^2}{\Omega_{DM}h^2}\right)\frac{\lambda_{\phi h}^2 f_N^2}{4\pi}\frac{\mu_{\phi,N}^2 m_N^2}{m_h^4 m_\phi^2}, \tag{5.25}$$

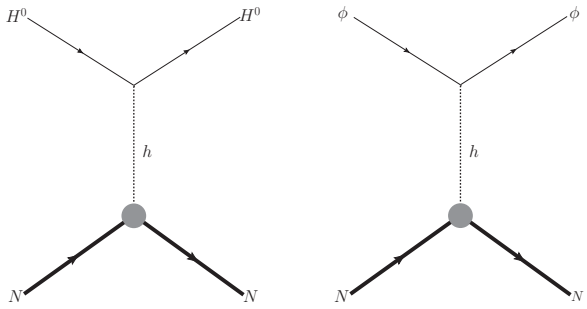

Figure 5.9: Spin independent direct detection processes for IDM (left) and scalar singlet DM (right).

where $\mu_{\phi,N} = \frac{m_\phi\ m_N}{m_\phi + m_N}$ and $\mu_{H^0,N} = \frac{m_{H^0}\ m_N}{m_{H^0} + m_N}$ are the reduced masses. $f_N = 0.2837$ represents the form factor of nucleon [90, 91] and $m_N = 0.939$ GeV represents nucleon mass. Importantly, the effective direct search cross-section for each individual component is modified by the fraction with which it is present in the universe, given by $\frac{\Omega_{H^0}h^2}{\Omega_{DM}h^2}$ for H^0 and $\frac{\Omega_\phi h^2}{\Omega_{DM}h^2}$ for ϕ [1].

To obtain relic density and DD cross sections of both the DM candidates numerically, we have used `MicrOmegas` [155]. It is noteworthy, that version 4.3 of `MicrOmegas` is capable of handling two component DM and we have cross-checked the solution from the code to match very closely to the numerical solution of CBEQ in Eqn. 5.23. For generating the model files compatible with `MicrOmegas`, we have implemented the model in `LanHEP` [156].

5.5.2 Role of DM-DM conversion in relic density

We first study the variation of relic density with respect to DM mass and other relevant parameters to extract the importance of DM-DM conversion in this two-component set up before elaborating on the relic density and direct search allowed parameter space of the model.

In Fig. 5.10 we plot relic densities of two DM candidates: $\Omega_{H^0}h^2$ in left panel and $\Omega_\phi h^2$ in right panel figures as function of m_{H^0} for different values of λ_c. We also keep m_ϕ fixed at 200 GeV here. Other parameters are chosen as mentioned in the inset of individual plots.

• Top left of Fig. 5.10: In this figure we have shown the variation of $\Omega_{H^0}h^2$ with m_{H^0} for different values of $\lambda_c = 0, 10^{-5}, 0.01, 0.2$ by yellow, blue, purple and black solid lines respectively. Pure IDM case (in a single component framework) is depicted by red dotted line, where also evidently $\lambda_c = 0$. It is important to note the other parameters kept fixed for this plot are: $\lambda_{\phi h} = 10^{-5}, \lambda_L = 0.1, m_{H^\pm} - m_{A^0} = m_{A^0} - m_{H^0} = 5$ GeV. We see that for $m_{H^0} < m_\phi$, relic density of H^0 changes significantly with the variation of λ_c. We also see that $\lambda_c = 0$ (in two component set-up) is way above the pure IDM case yielding a large relic density. Now, with slight increase in $\lambda_c = 10^{-5}$, relic density goes further up and then reduces significantly for larger $\lambda_c = 0.01, 0.2$. The interesting point is that the case of $\lambda_c = 0.2$ lies very close to the pure IDM case. It is therefore evident that the presence of the second DM component ϕ plays an important role in $\Omega_{H^0}h^2$ through the coupling λ_c. For $m_{H^0} < m_\phi$, relic density of the heavier component

[1] A more comprehensive bound on multipartite DM from direct search can be obtained from the recoil rate of the nucleus [54, 63].

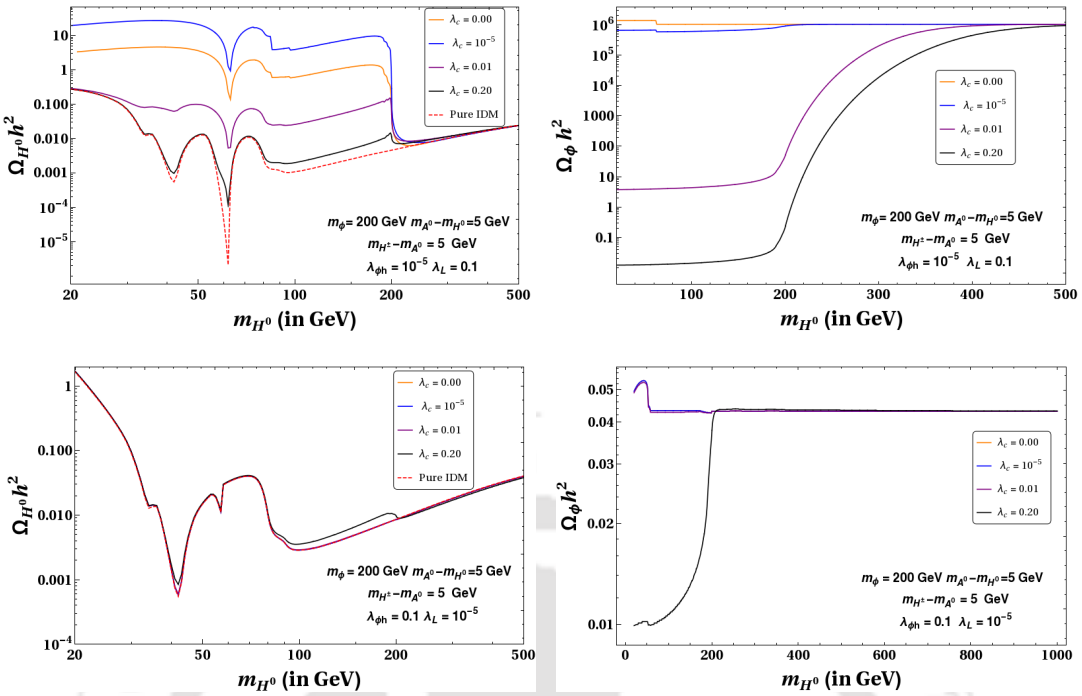

Figure 5.10: Relic Density of IDM, H^0 (left panel) and scalar DM, ϕ (right panel) as a function of IDM mass m_{H^0}, with different choices of λ_c. We illustrate two different combinations of DM-SM couplings, in the top panel: $\{\lambda_{\phi h} = 10^{-5},\ \lambda_L = 0.1\}$ and in bottom panel: $\{\lambda_{\phi h} = 0.1,\ \lambda_L = 10^{-5}\}$. Other parameters kept fixed, are mentioned in the inset of each figure.

ϕ can easily inherit the annihilation to other DM components $\{X, Y\} = \{H^0, A^0, H^\pm\}$ in addition to SM as[15, 23]:

$$\Omega_\phi h^2 \simeq \frac{854.45 \times 10^{-13} x_f}{\sqrt{g_*}(\langle\sigma v\rangle_{\phi\phi\to \text{ SM SM}} + \langle\sigma v\rangle_{\phi\phi\to XY})} \simeq \frac{0.1 \text{ pb}}{\langle\sigma v\rangle_{\phi\phi\to \text{ SM SM}} + \langle\sigma v\rangle_{\phi\phi\to XY}}, \quad (5.26)$$

where in the last step, we have used $g_* = 106.7$ and $x_f = 20$ [15]. However it is difficult to envisage the relic density for the lighter DM component due to such DM-DM conversion. This can be understood from the CBEQ for the two component DM as in Eqn. 5.23. Let us define the following notations first:

$$\begin{aligned} \langle\sigma v\rangle_{H^0 X\to SM}\ n_{H^0} n_X = \mathcal{F}_{H^0}\ ;\quad \langle\sigma v\rangle_{\phi\phi\to XY}\ n_\phi^2 = \mathcal{F}_{\phi\Phi}\ ; \\ \langle\sigma v\rangle_{\phi\phi\to SM}\ n_\phi^2 = \mathcal{F}_\phi;\qquad \langle\sigma v\rangle_{H^0 X\to\phi\phi}\ n_{H^0} n_X = \mathcal{F}_{\Phi\phi}\ . \end{aligned} \quad (5.27)$$

Again $\{X, Y\} = H^0, A^0, H^\pm$; as earlier. The CBEQ with above notation, turns out to be (assuming $m_\phi > m_{H^0}$):

$$\begin{aligned} \frac{dn_{H^0}}{dt} + 3Hn_{H^0} &\simeq -\mathcal{F}_{H^0} + \mathcal{F}_{\phi\Phi}\ ; \\ \frac{dn_\phi}{dt} + 3Hn_\phi &\simeq -\mathcal{F}_\phi - \mathcal{F}_{\phi\Phi}\ . \end{aligned} \quad (5.28)$$

In Eqn. 5.28, we neglected the equilibrium number densities as they are tiny near freeze-out, where the dynamics is under study. With $\lambda_c = 0$, and $\lambda_{\phi h} = 10^{-5}$, annihilation cross-sections for ϕ, ($\langle\sigma v\rangle_{\phi\ \phi\to \text{SM SM}}$ and $\langle\sigma v\rangle_{\phi\ \phi\to \text{X Y}}$) are very small. Hence ϕ freezes

out early and the number density of ϕ turns out to be large since $n_\phi \propto 1/\langle\sigma v\rangle_\phi^{\rm eff}$ where $\langle\sigma v\rangle_\phi^{\rm eff} \simeq \left(\langle\sigma v\rangle_{\phi\phi\to \text{ SM SM}} + \langle\sigma v\rangle_{\phi\phi\to X\ Y}\right)$ following Eqn. 5.26. Now, it is easy to appreciate that with $\lambda_c = 0$, and $\lambda_{\phi h} = 10^{-5}$, annihilation of ϕ to SM is larger than conversion to other DM (H^0), i.e. $\langle\sigma v\rangle_{\phi\phi\to \text{ SM SM}} \gg \langle\sigma v\rangle_{\phi\phi\to XY}$. However due to large ϕ abundance ($n_\phi \sim 0.1$)[2], $\mathcal{F}_{\phi\Phi}$ becomes comparable with $\mathcal{F}_{H^0}$. As these two terms ($\mathcal{F}_{\phi\Phi}$ and $\mathcal{F}_{H^0}$) appear in the evolution of n_{H^0} (Eqn. 5.28) with opposite sign, it is quite evident that effective annihilation cross-section for H^0 becomes small and hence n_{H^0} after freeze out turns out to be much larger than the pure IDM case. Next let us consider non zero but small λ_c ($= 10^{-5}$). Then $\langle\sigma v\rangle_{\phi\phi\to X\ Y}$ increases compared to the earlier case of $\lambda_c = 0$. However due to smallness of the coupling λ_c, this does not make any significant change in the number density of ϕ and $n_\phi \sim 0.1$ remains the same (as $\phi\ \phi \to$ SM SM still dominantly contributes to the total annihilation cross section of ϕ). Therefore, $\mathcal{F}_{\phi\Phi}$ increases and reduces the separation with $\mathcal{F}_{H^0}$. Hence the effective annihilation cross-section for H^0 turns out to be even smaller than $\lambda_c = 0$ case. Therefore, for $\lambda_c = 10^{-5}$ relic density increases further than that of $\lambda_c = 0$. For larger value of $\lambda_c = 0.01$, contribution from DM-DM conversion, $\langle\sigma v\rangle_{\phi\phi\to X\ Y}$ significantly rises and therefore the number density of n_ϕ drops to $n_\phi \sim 10^{-5}$, and therefore $\mathcal{F}_{\phi\Phi}$ becomes much smaller than $\mathcal{F}_{H^0}$. This increases the effective annihilation for H^0 and reduces relic density. This trend continues for higher values of λ_c and eventually leads to a vanishingly small $\mathcal{F}_{\phi\Phi}$ to closely mimic the case of single component IDM. The case of $m_{H^0} > m_\phi$ can also be understood from the CBEQ in this limit:

$$\begin{aligned} \frac{dn_{H^0}}{dt} + 3Hn_{H^0} &\simeq -\mathcal{F}_{H^0} - \mathcal{F}_{\Phi\phi}\ ; \\ \frac{dn_\phi}{dt} + 3Hn_\phi &\simeq -\mathcal{F}_\phi + \mathcal{F}_{\Phi\phi}\ . \end{aligned} \tag{5.29}$$

For $m_{H^0} > m_\phi$, relic density of H^0 can be written simply as

$$\Omega_{H^0}h^2 \simeq \frac{0.1\text{ pb}}{\langle\sigma v\rangle_{H^0X\to \text{ SM SM}} + \langle\sigma v\rangle_{H^0X\to\phi\phi}}. \tag{5.30}$$

The annihilation to SM ($\langle\sigma v\rangle_{H^0X\to \text{ SM SM}}$) due to gauge coupling is much larger than the conversion cross-section $\langle\sigma v\rangle_{H^0X\to\phi\phi}$ for all the choices of λ_c, so we do not find any distinction between all those cases.

• Top right of Fig. 5.10: In the top right panel, the same parameter space is used to show the variation of $\Omega_\phi h^2$ with respect to m_{H^0}. The dynamics is much simpler for $m_\phi > m_{H^0}$ (see BEQ. 5.28) where $\Omega_\phi h^2 \simeq \frac{0.1\text{ pb}}{\langle\sigma v\rangle_{\phi\phi\to \text{ SM SM}} + \langle\sigma v\rangle_{\phi\phi\to X\ Y}}$. With larger λ_c, the conversion to other DM ($\mathcal{F}_{\phi\Phi}$) becomes larger and relic density drops accordingly. For $m_\phi < m_{H^0}$, we see from Eqn. 5.29, that there is a competition between $\mathcal{F}_\phi$ and $\mathcal{F}_{\Phi\phi}$. With increasing m_{H^0}, $\langle\sigma v\rangle_{H^0X\to\phi\phi}$ decreases, therefore $\mathcal{F}_{\Phi\phi}$ decreases and eventually it becomes vanishingly small for $m_{H^0} \gtrsim 400$ GeV. The equation for n_ϕ then becomes equivalent to the single component case of ϕ where m_{H^0} is no more relevant for $\Omega_\phi h^2$.

• The bottom panel figures of Fig. 5.10 essentially indicate that with larger $\lambda_{\phi h}$, annihilation of ϕ to SM becomes large, resulting a smaller n_ϕ after freeze out. Therefore $\mathcal{F}_{\phi\Phi}$ in Eqn. 5.28 turns insignificant. On the other hand, $\mathcal{F}_{\Phi\phi}$ also becomes smaller than $\mathcal{F}_\phi$ in Eqn. 5.29. Together, relic density of the lighter DM component is not affected by the presence of a heavy DM component.

[2] n_ϕ can be calculated by using the formula $\Omega_\phi = \frac{n_\phi m_\phi}{\rho_c}$, where $\rho_c = 1.05\times10^{-5}h^2$ GeV cm^{-3}[15].

Before we move on, let us summarise the outcome of Fig. 5.10. We see here that relic density of lighter DM component is affected by the heavier one, when the annihilation cross-section to SM is tiny.

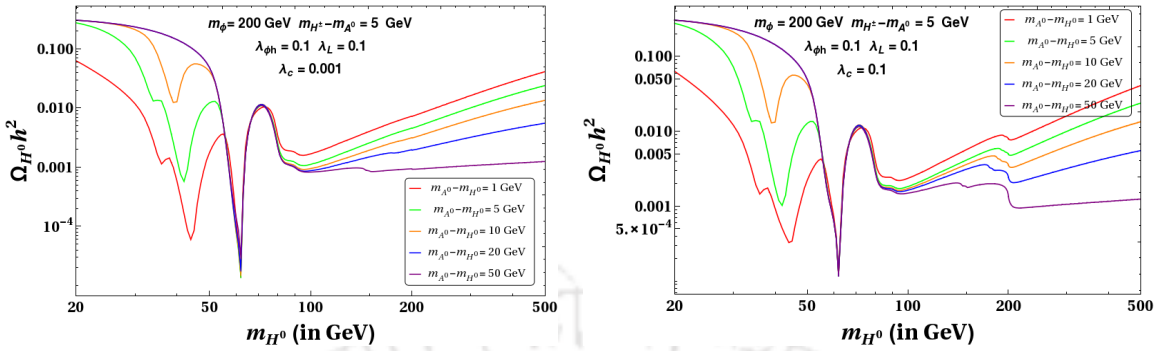

Figure 5.11: $\Omega_{H^0}h^2$ vs m_{H^0} for $\lambda_c = 0.001$ (left panel) and $\lambda_c = 0.1$ (right panel) with different choices of $m_{A^0} - m_{H^0}$ which are depicted by different coloured lines in the figure. The other parameters kept fixed are mentioned in the inset of each figure.

There is an interesting feature of IDM relic density coming from co-annihilation channels that we illustrate next in Fig. 5.11. We plot the variation of IDM relic density as function of DM mass m_{H^0} for different choices of $\Delta m = m_{A^0} - m_{H^0}$: $\{1 - 50\}$ GeV shown by different coloured lines. The other parameters are kept fixed and mentioned explicitly in the figure insets. Let us first focus on the left panel plot. We see that for $m_{H^0} < m_W$, with larger $\Delta m = m_{A^0} - m_{H^0}$, relic density is larger, which follows the usual convention of co-annihilation cross-section being reduced by Boltzmann suppression ($e^{-\Delta m/T}$) with larger splitting (Δm). However, for $m_{H^0} > m_W$, the phenomena is reverse and with larger mass splitting, relic density decreases. This is indeed intriguing, which can be understood by looking at the co-annihilation channels in Fig. 5.7. When $m_{H^0} < m_W$, co-annihilation occurs to SM only through the s-channel graph. However, for $m_{H^0} > m_W$, W final state opens up including that of t-channel graphs. The t-channel contributions inherit a negative sign to that of s-channel or contact interaction. This therefore causes a destructive interference and reduces the co-annihilation cross-section significantly for small Δm. When the splitting Δm increases, the t-channel term gets larger and reduces the effective destructive interference to increase the co-annihilation contribution even on top of the larger Boltzmann suppression. Therefore, we see that relic density in $m_{H^0} > m_W$ region becomes larger with larger Δm. The same feature prevails in the right panel figure. Here, for a larger λ_c, the relic density of H^0 goes further down due to annihilation to ϕ beyond $m_{H^0} > m_\phi$.

5.6 Relic density and Direct Search allowed parameter space

One of the important motivations of this analysis is to study interacting multi-component DM phenomenology for DM mass lying between $80 \leq m_{DM} \leq 500$ GeV for both the components in view of relic density ($0.1166 \leq \Omega_{DM}h^2 (\equiv \Omega_{H^0}h^2 + \Omega_\phi h^2) \leq 0.1206$ [146]) and direct detection (XENON 1T [27]) bounds. We would like to recall that for the individual scenarios, none of the DM components satisfy relic and direct detection

bounds simultaneously within this mass range (see section 5.4). Now in order to find a consistent parameter space in the set up, we perform a numerical scan of the relevant parameters within the specified ranges as mentioned below.

$$\begin{aligned} 80 \ \leq m_{H^0} \leq 500 \text{ GeV}, \ 80 \leq \ m_\phi \leq 500 \text{ GeV}, \\ 0 \ \leq m_{A^0} - m_{H^0} \leq 200 \text{ GeV}, \ 0 \leq \ m_{H^\pm} - m_{A^0} \leq 180 \text{ GeV}, \\ 0.001 \leq \lambda_L \leq 0.30, \quad 0.001 \leq \lambda_{\phi h} \leq 0.20 \ , \quad 0.01 \leq \lambda_c \leq 1.00 \ . \end{aligned} \tag{5.31}$$

We also note here that as λ_L and $\lambda_{\phi h}$ enters into direct search cross-sections for H^0 and ϕ DMs respectively, we keep those couplings in a moderate range, while λ_c governs DM-DM interactions, but do not directly enter into direct search bounds, therefore we choose a larger range (with natural values) for scanning λ_c. $\lambda_\phi = 0.001$ and $\lambda_\Phi = 0.001$ are kept fixed throughout the analysis since those are not relevant for DM phenomenology.

There are two possible mass hierarchies for the two-component DM set up relevant for phenomenological analysis: (i) $m_\phi > m_{H^0}$ and (ii) $m_\phi \leq m_{H^0}$, which we address separately below.

Case I: $m_\phi > m_{H^0}$

Primarily, in such a scenario, the main physics arises due to annihilation of ϕ to H^0, on top of their individual annihilation to SM to govern the freeze-out.

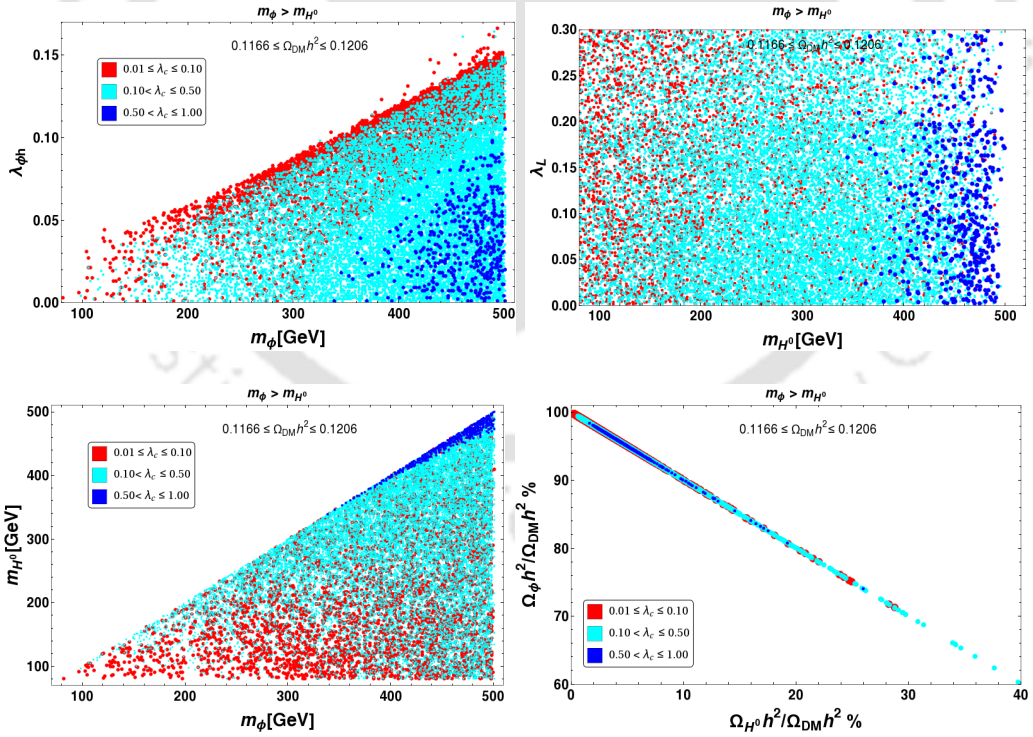

Figure 5.12: Relic Density allowed parameter space is shown in $m_\phi - \lambda_{\phi h}$ plane (top left), $m_{H^0} - \lambda_L$ plane (top right), $m_\phi - m_{H^0}$ plane (bottom left) and $\Omega_\phi h^2/\Omega_{DM}h^2(\%) - \Omega_{H^0}h^2/\Omega_{DM}h^2(\%)$ plane (bottom right) for the mass hierarchy $m_\phi > m_{H^0}$.

In Fig. 5.12, we show relic density allowed parameter space for the model in terms of different relevant parameters. In top left panel of Fig. 5.12, we have shown the relic

density satisfied (considering contribution from both ϕ and H^0 components) points in $m_\phi - \lambda_{\phi h}$ plane for different ranges of λ_c, as depicted in the figure with different colour codes. As seen from the plot, for a fixed m_ϕ, there is a maximum $\lambda_{\phi h}$. All possible values less than the maximum $\lambda_{\phi h}$ is also allowed subject to different choices of λ_c. The larger is λ_c, the smaller is the required $\lambda_{\phi h}$ thanks to the conversion of $\phi \to H^0$ to yield relic density. It is also noted that for large $\lambda_c \gtrsim 0.5$, as the DM-DM conversion is very high, the DM mass m_ϕ has to lie in the high mass region ($\gtrsim$ 400 GeV) to tame the annihilation cross-section within acceptable range. To summarise, this figure shows that due to the presence of second DM component, much larger parameter space (actually the over-abundant regions of the single component framework, compare Fig. 5.5) is allowed. Top right panel figure shows the relic density allowed parameter space in $m_{H^0} - \lambda_L$ plane again for different ranges of λ_c as in the left plot. It naturally depicts that λ_L is insensitive to m_{H^0} as the annihilation and co-annihilation cross-section of H^0 is mainly dictated by gauge interaction. However, we see a mild dependence on λ_c, such that when $\lambda_c \gtrsim 0.5$, the DM mass m_{H^0} has to be heavy $\gtrsim$ 400 GeV. This is because with large λ_c, DM-DM conversion is large; to achieve relic density of correct order, m_ϕ requires to be large and the conversion can only be tamed down by phase space suppression, i.e. by choosing H^0 mass as close as possible to ϕ mass ($m_{H^0} \sim m_\phi$). Bottom left figure correlates the DM masses to obtain correct density within $m_\phi > m_{H^0}$. We see that for small λ_c, particularly with higher m_ϕ, large m_{H^0} values are disfavoured in order to keep the DM-DM conversion in the right order. While for large λ_c, mass degeneracy is required ($m_{H^0} \sim m_\phi$) to tame the DM-DM conversion. Bottom right figure shows the relative contribution of relic density of the two DM components. First of all, this shows that ϕ contributes with larger share of relic density, while the relic density of H^0 can at most be 40% of the total. For small λ_c, contribution from H^0 is even smaller, as relic density contribution from ϕ gets larger due to small DM-DM conversion. However, with large λ_c, the DM-DM conversion for ϕ becomes larger and therefore the relic density of ϕ can easily span between $60 - 100\%$. With very high $\lambda_c \sim 1$, DM-DM conversion becomes too large, therefore to keep relic density in the correct ballpark, the DM mass (m_ϕ) has to be heavy and almost degenerate with the heavier DM ($m_{H^0} \sim m_\phi$). $\lambda_{\phi h}$ in such cases, requires to be very small, which are validated by some dark blue points with $\Omega_\phi h^2/\Omega_{DM} h^2 \sim 60\%$.

Relic density allowed parameters space consistent with direct search constraints where both DMs ϕ and H^0 simultaneously satisfy XENON 1T 2018 [157] bound (for different ranges of λ_c) are shown next in Fig. 5.13. This is illustrated in $m_\phi - \lambda_{\phi h}$ plane (top left panel), $m_{H^0} - \lambda_L$ plane (top right panel) and in $m_\phi - m_{H^0}$ plane (bottom panel) similar to Fig. 5.12. We have already mentioned that spin independent (SI) DM-nucleon cross-section depends on square of Higgs portal couplings of the respective DM candidates, $\lambda_{\phi h}$ for ϕ and λ_L for H^0 scaled by a pre-factor of the relative number density $\Omega_i h^2/\Omega_{DM} h^2$ ($i = \phi,\ H^0$). Since in this two component scenario, the dominant contribution is coming from ϕ DM, the pre-factor $\Omega_\phi h^2/\Omega_{DM} h^2 \sim 1$. On the other hand, for H^0 the pre-factor is small, $\Omega_{H^0} h^2/\Omega_{DM} h^2 < 1$, and will help H^0 reducing the effective direct search cross-section. Therefore, portal coupling $\lambda_{\phi h}$ is tightly constrained from XENON 1T bound to $\lambda_{\phi h} \lesssim 0.1$ for DM mass $m_\phi \lesssim 500$ GeV, as shown in top left panel of Fig. 5.13 (compare it with the top left panel of Fig. 5.12). Similarly in top right panel, the direct search allowed $m_{H^0} - \lambda_L$ plane for H^0 shows that a large region corresponding to higher λ_L is excluded as a function of

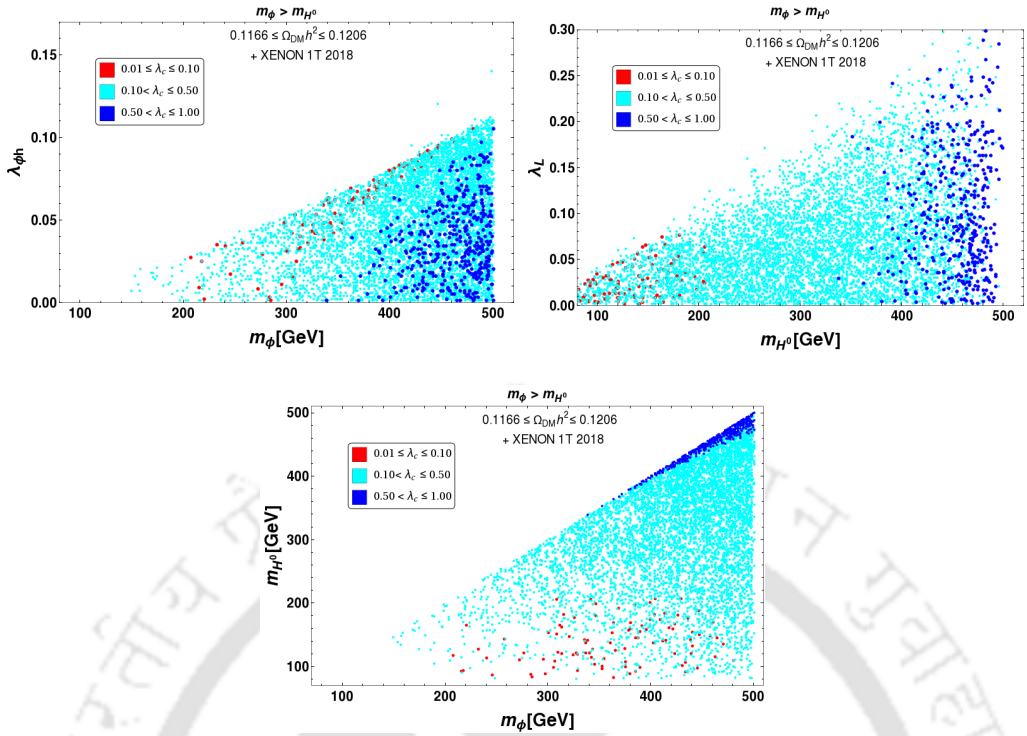

Figure 5.13: Relic Density and direct detection (XENON 1T 2018) allowed parameter space is shown in: $m_\phi - \lambda_{\phi h}$ plane (top left panel), $m_{H^0} - \lambda_L$ plane (top right panel) and $m_\phi - m_{H^0}$ plane (bottom panel). The scans are performed for for the mass hierarchy $m_\phi > m_{H^0}$.

m_{H^0} (again, compare it with top right panel of Fig. 5.12). A possible mass correlation after direct search bound are plotted in bottom panel of Fig. 5.13 in $m_\phi - m_{H^0}$ plane. The main outcomes from this figure are: (i) For $\lambda_c \le 0.1$, small $m_{H^0} \sim 200$ GeV is favoured, (ii) for moderate values of $\lambda_c \sim \{0.1 - 0.5\}$, there is no correlation and (iii) for large λ_c, only degenerate mass scenario ($m_\phi \sim m_{H^0}$) with large $m_\phi \sim 400$ GeV is allowed.

Case II: $m_\phi \le m_{H^0}$

Naturally here the conversion of heavier H^0 to the lighter component ϕ will mainly dictate the relic density of DM components on top their annihilations to SM. Relic density allowed parameter space for $m_\phi \le m_{H^0}$ is shown in Fig. 5.14. Again, this is illustrated in $m_\phi - \lambda_{\phi h}$ plane (top left), $m_{H^0} - \lambda_L$ plane (top right), $m_\phi - m_{H^0}$ plane (bottom left) and $\Omega_\phi h^2/\Omega_{DM}h^2(\%) - \Omega_{H^0}h^2/\Omega_{DM}h^2(\%)$ plane (bottom right). Different ranges of λ_c are shown by the same colour code as in Fig. 5.12, 5.13. Let us first focus on the top left figure. It shows that for small values of λ_c, relic density allowed parameter space points lie in the vicinity of single component framework of ϕ (red points in figure). In absence of a lighter mode, the relic density of ϕ is essentially governed by its annihilation to SM and due to small conversion cross-section the production of ϕ is also not large enough to change the conclusion. However, the situation changes significantly with larger λ_c (cyan and blue points), where we see again that the overabundant region of the single component scenario is getting allowed by relic density. In order to understand this let us remind ourself of the CBEQ for $m_\phi < m_{H^0}$ as depicted in Eqn. 5.29. In particular, the number density of ϕ is dictated by $\dot{n_\phi} + 3Hn_\phi \simeq -\mathcal{F}_\phi + \mathcal{F}_{\Phi\phi}$.

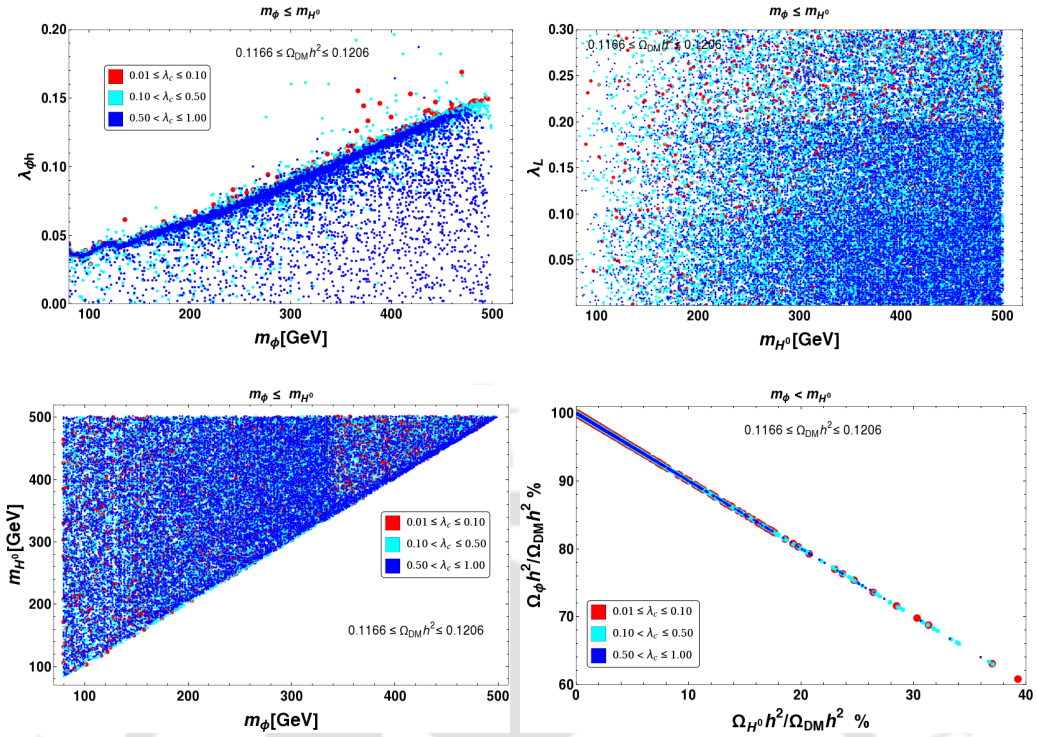

Figure 5.14: Relic Density allowed parameter space is shown in $m_\phi - \lambda_{\phi h}$ plane (top left), $m_{H^0} - \lambda_L$ plane (top right), $m_\phi - m_{H^0}$ plane (bottom left) and $\Omega_\phi h^2/\Omega_{DM}h^2(\%) - \Omega_{H^0}h^2/\Omega_{DM}h^2(\%)$ plane (bottom right) for the mass hierarchy $m_\phi \leq m_{H^0}$.

With larger λ_c and larger conversion, $\mathcal{F}_{\Phi\phi}$ increases to reduce the effective $\mathcal{F}_\phi$ that determines the relic of ϕ. Therefore, to keep the relic density of ϕ to correct order, $\mathcal{F}_\phi$ has to increase. Now recall, $\mathcal{F}_\phi = \langle\sigma v\rangle_{\phi\phi\to SM\ SM}(n_\phi)^2 \sim 1/\langle\sigma v\rangle_{\phi\phi\to SM\ SM}$ as $n_\phi \sim 1/\langle\sigma v\rangle_{\phi\phi\to SM\ SM}$. Therefore, to increase $\mathcal{F}_\phi$, one has to reduce the annihilation cross-section $\langle\sigma v\rangle_{\phi\phi\to SM\ SM}$. This is possible by reducing $\lambda_{\phi h}$ as we see here in the plot. Next let us discuss the top right figure. This figure in $m_{H^0} - \lambda_L$ plane essentially depicts that with larger λ_c, larger m_{H^0} is favoured to tame the DM conversion as well as annihilation cross-section to keep the relic within limit. The dependence however is not that much significant due to the presence of large number of co-annihilation channels which remain unaffected by λ_c. In the bottom left panel, mass correlation has been plotted and carries no information. Lastly, bottom right figure shows the relative relic density contributions of these two components. It is well understood that an additional channel for annihilation of H^0 only reduces the possibility of bringing $\Omega_{H^0}h^2$ in the correct ballpark due to already existing gauge mediated annihilation and co-annihilation channels. Therefore, for small λ_c, it is still possible to get a contribution from $\Omega_{H^0}h^2 \sim 40\%$, but that becomes harder with large λ_c, where the relic density contribution of H^0 is further limited to $\Omega_{H^0}h^2 \sim 20\%$.

Direct search constraints from XENON 1T 2018 on the relic density allowed points are shown in Fig. 5.15. To emphasise again, the demand of these plots are simultaneous satisfaction of XENON1T limit for both DM components. The main outcome of this plot is to see the absence of small λ_c points (red dots) upto $\lambda_c \sim 0.30$. This is simply due to the fact that, with small λ_c, the required $\lambda_{\phi h}$ is high enough for ϕ DM to be discarded by XENON1T data. The other important feature is that with larger λ_c,

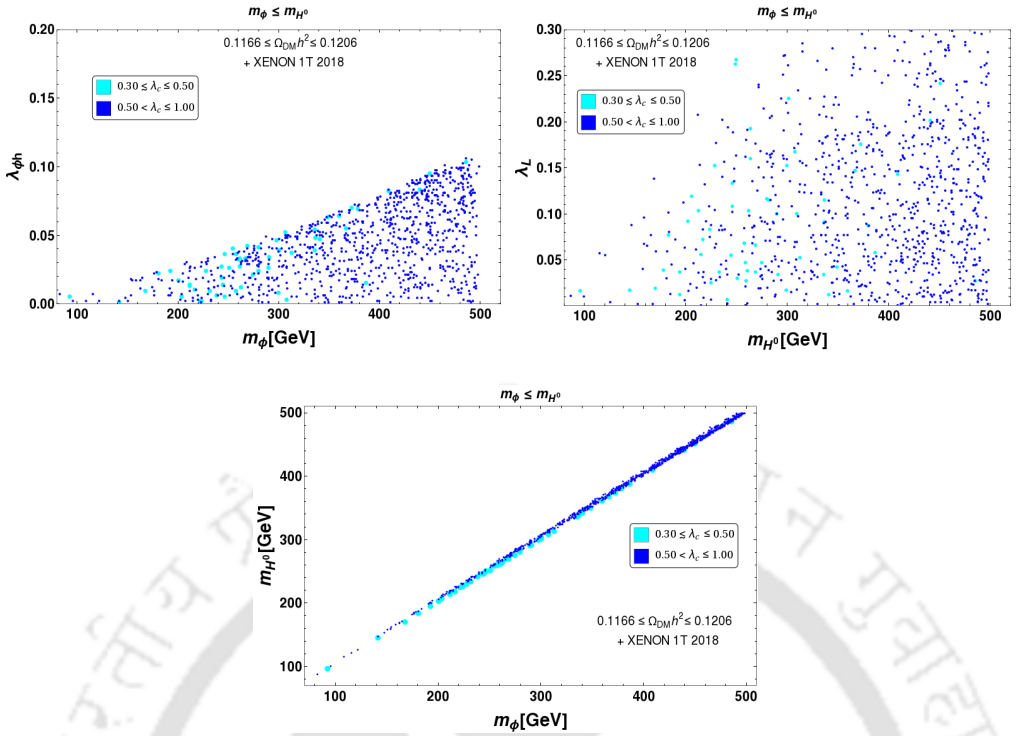

Figure 5.15: Relic Density and direct detection (XENON 1T 2018) allowed parameter space is shown in: $m_\phi - \lambda_{\phi h}$ plane (top left panel), $m_{H^0} - \lambda_L$ plane (top right panel) and $m_\phi - m_{H^0}$ plane (bottom panel). The scans are performed for for the mass hierarchy $m_\phi \leq m_{H^0}$.

larger DM masses are favoured. Lastly a very important conclusion comes from the bottom panel figure in the mass correlation plot. This shows, as only high λ_c region is allowed, the conversion of H^0 to ϕ still needs to be restricted and therefore the mass difference between the two DM components $(m_{H^0} - m_\phi)$ has to be very very small. These features are all distinct from that of $m_\phi > m_{H^0}$ region.

So far our discussion has been focused on DM mass region $m_{W^\pm} \leq m_{H^0}, m_\phi \leq 500$ GeV. But if $m_{H^0} < m_{W^\pm}$ or $m_\phi < m_{W^\pm}$, while other DM mass is heavier than $m_{W^\pm}$, the only region available for lighter DM with mass $< m_{W^\pm}$ are the Higgs and Z resonance regions: $m_{H^0} \sim \frac{m_Z}{2}$, $\frac{m_h}{2}$ and $m_\phi \sim \frac{m_h}{2}$. It is important to remind that the resonance regions are already available in absence of second DM component and therefore brings no new phenomenological outcome.

5.7 Electroweak Vacuum stability and High Scale Perturbativity in presence of RH neutrino and DM

One of the motivations of this work is to show that the presence of right handed neutrinos to yield correct neutrino masses in presence of multipartite DM. Although the neutrino sector considered here seems decoupled from the dark sector, is not completely true. The effect of the RH neutrinos alter the allowed DM parameter space when the model is validated at high scale. As already stated before, we employ type-I seesaw mechanism to generate the light neutrino mass, for which three RH neutrinos are

included in the set up.

5.7.1 Neutrino Yukawa couplings

We first describe the strategy in order to study their impact on RG evolution. For simplicity, the RH neutrino mass matrix M_N is considered to be diagonal with degenerate entries, *i.e.* $M_{N_{i=1,2,3}} = M_R$. It is to be noted that in the RG equation, $\text{Tr}[Y_\nu^\dagger Y_\nu]$ enters. In order to extract the information on Y_ν, we use the type-I seesaw formula for neutrino mass $m_\nu = Y_\nu^T Y_\nu \frac{v^2}{2M_R}$. Then, naively one would expect that large Yukawa couplings are possible with even heavier RH neutrino masses. For example with $M_R \sim 10^{14}$ GeV, Y_ν comes out to be 0.3 in order to obtain $m_\nu \simeq 0.05$ eV. However, contrary to this, it can be shown that even with smaller M_R one can achieve large values of $\text{Tr}[Y_\nu^\dagger Y_\nu]$, but effectively keeping $Y_\nu^T Y_\nu$ small, using a special flavor structure of Y_ν through Casas-Ibarra parametrization [119]. Note that our aim is to study the maximum effect coming from the right handed neutrino Yukawa, *i.e.* with large $\text{Tr}[Y_\nu^\dagger Y_\nu]$, on EW vacuum stability. For this purpose, we use the parametrisation by [158] and write Y_ν as

$$Y_\nu = \sqrt{2}\frac{\sqrt{M_R}}{v}\mathcal{R}\sqrt{m_\nu^d}\, U_{\text{PMNS}}^\dagger, \tag{5.32}$$

where m_ν^d is the diagonal light neutrino mass matrix and U_{PMNS} is the unitary matrix diagonalizing the neutrino mass matrix m_ν such that $m_\nu = U_{\text{PMNS}}^* m_\nu^d U_{\text{PMNS}}^\dagger$. Here $\mathcal{R}$ represents a complex orthogonal matrix which can be written as $\mathcal{R} = \mathcal{O}\exp(i\mathcal{A})$ with $\mathcal{O}$ as real orthogonal matrix and $\mathcal{A}$ as real antisymmetric matrices. Using above parametrisation, then one gets,

$$\text{Tr}[Y_\nu^\dagger Y_\nu] = \frac{2M_R}{v^2}\text{Tr}\Big[\sqrt{m_\nu^d}e^{2i\mathcal{A}}\sqrt{m_\nu^d}\Big]. \tag{5.33}$$

Note that the real antisymmetric matrix $\mathcal{A}$ however does not appear in the seesaw expression for neutrino mass as $m_\nu = \frac{Y_\nu^T Y_\nu v^2}{2M_R}$. Therefore with any suitable choice of $\mathcal{A}$, it would actually be possible to have relatively large Yukawa even with light M_R.

5.7.2 β functions and RG running

To study the high scale validity of this multi-component DM model with neutrino mass (including perturbativity and vacuum stability), we need to consider the RG running of the associated couplings. The framework contains few additional mass scales: one extra scalar singlet, one inert doublet and three RH neutrinos with mass $M_{N_{i=1,2,3}} (= M_R)$. Hence in the study of RG running, different couplings will enter into different mass scales. In DM phenomenology, we have considered the physical masses of DM sector particles within ~ 500 GeV. Then for simplicity, we can safely ignore the small differences between the dark sector particle masses and identify the single additional mass scale as m_{DM}. On the other hand, RH neutrinos are considered to be heavier than the scalars present in the model ($M_R > m_{DM}$). Hence, for running energy scale $\mu > m_{DM}$, we need to consider the couplings associated to DM sector in addition to SM while while for $\mu > M_{N_{i=1,2,3}}$, the neutrino couplings will additionally enter into the scenario. Below we provide the one loop β functions for the additional

for the couplings involved in our model, when $\mu > M_R$.

β functions of quartic scalar couplings [159]:

$$\begin{aligned}
\beta_{\lambda_H} &= \frac{27}{200}g_1^4 + \frac{9}{20}g_1^2g_2^2 + \frac{9}{8}g_2^4 - \frac{9}{5}g_1^2\lambda_H - 9g_2^2\lambda_H + 24\lambda_H^2 + 12\lambda_H y_t^2 - 6y_t^4 \\
&\quad + 2\lambda_1^2 + 2\lambda_1\lambda_2 + \lambda_2^2 + \lambda_3^2 + \frac{1}{2}\lambda_{\phi h}^2 + 4\lambda_H \mathrm{Tr}[Y_\nu^\dagger Y_\nu] - 2\mathrm{Tr}[(Y_\nu^\dagger Y_\nu)^2] \qquad (5.34)\\
\beta_{\lambda_3} &= -\frac{9}{5}g_1^2\lambda_3 - 9g_2^2\lambda_3 + 8\lambda_1\lambda_3 + 12\lambda_2\lambda_3 + 4\lambda_3\lambda_H + 4\lambda_3\lambda_\Phi + 6\lambda_3 y_t^2 + 2\lambda_3 \mathrm{Tr}[Y_\nu^\dagger Y_\nu],\\
\beta_{\lambda_2} &= +\frac{9}{5}g_1^2g_2^2 - \frac{9}{5}g_1^2\lambda_2 - 9g_2^2\lambda_2 + 8\lambda_1\lambda_2 + 4\lambda_2^2 + 8\lambda_3^2 + 4\lambda_2\lambda_H + 4\lambda_2\lambda_\Phi \\
&\quad + 6\lambda_2 y_t^2 + 2\lambda_2 \mathrm{Tr}[Y_\nu^\dagger Y_\nu],\\
\beta_{\lambda_1} &= \frac{27}{100}g_1^4 - \frac{9}{10}g_1^2g_2^2 + \frac{9}{4}g_2^4 - \frac{9}{5}g_1^2\lambda_1 - 9g_2^2\lambda_1 + 4\lambda_1^2 + 2\lambda_2^2 + 2\lambda_3^2 + 12\lambda_1\lambda_H \\
&\quad + 4\lambda_2\lambda_H + 12\lambda_1\lambda_\Phi + 4\lambda_2\lambda_\Phi + 6\lambda_1 y_t^2 + \lambda_c\lambda_{\phi h} + 2\lambda_1 \mathrm{Tr}[Y_\nu^\dagger Y_\nu],\\
\beta_{\lambda_\Phi} &= 24\lambda_\Phi^2 + 2\lambda_1^2 + 2\lambda_1\lambda_2 - 9g_2^2\lambda_\Phi + \frac{27}{200}g_1^4 + \frac{9}{20}g_1^2\Big(-4\lambda_\Phi + g_2^2\Big) + \frac{9}{8}g_2^4 \\
&\quad + \lambda_2^2 + \lambda_3^2 + \frac{1}{2}\lambda_c^2,\\
\beta_{\lambda_{\phi h}} &= -\frac{9}{10}g_1^2\lambda_{\phi h} - \frac{9}{2}g_2^2\lambda_{\phi h} + 4\lambda_{\phi h}^2 + 12\lambda_{\phi h}\lambda_H + \lambda_{\phi h}\lambda_\phi + 6\lambda_{\phi h} y_t^2 \\
&\quad + 4\lambda_1\lambda_c + 2\lambda_2\lambda_c + 2\lambda_{\phi h} Tr[Y_\nu^\dagger Y_\nu],\\
\beta_{\lambda_c} &= -\frac{9}{10}g_1^2\lambda_c - \frac{9}{2}g_2^2\lambda_c + 12\lambda_c\lambda_\Phi + 4\lambda_1\lambda_{\phi h} + 2\lambda_2\lambda_{\phi h} + \lambda_c\lambda_\Phi + 4\lambda_c^2,\\
\beta_{\lambda_\phi} &= 3\Big(4\lambda_c^2 + 4\lambda_{\phi h}^2 + \lambda_\phi^2\Big).
\end{aligned}$$

β functions of gauge couplings [159]:

$$\begin{aligned}
\beta_{g_1} &= \frac{21}{5}g_1^3,\\
\beta_{g_2} &= -3g_2^3,\\
\beta_{g_3} &= -7g_3^3.
\end{aligned} \qquad (5.36)$$

β functions of Yukawa couplings [159, 160]:

$$\begin{aligned}
\beta_{y_t} &= \frac{3}{2}y_t^3 + y_t\Big(3y_t^2 - 8g_3^2 - \frac{17}{20}g_1^2 - \frac{9}{4}g_2^2 + y_t \mathrm{Tr}[Y_\nu^\dagger Y_\nu]\Big),\\
\beta_{\mathrm{Tr}[Y_\nu^\dagger Y_\nu]} &= 3\mathrm{Tr}[(Y_\nu^\dagger Y_\nu)^2] + \mathrm{Tr}[Y_\nu^\dagger Y_\nu]\Big(-\frac{9}{10}g_1^2 - \frac{9}{2}g_2^2 + 6y_t^2 + 2\mathrm{Tr}[Y_\nu^\dagger Y_\nu]\Big).
\end{aligned} \qquad (5.37)$$

The above β functions are generated using the model implementation in the code `SARAH` [161]. The running of λ_H as in Eqn.(5.34) is influenced adversely mostly by top Yukawa coupling $y_t \sim \mathcal{O}(1)$ and right handed neutrino Yukawa coupling as $\mathrm{Tr}[Y_\nu^\dagger Y_\nu]$. On the other hand, multiparticle scalar DM couplings present in the model help in compensating the strong negative effect from y_t and $\mathrm{Tr}[Y_\nu^\dagger Y_\nu]$. To evaluate $\mathrm{Tr}[Y_\nu^\dagger Y_\nu]$, we employ Eq. 5.33. As an example, let us consider magnitude of all the entries of $\mathcal{A}$ to be equal, say a with all diagonal entries to be zero. Then using the best fit values

of neutrino mixing angles and cosnidering the mass of lightest neutrino zero, one can find for$M_R = 1$ TeV, $\text{Tr}[Y_\nu^\dagger Y_\nu]$ can be as large as 1 with $a = 8.1$[158, 162]. Equipped with all these β functions and strategy to estimate the relevant couplings present in them, let us now analyse the SM Higgs vacuum stability at high energy scale. Below we provide the stability and metastability criteria.

• **Stability criteria:** The stability of Higgs vacuum can be ensured by the condition $\lambda_H > 0$ at any scale. However, we have multiple scalars (SM Higgs doublet, one inert doublet and one gauge real singlet) in the model. Therefore we should ensure the boundedness or stability of the entire scalar potential in any field direction. This can be guaranteed by using the co-positivity criterion in Eqn. 5.9. Note that once λ_H becomes negative the other copositivity conditions no longer remain valid.

• **Metastability criteria:** On the other hand, when λ_H becomes negative, there may exist another deeper minimum other than the EW one. Then the estimate of the tunnelling probability $\mathcal{P}_T$ of the EW vacuum to the second minimum is essential to confirm the metastability of the Higgs vacuum. Obviously, the Universe can be in a metastable state only, provided the decay time of the EW vacuum is longer than the age of the Universe. The tunnelling probability is given by [163, 164],

$$\mathcal{P}_T = T_U^4 \mu_B^4 e^{-\frac{8\pi^2}{3|\lambda_H(\mu_B)|}}, \tag{5.38}$$

where T_U is the age of the Universe, μ_B is the scale at which tunnelling probability is maximized, determined from $\beta_{\lambda_H} = 0$. Therefore, solving above equation, we see that metastable Universe requires [163, 164] :

$$\lambda_H(\mu_B) \;>\; \frac{-0.065}{1 - \ln\left(\frac{v}{\mu_B}\right)}. \tag{5.39}$$

As noted in [163], for $\mu_B > M_P$ (Planck Scale, $M_P = 1.22 \times 10^{19}$ GeV), one can safely consider $\lambda_H(\mu_B) = \lambda_H(M_P)$. One should also note, that even with meatstability of Higgs vacuum, the instability in other field direction may also occur. The conditions to avoid the possible instability along various field directions for $\lambda_H < 0$ are listed below [165]:

(*i*) $\lambda_\Phi > 0$ to avoid the unboundedness of the potential along H^0, A^0 and $H^\pm$ directions,

(*ii*) $\lambda_1 > 0$ to ensure the stability along a direction between $H^\pm$ and h,

(*iii*) $\lambda_L > 0$ to ensure the stability along a direction between H^0 and h,

(*iv*) $\lambda_S > 0$, to avoid unboundedness of the potential along a direction between A^0 and h,

(*v*) $\lambda_\phi > 0$, otherwise the potential will be unbounded along ϕ direction,

(*vi*) $\lambda_{\phi h} > 0$, to ensure the stability along a direction between ϕ and h.

Now to begin the vacuum stability analysis in the present multi-component DM scenario, we first choose two benchmark values of DM masses (ϕ and H^0) which satisfy both the relic density and direct detection bounds. These along with corresponding values of other relevant parameters are denoted by the set of two benchmark points, BP1 and BP2, as tabulated in Table 5.2. These parameters are mentioned in the caption of Table 5.2 for both benchmark points. We also show the value of electroweak

BPs	m_{H^0}	m_ϕ	m_{A^0}	$m_{H^\pm}$	λ_L	$\lambda_{\phi h}$	λ_c	$\Omega_{H^0}h^2$	$\Omega_\phi h^2$	$\sigma^{eff}_{H^0}$ (cm^2)	σ^{eff}_{ϕ} (cm^2)
BP1	330	343	333	339	0.043	0.065	0.2	0.033	0.086	1.6×10^{-46}	2.2×10^{-46}
BP2	427	449	438	440	0.086	0.017	0.3	0.027	0.088	3.3×10^{-46}	1.0×10^{-47}

Table 5.2: Benchmark points used to analyse EW vacuum stability in our model. All masses are in GeVs. The other couplings used in these benchmark points play an important role; they are: BP1: $\{\lambda_1 = 0.285, \lambda_2 = -0.17, \lambda_3 = -0.033\}$, BP2: $\{\lambda_1 = 0.544, \lambda_2 = -0.215, \lambda_3 = -0.157\}$.

BPs	ΔS (10^{-4})	ΔT (10^{-4})	$\mu_{\gamma\gamma}$ (10^{-5})
BP1	-12	5.1	3
BP2	-9	2.5	3

Table 5.3: Estimate of electroweak precision parameters and $\mu_{\gamma\gamma}$ for the two benchmark points as chosen in Table 5.2.

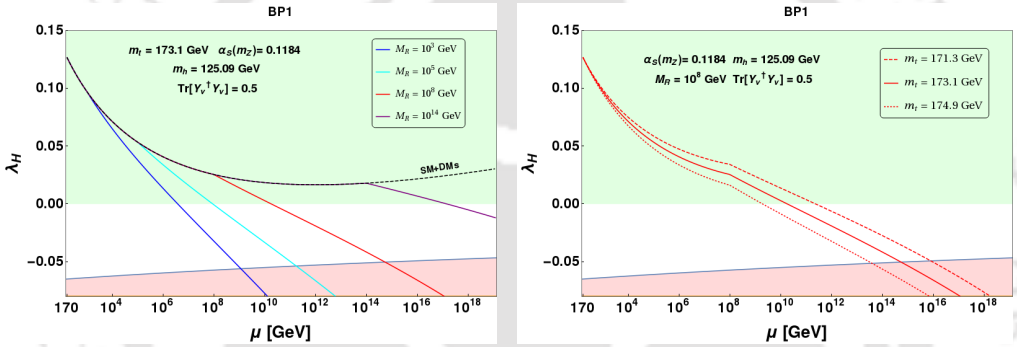

Figure 5.16: RG running of λ_H with energy scale for BP1. In left panel, we have shown the effect of different right handed neutrinos masses, M_R (indicated by different colours and mentioned in figure inset) for a fixed top quark mass $m_t = 173.1$ GeV. The black dotted line corresponds to the case when right handed neutrinos are absent in the scenario. In right panel, we choose a specific $M_R = 10^8$ GeV and consider top mass in 2σ range: $m_t = 173.1 \pm 0.9$ GeV. Tr$[Y_\nu^\dagger Y_\nu] = 0.5$ is kept constant in both plots.

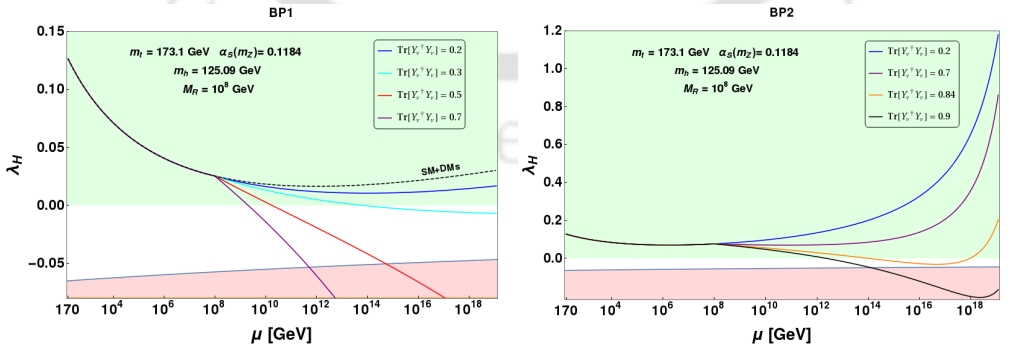

Figure 5.17: RG running of λ_H with energy scale μ for different values of Tr$[Y_\nu^\dagger Y_\nu]$ (shown in different colours and values are mentioned in the figure inset) for the benchmark points BP1 (left) and BP2 (right). Here we have chosen $M_R = 10^8$ GeV for illustration. The black dotted line here corresponds to the case when right handed neutrinos are absent in this scenario.

parameters and $\mu_{\gamma\gamma}$ for these two benchmark points in Table 5.3. We run the two loops RG equations for all the SM couplings and one loop RG equations for the other relevant couplings in the model from $\mu = m_t$ to M_P energy scale. We use the inital boundary values of all the SM couplings as provided in [163]. The boundary values have been evaluated at $\mu = m_t$ in [163] by taking various threshold corrections and mismatch between top pole mass and $\overline{MS}$ renormalised couplings into account.

In Fig. 5.16, we show the running of λ_H for BP1 as a function of energy scale μ. The left panel shows running of λ_H for different values of RH neutrino mass M_R, considering top quark mass $m_t = 173.1$ GeV, Higgs mass $m_h = 125.09$ GeV and $\text{Tr}[Y_\nu^\dagger Y_\nu] = 0.5$. As it is visible that for low value of $M_R \sim 10^4$ GeV, λ_H enters into unstable region at very early stage of its evolution (blue line in the figure). This has happened as the scalar couplings in β_{λ_H} (Eqn. 5.34) are not sufficiently large to counter the strong negative impact of $\text{Tr}[Y_\nu^\dagger Y_\nu]$ which brings down the λ_H shraply towards unstable region. On contrary, for large value of $M_R \sim 10^{14}$ GeV, the effect of Y_ν in β_{λ_H} starts at a comparatively larger energy scale than the earlier case. As a consequence, although λ_H becomes negative at some high energy scale, it stays in metastable region till M_P energy scale (violate line). Green region here describes stable, white region describes metastable (see Eqn. 5.39) and the red region indicates unstable solution for the potential. For comparison, we also display the evolution of λ_H (black dotted curve) in absence of RH neutrinos in the theory with the inclusion of scalar couplings (related to DM) only. This clearly shows that in absence of RH neutrinos, EW vacuum could be absolutely stable till M_P energy scale. In right panel of Fig. 5.16, we study the evolution of λ_H considering 2σ uncertainty of measured top mass m_t, keeping $m_h = 125.09$ GeV, $M_R = 10^8$ GeV and $\text{Tr}[Y_\nu^\dagger Y_\nu] = 0.5$ fixed. It is trivial to find that with the increase of top mass, λ_H crosses zero at earlier stage in its evolution.

Next we show the effect of $\text{Tr}[Y_\nu^\dagger Y_\nu]$ in the RG evolution of λ_H in Fig. 5.17 for BP1

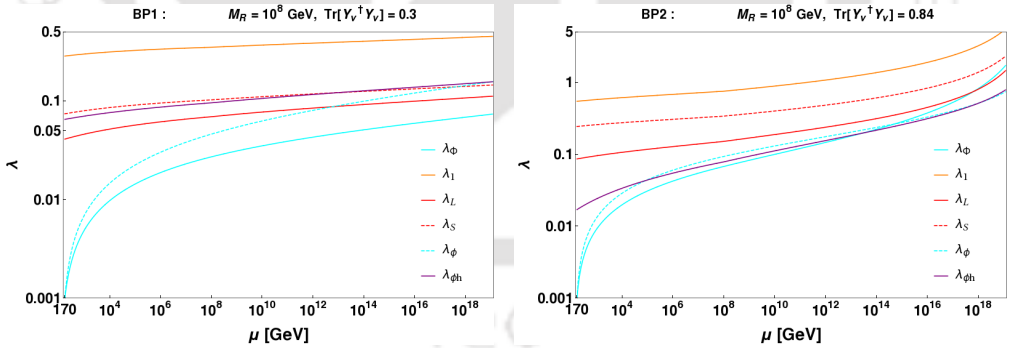

Figure 5.18: RG running of all the quartic couplings in metastability criteria for BP1 (left) and BP2 (right) to ensure the boundedness of the scalar potential in various field directions with energy scale μ for $\text{Tr}[Y_\nu^\dagger Y_\nu] = 0.3$ (left) and 0.84 (right). The choices of $\text{Tr}[Y_\nu^\dagger Y_\nu]$ are demonstrated in cyan (0.3) and in orange (0.84) in left and right panels of Fig. 5.17 to yield metastability.

(left) and BP2 (right). For the purpose we fix the RH neutrino mass scale $M_R = 10^8$ GeV. It can be seen from left panel that large value of $\text{Tr}[Y_\nu^\dagger Y_\nu] \sim 0.7$ brings down λ_H towards the negative values at earlier energy scale. This is obvious from the β function of λ_H as the amount of scalar couplings for BP1 are not that effective in presence of such large value of $\text{Tr}[Y_\nu^\dagger Y_\nu]$. With comparatively lesser value of $\text{Tr}[Y_\nu^\dagger Y_\nu] \sim 0.3$, the EW vacuum might be in metastable state provided other conditions $((i) - (vi))$

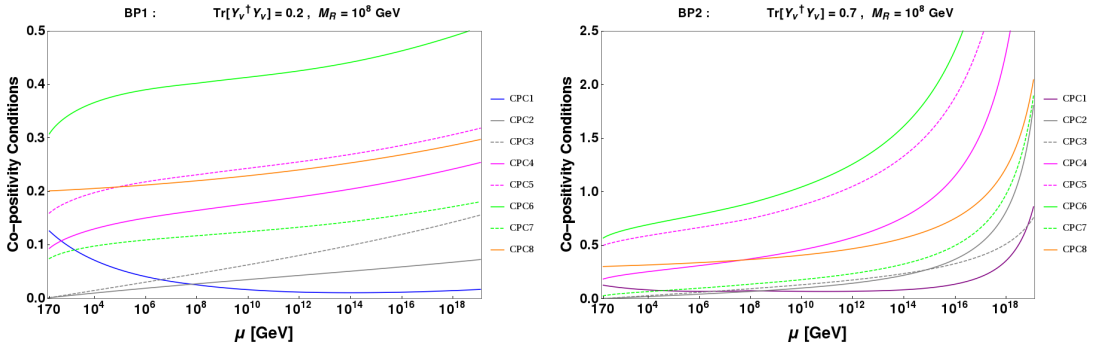

Figure 5.19: RG running of all copositivity criteria in Eqn. 5.9 for BP1 (left) and BP2 (right) to ensure the boundedness of the scalar potential in any field direction with energy scale μ for $\mathrm{Tr}[Y_\nu^\dagger Y_\nu] = 0.2$ (left) and 0.7 (right) The choices of $\mathrm{Tr}[Y_\nu^\dagger Y_\nu]$ are shown in dark blue and purple colours in left and right panels of Fig. 5.17 respectively to yield stability.

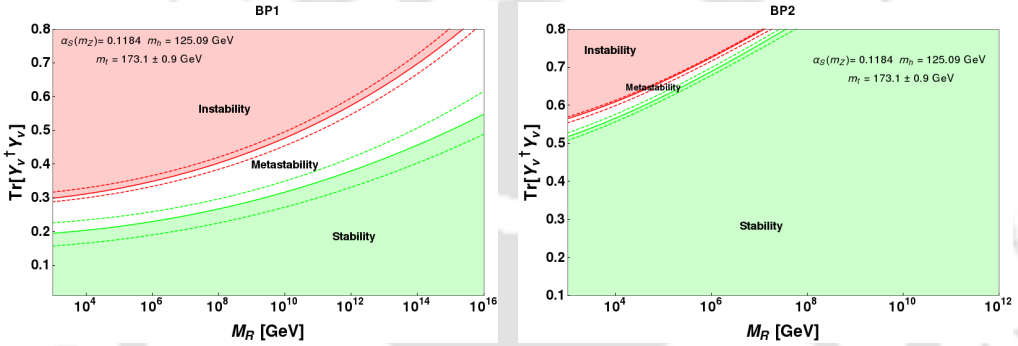

Figure 5.20: Stability, metastability and instability regions plot on $M_R - \mathrm{Tr}[Y_\nu^\dagger Y_\nu]$ plane for the benchmark point BP1 (left panel) and BP2 (right panel). For illustration we have considered top mass variation in 1σ range : 173.1 ± 0.9 GeV.

are satisfied as shown in left panel of Fig. 5.18. If we further reduce the value of $\mathrm{Tr}[Y_\nu^\dagger Y_\nu] \sim 0.2$ the EW vacuum might be absolutely stable. For the stability case we also show the satisfaction of all the copositivity criterias (Eqn. 5.9) in left panel of Fig. 5.19. This ensures the boundness of the scalar potential in any arbitary field direction. The analysis for BP2 turns out to be similar as observed from right panels of Fig. 5.17-5.19. Note that due to comparatively larger values of the scalar couplings in BP2, we achieve a better results in stability point of view than BP1.

Based on the inputs from above analysis, now we constrain $\mathrm{Tr}[Y_\nu^\dagger Y_\nu] - M_R$ parameter space using the stability, metastability and instability criteria (green, white and red regions respectively) for BP1 (left panel) and BP2 (right panel) in Fig. 5.20. The criteria has been set at Planck scale (M_P). We use $\alpha_S = 0.1184$ and $m_h = 125.09$ GeV for both the plots. The solid lines indicate the contour for $m_t = 173.1$ GeV while the dotted lines denote 2σ uncertainty of the measured value of m_t. It can be concluded from Fig. 5.20, that to have a stable/metastable EW vacuum, smaller values of M_R requires low $\mathrm{Tr}[Y_\nu^\dagger Y_\nu]$ and vice versa. One important distinction between the left and right panel figures, corresponding to two different benchmark points, is that BP2 has significantly larger parameter space available from high scale stability. This is because of the larger values of $\lambda_{1,2,3}$ parameters used in BP2 compared to BP1 (see Table 5.4 for details). Therefore, it can be concluded, that larger is the mass splitting in IDM

sector, the more favourable it is from the stability point of view. However there is an important catch to this statement, which we will illustrate next.

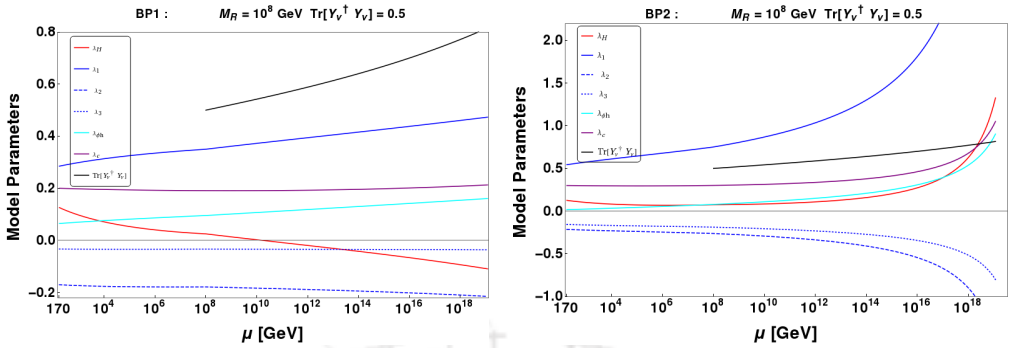

Figure 5.21: RG running of relevant coupling parameters for BP1 (left panel) and BP2 (right panel). $M_R = 10^8$ GeV, $\mathrm{Tr}[Y_\nu^\dagger Y_\nu] = 0.5$ and $m_t = 173.1$ GeV have been kept fixed in both plots.

In Fig. 5.21 we plot the running of all the individual couplings present in the set up. We see that (fortunately) for the two benchmark points used in the analysis, we are still okay with the perturbative limit at the high scale, *i.e.* all the couplings obey the perturbative limit, $|\lambda_i| < 4\pi$, $|\mathrm{Tr}[Y_\nu^\dagger Y_\nu]| < 4\pi$ at Planck scale. However, for BP1, with $M_R = 10^8$ GeV, and $\mathrm{Tr}[Y_\nu^\dagger Y_\nu] = 0.5$ as shown in the left panel yields unstable solution to EW vacuum with λ_H running negative. On the other hand, BP2 with same choices of right handed neutrino mass and Yukawa yields a stable vacuum. Therefore, once again we find that larger splitting in IDM sector is more favourable for EW vacuum stability, as we have also inferred before from Fig. 5.20. But, it turns out that as larger splitting in the IDM sector also uses larger values of $\lambda_{1,2,3}$, it is possible, that many of those points become non-perturbative i.e. $|\lambda_i| > 4\pi$ when run upto Planck scale. We will show in the next section, that this very phenomena disallows many of the relic density and direct search allowed parameter space of the model. Another point to end this section is to note that our available parameter space from DM constraints heavily depend on large DM-DM conversion, which naturally comes from large choices of the conversion coupling λ_c. It is natural, that some of those cases will also be discarded by the perturbative limit $|\lambda_c| < 4\pi$, when we evaluate the validity of the model at high scale.

5.7.3 Allowed parameter space of the model from high scale validity

Finally, we come to the point where we can assimilate all the constraints together, from DM constraints to high scale validity. In order to do that, we choose relic density and direct search allowed parameter space of the model as discussed in Section 5.6 and impose the high scale validity of the model till some energy scale μ by demanding:

- Stability of the scalar potential (Eqn.(5.9)) determined by satisfying copositivity conditions for any energy scale μ.
- Non-violation of perturbativity and unitarity of all the relevant couplings present in the model as defined in Eqns. 5.10 and 5.11.

Note that the high scale validity of the models does not depend on the structure of mass hierarchy of the DM candidates (*i.e.* on the sign of mass difference $m_{H^0} - m_\phi$). To study the EW vacuum stability we demand the positivity of λ_H at each energy scale

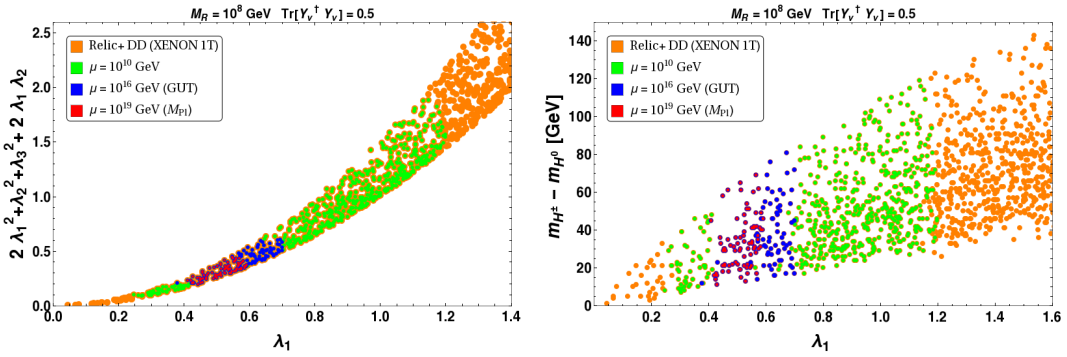

Figure 5.22: Relic density and direct search allowed points in $2\lambda_1^2+\lambda_2^2+\lambda_3^2+2\lambda_1\lambda_2$ versus λ_1 plane (left figure) and $m_{H^\pm} - m_{H^0}$ versus λ_1 plane (right figure) at EW scale (orange points). We also find high scale validity of the model following Eqns. 5.9, 5.10 and 5.11 by considering the high scale to be 10^{10} GeV (green), 10^{16} GeV (blue) and 10^{19} GeV (red). Right handed neutrino mass and Yukawa couplings are kept fixed at $M_R = 10^8$ GeV, $\text{Tr}[Y_\nu^\dagger Y_\nu] = 0.5$ with $m_t = 173.1$ GeV.

from EW to high scale μ. As evident from β_{λ_H} in Eqn. 5.34, a particular combination of the scalar couplings in the form of $2\lambda_1^2+\lambda_2^2+\lambda_3^2+2\lambda_1\lambda_2+\frac{1}{2}\lambda_{\phi h}^2$ determines the positivity of λ_H during its running. However the factor $\lambda_{\phi h} \lesssim 0.1$ is strongly constrained from the SI DD cross section bound for $m_\phi < 500$ GeV. Hence, we can assume safely that the factor $2\lambda_1^2+\lambda_2^2+\lambda_3^2+2\lambda_1\lambda_2$ without $\lambda_{\phi h}$ effectively determines the stability of Higgs vacuum in relic density and direct search allowed parameter space. It turns out that when $\lambda_H > 0$. all other copositivity conditions for all relic and DD cross section satisfied points in our model stays positive from $\mu = m_t$ to $\mu = M_P$.

In Fig. 5.22, we constrain relic density and direct search allowed points of the model

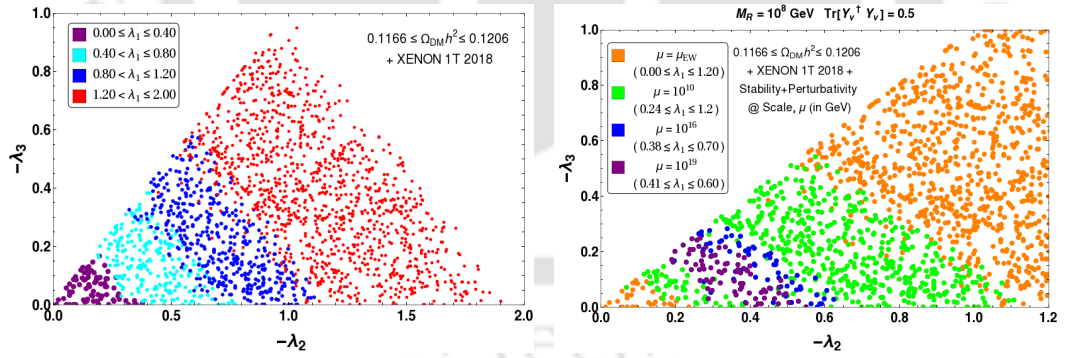

Figure 5.23: Relic density and direct search allowed points in $\lambda_2 - \lambda_3$ plane for different values of λ_1 (left). Allowed points in the same parameter space from DM constraints (orange), stability and perturbativity conditions following Eqns. 5.9-5.11 considering the high scale $\mu = \mu_{\rm EW}$, 10^{10} GeV (green), 10^{16} GeV (blue) and 10^{19} GeV (purple) (right).

in $2\lambda_1^2+\lambda_2^2+\lambda_3^2+2\lambda_1\lambda_2-\lambda_1$ plane to additionally satisfy perturbativity and vacuum stability conditions following Eqns. 5.9-5.11. Orange points satisfy relic density and DD bounds, while the green, blue and red points on top of that satisfy perturbativity and vacuum stability conditions upto high energy scales $\mu = 10^{10}$ GeV, 10^{16} GeV and 10^{19} GeV respectively. This very figure essentially shows that all those points with either small values of λ_1 (i.e. small $m_{H^\pm} - m_{H^0}$)are discarded due to stability of EW

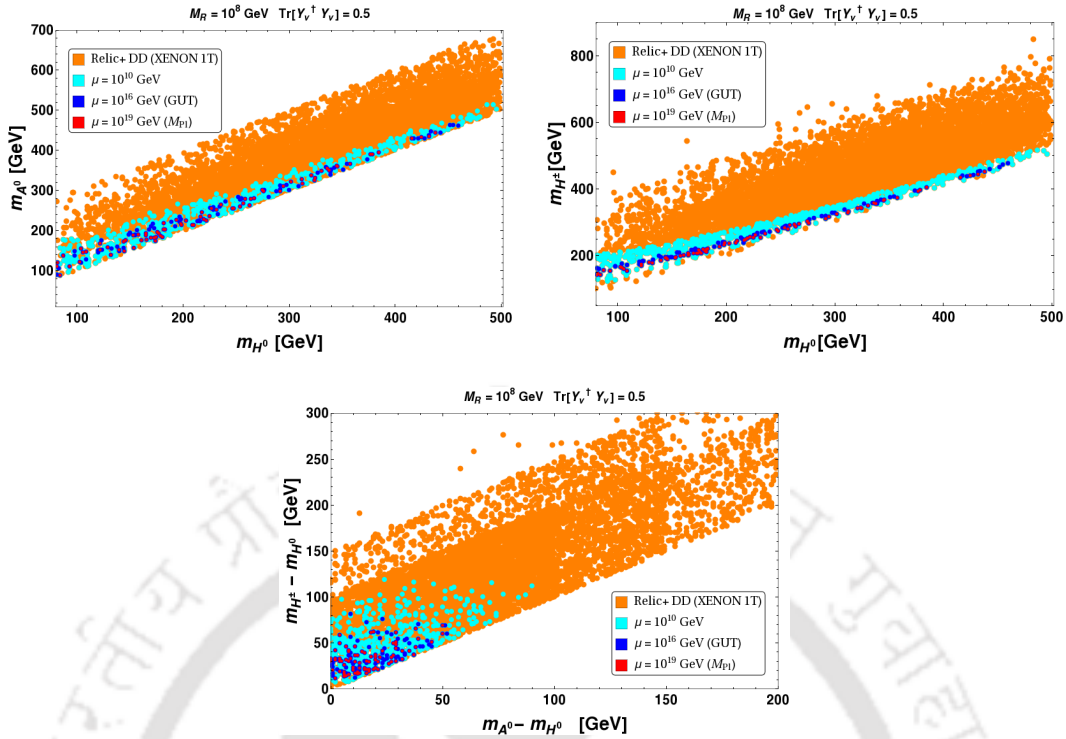

Figure 5.24: Relic density and direct search allowed points (orange) in $m_{A^0} - m_{H^0}$ (top left), $m_{H^\pm} - m_{H^0}$ (top left) and $\Delta m(= m_{A^0} - m_{H^0}) - \Delta M(= m_{H^\pm} - m_{H^0})$ (bottom). We further apply stability and perturbativity conditions following Eqns. 5.9-5.11 at different energy scales $\mu = 10^{10}$ GeV (light blue), 10^{16} GeV (dark blue) and 10^{19} GeV (red).

vacuum, while those with large λ_1 (i.e. large $m_{H^\pm} - m_{H^0}$)are discarded by perturbative limits of the coupling at high scale.

In Fig. 5.23 we study the correlation between the individual scalar couplings to satisfy the DM constraints, perturbativity limits and vacuum stability criteria. In left panel of Fig. 5.23, we show the DM relic density and DD cross section satisfied points in $\lambda_2 - \lambda_3$ plane for different values of λ_1. In right panel we first identify the relevant parameter space in the same plane which satisfy the DM constraints, the perturbativity bound and vacuum stability criteria till EW energy scale. Then we further impose perturbativity bound and vacuum stability conditions considering the high scale as $\mu = 10^{10}$ GeV, 10^6 GeV and 10^{19} GeV in addition to the DM constraints. It is seen that the lower portion of the available parameter space gets discarded by vacuum stability or high value of λ_c while perturbativity bounds constrain the higher values of the couplings. In this plot also we kept $M_R = 10^8$ GeV, $\text{Tr}[Y_\nu^\dagger Y_\nu] = 0.5$ with $m_t = 173.1$ GeV. We must also note that with larger M_R and smaller Yukawa $\text{Tr}[Y_\nu^\dagger Y_\nu]$, we could obtain a larger available parameter space from high scale validity.

In Fig. 5.24, we show the high scale validity of relic density and direct search allowed parameter space of the model in $m_{H^0} - m_{A^0}$ (top left), $m_{H^0} - m_{H^\pm}$ (top right) and $\Delta m(= m_{A^0} - m_{H^0}) - \Delta M(= m_{H^\pm} - m_{H^0})$ planes with $M_R = 10^8$ GeV and $\text{Tr}[Y_\nu^\dagger Y_\nu] = 0.5$ at different high energy scales $\mu = \{10^{10}, 10^{16}, 10^{19}\}$ GeVs denoted by light blue, dark blue and red points. The orange points are corresponding to relic and direct search allowed parameter space at EW scale. We see that larger

mass difference between inert higgs components, $\Delta m - \Delta M$ which are related with quartic couplings, $\lambda_{1,2,3}$ (see Eqn. 5.7), are discarded from perturbativity conditions mentioned in Eqn. 5.10. While the small mass differences between inert components are also excluded from stability criteria of Higgs potential.

5.8 Collider signature of Inert doublet DM at LHC

Inert doublet has been an attractive DM framework, due to the possibility of collider detection [166, 167]. Here, we relook into the possible collider search strategies of IDM at LHC in presence of a second scalar singlet DM component. It is also worth mentioning here that the real scalar singlet, which interacts with SM only through Higgs portal coupling, does not have any promising collider signature excepting mono-X signature arising out of initial state radiation (ISR), where X stands for $W, Z,$ jet. Such signals are heavily submerged in SM background due to weak production cross-section of DM in relic density and direct search allowed parameter space [65]. The charge components H^+, H^- of inert DM can be produced at LHC via Drell-Yan Z and γ mediation as well as through Higgs mediation. Further decay of $H^\pm$ to DM (H^0) and leptonic final states through on/off shell $W^\pm$ yields hadronically quiet opposite sign di-lepton plus missing energy (OSDL+$\not{E}_T$)[3], as shown in left panel of Fig. 5.25. In this study, we focus on this particular signal of inert dark matter as detailed below:

$$\text{Signal :: OSDL} + \not{E}_T \equiv \quad \ell^+\ell^- + (\not{E}_T): \quad p\,p \to H^+\ H^-,\ (H^- \to\ \ell^-\ \overline{\nu_\ell}\ H^0), \\ (H^+ \to \ell^+\ \nu_\ell\ H^0); \text{where}\ \ \ell = \{e, \mu\} \quad (5.40)$$

In the right panel of Fig. 5.25, we show variation of charged pair ($H^+\ H^-$) production

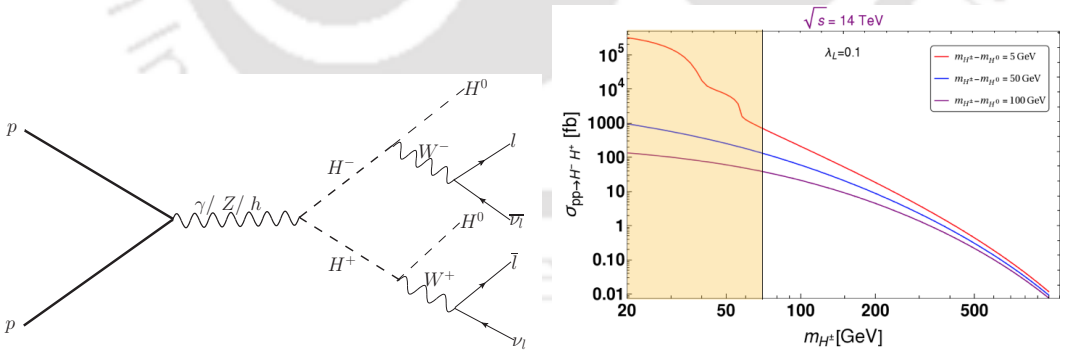

Figure 5.25: [Left] Feynman graph for OSDL+$\not{E}_T$ signature of IDM at LHC. [Right] Variation of production cross-section $\sigma_{pp\to H^+\ H^-}$ (in fb) with $m_{H^\pm}$ ($= m_{H^0} + \Delta M$) in GeV for different choices of $m_{H^\pm} - m_{H^0}$ for center-of-mass energy $\sqrt{s} = 14$ TeV at LHC. LEP limit on charged scalar is shown by the shaded region.

cross-section at LHC for center-of-mass energy $\sqrt{s} = 14$ TeV as a function of $m_{H^\pm} =$

[3]There are other possible signatures (for example, three lepton final state) of inert DM arising from the the combination of $H^\pm, A^0$ production and their subsequent decays, for a detailed list see [61, 167].

BPs	$\{ m_{H^0},\ m_\phi,\ m_{A^0},\ m_{H^\pm},\ \lambda_L,\ \lambda_{\phi h},\ \lambda_c \}$	$\Omega_{H^0}h^2$	$\Omega_\phi h^2$	$\sigma^{eff}_{H^0}$ (cm^2)	σ^{eff}_{ϕ} (cm^2)
BPC1	{ 209, 483, 213, 239, 0.006, 0.09, 0.13 }	0.0082	0.1084	3.7×10^{-47}	2.8×10^{-46}
BPC2	{ 129, 476, 158, 180, 0.011, 0.069, 0.13 }	0.0032	0.1175	6.7×10^{-47}	1.8×10^{-46}
BPC3	{ 100, 96, 127, 178, 0.010, 0.002, 0.56 }	0.0021	0.1156	6.8×10^{-47}	3.7×10^{-48}

BPs	$m_{H^\pm} - m_{H^0}$	$\{ \lambda_1,\ \lambda_2,\ \lambda_3 \}$	$\{ M_R,\ \mathrm{Tr}[Y_\nu^\dagger Y_\nu] \}$	Validity Scale (μ)
BPC1	30 ($< m_W$)	{ 0.456, −0.416, −0.028 }	$\{10^8,\ 0.5\}$	1.22×10^{19} (M_{pl})
BPC2	51 ($< m_W$)	{ 0.543, −0.383, −0.137 }	$\{10^8,\ 0.5\}$	1.22×10^{19} (M_{pl})
BPC3	78 ($\sim m_W$)	{ 0.737, −0.615, −0.101 }	$\{10^8,\ 0.5\}$	$\sim 10^{14}$

Table 5.4: DM masses, quartic couplings, relic densities and spin independent effective DM-neucleon cross-section of selected benchmark points for collider study. All benchmark points chosen here have $m_{H^\pm} - m_{H^0} < m_{W^\pm}$ for off-shell production of $W^\pm$. The maximum scale (μ) of Higgs vacuum satability and peturbativity in presence of right handed neutrinos are also noted. All masses and scales are in GeV.

$m_{H^0} + \Delta M$, where ΔM indicates the mass difference with the inert DM and serves as a very important variable for the signal characteristics. The plot on RHS show that production cross-section is decreasing with larger charged scalar mass $m_{H^\pm}$, where we have demonstrated three fixed values of $m_{H^\pm} - m_{H^0} = 5,\ 50$ and 100 GeV. Around $m_{H^\pm} \sim m_h/2$, there is a sharpe fall of production cross-section. This is because, for $m_{H^\pm} \leq m_h/2$, there is a significant contribution arising from Higgs production and its subsequent decay to the charged scalar components, which otherwise turns into an off-shell propagator to yield a subdued contribution to Drell-Yan production. Following [168], a conservative bound on the charge scalars is applied here as $m_{H^\pm} \geq 70$ GeV, as indicated in the RHS plot of Fig. 5.25.

We next choose a set of benchmark points (BPs) allowed from DM relic, direct search constraints as well as from Higgs invisible decay constraints for performing collider simulation, shown in Table 5.4 and Table 5.5. The BPs are also allowed from absolute Higgs vacuum stability and perturbativity limits in presence of right handed neutrinos, valid upto scale μ as mentioned in the tables. The benchmark points are divided into two categories: (BPC1-BPC3) in Table 5.4 correspond to $\Delta M = m_{H^\pm} - m_{H^0} \lesssim m_{W^\pm}$ where the charged scalar, $H^\pm$ decay through off-shell $W^\pm$. On the other hand, benchmark points (BPD1-BPD2) in Table 5.5 correspond to $\Delta M = m_{H^\pm} - m_{H^0} > m_{W^\pm}$, where the charged scalar $H^\pm$ decay through on-shell $W^\pm$. Each table (Table 5.4 and Table 5.5) consists of two parts: the first part contains all the relevant dark sector masses, couplings, relic density and direct search cross-sections of both DM components. The second part demonstrates the mass difference ($\Delta M = m_{H^\pm} - m_{H^0}$), choice of right handed neutrino mass, neutrino Yukawa and the maximum scale of validity (μ) of the Higgs vacuum.

The simulation technique adopted here is as follows. We first implemented the model in `FeynRule` [108] to generate UFO file which is required to feed into event generator `Madgraph`[109]. Then these events are passed to `Pythia` [110] for hadronization.

BPs	$\{ m_{H^0},\ m_{\phi},\ m_{A^0},\ m_{H^\pm},\ \lambda_L,\ \lambda_{\phi h},\ \lambda_c \}$	$\Omega_{H^0}h^2$	$\Omega_{\phi}h^2$	$\sigma^{eff}_{H^0}$ (cm^2)	σ^{eff}_{ϕ} (cm^2)
BPD1	{ 92, 386, 155, 198, 0.004, 0.063, 0.10 }	0.0032	0.1167	4.5×10^{-47}	2.2×10^{-46}
BPD2	{ 90, 437, 136, 233, 0.006, 0.077, 0.11 }	0.0030	0.1150	6.9×10^{-47}	2.6×10^{-46}

BPs	$m_{H^\pm} - m_{H^0}$	$\{ \lambda_1,\ \lambda_2,\ \lambda_3 \}$	$\{ M_R,\ \mathrm{Tr}[Y_\nu^\dagger Y_\nu] \}$	Validity Scale (μ)
BPD1	106 ($> m_W$)	{ 1.024, −0.7588, −0.2571 }	$\{10^8,\ 0.5\}$	10^{10}
BPD2	143 ($> m_W$)	{ 1.538, −1.354, −0.1718 }	$\{10^6,\ 0.5\}$	10^8

Table 5.5: DM masses, quartic couplings, relic densities and spin independent effective DM-neucleon cross-section of selected benchmark points for collider study. All benchmark points chosen here have $m_{H^\pm} - m_{H^0} > m_{W^\pm}$ for on-shell production of $W^\pm$. The maximum scale (μ) of Higgs vacuum satability and peturbativity in presence of right handed neutrinos are also noted. All masses and scales are in GeV.

All parton level leading order (LO) signal events and SM background events[4] are generated in `Madgraph` at $\sqrt{s} = 14$ TeV using `cteq6l1` [112] parton distribution. Leptons ($\ell = e, \mu$) isolation, jet and unclustered event formation to mimic to the actual collider environment are performed as follows:
(i) Lepton isolation: The minimum transverse momentum required to identify a lepton ($\ell = e, \mu$) has been kept as $p_T > 20$ GeV and we also require the lepton to be produced in the central region of detector followed by pseudorapidity selection as $|\eta| < 2.5$. Two leptons are separated from each other with minimum distance $\Delta R \geq 0.2$ in $\eta - \phi$ plane. To separate leptons from jets we further imposed $\Delta R \geq 0.4$.
(ii) Jet formation: For jet formation, we used cone algorithm `PYCELL` in built in `Pythia`. All partons within a cone of $\Delta R \leq 0.4$ around a jet initiator with $p_T > 20$ GeV is identified to form a jet. It is important to identify jets in our case because we require the final state signal to be hadronically quiet i.e. to have zero jets.
(iii) Unclustered Objects: All final state objects with $0.5 < p_T < 20$ GeV and $2.5 < |\eta| < 5$ are considered as unclustered objects. Those objects neither form jets nor identified as isolated leptons and they only contribute to missing energy.
The main idea is to see if the signal events rise over SM background. For that there are three key kinematic variables where the signal and background show different sensitivity. They are:

- *Missing Energy ($\not{E}_T$):* The most important signature of DM being produced at collider. This is defined by a *vector sum* of transverse momentum of all the missing particles (those are not registered in the detector); this in turn can be estimated form the momentum imbalance in the transverse direction associated to the visible particles. Thus missing energy (MET) is defined as:

$$\not{E}_T = -\sqrt{(\sum_{\ell,j} p_x)^2 + (\sum_{\ell,j} p_y)^2}, \tag{5.41}$$

  where the sum runs over all visible objects that include the leptons, jets and the unclustered components.

[4]There are several SM process which contribute to the chosen $\ell^+\ell^- + (\not{E}_T)$ signal, dominant processes are: $t\bar{t}$, W^+W^-, ZZ and W^+W^-Z.

- *Transverse Mass (H_T):* Transverse mass of an event is identified with the *scalar sum* of the transverse momentum of objects reconstructed in a collider event, namely lepton and jets as defined above.

$$H_T = \sum_{\ell,j} \sqrt{(p_x)^2 + (p_y)^2}. \tag{5.42}$$

- *Invariant mass ($m_{\ell\ell}$):* Invariant mass of opposite sign dilepton hints to the parent particle, from which the leptons have been produced and thus helps segregating signal from background. This is defined as:

$$m_{\ell^+\ell^-} = \sqrt{(\sum_{\ell^+\ell^-} p_x)^2 + (\sum_{\ell^+\ell^-} p_y)^2 + (\sum_{\ell^+\ell^-} p_z)^2}. \tag{5.43}$$

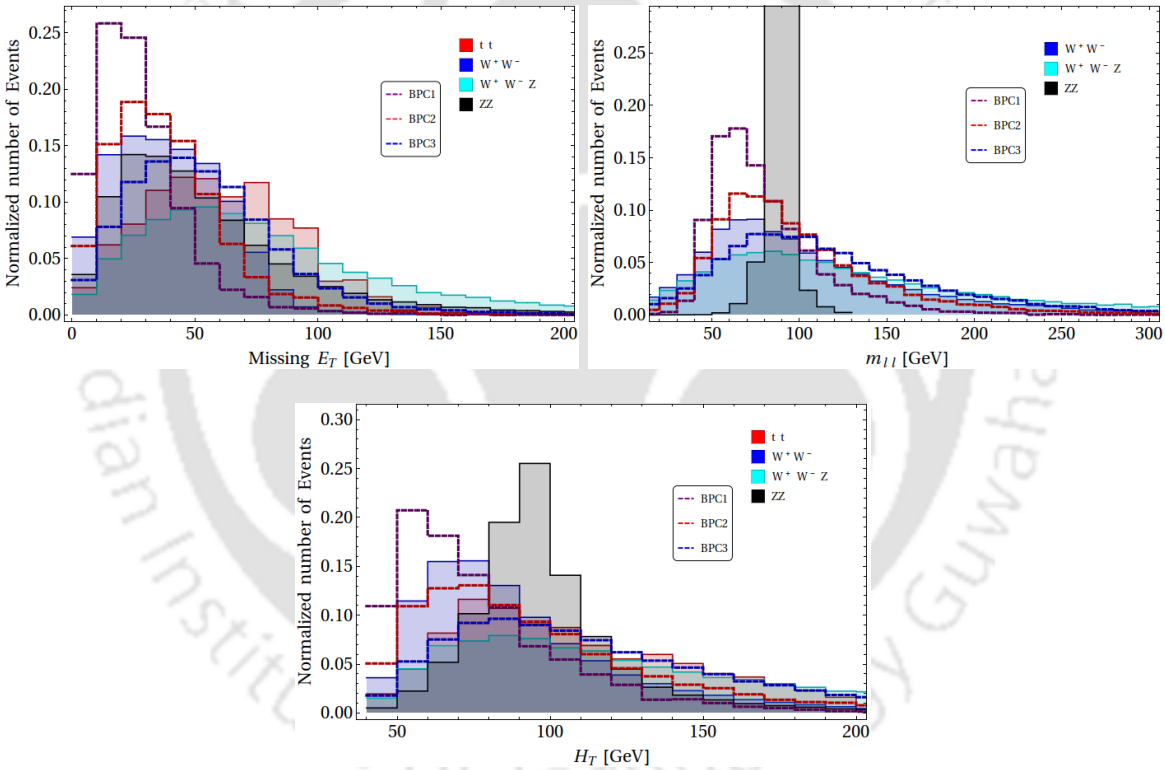

Figure 5.26: Distribution of missing energy ($\not{E}_T$), invariant mass of OSDL ($m_{\ell^+\ell^-}$) and transverse mass (H_T) for signal events $\ell^+\ell^- + (\not{E}_T)$ and dominant SM background events at LHC with $\sqrt{s} =$ 14 TeV .

The distribution of missing energy ($\not{E}_T$), invariant mass of opposite sign dilepton ($m_{\ell^+\ell^-}$) and transverse mass (H_T) for the BPs along with dominant SM background events are shown in Fig. 5.26 top left, top right and bottom panel respectively. All BPs depicted in Fig. 5.26 correspond to $m_{H^\pm} - m_{H^0} \equiv \Delta M < m_{W^\pm}$ where opposite sign dilepton are produced from off-shell $W^\pm$ mediator. All the distributions are normalised to one event. Missing energy (as well as H_T) distributions of BPs (BPC1-BPC3) show that the peak of distribution for the signal is on the left of SM background. This is because the benchmark points are characterised by small ΔM, where the charged

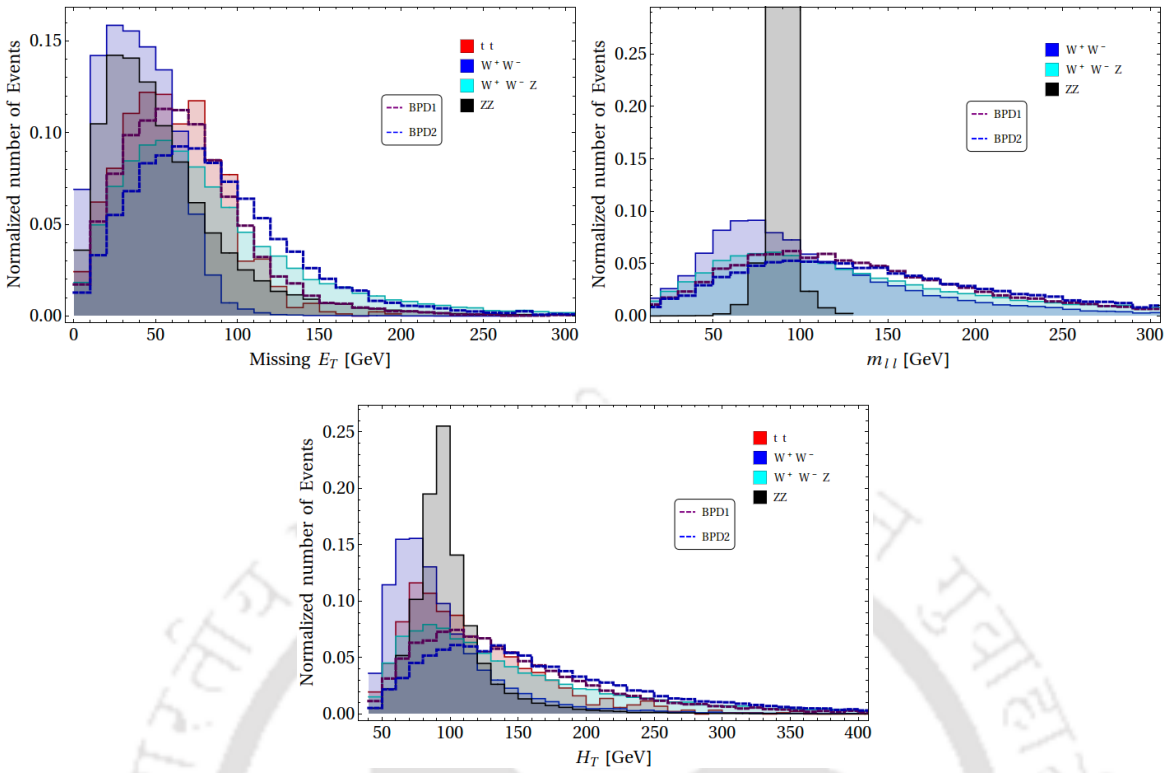

Figure 5.27: Distribution of missing energy ($\not{E}_T$), invariant mass of OSDL ($m_{\ell^+\ell^-}$) and transverse mass (H_T) for signal events $\ell^+\ell^- + (\not{E}_T)$ and dominant SM background events at LHC with $\sqrt{s} =$ 14 TeV .

scalars and inert DM have small mass splitting. Therefore, such situations are visibly segregated from SM background by MET and H_T distribution. Clearly, when ΔM becomes $m_{W^\pm}$ (for example, BPC3) the distribution closely mimic SM background. Therefore the signal events for this class of benchmark points can survive for a suitable upper $\not{E}_T$ and H_T cut while reducing SM backgrounds. It is important to take a note that OSDL events coming from ZZ background naturally peaks at m_Z in $m_{\ell\ell}$ distribution. Therefore, we use invariant mass cut in the Z mass window to get rid of this background.

The situation is reversed for larger splitting between the charged scalar component with DM, i.e $\Delta M \equiv m_{H^\pm} - m_{H^0} > m_{W^\pm}$ corresponding to BPs (BPD1-BPD2) as in Table 5.5. The distributions of $\not{E}_T$, $m_{\ell\ell}$ and H_T therefore become flatter and peak of the distribution shifts to higher value as shown in Fig. 5.27. In such cases the signal events for large ΔM can be separated from SM background at a suitable lower end cut of $\not{E}_T$ and H_T.
Therefore the selection cuts used in this analysis are summarised as follows:

- Invariant mass ($m_{\ell\ell}$) cuts: $m_{\ell\ell} < (m_Z - 15)$ GeV and $m_{\ell\ell} > (m_Z + 15)$ GeV.
- H_T cuts:
  - $H_T < 70$ when $m_{H^\pm} - m_{H^0} < m_{W^\pm}$.
  - $H_T > 150, 200$ when $m_{H^\pm} - m_{H^0} > m_{W^\pm}$.

- $\not{E}_T$ cuts:
  - $\not{E}_T < 30, 40$ when $m_{H^\pm} - m_{H^0} < m_{W^\pm}$.
  - $\not{E}_T > 100, 150$ when $m_{H^\pm} - m_{H^0} > m_{W^\pm}$.

BPs	$\sigma^{\rm OSD}$ (fb)	$\not{E}_T$ (GeV)	H_T (GeV)	$\sigma^{\rm OSD}_{\rm eff}$(fb)	$N^{\rm OSD}_{\rm eff}@\mathcal{L} = 10^2 {\rm fb}^{-1}$
BPC1	9.16	< 30	< 70	0.28	28
		< 40		0.33	33
BPC2	27.14	< 30	< 70	0.72	72
		< 40		0.97	97
BPC3	28.65	< 30	< 70	0.35	35
		< 40		0.55	55

Table 5.6: Signal cross-section for BPC1-BPC3 after the selection cuts are employed.

We next turn to signal and background events that survive after the selection cuts are employed. The signal events are listed in Table 5.6 for BPC1-BPC3.

Similarly, signal events for BPD1-BPD2 are listed in Table 5.7 using a lower cut on

BPs	$\sigma^{\rm OSD}$ (fb)	$\not{E}_T$ (GeV)	H_T (GeV)	$\sigma^{\rm OSD}_{\rm eff}$(fb)	$N^{\rm OSD}_{\rm eff}@\mathcal{L} = 10^2 {\rm fb}^{-1}$
BPD1	19.91	>100	>150	0.75	75
			>200	0.48	48
		>150	> 150	0.23	23
			>200	0.21	21
BPD2	11.16	>100	>150	0.87	87
			>200	0.59	59
		>150	> 150	0.34	34
			>200	0.29	29

Table 5.7: Signal cross-section for BPD1-BPD2 after the selection cuts are employed.

$\not{E}_T$ and H_T. The signal cross-section and event numbers for this class of points are much smaller due to the fact that the charged scalar masses are on higher side as for all of the cases $\Delta m > m_W$ independent of DM masses. However, the SM background events get even more suppressed with the set of $\not{E}_T$, H_T cuts. The SM background cross-section and event numbers after cut flow is mentioned in Table 5.8. Therefore, in

SM Bkg.	$\sigma^{\rm OSD}$ (fb)	$\not{E}_T$ (GeV)	H_T (GeV)	$\sigma^{\rm OSD}_{\rm eff}$(fb)	$N^{\rm OSD}_{\rm eff}@\mathcal{L} = 10^2 {\rm fb}^{-1}$
$t\,\bar{t}$	36.69×10^3	< 30	< 70	6.23	623
		< 40		10.27	1027
		>100	>150	10.64	1064
			>200	4.40	440
		>150	> 150	1.47	147
			>200	1.10	110
$W^+\,W^-$	4.74×10^3	< 30	< 70	131.18	13118
		< 40		187.89	18789
		>100	>150	7.72	772
			>200	4.97	4.97
		>150	> 150	1.23	123
			>200	1.18	118
$Z\,Z$	0.25×10^3	< 30	< 70	0.53	53
		< 40		0.69	69
		>100	>150	0.18	18
			>200	0.05	5
		>150	> 150	0.09	9
			>200	0.04	4
$W^+\,W^-Z$	1.00	< 30	< 70	0.01	1
		< 40		0.02	2
		>100	>150	0.06	6
			>200	0.04	4
		>150	> 150	0.03	3
			>200	0.02	2

Table 5.8: Dominant SM background contribution to $\ell^+\ell^- + (\not{E}_T)$ signal events for $\sqrt{s} = 14$ TeV at LHC. The effective number of final state background events with different $\not{E}_T$, H_T and $m_{\ell\ell}$ cuts are tabulated for luminosity $\mathcal{L} = 100\ fb^{-1}$. To incorporate the Next-to-Leading order (NLO) cross section of SM background we have used appropriate K-factors [111].

spite of smaller signal events in this region of parameter space with BPD benchmark points, the discovery potential of the signal requires similar luminosity to that of BPC cases.

Finally we present the discovery reach of the signal events in terms of significance $\sigma = \frac{S}{\sqrt{S+B}}$, where S denotes signal events and B denotes SM background events in terms of luminosity. This is shown in Fig. 5.28. This shows that the benchmark points that characterise the two component DM framework, can yield a visible signature at high luminosity with $\mathcal{L} \sim 500$ fb^{-1} depending on the charged scalar mass and its splitting with DM for the case $m_{H^\pm} - m_{H^0} > m_{W^\pm}$.

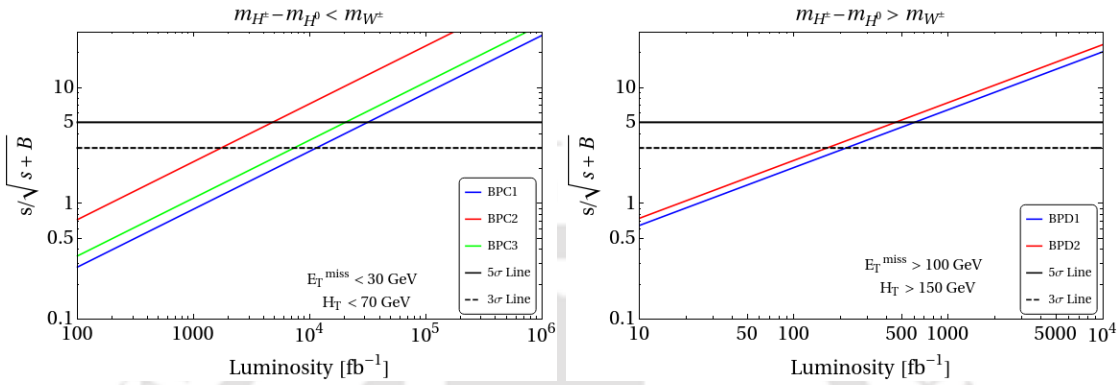

Figure 5.28: Signal significance of some select benchmark points at LHC for $\sqrt{s} = 14$ TeV, in terms of Luminosity (fb^{-1}). 3σ and 5σ lines are shown. Left: Points with $\Delta M < m_W$; Right: Points with $\Delta M > m_W$.

5.9 Summary and Conclusions

We have studied a two component scalar DM model in presence of right handed neutrinos that address neutrino mass generation through type I seesaw. The DM components are (i) a singlet scalar and (ii) an inert scalar doublet, both studied extensively as single component DM in literature. We show that the presence of second component enlarges the available parameter space significantly considering relic density and direct search constraints. In particular, the inert scalar DM will now be allowed in the so called 'desert region': $\{m_W - 550\}$ GeV. Also for singlet scalar, we can now revive it below TeV, which is otherwise discarded (except Higgs resonance) from direct search in single component framework. The results obtained for DM analysis crucially depends on DM-DM conversion, which have been demonstrated in details.

We also study the high scale perturbativity and vacuum stability of the Higgs potential by analysing two loop RGE β functions. This in turn puts further constraints on the available DM parameter space of the model. One of the important conclusions obtained are that the mass splitting of the charged scalar component to the corresponding DM component of inert doublet is crucially tamed depending on the absolute stability scale of the scalar potential, coming from the perturbativity constraint on the quartic and Yukawa coupling. For example, we find :

- Validity scale (μ) $\sim$ intermediate scale (10^{10} GeV): $\Delta M = m_{H^\pm} - m_{H^0} \sim \{7 - 120\}$ GeV,
- Validity scale (μ) $\sim$ Planck scale (10^{19} GeV): $\Delta M = m_{H^\pm} - m_{H^0} \sim \{11 - 70\}$ GeV,

with RH neutrino mass $M_R = 10^8$ GeV and Yukawa $\mathrm{Tr}[Y_\nu^\dagger Y_\nu] = 0.5$. The presence of RHNs in the model not only helps us addressing the neutrino masses but also controls the high scale validity of the model parameters, for example, low ΔM regions. This is how the neutrino and dark sector constraints affect each other.

Inert Higgs having charged scalars have collider detectability. We point out that the collider search prospect of the charged components are not only limited to low DM masses ($< m_W$), but is open to a larger mass range in presence of the second DM component, even after taking the high scale validity constraints. We exemplified this at LHC for hadronically quiet dilepton channel with missing energy, where ΔM, turns out to be a crucial kinematic parameter, constrained from DM, high scale validity and neutrino sector. At LHC, due to its $t\bar{t}$ background, high ΔM regions can be segregated from SM background more efficiently at the cost of small production cross section. Low ΔM regions are more affected by SM background, although the signal cross-section is high. Therefore, collider discovery of this model requires higher than the currently proposed high luminosity limit of LHC. On the other hand, e^+e^- annihilation have better possibility to explore low ΔM regions absent $t\bar{t}$ background. Here, we would like to comment that there are several studies that have been done in this direction, but the high scale validity constraint may alter the conclusion significantly as we demonstrate.

Finally, we would like to mention that the analysis performed here, although focus on a specific model set up, but there are some generic conclusions that can be borrowed. For example, if the two DM components have sufficient interaction in between, the available parameter space will be enlarged significantly from both relic density and direct search. The conversion of one DM into the other may also affect the collider outcome of the DM significantly. It is obvious that richer signal is obtained when we have larger multiplets in dark sector (as scalar doublet produces two lepton final state in the analysis). It is also possible that the dark sector and neutrino sector although may not inherit a common origin, the high scale validity of the model can bring them together.

Chapter 6

Sumarry and Future Direction

In summary, multipartite DM models with DM-DM interaction within dark sector does not affect direct search cross section at tree level but affects freeze-out of heavier DM component (and of lighter component when the annihilation to SM is low). Hence evidently multipartite frameworks yield a larger region of parameter space available from relic density and direct detection constraints. Such effects are demonstrated by our works considered in the thesis [16, 23, 169]. Beyond the models considered in the thesis, we also worked in several other multipartite frameworks, where DM-DM conversion together with semi-annihilation and co-annihilation effects bring down the available parameter space to future sensitivities of direct search. One such example was the multipartite scalar DM framework with $\mathcal{Z}_3$ symmetry[94].

The effect of DM-DM conversion also plays a crucial role in DM searches at LHC by for example, enlarging the mass splitting between charged and DM component which can help to segregate the signal from SM background by missing energy cut at collider. Such features may be key in discovery of DM in near future collider run as pointed out by our work [169] and have never been mentioned before to the best of our knowledge. High scale validity constraints on single component scalar DM framework in presence of right handed neutrinos may completely wash away the parameter space sensitive to collider detection, which one may reinstate in presence of two DM components [16].

Together, multipartite DM frameworks provide with a lot of possibilities to explore. Some key features are described in the thesis. These efforts still leave many other possibilities of multipartite DM scenarios involving an admixture of WIMP-FIMP, WIMP-SIMP and FIMP-SIMP scenarios to explore. They may offer some new dynamics and discovery potential of this 'known-unknown' dark sector.

However, discovery potential of a multipartite DM models at direct search require a lot more effort. For example, while projecting the direct search prospect of an individual component (say, ith component) in a multipartite DM framework, we use effective DM-nucleon cross-section by multiplying with the fraction of relic density $\sigma^i_{eff} = \frac{\Omega^i}{\Omega_{tot}}\sigma_{DM-N}$ with which the DM is present in the universe. It is a naive mechanism and a concrete idea of how multipartite DM can actually leave its imprint in the direct search detector through recoil is not very clear. Recently, a more comprehensive analysis for multipartite DM to interact with direct search experiment have been proposed [54, 63, 170]. The total recoil rate at energy E_R of the target nucleus (A, Z) with mass m_A for a two-component DM scenario is used so that

$$R_A(E_R) = R_A^{(1)}(E_R) + R_A^{(2)}(E_R), \tag{6.1}$$

where the individual recoil rates ($R_A^{(1,2)}(E_R)$) depends on the local DM density of that individual component, its velocity distribution in the DM halo and its interaction cross-section with nucleon (σ_i) folded with nuclear form factor. It has also been pointed that a kink may be observed in the combined rate which might reveal the presence of multipartite DM framework. Now it is important to investigate such possibilities in simpler WIMP like frameworks (two scalar singlets, one scalar one fermion etc) as we have addressed and a possible change in mixed (eg: WIMP-SIMP) frameworks. One may also address the same using DM effective field theory in a model independent analysis. It is also important to note that direct search sensitivity will soon hit the so-called neutrino floor when the direct search signal strength reaches cosmic neutrino interaction strength with nucleon. It will be interesting to address how one may disentangle the two cases (may be through the studies of annual signal modulation !) when DM-Nucleon interaction cross-section is predicted to be that low in many multipartite DM scenarios as we demonstrated.

Similarly, enhancement in collider search sensitivity due to the presence of multipartite DM has been guided mainly by the larger parameter space available due to DM-DM conversion or co-annihilation effects. However, that do not confront the question, that how one may discover multipartite frameworks at collider. There is no uniform guiding principle, but a more systematic analysis can be performed by addressing the following situations:

- Two DM components yielding same signature, but have different masses and couplings to visible sector and both are of WIMP nature. One may explore a possible change to $\not{E}_T$, H_T variables in terms of peak and end point together to infer something out of it.

- Two DM components, both of WIMP nature may yield different signal but the strengths of them are guided by their contribution to relic density.

- Two DM components, one of WIMP nature and one of FIMP category may yield a combination of signal excess versus a stable charge track. Again, the signal strengths may indicate their contribution to relic abundance.

- Finally, the signal at collider will have a correlation to direct search signal of DM. This also needs be addressed in multipartite DM frameworks.

To conclude, the thesis has addressed some possibilities of multipartite DM frameowrks, but leaves many unexplored. While plethora of DM interpretations require to be studied, a more concrete idea of a possible dark sector can only come from a signal at either direct or collider search to pin down further search strategy of DM.

Appendix A

Thermal average cross-section

Here we show the details derivation of BEQ in terms of DM number density as in Eqn.2.6. The number changing process considered here are:

$$\mathrm{DM}(p_1)\quad \mathrm{DM}(p_2)\quad \leftrightarrow\quad \mathrm{SM}(p_3)\quad \mathrm{SM}(p_4)\ .$$

The expression of $(\sigma v^2)_{2_{\rm DM}\to 2_{\rm SM}}$ is given by,

$$(\sigma v^2)_{2_{\rm DM}\to 2_{\rm SM}} = \frac{1}{(2E_1)(2E_2)}\int \frac{g_{\rm SM}\ d^3\mathbf{p_3}}{(2\pi)^3\ 2E_3}\ \frac{g_{\rm SM}\ d^3\mathbf{p_4}}{(2\pi)^3\ 2E_4} \times (2\pi)^4\delta^4(p_1+p_2-p_3-p_4)\times|\mathcal{M}_{\rm DM\to SM}|^2 \quad \text{(A.1)}$$

The definition of thermal average cross section, $\langle\sigma v^2\rangle_{2_{\rm DM}\to 2_{\rm SM}}$ is given by

$$\begin{aligned}\langle\sigma v^2\rangle_{2_{\rm DM}\to 2_{\rm SM}} &= \frac{1}{n^{\rm EQ}_{\rm DM}\ n^{\rm EQ}_{\rm DM}}\int \frac{g_{\rm DM}\ d^3\mathbf{p_1}}{(2\pi)^3\ 2E_1}\ \frac{g_{\rm DM}\ d^3\mathbf{p_2}}{(2\pi)^3 2E_2}\quad f^{\rm EQ}_{\rm DM}\ f^{\rm EQ}_{\rm DM}\ (\sigma v^2)_{2_{\rm DM}\to 2_{\rm SM}}\\ &= \frac{1}{n^{\rm EQ}_{\rm DM}\ n^{\rm EQ}_{\rm DM}}\int \frac{g_{\rm DM}\ d^3\mathbf{p_1}}{(2\pi)^3\ 2E_1}\ \frac{g_{\rm DM}\ d^3\mathbf{p_2}}{(2\pi)^3\ 2E_2}\ \frac{g_{\rm SM}\ d^3\mathbf{p_3}}{(2\pi)^3\ 2E_3}\ \frac{g_{\rm SM}\ d^3\mathbf{p_4}}{(2\pi)^3\ 2E_4}\\ &\quad\times(2\pi)^4\delta^4(p_1+p_2-p_3-p_4)|\mathcal{M}_{\rm DM\to SM}|^2\ f^{\rm EQ}_{\rm DM}\ f^{\rm EQ}_{\rm DM},\end{aligned} \quad \text{(A.2)}$$

where

$$n^{\rm EQ}_{\rm DM} = \frac{g_{\rm DM}}{(2\pi)^3}\int d^3\mathbf{p}\ f^{\rm EQ}_{\rm DM}. \quad \text{(A.3)}$$

The BEQ for the process $2_{\rm DM}\to 2_{\rm SM}$ can be expressed as

$$\begin{aligned}\frac{n_{\rm DM}}{dt}+3Hn_{\rm DM} &= -\int \frac{g_{\rm DM}\ d^3\mathbf{p_1}}{(2\pi)^3\ 2E_1}\ \frac{g_{\rm DM}\ d^3\mathbf{p_2}}{(2\pi)^3\ 2E_2}\ \frac{g_{\rm SM}\ d^3\mathbf{p_3}}{(2\pi)^3\ 2E_3}\ \frac{g_{\rm SM}\ d^3\mathbf{p_4}}{(2\pi)^3\ 2E_4}\\ &\quad\times(2\pi)^4\delta^4(p_1+p_2-p_3-p_4)\times|\mathcal{M}_{\rm DM\to SM}|^2\left[\ f_{\rm DM}\ f_{\rm DM}-\ f_{\rm SM}\ f_{\rm SM}\right]\\ &= -\int \frac{g_{\rm DM}\ d^3\mathbf{p_1}}{(2\pi)^3\ 2E_1}\ \frac{g_{\rm DM}\ d^3\mathbf{p_2}}{(2\pi)^3\ 2E_2}\ \frac{g_{\rm SM}\ d^3\mathbf{p_3}}{(2\pi)^3\ 2E_3}\ \frac{g_{\rm SM}\ d^3\mathbf{p_4}}{(2\pi)^3\ 2E_4}\\ &\quad\times(2\pi)^4\delta^4(p_1+p_2-p_3-p_4)\times|\mathcal{M}_{\rm DM\to SM}|^2\\ &\quad\times\left[\frac{f^{\rm EQ}_{\rm DM}f^{\rm EQ}_{\rm DM}}{n^{\rm EQ}_{\rm DM}n^{\rm EQ}_{\rm DM}}\ n_{\rm DM}\ n_{\rm DM}-\frac{f^{\rm EQ}_{\rm SM}f^{\rm EQ}_{\rm SM}}{n^{\rm EQ}_{\rm SM}n^{\rm EQ}_{\rm SM}}\ n_{\rm SM}\ n_{\rm SM}\right],\end{aligned} \quad \text{(A.4)}$$

where f replaced as $f = \frac{f^{\rm EQ}}{n^{\rm EQ}} n$. At equilibrium : $f^{\rm EQ}_{\rm SM} = f^{\rm EQ}_{\rm DM}$ and $n^{\rm EQ}_{\rm SM} = n_{\rm SM}$. Now above BEQ reads as

$$\begin{aligned}
\frac{n_{\rm DM}}{dt} + 3Hn_{\rm DM} &= -\int \frac{g_{\rm DM}\, d^3\mathbf{p_1}}{(2\pi)^3\ 2E_1} \frac{g_{\rm DM}\, d^3\mathbf{p_2}}{(2\pi)^3\ 2E_2} \frac{g_{\rm SM}\, d^3\mathbf{p_3}}{(2\pi)^3\ 2E_3} \frac{g_{\rm SM}\, d^3\mathbf{p_4}}{(2\pi)^3\ 2E_4} \\
&\quad \times (2\pi)^4 \delta^4(p_1 + p_2 - p_3 - p_4) \times |\mathcal{M}_{\rm DM\to SM}|^2 \\
&\quad \times \frac{f^{\rm EQ}_{\rm DM} f^{\rm EQ}_{\rm DM}}{n^{\rm EQ}_{\rm DM} n^{\rm EQ}_{\rm DM}} \Big[n_{\rm DM}\ n_{\rm DM} - n^{\rm EQ}_{\rm DM}\ n^{\rm EQ}_{\rm DM} \Big] \\
&= -\frac{1}{n^{\rm EQ}_{\rm DM} n^{\rm EQ}_{\rm DM}} \int \frac{g_{\rm DM}\, d^3\mathbf{p_1}}{(2\pi)^3\ 2E_1} \frac{g_{\rm DM}\, d^3\mathbf{p_2}}{(2\pi)^3\ 2E_2} \frac{g_{\rm SM}\, d^3\mathbf{p_3}}{(2\pi)^3\ 2E_3} \frac{g_{\rm SM}\, d^3\mathbf{p_4}}{(2\pi)^3\ 2E_4} \\
&\quad \times (2\pi)^4 \delta^4(p_1 + p_2 - p_3 - p_4) \times |\mathcal{M}_{\rm DM\to SM}|^2 \\
&\quad \times f^{\rm EQ}_{\rm DM} f^{\rm EQ}_{\rm DM} \Big[n_{\rm DM}\ n_{\rm DM} - n^{\rm EQ}_{\rm DM}\ n^{\rm EQ}_{\rm DM} \Big] \\
&= -\langle \sigma v \rangle_{2_{\rm DM}\to 2_{\rm SM}} \Big[n^2_{DM} - \Big(n^{\rm EQ}_{\rm DM} \Big)^2 \Big] \qquad \text{(A.5)}
\end{aligned}$$

Now we derive general expression of $\langle \sigma v^2 \rangle_{2_{\rm DM}\to 2_{\rm SM}}$ for any $2_{\rm DM} \to 2_{\rm SM}$ process considering squre of the matrix amplitude, $|\mathcal{M}_{\rm DM\to SM}|^2$ independent of outgoing particles momentum. Then the Eqn. A.1 is expressed as

$$\begin{aligned}
(\sigma v^2)_{2_{\rm DM}\to 2_{\rm SM}} &= \frac{1}{(2E_1)(2E_2)} \frac{|\mathcal{M}_{\rm DM\to SM}|^2}{(2\pi)^6} \int \frac{g_{\rm SM}\, d^3\mathbf{p_3}}{2E_3} \frac{g_{\rm SM}\, d^3\mathbf{p_4}}{2E_4} \\
&\quad \times (2\pi)^4 \delta^3(\mathbf{p_1} + \mathbf{p_2} - \mathbf{p_3} - \mathbf{p_4}) \delta(E_1 + E_2 - E_3 - E_4) \qquad \text{(A.6)}
\end{aligned}$$

In the center of mass frame $\mathbf{p_1} + \mathbf{p_2} = 0$ and $E_1 = E_2 = \frac{\sqrt{s}}{2}$. Now,

$$\begin{aligned}
(\sigma v^2)_{2_{\rm DM}\to 2_{\rm SM}} &= \frac{1}{s} \frac{|\mathcal{M}_{\rm DM\to SM}|^2}{(2\pi)^2} \int \frac{d^3\mathbf{p_3}}{2E_3} \frac{d^3\mathbf{p_4}}{2E_4} \\
&\quad \delta^3(\mathbf{p_3} + \mathbf{p_4})\ \delta\Big(2\ m_{\rm DM} - \sqrt{\mathbf{p_3}^2 + m^2_{\rm SM}} - \sqrt{\mathbf{p_4}^2 + m^2_{\rm SM}} \Big) \\
&= \frac{1}{s} \frac{|\mathcal{M}_{\rm DM\to SM}|^2}{(2\pi)^2} \int \frac{d^3\mathbf{p_3}}{2E_3} \frac{1}{2\sqrt{\mathbf{p_3}^2 + m^2_{\rm SM}}} \delta(\sqrt{s} - 2\sqrt{\mathbf{p_3}^2 + m^2_{\rm SM}}) \\
&= \frac{1}{s} \frac{|\mathcal{M}_{\rm DM\to SM}|^2}{(2\pi)^2} \pi \int \frac{\mathbf{p_3}^2 d\mathbf{p_3}}{\mathbf{p_3}^2 + m^2_{\rm SM}} \delta\Big(\sqrt{s} - 2\sqrt{\mathbf{p_3}^2 + m^2_{\rm SM}} \Big) \\
&= \frac{1}{s} \frac{|\mathcal{M}_{\rm DM\to SM}|^2}{(2\pi)^2} \frac{\pi}{2} \int \frac{\mathbf{p_3}^2 d\mathbf{p_3}}{\mathbf{p_3}^2 + m^2_{\rm SM}} \delta\Big(\frac{\sqrt{s}}{2} - \sqrt{\mathbf{p_3}^2 + m^2_{\rm SM}} \Big) \\
&= \frac{1}{8\pi s} |\mathcal{M}_{\rm DM\to SM}|^2 \sqrt{1 - \frac{4m^2_{\rm SM}}{s}}. \qquad \text{(A.7)}
\end{aligned}$$

$n^{\rm EQ}_i$ can be expressed in terms of modified Bessel's function as [22],

$$\begin{aligned}
n^{\rm EQ}_{\rm DM} &= \frac{g_{\rm DM}}{(2\pi)^3} \int d^3\mathbf{p}\ f^{\rm EQ}_{\rm DM} \\
&= \frac{g_{\rm DM}}{(2\pi)^3} \times 4\pi m^3_{\rm DM} \int \Big(\frac{E_{\rm DM}}{m_{\rm DM}} \Big) \Big(\sqrt{\Big(\frac{E_{\rm DM}}{m_{\rm DM}} \Big)^2 - 1} \Big)\ e^{-(\frac{E_{\rm DM}}{m_{\rm DM}})(\frac{m_{\rm DM}}{T})} d\Big(\frac{E_{\rm DM}}{m_{\rm DM}} \Big) \\
&= \frac{g_{\rm DM}}{(2\pi)^3}\ 4\pi m^2_{\rm DM} T K_2(m_{\rm DM}/T). \qquad \text{(A.8)}
\end{aligned}$$

Appendix B

Two Loop SM Beta functions

Here we write the two loop β functions for gauge couplings, Yukawa coupling and Higgs quartic couplings in SM.

Gauge Couplings

$$\beta_{g_1}^{(1)} = \frac{41}{10} g_1^3 \tag{B.1}$$

$$\beta_{g_1}^{(2)} = \frac{1}{50} g_1^3 \Big(135 g_2^2 + 199 g_1^2 + 440 g_3^2 - 85 y_t^2 \Big) \tag{B.2}$$

$$\beta_{g_2}^{(1)} = -\frac{19}{6} g_2^3 \tag{B.3}$$

$$\beta_{g_2}^{(2)} = \frac{1}{30} g_2^3 \Big(175 g_2^2 + 27 g_1^2 + 360 g_3^2 - 45 y_t^2 \Big) \tag{B.4}$$

$$\beta_{g_3}^{(1)} = -7 g_3^3 \tag{B.5}$$

$$\beta_{g_3}^{(2)} = -\frac{1}{10} g_3^3 \Big(-11 g_1^2 + 20 y_t^2 + 260 g_3^2 - 45 g_2^2 \Big) \tag{B.6}$$

Quartic scalar couplings

$$\begin{aligned}\beta_{\lambda_H}^{(1)} &= +\frac{27}{200} g_1^4 + \frac{9}{20} g_1^2 g_2^2 + \frac{9}{8} g_2^4 - \frac{9}{5} g_1^2 \lambda_H - 9 g_2^2 \lambda_H + 24 \lambda_H^2 + 12 \lambda_H y_t^2 - 6 y_t^4 \\ &\quad + \Big(\lambda_{ah}^2 + \lambda_{ch}^2 \Big)\end{aligned} \tag{B.7}$$

$$\begin{aligned}\beta_{\lambda_H}^{(2)} &= -\frac{3411}{2000} g_1^6 - \frac{1677}{400} g_1^4 g_2^2 - \frac{289}{80} g_1^2 g_2^4 + \frac{305}{16} g_2^6 + \frac{1887}{200} g_1^4 \lambda_H + \frac{117}{20} g_1^2 g_2^2 \lambda_H - \frac{73}{8} g_2^4 \lambda_H \\ &\quad + \frac{108}{5} g_1^2 \lambda_H^2 + 108 g_2^2 \lambda_H^2 - 312 \lambda^3 - \frac{171}{100} g_1^4 y_t^2 + \frac{63}{10} g_1^2 g_2^2 y_t^2 - \frac{9}{4} g_2^4 y_t^2 \\ &\quad + \frac{17}{2} g_1^2 \lambda_H y_t^2 + \frac{45}{2} g_2^2 \lambda_H y_t^2 + 80 g_3^2 \lambda_H y_t^2 - 144 \lambda_H^2 y_t^2 - \frac{8}{5} g_1^2 y_t^4 - 32 g_3^2 y_t^4 - 3 \lambda_H y_t^4 + 30 y_t^6\end{aligned} \tag{B.8}$$

Yukawa Couplings

$$\beta_{y_t}^{(1)} = \frac{3}{2}y_t^3 + y_t\Big(3y_t^2 - 8g_3^2 - \frac{17}{20}g_1^2 - \frac{9}{4}g_2^2\Big) \tag{B.9}$$

$$\begin{aligned}\beta_{y_t}^{(2)} = &+\frac{1}{80}\Big(120y_t^5 + y_t^3\Big(1280g_3^2 + 223g_1^2 - 540y_t^2 + 675g_2^2 - 960\lambda_H\Big)\Big)\\ &+ y_t\Big(\frac{1187}{600}g_1^4 - \frac{9}{20}g_1^2g_2^2 - \frac{23}{4}g_2^4 + \frac{19}{15}g_1^2g_3^2 + 9g_2^2g_3^2 - 108g_3^4 + 6\lambda_H^2\\ &+ \frac{17}{8}g_1^2y_t^2 + \frac{45}{8}g_2^2y_t^2 + 20g_3^2y_t^2 - \frac{27}{4}y_t^4\Big)\end{aligned} \tag{B.10}$$

Appendix C

Single Component vector-like fermion DM

We demonstrate the Feynman graphs and annihilation cross-section of a single component singlet doublet vector like fermion in this Appendix. The freeze-out of N_1 DM is controlled by the annihilation and co-annihilation channels as shown in Fig. C.1, C.2, C.3. This is mainly driven by gauge mediation and Higgs mediation apart from the t-channel heavy fermion $(N_2, N^{\pm})$ mediation.

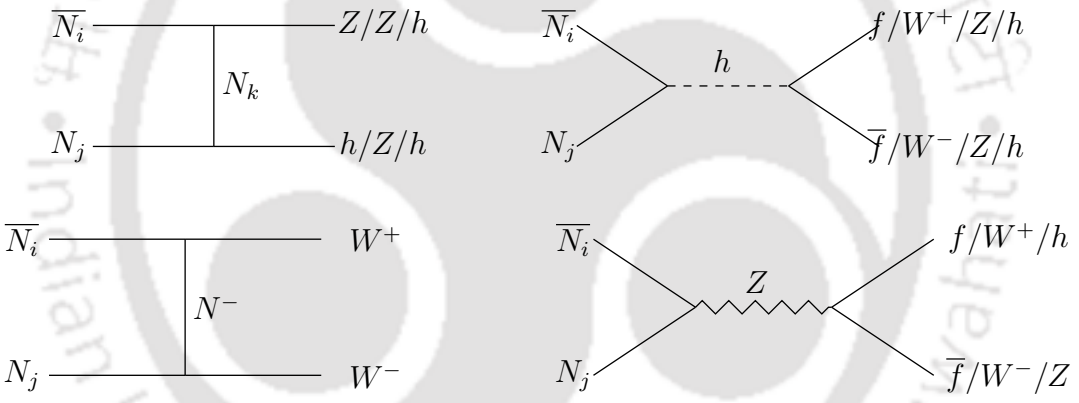

Figure C.1: Annihilation $(i = j)$ and Co-annihilation $(i \neq j)$ of fermion DM. Here $(i, j, k = 1, 2)$.

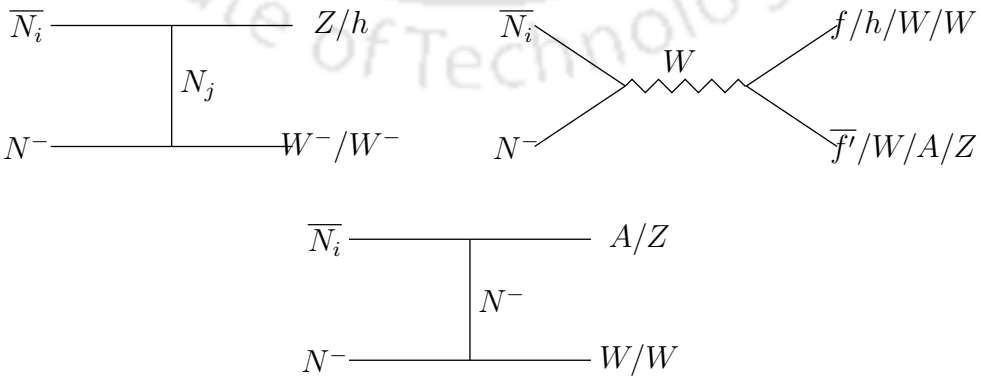

Figure C.2: Co-annihilation process of N_i $(i = 1, 2)$ with the charge component N^- to SM particles.

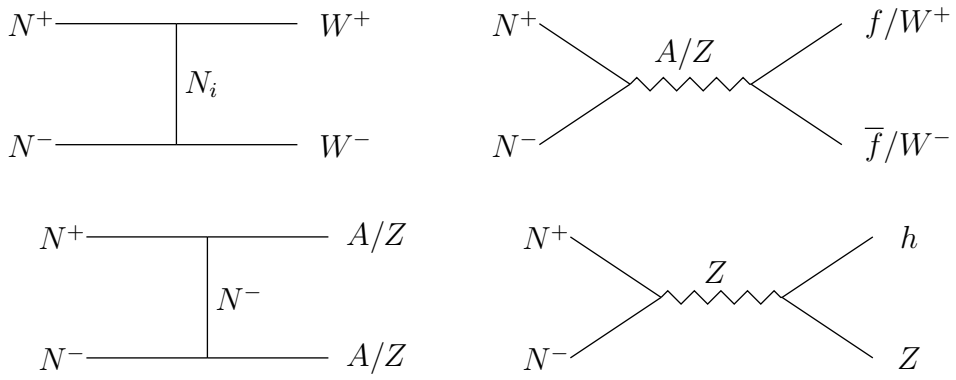

Figure C.3: Co-Annihilation process of charged fermions $N^{\pm}$ to SM particles in final states .

Relic density of vector like fermion DM is then governed by the effective number changing cross-section following [171],

$$\begin{aligned}\langle\sigma v\rangle_{N_1}^{eff} &= \frac{g_1^2}{g_{eff}^2}\langle\sigma v\rangle_{\overline{N_1}N_1} + \frac{2g_1g_2}{g_{eff}^2}\langle\sigma v\rangle_{\overline{N_1}N_2}\left(1+\frac{\Delta m}{m_{N_1}}\right)^{\frac{3}{2}} e^{-x\frac{\Delta m}{m_{N_1}}} \\ &+\frac{2g_1g_3}{g_{eff}^2}\langle\sigma v\rangle_{\overline{N_1}N^-}\left(1+\frac{\Delta m}{m_{N_1}}\right)^{\frac{3}{2}} e^{-x\frac{\Delta m}{m_{N_1}}} \\ &+\frac{2g_2g_3}{g_{eff}^2}\langle\sigma v\rangle_{N^+N_2}\left(1+\frac{\Delta m}{m_{N_1}}\right)^{3} e^{-2x\frac{\Delta m}{m_{N_1}}} \\ &+\frac{g_2^2}{g_{eff}^2}\langle\sigma v\rangle_{\overline{N_2}N_2}\left(1+\frac{\Delta m}{m_{N_1}}\right)^{3} e^{-2x\frac{\Delta m}{m_{N_1}}} \\ &+\frac{g_3^2}{g_{eff}^2}\langle\sigma v\rangle_{N^+N^-}\left(1+\frac{\Delta m}{m_{N_1}}\right)^{3} e^{-2x\frac{\Delta m}{m_{N_1}}}. \end{aligned} \tag{C.1}$$

In above equation, g_{eff}, defined as effective degrees of freedom, is given by

$$g_{eff} = g_1 + g_2\left(1+\frac{\Delta m}{m_{N_1}}\right)^{\frac{3}{2}} e^{-x\frac{\Delta m}{m_{N_1}}} + g_3\left(1+\frac{\Delta m}{m_{N_1}}\right)^{\frac{3}{2}} e^{-x\frac{\Delta m}{m_{N_1}}}, \tag{C.2}$$

where g_1, g_2 and g_3 are the degrees of freedom of N_1, N_2 and N^- respectively and $x = x_f = \frac{m_{N_1}}{T_f}$, where T_f is the freeze out temperature of N_1. Then relic density will be given by [15, 23] :

$$\Omega h^2 = \frac{854.45\times10^{-13}}{\sqrt{106.7}}\frac{x_f}{\langle\sigma v\rangle_{N_1}^{eff}}, \tag{C.3}$$

assuming $x_f \sim 20$.

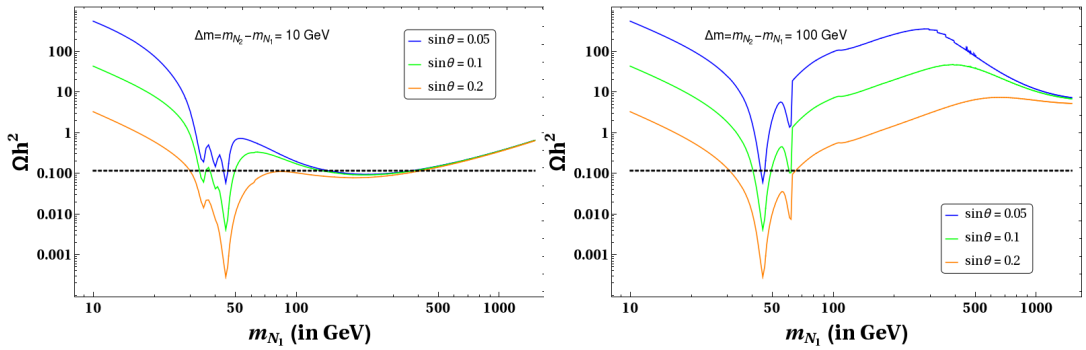

Figure C.4: Relic density of N_1 as a function of DM mass, m_{N_1} with different mixing angle, $\sin\theta = 0.05$ (blue), $\sin\theta = 0.1$ (green) and $\sin\theta = 0.2$ (orange). Each plot corresponds to fixed Δm: $= 10$ GeV (left), 100 GeV (right). Black dashed line indicates observed relic density $0.1133 \leq \Omega_{DM}h^2 \leq 0.1189$.

Variation of relic density of fermion DM is shown as a function of DM mass, for a fixed $\Delta m = 10$ GeV (left panel of the Fig. C.4) and 100 GeV (right panel of the Fig. C.4) and different choices of mixing angle,$\sin\theta$. We note that the annihilation cross-section is larger when we take larger values of $\sin\theta$, due to larger $SU(2)$ component, resulting smaller relic density. The resonance drop at $m_Z/2$ and at $m_h/2$ is observed due to s-channel Z and H mediated contributions. For $\Delta m = 100$ GeV, due to smaller co-annihilation contribution relic density increases compared to $\Delta m = 10$ GeV case.

Appendix D

Tree Level Unitarity Constraints

In this section, we perform the analysis to find the tree level unitarity limits on quartic couplings present in our model at high energy. The scattering amplitude for any $2 \to 2$ process can be expressed in terms of the Legendre polynomial as [172]

$$\mathcal{M}^{2\to 2} = 16\pi \sum_{l=0}^{\infty} a_l (2l+1) P_l(\cos\theta), \tag{D.1}$$

where θ is the scattering angle and $P_l(\cos\theta)$ is the Legendre polynomial of order l. In the high-energy limit, only the s-wave ($l = 0$) partial amplitude a_0 will determine the leading energy dependence of the scattering processes. The unitarity constraint turns out to be [133, 134, 172]

$$\text{Re } |a_0| < \frac{1}{2}. \tag{D.2}$$

The constraint in Eqn.(D.2) can be further converted to a bound on the scattering amplitude $\mathcal{M}$ [133, 134, 172]:

$$|\mathcal{M}| < 8\pi. \tag{D.3}$$

In the present set up, we have multiple possible $2 \to 2$ scattering processes. Therefore, we need to construct a matrix ($M^{2\to 2}_{i;j} = \mathcal{M}_{i\to j}$) by considering all possible two particle states. Finally, we calculate the eigenvalues of $\mathcal{M}$ and employ the bound as in Eqn. (D.3). In the high-energy limit, we express the SM Higgs doublet as $H^T = \left(w^+ \ \frac{h+iz}{\sqrt{2}}\right)$. Then, the scalar potential in Eqn.(5.2) gives rise to 19 neutral combinations of two particle states:

$$w^+w^-,\ H^+H^-,\ \frac{hh}{\sqrt{2}},\ \frac{zz}{\sqrt{2}},\ \frac{H^0H^0}{\sqrt{2}},\ \frac{A^0A^0}{\sqrt{2}},\ \frac{\phi\phi}{\sqrt{2}},\ h\ z,\ H^0\ A^0,\ w^+H^-,\ H^+w^-,$$
$$h\ H^0,\ h\ A^0,\ z\ H^0,\ z\ A^0,\ h\ \phi,\ z\ \phi,\ H^0\ \phi,\ A^0\ \phi\ . \tag{D.4}$$

and 10 singly charged two-particle states:

$$h\ w^+,\ z\ w^+,\ H^0H^+,\ A^0H^+,\ h\ H^+,\ z\ H^+,\ H^0\ w^+,\ A^0\ w^+,\ \phi\ w^+,\ \phi\ H^+\ . \tag{D.5}$$

Therefore, we can write the scattering amplitude matrix (M) in block-diagonal form by decomposing it into a neutral (NC) and singly charged(SC) sector as

$$M = \begin{pmatrix} M^{NC}_{19\times19} & 0 \\ 0 & M^{SC}_{10\times10} \end{pmatrix}. \tag{D.6}$$

where the sub-matrices are given by

$$M^{NC}{}_{19\times19} = \begin{pmatrix} (M_1^{NC})_{7\times7} & 0 & 0 & 0 \\ 0 & (M_2^{NC})_{2\times2} & 0 & 0 \\ 0 & 0 & (M_3^{NC})_{6\times6} & 0 \\ 0 & 0 & 0 & (M_4^{NC})_{4\times4} \end{pmatrix} \tag{D.7}$$

with

$$M_1^{NC} = \begin{pmatrix} 4\lambda_H & \lambda_1+\lambda_2+\lambda_3 & \sqrt{2}\lambda_H & \sqrt{2}\lambda_H & \frac{\lambda_1}{\sqrt{2}} & \frac{\lambda_1}{\sqrt{2}} & \frac{\lambda_{\phi h}}{\sqrt{2}} \\ \lambda_1+\lambda_2+\lambda_3 & 4\lambda_\Phi & \frac{\lambda_1}{\sqrt{2}} & \frac{\lambda_1}{\sqrt{2}} & \sqrt{2}\lambda_\Phi & \sqrt{2}\lambda_\Phi & \frac{\lambda_c}{\sqrt{2}} \\ \sqrt{2}\lambda_H & \frac{\lambda_1}{\sqrt{2}} & 3\lambda_H & \lambda_H & 2\left(\frac{\lambda_1}{4}+\frac{\lambda_2}{4}+\frac{\lambda_3}{4}\right) & 2\left(\frac{\lambda_1}{4}+\frac{\lambda_2}{4}+\frac{\lambda_3}{4}\right) & \frac{\lambda_{\phi h}}{2} \\ \sqrt{2}\lambda_H & \frac{\lambda_1}{\sqrt{2}} & \lambda_H & 3\lambda_H & 2\left(\frac{\lambda_1}{4}+\frac{\lambda_2}{4}+\frac{\lambda_3}{4}\right) & 2\left(\frac{\lambda_1}{4}+\frac{\lambda_2}{4}+\frac{\lambda_3}{4}\right) & \frac{\lambda_{\phi h}}{2} \\ \frac{\lambda_1}{\sqrt{2}} & \sqrt{2}\lambda_\Phi & 2\left(\frac{\lambda_1}{4}+\frac{\lambda_2}{4}+\frac{\lambda_3}{4}\right) & 2\left(\frac{\lambda_1}{4}+\frac{\lambda_2}{4}+\frac{\lambda_3}{4}\right) & 3\lambda_\Phi & \lambda_\Phi & \frac{\lambda_c}{2} \\ \frac{\lambda_1}{\sqrt{2}} & \sqrt{2}\lambda_\Phi & 2\left(\frac{\lambda_1}{4}+\frac{\lambda_2}{4}+\frac{\lambda_3}{4}\right) & 2\left(\frac{\lambda_1}{4}+\frac{\lambda_2}{4}+\frac{\lambda_3}{4}\right) & \lambda_\Phi & 3\lambda_\Phi & \frac{\lambda_c}{2} \\ \frac{\lambda_{\phi h}}{\sqrt{2}} & \frac{\lambda_c}{\sqrt{2}} & \frac{\lambda_{\phi h}}{2} & \frac{\lambda_{\phi h}}{2} & \frac{\lambda_c}{2} & \frac{\lambda_c}{2} & \frac{\lambda_\phi}{2} \end{pmatrix}, \tag{D.8}$$

$$M_3^{NC} = \begin{pmatrix} \lambda_1+\lambda_2+\lambda_3 & 0 & \frac{\lambda_2}{2}+\frac{\lambda_3}{2} & \frac{i\lambda_2}{2}+\frac{i\lambda_3}{2} & -\frac{i\lambda_2}{2}-\frac{i\lambda_3}{2} & \frac{\lambda_2}{2}+\frac{\lambda_3}{2} \\ 0 & \lambda_1+\lambda_2+\lambda_3 & \frac{\lambda_2}{2}+\frac{\lambda_3}{2} & -\frac{i\lambda_2}{2}-\frac{i\lambda_3}{2} & \frac{i\lambda_2}{2}+\frac{i\lambda_3}{2} & \frac{\lambda_2}{2}+\frac{\lambda_3}{2} \\ \frac{\lambda_2}{2}+\frac{\lambda_3}{2} & \frac{\lambda_2}{2}+\frac{\lambda_3}{2} & 4\left(\frac{\lambda_1}{4}+\frac{\lambda_2}{4}+\frac{\lambda_3}{4}\right) & 0 & 0 & 0 \\ -\frac{i\lambda_2}{2}-\frac{i\lambda_3}{2} & \frac{i\lambda_2}{2}+\frac{i\lambda_3}{2} & 0 & 4\left(\frac{\lambda_1}{4}+\frac{\lambda_2}{4}+\frac{\lambda_3}{4}\right) & 0 & 0 \\ \frac{i\lambda_2}{2}+\frac{i\lambda_3}{2} & -\frac{i\lambda_2}{2}-\frac{i\lambda_3}{2} & 0 & 0 & 4\left(\frac{\lambda_1}{4}+\frac{\lambda_2}{4}+\frac{\lambda_3}{4}\right) & 0 \\ \frac{\lambda_2}{2}+\frac{\lambda_3}{2} & \frac{\lambda_2}{2}+\frac{\lambda_3}{2} & 0 & 0 & 0 & 4\left(\frac{\lambda_1}{4}+\frac{\lambda_2}{4}+\frac{\lambda_3}{4}\right) \end{pmatrix}, \tag{D.9}$$

$$M_2^{NC} = \begin{pmatrix} 2\lambda_H & 0 \\ 0 & 2\lambda_\Phi \end{pmatrix}, \qquad M_4^{NC} = \begin{pmatrix} \lambda_{\phi h} & 0 & 0 & 0 \\ 0 & \lambda_{\phi h} & 0 & 0 \\ 0 & 0 & \lambda_c & 0 \\ 0 & 0 & 0 & \lambda_c \end{pmatrix}. \tag{D.10}$$

and

$$M^{SC} = \begin{pmatrix} 2\lambda_H & 0 & \frac{\lambda_2}{2}+\frac{\lambda_3}{2} & \frac{i\lambda_2}{2}+\frac{i\lambda_3}{2} & 0 & 0 & 0 & 0 & 0 & 0 \\ 0 & 2\lambda_H & -\frac{i\lambda_2}{2}-\frac{i\lambda_3}{2} & \frac{\lambda_2}{2}+\frac{\lambda_3}{2} & 0 & 0 & 0 & 0 & 0 & 0 \\ \frac{\lambda_2}{2}+\frac{\lambda_3}{2} & \frac{i\lambda_2}{2}+\frac{i\lambda_3}{2} & 2\lambda_\Phi & 0 & 0 & 0 & 0 & 0 & 0 & 0 \\ -\frac{i\lambda_2}{2}-\frac{i\lambda_3}{2} & \frac{\lambda_2}{2}+\frac{\lambda_3}{2} & 0 & 2\lambda_\Phi & 0 & 0 & 0 & 0 & 0 & 0 \\ 0 & 0 & 0 & 0 & \lambda_1 & 0 & \frac{\lambda_2}{2}+\frac{\lambda_3}{2} & -\frac{i\lambda_2}{2}-\frac{i\lambda_3}{2} & 0 & 0 \\ 0 & 0 & 0 & 0 & 0 & \lambda_1 & \frac{i\lambda_2}{2}+\frac{i\lambda_3}{2} & \frac{\lambda_2}{2}+\frac{\lambda_3}{2} & 0 & 0 \\ 0 & 0 & 0 & 0 & \frac{\lambda_2}{2}+\frac{\lambda_3}{2} & -\frac{i\lambda_2}{2}-\frac{i\lambda_3}{2} & \lambda_1 & 0 & 0 & 0 \\ 0 & 0 & 0 & 0 & \frac{i\lambda_2}{2}+\frac{i\lambda_3}{2} & \frac{\lambda_2}{2}+\frac{\lambda_3}{2} & 0 & \lambda_1 & 0 & 0 \\ 0 & 0 & 0 & 0 & 0 & 0 & 0 & 0 & \lambda_{\phi h} & 0 \\ 0 & 0 & 0 & 0 & 0 & 0 & 0 & 0 & 0 & \lambda_c \end{pmatrix} \tag{D.11}$$

After determining the eigenvalues of Eqn.(D.6) we conclude that tree level unitarity constraints in this set up are following:

$$\begin{aligned} |\lambda_H| < 4\pi, \quad |\lambda_\Phi| < 4\pi, \\ |\lambda_c| < 8\pi, \quad |\lambda_{\phi h}| < 8\pi, \\ |\lambda_1| < 8\pi, \quad |\lambda_1 + 2(\lambda_2 + \lambda_3)| < 8\pi \\ |\lambda_1 + \lambda_2 + \lambda_3| < 8\pi, \quad |\lambda_1 - \lambda_2 - \lambda_3| < 8\pi, \\ |(\lambda_\Phi + \lambda_H) \pm \sqrt{(\lambda_2 + \lambda_3)^2 + (\lambda_H - \lambda_\Phi)^2}| < 8\pi, \\ \text{and} \quad |x_{1,2,3}| < 16\pi \end{aligned} \tag{D.12}$$

where $x_{1,2,3}$ be the roots of following cubic equation

$$\begin{aligned} & x^3 + x^2(-12\lambda_H - 12\lambda_\Phi - \lambda_\phi) + x(-16\lambda_1^2 - 16\lambda_1\lambda_2 - 16\lambda_1\lambda_3 - 4\lambda_2^2 - 8\lambda_2\lambda_3 \\ & -4\lambda_3^2 - 4\lambda_c^2 + 144\lambda_H\lambda_\Phi + 12\lambda_H\lambda_\phi + 12\lambda_\Phi\lambda_\phi - 4\lambda_{\phi h}^2) + 16\lambda_1^2\lambda_\phi + 16\lambda_1\lambda_2\lambda_\phi \\ & +16\lambda_1\lambda_3\lambda_\phi - 32\lambda_1\lambda_c\lambda_{\phi h} + 4\lambda_2^2\lambda_\phi + 8\lambda_2\lambda_3\lambda_\phi - 16\lambda_2\lambda_c\lambda_{\phi h} + 4\lambda_3^2\lambda_\phi \\ & -16\lambda_3\lambda_c\lambda_{\phi h} + 48\lambda_c^2\lambda_H - 144\lambda_H\lambda_\Phi\lambda_\phi + 48\lambda_\Phi\lambda_{\phi h}^2 \ = 0 \end{aligned} \tag{D.13}$$

भारतीय प्रौद्योगिकी संस्थान गुवाहाटी
Indian Institute of Technology Guwahati

Bibliography

[1] S. L. Glashow, *Partial Symmetries of Weak Interactions*, *Nucl. Phys.* **22** (1961) 579–588.

[2] S. Weinberg, *A Model of Leptons*, *Phys. Rev. Lett.* **19** (1967) 1264–1266.

[3] F. Englert and R. Brout, *Broken Symmetry and the Mass of Gauge Vector Mesons*, *Phys. Rev. Lett.* **13** (1964) 321–323.

[4] P. W. Higgs, *Broken Symmetries and the Masses of Gauge Bosons*, *Phys. Rev. Lett.* **13** (1964) 508–509.

[5] G. S. Guralnik, C. R. Hagen and T. W. B. Kibble, *Global Conservation Laws and Massless Particles*, *Phys. Rev. Lett.* **13** (1964) 585–587.

[6] F. Zwicky, *On the Masses of Nebulae and of Clusters of Nebulae*, *Astrophys. J.* **86** (1937) 217–246.

[7] G. Bertone, D. Hooper and J. Silk, *Particle dark matter: Evidence, candidates and constraints*, *Phys. Rept.* **405** (2005) 279–390, [hep-ph/0404175].

[8] WMAP collaboration, D. N. Spergel et al., *Wilkinson Microwave Anisotropy Probe (WMAP) three year results: implications for cosmology*, *Astrophys. J. Suppl.* **170** (2007) 377, [astro-ph/0603449].

[9] N. Jarosik et al., *Seven-Year Wilkinson Microwave Anisotropy Probe (WMAP) Observations: Sky Maps, Systematic Errors, and Basic Results*, *Astrophys. J. Suppl.* **192** (2011) 14, [1001.4744].

[10] W. Hu and S. Dodelson, *Cosmic microwave background anisotropies*, *Ann. Rev. Astron. Astrophys.* **40** (2002) 171–216, [astro-ph/0110414].

[11] Planck collaboration, P. A. R. Ade et al., *Planck 2013 results. XVI. Cosmological parameters*, *Astron. Astrophys.* **571** (2014) A16, [1303.5076].

[12] V. C. Rubin and W. K. Ford, Jr., *Rotation of the Andromeda Nebula from a Spectroscopic Survey of Emission Regions*, *Astrophys. J.* **159** (1970) 379–403.

[13] E. Hayashi and S. D. M. White, *How Rare is the Bullet Cluster?*, *Mon. Not. Roy. Astron. Soc.* **370** (2006) L38–L41, [astro-ph/0604443].

[14] S. Profumo, *An Introduction to Particle Dark Matter*. World Scientific, 2017, 10.1142/q0001.

[15] E. W. Kolb and M. S. Turner, *The Early Universe*, *Front. Phys.* **69** (1990) 1–547.

[16] S. Bhattacharya, P. Ghosh and S. Verma, *SIMPler realisation of Scalar Dark Matter*, 1904.07562.

[17] G. D'Amico, M. Kamionkowski and K. Sigurdson, *Dark Matter Astrophysics*, 0907.1912.

[18] C. Balázs, T. Li and J. L. Newstead, *Observations are confirming the WIMP paradigm*, in *Proceedings, 10th Patras Workshop on Axions, WIMPs and WISPs (AXION-WIMP 2014): Geneva, Switzerland, June 29-July 4, 2014*, pp. 3–6, 2014. DOI.

[19] Y. Hochberg, E. Kuflik, T. Volansky and J. G. Wacker, *Mechanism for Thermal Relic Dark Matter of Strongly Interacting Massive Particles*, *Phys. Rev. Lett.* **113** (2014) 171301, [1402.5143].

[20] S.-M. Choi and H. M. Lee, *SIMP dark matter with gauged Z_3 symmetry*, *JHEP* **09** (2015) 063, [1505.00960].

[21] L. J. Hall, K. Jedamzik, J. March-Russell and S. M. West, *Freeze-In Production of FIMP Dark Matter*, *JHEP* **03** (2010) 080, [0911.1120].

[22] L. Feng, S. Profumo and L. Ubaldi, *Closing in on singlet scalar dark matter: LUX, invisible Higgs decays and gamma-ray lines*, *JHEP* **03** (2015) 045, [1412.1105].

[23] S. Bhattacharya, P. Poulose and P. Ghosh, *Multipartite Interacting Scalar Dark Matter in the light of updated LUX data*, *JCAP* **1704** (2017) 043, [1607.08461].

[24] P. Gondolo and G. Gelmini, *Cosmic abundances of stable particles: Improved analysis*, *Nucl. Phys.* **B360** (1991) 145–179.

[25] M. Klasen, M. Pohl and G. Sigl, *Indirect and direct search for dark matter*, *Prog. Part. Nucl. Phys.* **85** (2015) 1–32, [1507.03800].

[26] C. Rott, *Status of Dark Matter Searches (Rapporteur Talk)*, *PoS* **ICRC2017** (2018) 1119, [1712.00666].

[27] XENON collaboration, E. Aprile et al., *First Dark Matter Search Results from the XENON1T Experiment*, *Phys. Rev. Lett.* **119** (2017) 181301, [1705.06655].

[28] MAGIC, Fermi-LAT collaboration, M. L. Ahnen et al., *Limits to Dark Matter Annihilation Cross-Section from a Combined Analysis of MAGIC and Fermi-LAT Observations of Dwarf Satellite Galaxies*, *JCAP* **1602** (2016) 039, [1601.06590].

[29] R. W. Schnee, *Introduction to dark matter experiments*, in *Physics of the large and the small, TASI 09, proceedings of the Theoretical Advanced Study Institute in Elementary Particle Physics, Boulder, Colorado, USA, 1-26 June 2009*, pp. 775–829, 2011. 1101.5205. DOI.

[30] A. H. G. Peter, *Dark Matter: A Brief Review*, 1201.3942.

[31] P. Cushman et al., *Working Group Report: WIMP Dark Matter Direct Detection*, in *Proceedings, 2013 Community Summer Study on the Future of U.S. Particle Physics: Snowmass on the Mississippi (CSS2013): Minneapolis, MN, USA, July 29-August 6, 2013*, 2013. 1310.8327.

[32] J. Abdallah et al., *Simplified Models for Dark Matter Searches at the LHC*, *Phys. Dark Univ.* **9-10** (2015) 8–23.

[33] D. Abercrombie et al., *Dark Matter Benchmark Models for Early LHC Run-2 Searches: Report of the ATLAS/CMS Dark Matter Forum*, 1507.00966.

[34] M. Aoki, M. Duerr, J. Kubo and H. Takano, *Multi-Component Dark Matter Systems and Their Observation Prospects*, *Phys. Rev.* **D86** (2012) 076015, [1207.3318].

[35] Planck collaboration, P. A. R. Ade et al., *Planck 2015 results. XIII. Cosmological parameters*, *Astron. Astrophys.* **594** (2016) A13, [1502.01589].

[36] K. S. Babu and C. N. Leung, *Classification of effective neutrino mass operators*, *Nucl. Phys.* **B619** (2001) 667–689, [hep-ph/0106054].

[37] E. K. Akhmedov, G. C. Branco and M. N. Rebelo, *Seesaw mechanism and structure of neutrino mass matrix*, *Phys. Lett.* **B478** (2000) 215–223, [hep-ph/9911364].

[38] Particle Data Group collaboration, M. Tanabashi, K. Hagiwara, K. Hikasa, K. Nakamura, Y. Sumino, F. Takahashi et al., *Review of particle physics*, *Phys. Rev. D* **98** (Aug, 2018) 030001.

[39] J. R. Espinosa, *Vacuum Stability and the Higgs Boson*, *PoS* **LATTICE2013** (2014) 010, [1311.1970].

[40] LUX collaboration, D. S. Akerib et al., *Improved Limits on Scattering of Weakly Interacting Massive Particles from Reanalysis of 2013 LUX Data*, *Phys. Rev. Lett.* **116** (2016) 161301, [1512.03506].

[41] LUX collaboration, D. S. Akerib et al., *Results from a search for dark matter in the complete LUX exposure*, *Phys. Rev. Lett.* **118** (2017) 021303, [1608.07648].

[42] XENON100 collaboration, E. Aprile et al., *Implications on Inelastic Dark Matter from 100 Live Days of XENON100 Data*, *Phys. Rev.* **D84** (2011) 061101, [1104.3121].

[43] XENON100 collaboration, E. Aprile et al., *Dark Matter Results from 100 Live Days of XENON100 Data*, *Phys. Rev. Lett.* **107** (2011) 131302, [1104.2549].

[44] XENON collaboration, M. Messina, *Latest results of 1 tonne x year Dark Matter Search with XENON1T*, *PoS* **EDSU2018** (2018) 017.

[45] PandaX collaboration, H. Zhang et al., *Dark matter direct search sensitivity of the PandaX-4T experiment*, *Sci. China Phys. Mech. Astron.* **62** (2019) 31011, [1806.02229].

[46] PandaX-II collaboration, X. Cui et al., *Dark Matter Results From 54-Ton-Day Exposure of PandaX-II Experiment*, *Phys. Rev. Lett.* **119** (2017) 181302, [1708.06917].

[47] Q.-H. Cao, E. Ma, J. Wudka and C. P. Yuan, *Multipartite dark matter*, 0711.3881.

[48] S. Bhattacharya, A. Drozd, B. Grzadkowski and J. Wudka, *Two-Component Dark Matter*, *JHEP* **10** (2013) 158, [1309.2986].

[49] A. Biswas, D. Majumdar, A. Sil and P. Bhattacharjee, *Two Component Dark Matter : A Possible Explanation of 130 GeV $\gamma-$ Ray Line from the Galactic Centre*, *JCAP* **1312** (2013) 049, [1301.3668].

[50] L. Bian, R. Ding and B. Zhu, *Two Component Higgs-Portal Dark Matter*, *Phys. Lett.* **B728** (2014) 105–113, [1308.3851].

[51] S. Esch, M. Klasen and C. E. Yaguna, *A minimal model for two-component dark matter*, *JHEP* **09** (2014) 108, [1406.0617].

[52] A. Karam and K. Tamvakis, *Dark Matter from a Classically Scale-Invariant $SU(3)_X$*, *Phys. Rev.* **D94** (2016) 055004, [1607.01001].

[53] A. Dutta Banik, M. Pandey, D. Majumdar and A. Biswas, *Two component WIMP–FImP dark matter model with singlet fermion, scalar and pseudo scalar*, *Eur. Phys. J.* **C77** (2017) 657, [1612.08621].

[54] A. Ahmed, M. Duch, B. Grzadkowski and M. Iglicki, *Multi-Component Dark Matter: the vector and fermion case*, *Eur. Phys. J.* **C78** (2018) 905, [1710.01853].

[55] M. Aoki, D. Kaneko and J. Kubo, *Multicomponent Dark Matter in Radiative Seesaw Models*, *Front.in Phys.* **5** (2017) 53, [1711.03765].

[56] A. Poulin and S. Godfrey, *Multicomponent dark matter from a hidden gauged SU(3)*, *Phys. Rev.* **D99** (2019) 076008, [1808.04901].

[57] M. Aoki and T. Toma, *Boosted Self-interacting Dark Matter in a Multi-component Dark Matter Model*, *JCAP* **1810** (2018) 020, [1806.09154].

[58] S. Yaser Ayazi and A. Mohamadnejad, *Scale-Invariant Two Component Dark Matter*, *Eur. Phys. J.* **C79** (2019) 140, [1808.08706].

[59] B. Barman, S. Bhattacharya and M. Zakeri, *Multipartite Dark Matter in $SU(2)_N$ extension of Standard Model and signatures at the LHC*, *JCAP* **1809** (2018) 023, [1806.01129].

[60] S. Chakraborti and P. Poulose, *Interplay of Scalar and Fermionic Components in a Multi-component Dark Matter Scenario*, 1808.01979.

[61] S. Chakraborti, A. Dutta Banik and R. Islam, *Probing Multicomponent Extension of Inert Doublet Model with a Vector Dark Matter*, 1810.05595.

[62] S. Bhattacharya, A. K. Saha, A. Sil and J. Wudka, *Dark Matter as a remnant of SQCD Inflation*, *JHEP* **10** (2018) 124, [1805.03621].

[63] J. Herrero-Garcia, A. Scaffidi, M. White and A. G. Williams, *On the direct detection of multi-component dark matter: sensitivity studies and parameter estimation*, *JCAP* **1711** (2017) 021, [1709.01945].

[64] J. Herrero-Garcia, A. Scaffidi, M. White and A. G. Williams, *On the direct detection of multi-component dark matter: implications of the relic abundance*, *JCAP* **1901** (2019) 008, [1809.06881].

[65] H. Han, J. M. Yang, Y. Zhang and S. Zheng, *Collider Signatures of Higgs-portal Scalar Dark Matter*, *Phys. Lett.* **B756** (2016) 109–112, [1601.06232].

[66] V. Silveira and A. Zee, *SCALAR PHANTOMS*, *Phys. Lett.* **161B** (1985) 136–140.

[67] J. McDonald, *Gauge singlet scalars as cold dark matter*, *Phys. Rev.* **D50** (1994) 3637–3649, [hep-ph/0702143].

[68] W.-L. Guo and Y.-L. Wu, *The Real singlet scalar dark matter model*, *JHEP* **10** (2010) 083, [1006.2518].

[69] A. Drozd, B. Grzadkowski and J. Wudka, *Multi-Scalar-Singlet Extension of the Standard Model - the Case for Dark Matter and an Invisible Higgs Boson*, *JHEP* **04** (2012) 006, [1112.2582].

[70] J. M. Cline and K. Kainulainen, *Electroweak baryogenesis and dark matter from a singlet Higgs*, *JCAP* **1301** (2013) 012, [1210.4196].

[71] H. Han and S. Zheng, *Higgs-portal Scalar Dark Matter: Scattering Cross Section and Observable Limits*, *Nucl. Phys.* **B914** (2017) 248–256, [1510.06165].

[72] I. Chakraborty and A. Kundu, *Controlling the fine-tuning problem with singlet scalar dark matter*, *Phys. Rev.* **D87** (2013) 055015, [1212.0394].

[73] WMAP collaboration, G. Hinshaw et al., *Nine-Year Wilkinson Microwave Anisotropy Probe (WMAP) Observations: Cosmological Parameter Results*, *Astrophys. J. Suppl.* **208** (2013) 19, [1212.5226].

[74] H. Davoudiasl, R. Kitano, T. Li and H. Murayama, *The New minimal standard model*, *Phys. Lett.* **B609** (2005) 117–123, [hep-ph/0405097].

[75] J. Elias-Miro, J. R. Espinosa, G. F. Giudice, H. M. Lee and A. Strumia, *Stabilization of the Electroweak Vacuum by a Scalar Threshold Effect*, *JHEP* **06** (2012) 031, [1203.0237].

[76] K. Kannike, *Vacuum Stability of a General Scalar Potential of a Few Fields*, *Eur. Phys. J.* **C76** (2016) 324, [1603.02680].

[77] G. Cynolter, E. Lendvai and G. Pocsik, *Note on unitarity constraints in a model for a singlet scalar dark matter candidate*, *Acta Phys. Polon.* **B36** (2005) 827–832, [hep-ph/0410102].

[78] T. G. Steele, Z.-W. Wang, D. Contreras and R. B. Mann, *Viable dark matter via radiative symmetry breaking in a scalar singlet Higgs portal extension of the standard model*, *Phys. Rev. Lett.* **112** (2014) 171602, [1310.1960].

[79] J. M. Cline, K. Kainulainen, P. Scott and C. Weniger, *Update on scalar singlet dark matter*, *Phys. Rev.* **D88** (2013) 055025, [1306.4710].

[80] A. Bandyopadhyay, S. Chakraborty, A. Ghosal and D. Majumdar, *Constraining Scalar Singlet Dark Matter with CDMS, XENON and DAMA and Prediction for Direct Detection Rates*, *JHEP* **11** (2010) 065, [1003.0809].

[81] C. P. Burgess, M. Pospelov and T. ter Veldhuis, *The Minimal model of nonbaryonic dark matter: A Singlet scalar*, *Nucl. Phys.* **B619** (2001) 709–728, [hep-ph/0011335].

[82] K. Kannike, *Vacuum Stability Conditions From Copositivity Criteria*, *Eur. Phys. J.* **C72** (2012) 2093, [1205.3781].

[83] M. E. Peskin and T. Takeuchi, *Estimation of oblique electroweak corrections*, *Phys. Rev.* **D46** (1992) 381–409.

[84] G. Bélanger, F. Boudjema, A. Pukhov and A. Semenov, *micrOMEGAs4.1: two dark matter candidates*, *Comput. Phys. Commun.* **192** (2015) 322–329, [1407.6129].

[85] Z.-P. Liu, Y.-L. Wu and Y.-F. Zhou, *Enhancement of dark matter relic density from the late time dark matter conversions*, *Eur. Phys. J.* **C71** (2011) 1749, [1101.4148].

[86] G. Steigman, B. Dasgupta and J. F. Beacom, *Precise Relic WIMP Abundance and its Impact on Searches for Dark Matter Annihilation*, *Phys. Rev.* **D86** (2012) 023506, [1204.3622].

[87] M. Srednicki, R. Watkins and K. A. Olive, *Calculations of Relic Densities in the Early Universe*, *Nucl. Phys.* **B310** (1988) 693.

[88] K. Ghorbani and H. Ghorbani, *Scalar split WIMPs in future direct detection experiments*, *Phys. Rev.* **D93** (2016) 055012, [1501.00206].

[89] G. Belanger, F. Boudjema, A. Pukhov and A. Semenov, *Dark matter direct detection rate in a generic model with micrOMEGAs 2.2*, *Comput. Phys. Commun.* **180** (2009) 747–767, [0803.2360].

[90] J. M. Alarcon, J. Martin Camalich and J. A. Oller, *The chiral representation of the πN scattering amplitude and the pion-nucleon sigma term*, *Phys. Rev.* **D85** (2012) 051503, [1110.3797].

[91] J. M. Alarcon, L. S. Geng, J. Martin Camalich and J. A. Oller, *The strangeness content of the nucleon from effective field theory and phenomenology*, *Phys. Lett.* **B730** (2014) 342–346, [1209.2870].

[92] J. D. Lewin and P. F. Smith, *Review of mathematics, numerical factors, and corrections for dark matter experiments based on elastic nuclear recoil*, *Astropart. Phys.* **6** (1996) 87–112.

[93] J. R. Espinosa, C. Grojean, M. Muhlleitner and M. Trott, *First Glimpses at Higgs' face*, *JHEP* **12** (2012) 045, [1207.1717].

[94] S. Bhattacharya, P. Ghosh, T. N. Maity and T. S. Ray, *Mitigating Direct Detection Bounds in Non-minimal Higgs Portal Scalar Dark Matter Models*, *JHEP* **10** (2017) 088, [1706.04699].

[95] P. Ghosh, A. K. Saha and A. Sil, *Study of Electroweak Vacuum Stability from Extended Higgs Portal of Dark Matter and Neutrinos*, *Phys. Rev.* **D97** (2018) 075034, [1706.04931].

[96] S. Bhattacharya, N. Sahoo and N. Sahu, *Minimal vectorlike leptonic dark matter and signatures at the LHC*, *Phys. Rev.* **D93** (2016) 115040, [1510.02760].

[97] S. Bhattacharya, N. Sahoo and N. Sahu, *Singlet-Doublet Fermionic Dark Matter, Neutrino Mass and Collider Signatures*, *Phys. Rev.* **D96** (2017) 035010, [1704.03417].

[98] M. Hoferichter, P. Klos, J. Menéndez and A. Schwenk, *Improved limits for Higgs-portal dark matter from LHC searches*, *Phys. Rev. Lett.* **119** (2017) 181803, [1708.02245].

[99] S. Bhattacharya, B. Karmakar, N. Sahu and A. Sil, *Flavor origin of dark matter and its relation with leptonic nonzero θ_{13} and Dirac CP phase δ*, *JHEP* **05** (2017) 068, [1611.07419].

[100] P. Pal, *An Introductory Course of Particle Physics*. Taylor & Francis, 2014.

[101] F. Pisano and A. T. Tran, *Anomaly cancellation in a class of chiral flavor gauge models*, in *14th Brazilian Meeting on Particles and Fields Caxambu, Brazil, September 29-October 3, 1993*, 1993.

[102] Particle Data Group collaboration, M. Tanabashi et al., *Review of Particle Physics*, *Phys. Rev.* **D98** (2018) 030001.

[103] LUX collaboration, D. S. Akerib et al., *Limits on spin-dependent WIMP-nucleon cross section obtained from the complete LUX exposure*, *Phys. Rev. Lett.* **118** (2017) 251302, [1705.03380].

[104] XENON collaboration, E. Aprile et al., *Dark Matter Search Results from a One Tonne× Year Exposure of XENON1T*, 1805.12562.

[105] XENON collaboration, E. Aprile et al., *Physics reach of the XENON1T dark matter experiment*, *JCAP* **1604** (2016) 027, [1512.07501].

[106] J. A. Casas, D. G. Cerdeño, J. M. Moreno and J. Quilis, *Reopening the Higgs portal for single scalar dark matter*, *JHEP* **05** (2017) 036, [1701.08134].

[107] S. Bahrami, M. Frank, D. K. Ghosh, N. Ghosh and I. Saha, *Dark matter and collider studies in the left-right symmetric model with vectorlike leptons*, *Phys. Rev.* **D95** (2017) 095024, [1612.06334].

[108] A. Alloul, N. D. Christensen, C. Degrande, C. Duhr and B. Fuks, *FeynRules 2.0 - A complete toolbox for tree-level phenomenology*, *Comput. Phys. Commun.* **185** (2014) 2250–2300, [1310.1921].

[109] J. Alwall, M. Herquet, F. Maltoni, O. Mattelaer and T. Stelzer, *MadGraph 5 : Going Beyond*, *JHEP* **06** (2011) 128, [1106.0522].

[110] T. Sjostrand, S. Mrenna and P. Z. Skands, *PYTHIA 6.4 Physics and Manual*, *JHEP* **05** (2006) 026, [hep-ph/0603175].

[111] J. Alwall, R. Frederix, S. Frixione, V. Hirschi, F. Maltoni, O. Mattelaer et al., *The automated computation of tree-level and next-to-leading order differential cross sections, and their matching to parton shower simulations*, *JHEP* **07** (2014) 079, [1405.0301].

[112] R. Placakyte, *Parton Distribution Functions*, in *Proceedings, 31st International Conference on Physics in collisions (PIC 2011): Vancouver, Canada, August 28-September 1, 2011*, 2011. 1111.5452.

[113] J. Martin, C. Ringeval and V. Vennin, *Encyclopædia Inflationaris*, *Phys. Dark Univ.* **5-6** (2014) 75–235, [1303.3787].

[114] J. Martin, *The Observational Status of Cosmic Inflation after Planck*, *Astrophys. Space Sci. Proc.* **45** (2016) 41–134, [1502.05733].

[115] K. Freese, E. I. Sfakianakis, P. Stengel and L. Visinelli, *The Higgs Boson can delay Reheating after Inflation*, *JCAP* **1805** (2018) 067, [1712.03791].

[116] R. Rangarajan and N. Sahu, *Perturbative Reheating and Gravitino Production in Inflationary Models*, *Phys. Rev.* **D79** (2009) 103534, [0811.1866].

[117] E. Gabrielli, M. Heikinheimo, K. Kannike, A. Racioppi, M. Raidal and C. Spethmann, *Towards Completing the Standard Model: Vacuum Stability, EWSB and Dark Matter*, *Phys. Rev.* **D89** (2014) 015017, [1309.6632].

[118] C.-S. Chen and Y. Tang, *Vacuum stability, neutrinos, and dark matter*, *JHEP* **04** (2012) 019, [1202.5717].

[119] W. Rodejohann and H. Zhang, *Impact of massive neutrinos on the Higgs self-coupling and electroweak vacuum stability*, *JHEP* **06** (2012) 022, [1203.3825].

[120] L. Delle Rose, C. Marzo and A. Urbano, *On the stability of the electroweak vacuum in the presence of low-scale seesaw models*, *JHEP* **12** (2015) 050, [1506.03360].

[121] M. Lindner, H. H. Patel and B. Radovčić, *Electroweak Absolute, Meta-, and Thermal Stability in Neutrino Mass Models*, *Phys. Rev.* **D93** (2016) 073005, [1511.06215].

[122] J. Chakrabortty, M. Das and S. Mohanty, *Constraints on TeV scale Majorana neutrino phenomenology from the Vacuum Stability of the Higgs*, *Mod. Phys. Lett.* **A28** (2013) 1350032, [1207.2027].

[123] C. Coriano, L. Delle Rose and C. Marzo, *Vacuum Stability in U(1)-Prime Extensions of the Standard Model with TeV Scale Right Handed Neutrinos*, *Phys. Lett.* **B738** (2014) 13–19, [1407.8539].

[124] J. N. Ng and A. de la Puente, *Electroweak Vacuum Stability and the Seesaw Mechanism Revisited*, *Eur. Phys. J.* **C76** (2016) 122, [1510.00742].

[125] C. Bonilla, R. M. Fonseca and J. W. F. Valle, *Vacuum stability with spontaneous violation of lepton number*, *Phys. Lett.* **B756** (2016) 345–349, [1506.04031].

[126] S. Khan, S. Goswami and S. Roy, *Vacuum Stability constraints on the minimal singlet TeV Seesaw Model*, *Phys. Rev.* **D89** (2014) 073021, [1212.3694].

[127] I. Garg, S. Goswami, V. K. N. and N. Khan, *Electroweak vacuum stability in presence of singlet scalar dark matter in TeV scale seesaw models*, *Phys. Rev.* **D96** (2017) 055020, [1706.08851].

[128] N. Chakrabarty, D. K. Ghosh, B. Mukhopadhyaya and I. Saha, *Dark matter, neutrino masses and high scale validity of an inert Higgs doublet model*, *Phys. Rev.* **D92** (2015) 015002, [1501.03700].

[129] D. K. Ghosh, N. Ghosh, I. Saha and A. Shaw, *Revisiting the high-scale validity of the type II seesaw model with novel LHC signature*, *Phys. Rev.* **D97** (2018) 115022, [1711.06062].

[130] R. N. Mohapatra and G. Senjanovic, *Neutrino Mass and Spontaneous Parity Nonconservation*, *Phys. Rev. Lett.* **44** (1980) 912.

[131] J. Schechter and J. W. F. Valle, *Neutrino Masses in SU(2) x U(1) Theories*, *Phys. Rev.* **D22** (1980) 2227.

[132] J. Chakrabortty, P. Konar and T. Mondal.

[133] J. Horejsi and M. Kladiva, *Tree-unitarity bounds for THDM Higgs masses revisited*, *Eur. Phys. J.* **C46** (2006) 81–91, [hep-ph/0510154].

[134] G. Bhattacharyya and D. Das, *Scalar sector of two-Higgs-doublet models: A minireview*, *Pramana* **87** (2016) 40, [1507.06424].

[135] A. Arhrib, R. Benbrik and N. Gaur, $H \to \gamma\gamma$ *in Inert Higgs Doublet Model*, *Phys. Rev.* **D85** (2012) 095021, [1201.2644].

[136] R. Barbieri, L. J. Hall and V. S. Rychkov, *Improved naturalness with a heavy Higgs: An Alternative road to LHC physics*, *Phys. Rev.* **D74** (2006) 015007, [hep-ph/0603188].

[137] GFITTER GROUP collaboration, M. Baak, J. Cúth, J. Haller, A. Hoecker, R. Kogler, K. Mönig et al., *The global electroweak fit at NNLO and prospects for the LHC and ILC*, *Eur. Phys. J.* **C74** (2014) 3046, [1407.3792].

[138] E. Lundstrom, M. Gustafsson and J. Edsjo, *The Inert Doublet Model and LEP II Limits*, *Phys. Rev.* **D79** (2009) 035013, [0810.3924].

[139] A. Pierce and J. Thaler, *Natural Dark Matter from an Unnatural Higgs Boson and New Colored Particles at the TeV Scale*, *JHEP* **08** (2007) 026, [hep-ph/0703056].

[140] Q.-H. Cao, E. Ma and G. Rajasekaran, *Observing the Dark Scalar Doublet and its Impact on the Standard-Model Higgs Boson at Colliders*, *Phys. Rev.* **D76** (2007) 095011, [0708.2939].

[141] A. Djouadi, *The Anatomy of electro-weak symmetry breaking. II. The Higgs bosons in the minimal supersymmetric model*, *Phys. Rept.* **459** (2008) 1–241, [hep-ph/0503173].

[142] B. Swiezewska and M. Krawczyk, *Diphoton rate in the inert doublet model with a 125 GeV Higgs boson*, *Phys. Rev.* **D88** (2013) 035019, [1212.4100].

[143] M. Krawczyk, D. Sokolowska, P. Swaczyna and B. Swiezewska, *Constraining Inert Dark Matter by $R_{\gamma\gamma}$ and WMAP data*, *JHEP* **09** (2013) 055, [1305.6266].

[144] ATLAS collaboration, G. Aad et al., *Measurement of Higgs boson production in the diphoton decay channel in pp collisions at center-of-mass energies of 7 and 8 TeV with the ATLAS detector*, *Phys. Rev.* **D90** (2014) 112015, [1408.7084].

[145] CMS collaboration, V. Khachatryan et al., *Observation of the diphoton decay of the Higgs boson and measurement of its properties*, *Eur. Phys. J.* **C74** (2014) 3076, [1407.0558].

[146] PLANCK collaboration, N. Aghanim et al., *Planck 2018 results. VI. Cosmological parameters*, 1807.06209.

[147] S. Vagnozzi, E. Giusarma, O. Mena, K. Freese, M. Gerbino, S. Ho et al., *Unveiling ν secrets with cosmological data: neutrino masses and mass hierarchy*, *Phys. Rev.* **D96** (2017) 123503, [1701.08172].

[148] P. F. de Salas, D. V. Forero, C. A. Ternes, M. Tortola and J. W. F. Valle, *Status of neutrino oscillations 2018: 3σ hint for normal mass ordering and improved CP sensitivity*, *Phys. Lett.* **B782** (2018) 633–640, [1708.01186].

[149] I. Esteban, M. C. Gonzalez-Garcia, M. Maltoni, I. Martinez-Soler and T. Schwetz, *Updated fit to three neutrino mixing: exploring the accelerator-reactor complementarity*, *JHEP* **01** (2017) 087, [1611.01514].

[150] A. Ilakovac and A. Pilaftsis, *Flavor violating charged lepton decays in seesaw-type models*, *Nucl. Phys.* **B437** (1995) 491, [hep-ph/9403398].

[151] D. Tommasini, G. Barenboim, J. Bernabeu and C. Jarlskog, *Nondecoupling of heavy neutrinos and lepton flavor violation*, *Nucl. Phys.* **B444** (1995) 451–467, [hep-ph/9503228].

[152] D. N. Dinh, A. Ibarra, E. Molinaro and S. T. Petcov, *The $\mu - e$ Conversion in Nuclei, $\mu \to e\gamma, \mu \to 3e$ Decays and TeV Scale See-Saw Scenarios of Neutrino Mass Generation*, *JHEP* **08** (2012) 125, [1205.4671].

[153] G. Bambhaniya, P. Bhupal Dev, S. Goswami, S. Khan and W. Rodejohann, *Naturalness, Vacuum Stability and Leptogenesis in the Minimal Seesaw Model*, *Phys. Rev.* **D95** (2017) 095016, [1611.03827].

[154] L. Lopez Honorez, E. Nezri, J. F. Oliver and M. H. G. Tytgat, *The Inert Doublet Model: An Archetype for Dark Matter*, *JCAP* **0702** (2007) 028, [hep-ph/0612275].

[155] D. Barducci, G. Belanger, J. Bernon, F. Boudjema, J. Da Silva, S. Kraml et al., *Collider limits on new physics within micrOMEGAs 4.3*, *Comput. Phys. Commun.* **222** (2018) 327–338, [1606.03834].

[156] A. Semenov, *LanHEP: A Package for the automatic generation of Feynman rules in field theory. Version 3.0*, *Comput. Phys. Commun.* **180** (2009) 431–454, [0805.0555].

[157] XENON collaboration, E. Aprile et al., *First results on the scalar WIMP-pion coupling, using the XENON1T experiment*, *Phys. Rev. Lett.* **122** (2019) 071301, [1811.12482].

[158] J. A. Casas and A. Ibarra, *Oscillating neutrinos and muon —¿ e, gamma*, *Nucl. Phys.* **B618** (2001) 171–204, [hep-ph/0103065].

[159] G. C. Branco, P. M. Ferreira, L. Lavoura, M. N. Rebelo, M. Sher and J. P. Silva, *Theory and phenomenology of two-Higgs-doublet models*, *Phys. Rept.* **516** (2012) 1–102, [1106.0034].

[160] Yu. F. Pirogov and O. V. Zenin, *Two loop renormalization group restrictions on the standard model and the fourth chiral family*, *Eur. Phys. J.* **C10** (1999) 629–638, [hep-ph/9808396].

[161] F. Staub, *SARAH 4 : A tool for (not only SUSY) model builders*, *Comput. Phys. Commun.* **185** (2014) 1773–1790, [1309.7223].

[162] W.-l. Guo, Z.-z. Xing and S. Zhou, *Neutrino Masses, Lepton Flavor Mixing and Leptogenesis in the Minimal Seesaw Model*, *Int. J. Mod. Phys.* **E16** (2007) 1–50, [hep-ph/0612033].

[163] D. Buttazzo, G. Degrassi, P. P. Giardino, G. F. Giudice, F. Sala, A. Salvio et al., *Investigating the near-criticality of the Higgs boson*, *JHEP* **12** (2013) 089, [1307.3536].

[164] G. Isidori, G. Ridolfi and A. Strumia, *On the metastability of the standard model vacuum*, *Nucl. Phys.* **B609** (2001) 387–409, [hep-ph/0104016].

[165] N. Khan and S. Rakshit, *Constraints on inert dark matter from the metastability of the electroweak vacuum*, *Phys. Rev.* **D92** (2015) 055006, [1503.03085].

[166] M. Gustafsson, S. Rydbeck, L. Lopez-Honorez and E. Lundstrom, *Status of the Inert Doublet Model and the Role of multileptons at the LHC*, *Phys. Rev.* **D86** (2012) 075019, [1206.6316].

[167] A. Bhardwaj, P. Konar, T. Mandal and S. Sadhukhan, *Probing Inert Doublet Model using jet substructure with multivariate analysis*, 1905.04195.

[168] J. Kalinowski, W. Kotlarski, T. Robens, D. Sokolowska and A. F. Zarnecki, *Benchmarking the Inert Doublet Model for e^+e^- colliders*, *JHEP* **12** (2018) 081, [1809.07712].

[169] S. Bhattacharya, P. Ghosh and N. Sahu, *Multipartite Dark Matter with Scalars, Fermions and signatures at LHC*, *JHEP* **02** (2019) 059, [1809.07474].

[170] C.-S. Chen and Y.-H. Lin, *On the evolution process of two-component dark matter in the Sun*, *JHEP* **04** (2018) 074, [1802.06956].

[171] K. Griest and D. Seckel, *Three exceptions in the calculation of relic abundances*, *Phys. Rev.* **D43** (1991) 3191–3203.

[172] B. W. Lee, C. Quigg and H. B. Thacker, *Weak Interactions at Very High-Energies: The Role of the Higgs Boson Mass*, *Phys. Rev.* **D16** (1977) 1519.